AFRL-PR-WP-TR-1999-2053

CREEP BEHAVIOR OF THIN LAMINATES OF IRON-COBALT ALLOYS FOR USE IN SWITCHED RELUCTANCE MOTORS AND GENERATORS

RICHARD T. FINGERS

JUNE 1999

FINAL REPORT FOR 1 JULY 1995 – 30 JUNE 1998

Approved for public release; distribution unlimited

PROPULSION DIRECTORATE
AIR FORCE RESEARCH LABORATORY
AIR FORCE MATERIEL COMMAND
WRIGHT-PATTERSON AFB OH 45433-7251

DTIC QUALITY INSPECTED 4

19990820 076

NOTICE

USING GOVERNMENT DRAWINGS, SPECIFICATIONS, OR OTHER DATA INCLUDED IN THIS DOCUMENT FOR ANY PURPOSE OTHER THAN GOVERNMENT PROCUREMENT DOES NOT IN ANY WAY OBLIGATE THE US GOVERNMENT. THE FACT THAT THE GOVERNMENT FORMULATED OR SUPPLIED THE DRAWINGS, SPECIFICATIONS, OR OTHER DATA DOES NOT LICENSE THE HOLDER OR ANY OTHER PERSON OR CORPORATION; OR CONVEY ANY RIGHTS OR PERMISSION TO MANUFACTURE, USE, OR SELL ANY PATENTED INVENTION THAT MAY RELATE TO THEM.

THIS REPORT IS RELEASABLE TO THE NATIONAL TECHNICAL INFORMATION SERVICE (NTIS). AT NTIS IT WILL BE AVAILABLE TO THE GENERAL PUBLIC, INCLUDING FOREIGN NATIONS.

THIS TECHNICAL REPORT HAS BEEN REVIEWED AND APPROVED FOR PUBLICATION.

RICHARD T. FINGERS, PhD
Power Generation & Thermal Mgt Branch
Power Division

C. Scott Rubertus
C. SCOTT RUBERTUS, Chief
Power Generation & Thermal Mgt Branch
Power Division

Joe McNamee
JOE MCNAMEE, Major, USAF
Deputy Chief
Power Division

Do not return copies of this report unless contractual obligations or notice on a specific document require its return

REPORT DOCUMENTATION PAGE

Form Approved
OMB No. 0704-0188

Public reporting burden for this collection of information is estimated to average 1 hour per response, including the time for reviewing instructions, searching existing data sources, gathering and maintaining the data needed, and completing and reviewing the collection of information. Send comments regarding this burden estimate or any other aspect of this collection of information, including suggestions for reducing this burden, to Washington Headquarters Services, Directorate for Information Operations and Reports, 1215 Jefferson Davis Highway, Suite 1204, Arlington, VA 22202-4302, and to the Office of Management and Budget, Paperwork Reduction Project (0704-0188), Washington, DC 20503.

1. AGENCY USE ONLY *(Leave blank)*

2. REPORT DATE
JUNE 1999

3. REPORT TYPE AND DATES COVERED
FINAL REPORT 1 July 1995 - 30 June 1998

4. TITLE AND SUBTITLE
CREEP BEHAVIOR OF THIN LAMINATES OF IRON COBALT ALLOYS FOR USE IN SWITCHED RELUCTANCE MOTORS AND GENERATORS

5. FUNDING NUMBERS
C: IN-HOUSE
PE 62203F
PR 3145
TA 01
WU C7

6. AUTHOR(S)
Dr. R. T. Fingers

7. PERFORMING ORGANIZATION NAME(S) AND ADDRESS(ES)
Propulsion Directorate
Air Force Research Laboratory
Air Force Material Command
Wright Patterson Air Force Base, Ohio 45433-7251

8. PERFORMING ORGANIZATION REPORT NUMBER

9. SPONSORING/MONITORING AGENCY NAME(S) AND ADDRESS(ES)
Propulsion Directorate
Air Force Research Laboratory
Air Force Material Command
Wright Patterson Air Force Base, Ohio 45433-7251
POC: Richard T. Fingers, AFRL/PRPG, 937-255-6241

10. SPONSORING/MONITORING AGENCY REPORT NUMBER
AFRL-PR-WP-TR-1999-2053

11. SUPPLEMENTARY NOTES

12a. DISTRIBUTION AVAILABILITY STATEMENT
Approved for Public Release; Distribution is Unlimited

12b. DISTRIBUTION CODE

13. ABSTRACT *(Maximum 200 words)*

The United States Air Force is in the process of developing magnetic bearings as well as an aircraft Integrated Power Unit and an Internal Starter/Generator for main propulsion engines. These efforts are the driving force behind a new emphasis to develop magnetic materials with strengths in excess of 80 ksi up to about 1000 degrees F. Hiperco Alloy 50HS is one of the leading candidates for application and is the focus of this effort. Tensile testing provided stress versus strain behaviors that clearly indicated: a yield point, Luders elongation, the Portevin-LeChatelier effect at elevated temperatures, and, most often a section of homogeneous deformation that concluded with necking and fracture. Creep testing indicated two distinct types of behavior. The first was a traditional response with primary, secondary, and tertiary stages, while the second type could be characterized by an abrupt increase in steady-state strain rate. Analyses of the mechanical behavior included double linea regression of empirically modeled data, scanning electron microscopy, isochronous stress-strain relations, and constant strai rate testing. Also, elastic and creep deformation analyses were done, which incorporated material property data and materia constants determined along with stress and displacement profiles for a specific design configuration.

14. SUBJECT TERMS
High Temperature Iron Cobalt Alloy Laminates Creep Tensile
Motor Generator Rotor Switched Reluctance Hiperco
Mechanical Testing

15. NUMBER OF PAGES
209

16. PRICE CODE

17. SECURITY CLASSIFICATION OF REPORT	**18. SECURITY CLASSIFICATION OF THIS PAGE**	**19. SECURITY CLASSIFICATION OF ABSTRACT**	**20. LIMITATION OF ABSTRACT**
UNCLASSIFIED	UNCLASSIFIED	UNCLASSIFIED	SAR

Standard Form 298 (Rev. 2-89) (EG)
Prescribed by ANSI Std. 239.18
Designed using Perform Pro, WHS/DIOR, Oct 94

TABLE OF CONTENTS

1. Introduction and Literature Review..........1
1.1 Motivation..........1
1.2 Deformation Fundamentals..........4
1.3 Basic Creep Phenomena..........15
1.4 Problem Statement..........24
1.5 Approach..........25

2. Material..........27
2.1 Material Description..........27
2.2 Constituents and Microstructure..........30
2.3 Manufacturing Process..........33

3. Experimental Techniques..........35
3.1 Specimen Preparation..........35
3.1.1 Tensile Specimens..........37
3.1.2 Creep Specimens..........38
3.2 Tensile Testing..........38
3.3 Constant Strain Rate Testing..........40
3.4 Creep Testing..........40
3.5 Microstructural Analysis..........42
3.6 X-Ray Diffraction Analysis..........44

4. Results and Discussion..........45
4.1 Tensile Testing..........45
4.1.1 Screening Phase..........45
4.1.2 Characterization Phase..........48
4.1.3 Constant Strain Rate Testing..........61
4.2 Creep Testing..........67
4.2.1 Creep Test Results..........67
4.2.2 Isochronous Stress Versus Strain..........97
4.2.3 Times To A Percent Creep Strain..........105
4.3 Creep Behavior Modeling..........112
4.3.1 Power Law Model..........112
4.3.2 Power Law Breakdown..........128
4.4 Microstructural Analysis..........130
4.5 X-Ray Diffraction Analysis..........133

5. Research Application..........139
5.1 Equilibrium Element..........139
5.2 Estimation of Elastic Deformation of an IPU Rotor Laminate..........146
5.2.1 Elastic Configuration #1..........151
5.2.2 Elastic Configuration #2..........153
5.2.3 Elastic Configuration #3..........155
5.2.4 Elastic Configuration #4..........157
5.3 Estimation of Creep Deformation of an IPU Rotor Laminate..........159
5.4 Analysis Impact..........167

6. Summary/Conclusions..........185
6.1 Accomplishments..........185
6.1.1 Tensile Testing..........185

6.1.2 Creep Testing *186*
6.2 Limitations and Applications 188
6.3 Future Research Topics 189
6.4 Study Impact 189

7. References 191

8. Appendix A 198

LIST OF FIGURES

Figure 1.1 Integrated Power Unit (IPU) Basic Configuration 2
Figure 1.2 Internal starter/Generator (IS/G) Application 3
Figure 1.3 Switched Reluctance Motor Rotor and Stator Laminates 5
Figure 1.4 Schematic of Typical Stress Versus Strain Behavior 7
Figure 1.5 A Reproduction of a Pen Plot of Stress Versus Strain Behavior of HA50HS Material Tested in the 45° Orientation to Rolling Direction at Room Temperature, Which Exhibits a Sharp Yield Point, Lüders Elongation, and the Beginning of Work Hardening 8
Figure 1.6 Reproduction of a Pen Plot of the Stress Versus Strain Behavior of HA50HS Material Tested in the 45° Orientation to the Rolling Direction at 1000°F, Which Exhibits Lüders Elongation, the Portevin-LeChatelier Effect, and the Beginning of Work Hardening 12
Figure 1.7 Schematic of a Typical Creep Curve 16
Figure 2.1 B2 Ordered Microstructure 31
Figure 2.2 SEM Micrograph of HA50HS Annealed for One Hour at 1300°F 32
Figure 3.1 Furnace Rack Used By Wall Colmonoy to Heat Treat Various Iron-Cobalt Test Specimens 36
Figure 3.2 Tensile Specimen Configurations 39
Figure 3.3 Tensile Specimen Inserted in Grips and Extensometer Frame With Thermocouples in Place 41
Figure 3.4 Creep Test Frame and Furnace with Aluminum Arms, Quartz Rod, and LVDT 43
Figure 4.1 Upper Yield Strength of HA50HS Specimens Tested in the Transverse Orientation as a Function of Anneal Temperature 46
Figure 4.2 Upper Yield Strength of HA50HS T1 Specimens Tested as a Function of Orientation to the Rolling Direction 47
Figure 4.3 Typical Stress Versus Strain Response for a HA50HS Iron-Cobalt Alloy Tested in the 45° Orientation to the Rolling Direction at (Top) Room Temperature, and (Bottom) at 1000°F 49
Figure 4.4 Formation of Lüders Bands on a HA50HS Tensile Specimen Tested in the 45 Degree Orientation at 800°F 51
Figure 4.5 Elastic Modulus Versus Temperature for HA50HS as Determined for the 45 Degree Orientation to Rolling Direction 52
Figure 4.6 Elastic Strain Versus Temperature of HA50HS Specimens Tested in the 45 Degree Orientation 53
Figure 4.7 Upper Yield Strength Versus Temperature of HA50HS Specimens Tested in the 45 Degree Orientation 54
Figure 4.8 Average Yield Strengths of HA50HS Specimens Tested in the 45 Degree Orientation 56
Figure 4.9 Lüders Strain (Yield Point Elongation) Versus Temperature of HA50HS Specimens Tested in the 45 Degree Orientation 59
Figure 4.10 Ultimate Tensile Strength Versus Test Temperature of HA50HS Specimens Tested in the 45 Degree Orientation 60
Figure 4.11 Total Elongation Versus Test Temperature of HA50HS Specimens Tested in the 45 Degree Orientation 62
Figure 4.12 SEM Micrograph of Fracture Surface of HA50HS Tensile Specimen Tested at Room Temperature in the 45 Degree Orientation to the Rolling Direction Orientation 63
Figure 4.13 Strain Rate Sensitivity Curves at 800°F Corresponding to the Maximum and Minimum Serration Stress Levels 65
Figure 4.14 Strain Rate Sensitivity Curves at 900°F Corresponding to the Maximum and Minimum Serration Stress Levels 66
Figure 4.15 Creep Strain Versus Time Response of HA50HS Specimens Tested at 700°F 69
Figure 4.16 Creep Strain Versus Time Response of HA50HS Specimens Tested at 800°F 70
Figure 4.17 Creep Strain Versus Time Response of HA50HS Specimens Tested at 850°F 73
Figure 4.18 Creep Strain Versus Time Response of HA50HS Specimens Tested at 900°F 75

Figure 4.19 Creep Strain Versus Time Response of HA50HS Specimens Tested at 950°F 78
Figure 4.20 Creep Strain Versus Time Response of HA50HS Specimens Tested at 1000°F 81
Figure 4.21 Creep Strain Versus Time Response of HA50HS Specimens Tested at 1100°F 85
Figure 4.22 Creep Strain Versus Time Response of HA50HS Specimens Tested at 65 ksi 88
Figure 4.23 Creep Strain Versus Time Response of HA50HS Specimens Tested at 75 ksi 89
Figure 4.24 Creep Strain Versus Time Response of HA50HS Specimens Tested at 80 ksi 91
Figure 4.25 Creep Strain Versus Time Response of HA50HS Specimens Tested at 85 ksi 92
Figure 4.26 Creep Strain Versus Time Response of HA50HS Specimens Tested at 90 ksi 94
Figure 4.27 Creep Strain Versus Time Response of HA50HS Specimens Tested at 100 ksi 95
Figure 4.28 Creep Strain Versus Time Response of HA50HS Specimens Tested at 120 ksi 96
Figure 4.29 Isochronous Stress-Strain Curves of HA50HS Specimens Tested at 800°F 98
Figure 4.30 Isochronous Stress-Strain Curves of HA50HS Specimens Tested at 900°F 99
Figure 4.31 Isochronous Stress-Strain Curves (Up to 90 ksi) of HA50HS Specimens Tested at 900°F 100
Figure 4.32 Isochronous Stress-Strain Curves of HA50HS Specimens Tested at 1000°F 101
Figure 4.33 Isochronous Stress-Strain Curves of HA50HS Specimens Tested at 1100°F 102
Figure 4.34 Time Required for HA50HS Specimen to Reach 0.1% Creep Strain as a Function of Applied Stress and Temperature 107
Figure 4.35 Time Required for HA50HS Specimen to Reach 0.2% Creep Strain as a Function of Applied Stress and Temperature 108
Figure 4.36 Time Required for HA50HS Specimen to Reach 0.5% Creep Strain as a Function of Applied Stress and Temperature 109
Figure 4.37 Time Required for HA50HS Specimen to Reach 1.0% Creep Strain as a Function of Applied Stress and Temperature 110
Figure 4.38 Time Required for HA50HS Specimen to Reach 2.0% Creep Strain as a Function of Applied Stress and Temperature 111
Figure 4.39 Time Required for HA50HS Specimen to Fracture as a Function of Applied Stress and Temperature 113
Figure 4.40 Typical Responses of the Three Distinguishable Creep Type Deformations 117
Figure 4.41 Creep Deformation Types of HA50HS Specimens Subjected to Stresses Below the Minimum Serration Stress (Type-A), Between the Minimum and the Maximum Serration Stresses (Type-B), and Above the Maximum Serration Stress (Type-C) 118
Figure 4.42 Predicted and Actual Steady-State Strain Rates Corresponding to Type-A Creep Behavior of a HA50HS Specimen as a Function of Applied Stress and Temperature 119
Figure 4.43 Predicted and Actual Steady-State Strain Rates Corresponding to the First Linear Portion of Type-B Creep Behavior of a HA50HS Specimen as a Function of Applied Stress and Temperature 121
Figure 4.44 Predicted and Actual Steady-State Strain Rates Corresponding to the Second Linear Portion of Type-B Creep Behavior of a HA50HS Specimen as a Function of Applied Stress and Temperature 123
Figure 4.45 Predicted and Actual Steady-State Strain Rates Corresponding to Type-C Creep Behavior of a HA50HS Specimen as a Function of Applied Stress and Temperature 124
Figure 4.46 Predicted and Actual Steady-State Strain Rates Corresponding to a Consolidation of Type-A and the First Linear Portion of Type-B Creep Behaviors of a HA50HS Specimen as a Function of Applied Stress and Temperature 127
Figure 4.47 Predicted and Actual Steady-State Strain Rates Corresponding to Type-B2 Creep Behavior in the Power Law Breakdown Regime of a HA50HS Specimen 131
Figure 4.48 Predicted and Actual Steady-State Strain Rates Corresponding to Type-C Creep Behavior in the Power Law Breakdown Regime of a HA50HS Specimen 132
Figure 4.49 Optical Micrographs of a HA50HS Creep Specimen Tested at 110 ksi and 800°F in the 45 Degree Orientation to the Rolling Direction: (a- 500x, b-1000x) 134
Figure 4.50 SEM Micrograph (10,000x) of a HA50HS Creep Specimen Tested at 110 ksi and 800°F in the 45 Degree Orientation to the Rolling Direction 135
Figure 5.1 Possible Integrated Power Unit Rotor Geometry 140

Figure 5.2 Equilibrium Element of a Constant Thickness, Rotating Disk Subjected to Radial and Tangential Stresses 141
Figure 5.3 Elastically Determined Stress Profiles For Rotor Configuration #1 Tested at 1000°F, While Spinning at 55,000 RPM 168
Figure 5.4 Elastically Determined Displacement Profiles For Rotor Configuration #1 Tested at 1000°F, While Spinning at 55,000 RPM 169
Figure 5.5 Elastically Determined Stress Profiles For Rotor Configuration #2 Tested at 1000°F, While Spinning at 55,000 RPM 171
Figure 5.6 Elastically Determined Displacement Profiles For Rotor Configuration #3 Tested at 1000°F, While Spinning at 55,000 RPM 172
Figure 5.7 Elastically Determined Stress Profiles For Rotor Configuration #3 Tested at 1000°F, While Spinning at 55,000 RPM 173
Figure 5.8 Elastically Determined Displacement Profiles For Rotor Configuration #3 Tested at 1000°F, While Spinning at 55,000 RPM 174
Figure 5.9 Elastically Determined Stress Profiles For Rotor Configuration #4 Tested at 1000°F, While Spinning at 55,000 RPM 176
Figure 5.10 Elastically Determined Displacement Profiles For Rotor Configuration #4 Tested at 1000°F, While Spinning at 55,000 RPM 177
Figure 5.11 Creep Stress Profiles For Rotor Configuration #3 Tested at 1000°F (800K), While Spinning at 55,000 RPM 178
Figure 5.12 Creep Displacement Profiles For Rotor Configuration #3 Tested at 1000°F (800K), While Spinning at 55,000 RPM 179
Figure 5.13 Calculated Inner Radius Deformations of Rotor Configuration #3, Tested at 1000°F, as a Function of the Rotor Speed 181
Figure 5.14 Calculated Hub Radius Deformations of Rotor Configuration #3, Tested at 1000°F, as a Function of the Rotor Speed 182
Figure 5.15 Calculated Elastic and Creep Deformations and Estimated Total Displacement of the Hub Radius of Rotor Configuration #3, Tested at 1000°F, as a Function of the Rotor Speed .. 183

LIST OF TABLES

Table 1.1 Typical Values of Exponents Used in the Steady-State Creep Equation........................22

Table 2.1 Chemical Composition (wt%) of Carpenter's Fe-Co Alloys..29

Table 4.1 Creep Test Data Used in the Series of Linear Regression Analyses..............................115

Table 4.2 Creep Constants and Statistical Values for HA50HS as Determined by Multiple Linear Regression Analysis...126

Table 4.3 Calculated X-Ray Diffraction Peak Locations 137

1. Introduction and Literature Review

1.1 Motivation

A national initiative is underway to develop and test a more electric aircraft (MEA) and is being led by the U.S. Air Force Research Laboratory at Wright-Patterson Air Force Base, Ohio. The MEA concept is based on utilizing electric power to drive aircraft subsystems which are currently driven by a combination of hydraulic, pneumatic, electric and mechanical power transfer systems. Increasing use of electric power is seen as the direction of technological opportunity based on rapidly evolving power electronics, fault tolerant electrical power distribution systems, and electric driven flight control actuator systems [1, 2, 3, 4].

A major objective of this effort is to increase military aircraft reliability, maintainability, and supportability and to drastically reduce the need for ground support equipment. Currently, twenty-four C-141 cargo aircraft loads of supplies, equipment, and personnel are required for the deployment of a squadron of sixteen F-16 fighter aircraft [1]. A significant reduction in the cumbersome logistics support may be obtained through the development of these advanced power technologies. This advancement will be accomplished through the continued development of magnetic bearings as well as an aircraft integrated power unit (IPU) and a starter generator (IS/G) internal to an aircraft main propulsion engine. The basic configuration of the IPU is represented by the schematic in Figure 1.1. Although this representation has been dramatically simplified, it depicts some of the very important aspects of a typical configuration [5, 6]. It is apparent that the IPU is a complete turbomachine providing output power. Also, this particular design places the switched reluctance starter generator aft of the compressor which adds work to the airflow as it is compressed. Hence, the compressor discharge air, which is used for cooling the rotor, is hot! Some estimates of the available cooling air are as high as 600°F. The true operating temperatures for the rotor materials would also be affected by the heat generated from the spinning poled rotor due to the magnetic core losses as well as the aerodynamic pumping losses [5]. A cut away view of an F-110 main propulsion engine, as illustrated in Figure 1.2, details the incorporation of the rotor and stator components of the IS/G into the engine. The development of the IS/G represents one of the highest power-rated motor/generator systems in switched reluctance technology [7, 8, 9]. These advanced technologies will enable the elimination of the troublesome conventional auxiliary components, such as: oil lubrication/ball bearing systems, turbine inlet stator/nozzles,

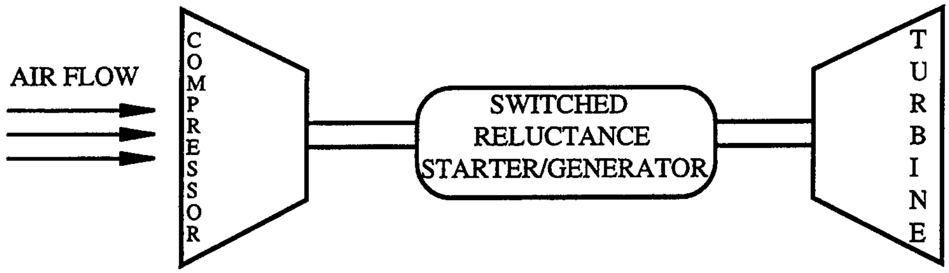
AIR FLOW
COMPRESSOR
SWITCHED RELUCTANCE STARTER/GENERATOR
TURBINE

Figure 1.1 Integrated Power Unit (IPU) Basic Configuration.

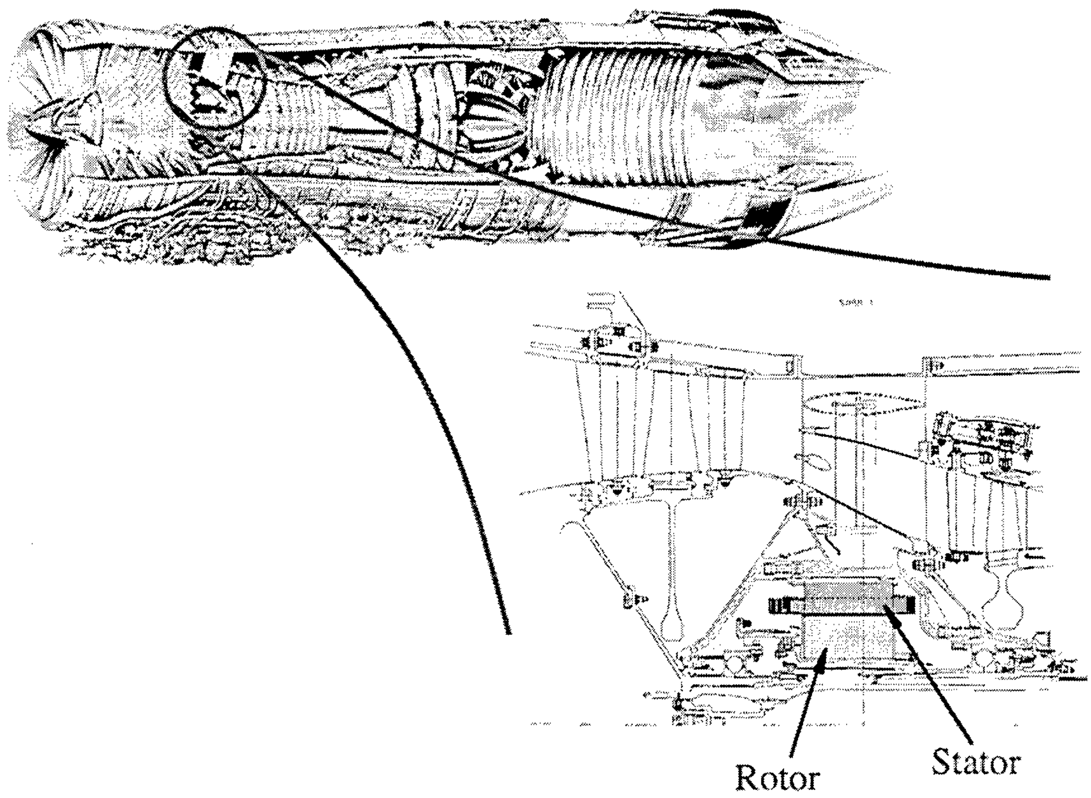
Rotor
Stator

Figure 1.2 Internal Starter/Generator (IS/G) Application.

instrumentation, accessory gearbox driven fuel and lubrication pumps, and hydromechanical fuel controls.

As with many advanced developments, there exists a variety of technical challenges that must be addressed to enable the successful transition of technology from the laboratory to the field. Uncontained magnetic fields and stray electric currents are a concern whenever rotating machinery is involved [10]. Switched reluctance machinery is also subject to the possibility of relatively large lateral forces directed upon the central shaft [11]. Another particular design challenge involves the structural integrity of the IPU and the IS/G. These units require a high power density in order to provide the electrical power of sufficient quantity for all of the aircraft secondary power functions. The rotors and stators of the turbomachines are made of many thin laminates of soft magnetic material. The number of rotor and stator poles can vary as a function of the size and desired application of the machine. A typical IPU application might utilize six stator poles and four rotor poles, as depicted in Figure 1.3. A typical IS/G application might be optimized with an 18/12 poled stator/rotor configuration. The IS/G rotor and stator rings are significantly larger in diameter than those associated with an IPU design in order to fit around the shaft, which runs through the center of the main propulsion engine. The windings, for both applications, are located on the stators rather than the rotors, thereby allowing a higher rotational speed and operating temperature for the rotor. Nevertheless, the necessary rotor speeds and temperatures require a high strength magnetic material capable of sustained integrity in a high temperature environment.

Considering the proposed high temperature and high stress operating environments, a thorough understanding of the mechanical behavior, specifically creep, of the rotor material is the focus of this study as it is essential for the successful design and operation of the switched reluctance starter/generators. The successful development of these high performance power generating components is a high priority to the United States Air Force, as it is crucial for the development of the More Electric Aircraft, as well as other future military and commercial aircraft [12,13,14].

1.2 Deformation Fundamentals

A study of creep deformation would not be complete without a thorough investigation of the corresponding tensile behavior. Tensile tests are done to document a specimen's response to a specific loading condition. Most tensile data are generated by conducting uniaxial tests with a constant crosshead speed in order to measure the material deformation

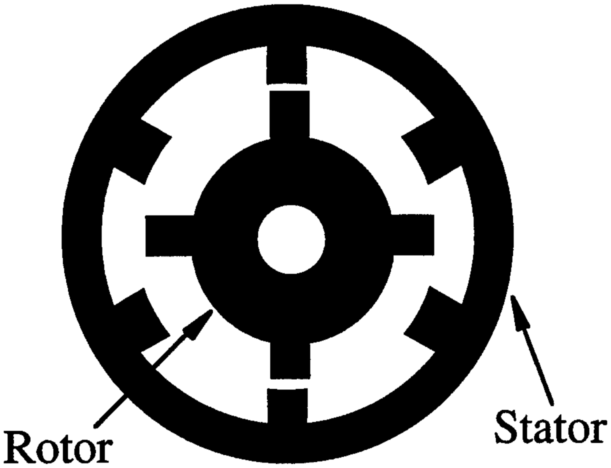
Rotor
Stator

Figure 1.3 Switched Reluctance Motor Rotor and Stator Laminates.

response as a function of the applied load. The applied load per unit area is known as stress. Engineering stress, which is predominantly used throughout industry, utilizes the original cross-sectional area, while a true stress measurement takes into account the continual reduction in cross-sectional area.

The deformation response, or strain, of the specimen is defined as the change in gage length over the initial gage length. Total strain may be comprised of two types: elastic and plastic. Elastic strain is not permanent and the amount of elastic deformation will return to zero once the applied load is removed. This elastic behavior is represented by the initial, linear portion of a stress versus strain curve. The slope of this line is known as Young's Modulus or, simply, the elastic modulus. Plastic deformation, however, is permanent and does not return to zero upon unloading. Traditionally, plastic strain relates to stress by a power law function due to a work hardening effect. The strength which corresponds to the end of the elastic and the beginning of the plastic regimes is defined as the yield strength. Since most materials transition gradually from the linear to the power law response a strain offset is usually selected to define this point and corresponding yield strength. Typically this strain offset is 0.002 and is illustrated in Figure 1.4.

For some materials, such as low carbon steels and ordered intermetallic alloys, the transition from elastic to plastic deformation is more easily identified by a sharp yield point. This sudden drop in the stress required to continue straining may be as large as fifty percent although a more common drop would be on the order of ten percent. This lower stress is known as the lower yield point and is the stress required to continue plastic deformation with little or no increase in stress. The elongation which occurs at a constant load is called the yield point elongation, or Lüders elongation [16]. Yield point elongation is a heterogeneous deformation. The upper yield point registered on a stress versus strain plot represents the formation of a band of deformed material. The band initiation often occurs at a stress concentration such as a fillet radius or an extensometer attachment location. As the band forms, the applied load drops to the lower yield stress at which point the band propagates from one end of the gage length to the other. Eventually this perfectly plastic behavior stops, as the entire gage length is deformed in this manner, and a work hardening region prevails. This type of behavior is illustrated if Figure 1.5.

Work hardening occurs as microscopic defects interact and tangle to make the material more difficult to deform. The maximum stress level achieved is defined as the ultimate tensile strength. At this point the stress becomes more localized and the cross-sectional area

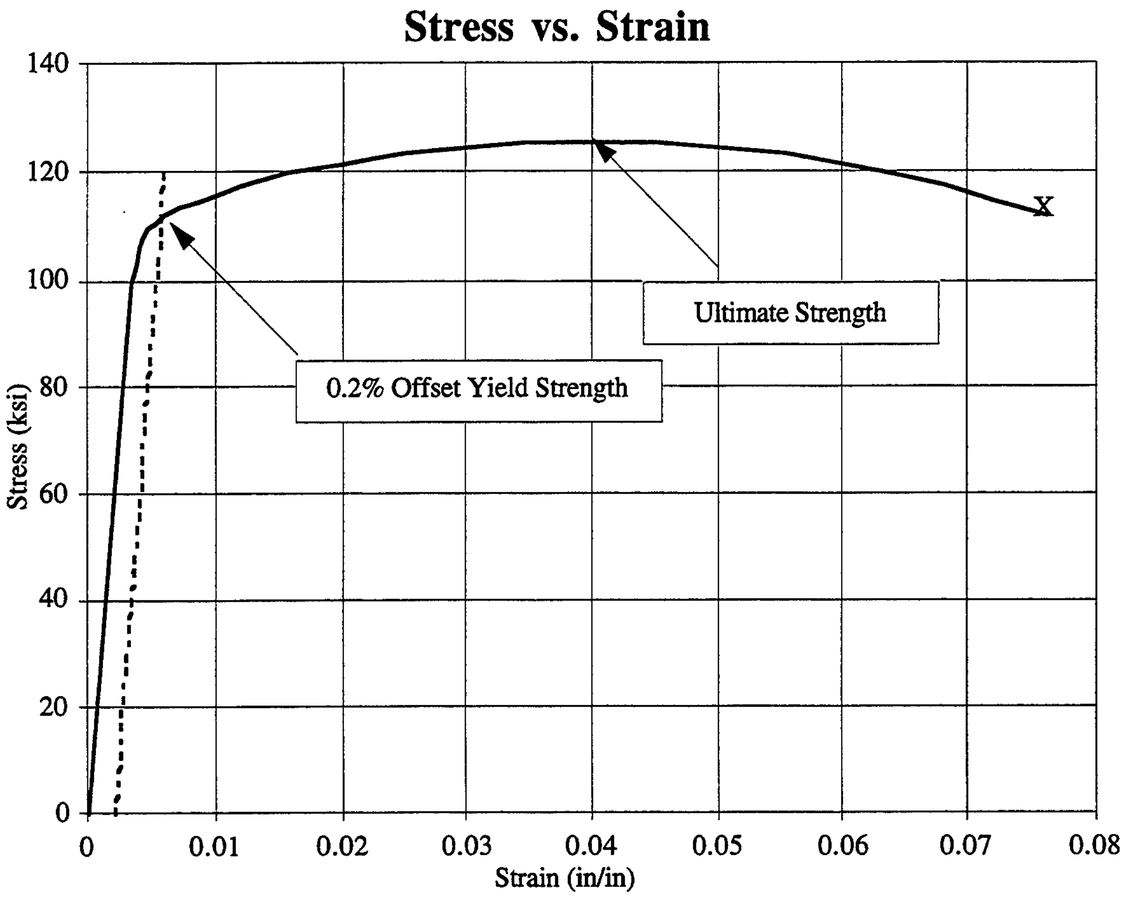

Figure 1.4 Schematic of a Typical Stress Versus Strain Behavior.

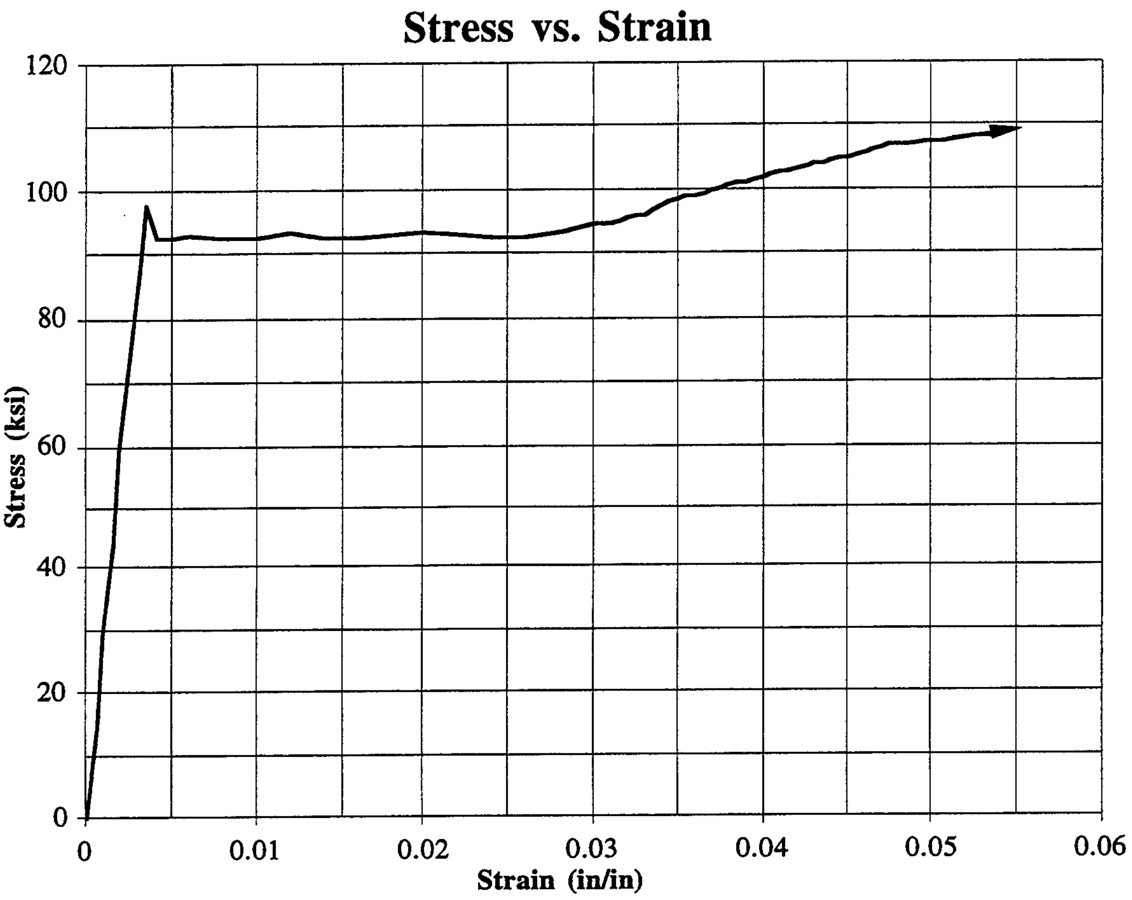

Figure 1.5 A Reproduction of a Pen Plot of Stress Versus Strain Behavior of HA50HS Material Tested in the 45° Orientation to Rolling Direction at Room Temperature, Which Exhibits a Sharp Yield Point, Lüders Elongation, and the Beginning of Work Hardening.

significantly decreases due to necking of the specimen. Voids then begin to form and subsequently lead to a ductile fracture. There are various types of microscopic defects that may be found in a crystal lattice of atoms [15]. Atomic vacancies, and interstitial and substitutional atoms are all types of point defects. Dislocations, grain boundaries and precipitates are also crystal defects that influence mechanical behavior. Specifically, it is the movement of various types of dislocations that enables a material to deform plastically. For dislocation motion to occur, atomic diffusion must take place. Since diffusion is a thermally controlled process, it makes sense that plastic deformation is temperature dependent.

As dislocations travel they tend to interact with one another and with other crystal defects, which results in their impedance, or pinning, and strain hardening. They may also interact in a manner to form new dislocation sources. The understanding of dislocation formation and subsequent motion is fundamental to the development of creep deformation theories.

According to the original Cottrell theory [17], the upper yield point phenomenon is caused by the interaction of dislocations to form an atmosphere which acts to pin down the dislocations. A stress greater than that normally required to move a dislocation is then required to free it from the pinning atmosphere. This greater stress corresponds to the upper yield point and is coincident with the formation of the first Lüders band. The lower yield point represents the stress required to move the freed dislocations which propagate the Lüders front along the gage section. Yield point phenomena in room temperature tensile tests of iron have been attributed to relatively small amounts of carbon or nitrogen in interstitial solid solution [18].

The aspect of Cottrell's theory involving the pinning of dislocations by segregating carbon and nitrogen atoms is rarely disputed. Whether these original dislocations are ever freed, however, is sometimes debated. Leslie claims that dislocations that exist before straining of low-carbon steels are firmly locked by carbon and nitrogen atoms and are usually not freed by the applied stress [19]. Pre-existing dislocations observed in B2 ordered NiA1 single crystals were found to be immobile during the entire deformation process, all the way to specimen fracture [20]. Johnston and Gilman propose three conditions that are required for abrupt yielding: a low density of mobile dislocations in the specimen prior to straining; rapid generation and multiplication of dislocations; and a slight dependence of dislocation velocity on stress [21]. In annealed iron the dislocation density is low. It is speculated that the annealing process of the iron-cobalt specimens used in this study also result in a low density of mobile dislocations.

Through transmission electron microscopy, Ghosh and Crimp were able to observe the generation of new dislocations as a result of the tensile straining of an ordered NiA1 specimen [20]. Infrequently, homogeneous nucleation of dislocations occurs in a perfect lattice due to stress alone. More often, however, heterogeneously formed dislocations occur as a result of stress and pre-existing defects in the crystal lattice. Crystal defects such as grain corners, grain edges, and external stress raisers act as stress concentrations to create dislocations. Even with the consideration of crystal defects, the high dislocation density often observed in cold-rolled metals can only be explained by some multiplication process such as the Frank-Read source [19]. By using a transmission electron microscope to measure dislocation velocity, Leslie derives a comprehensive expression that does not require the releasing of pinned dislocations.

A detailed description of the formation of a Lüders band is given by Leslie [19]. Polycrystalline metals comprised of fine grains may exhibit as few as 1% of the grains crossed by slip bands when subjected to stresses below the upper yield point. In order for a slip band to be able to cross a grain, the applied stress must be large enough to activate a dislocation source and to propagate the dislocations along the operative slip system. The slip bands continue to propagate through nearby grains as the stress continues to increase. Also, as the applied stress increases so does the dislocation velocity and the size of the slipped region. As the entire cross-section is traversed, the slipped region becomes a Lüders band. Because of the stress concentrations resulting from the localized reduction in cross-sectional area the Lüders band front will propagate, at a nearly constant stress, along the entire gage length. Frequently Lüders bands will form at more than one stress concentration site. The band front is typically oriented at 45° to 50° to the tensile axis [22].

The formation of solute atmospheres around dislocations is also attributed to the phenomenon of strain aging. If a tensile specimen is loaded to a point beyond the upper yield point and then unloaded, the stress versus strain curve follows a path back to zero stress that is parallel to the elastic deformation. Typically, if this specimen is subsequently reloaded, it returns to the point of unloading and continues as before. If a sufficient amount of time has elapsed, however, a new yield point is formed at the point of the previous unloading and the material is effectively strengthened. The aging process allows for the dislocations in motion just prior to unloading to be pinned down by solute atmospheres. Since solute atoms must diffuse through the lattice in order to lock the dislocations, the hardening of the material depends on aging temperature as well as time. The formation of an upper yield point as explained by Cottrell [17] and the recurrence of a yield point due to aging are not normally observed in iron and low carbon steels tested at elevated temperatures [18]. The additional thermal energy at these temperatures causes the solute atmospheres to disperse from the dislocations.

Static strain aging effects on low carbon steels, such as: the recurrence of a yield point; an increase in ultimate strength and rate of work hardening; and a sharp decrease in ductility, can approach their maxima at interstitial concentrations of only about 0.002%. The carbon content of the HA50HS is 0.01%. According to Leslie, the Cottrell-Bilby model sufficiently explains only the recurrence of the yield point. It is generally accepted that once the dislocations are pinned by the solute atoms during the aging process they are not released for the remainder of the testing. Instead, stress concentrations allow for the generation and multiplication of new dislocations. This increased dislocation density sufficiently explains the remaining static strain aging effects: increase in ultimate strength and work hardening rate, and a sharp decrease in ductility [19].

Aging effects that occur during the deformation process are known as dynamic strain aging. At sufficiently high temperatures the interaction between the solute atoms and the dislocations require less time. Dynamic strain aging occurs over a range of temperatures and increasing the strain rate increases the upper and lower limits of this range. Within the dynamic strain aging interval of temperatures, the plastic deformation becomes unstable and sharp load drops appear as a serrated flow is registered on a stress versus strain plot. Figure 1.6 depicts this type of response. The snagging of dislocations and the corresponding serrated flow is known as the Portevin-LeChatelier (PLC) effect. The PLC effect was first investigated by A. Portevin and F. LeChatelier [23] and is discussed in many texts [19, 24-26]. Nabarro is one of many researchers who has studied the dynamic strain aging phenomenon and has suggested that this phenomenon is directly related to the drag stress placed on the moving dislocations by the solute atoms [27]. Dinhut et al. have reported the existence of the PLC effect in iron-cobalt alloys. The appearance of the characteristic serrated flow was documented as a function of strain rate and temperature [28].

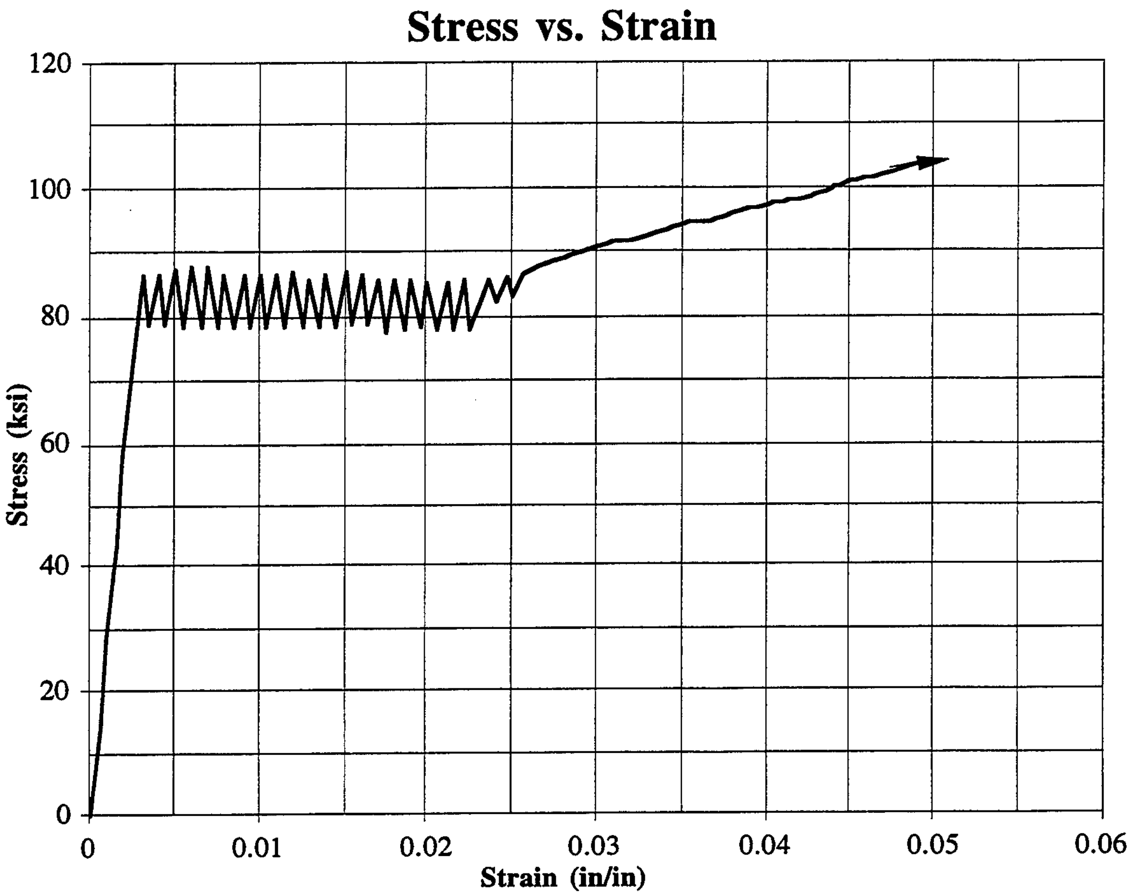

Figure 1.6 Reproduction of a Pen Plot of the Stress Versus Strain Behavior of HA50HS Material Tested in the 45° Orientation to the Rolling Direction at 1000°F, Which Exhibits Lüders Elongation, the Portevin-LeChatelier Effect, and the Beginning of Work Hardening.

As the upper yield point is affected by strain rate, specimen geometry, and alignment, it is more appropriate to track the lower yield point for the purpose of strength comparisons. It has been shown by Hall that this lower yield point does indeed follow the Petch-Hall relationship, which relates yield strength to grain size [26]. The yield point phenomena are also directly related to temperature. For instance, body centered cubic polycrystalline iron normally exhibits an obvious yield point at room temperature. As the test temperature is lowered the upper yield point becomes more pronounced. As the test temperature is raised above room temperature the upper and lower yield points and the yield point elongation gradually disappear, to be replaced by curves exhibiting serrated flow associated with the PLC effect [26]. Hall also reports that at elevated temperatures the dislocation density of specimens is almost ten times that of specimens deformed to the same strain levels at room temperature. This claim then supports the theory that new dislocations are being formed and pinned rather than the continual unpinning, or repeated snagging, of a lesser number of dislocations. It was also reported that transmission electron microscopy showed that undeformed regions of a Ni_3Al alloy ribbon were essentially free of dislocations, while the heterogeneously deformed regions were highly dislocated [29]. The dislocations were in a planar array form which supports the dislocation generation process rather than the dislocation breaking away mechanisms. This finding supports the proposition by Korbel that the heterogeneous plastic deformation requires the influence of a great many dislocations [30].

Ordered intermetallic alloys have been documented as exhibiting the yield point phenomenon followed by a region of Lüders elongation [31-34]. This type of behavior is somewhat common among mild steels at relatively low temperatures and other alloys which possess some degree of ordering [19, 26, 35]. Much of the early work done on the mechanical behaviors of ordered intermetallic alloys and specifically on the iron-cobalt alloys was done by N.S. Stoloff while working in the Scientific Laboratory of Ford Motor Company. In a paper co-authored with R.G. Davies, also of Ford Motor Company, Stoloff investigated the effects of long range order on the deformation modes of an equimolar iron-cobalt alloy containing 2% vanadium [36]. They prepared the specimens to possess a fine grained structure with an average grain size of approximately 0.005 inches in diameter. He also determined that the maximum degree of order obtainable for this alloy is represented by an ordering parameter of about 0.92. As with other ordered systems a peak in yield stress was reported at a critical degree of order. Stoloff and Davies explain this behavior as a transition of the prominent deformation mechanism from the interaction of unit dislocations with a partially ordered lattice to the interaction of super dislocations with an almost perfectly ordered lattice.

As a typical dislocation moves through a superlattice it will disorder the trailing material in the form of an antiphase boundary. In order to minimize the energy required to create the antiphase boundary the unit dislocations tend to move in pairs that are connected by a length of antiphase boundary. This pairing of dislocations preserves order and is often known as a superlattice dislocation [37]. The equilibrium length of the antiphase boundary is determined by the energy balance between the mutual repulsive force of the unit dislocation and the surface tension of the antiphase boundary.

When the superlattice dislocation spacing or, antiphase boundary length, is greater than some critical value, the unit dislocations comprising the superlattice dislocation are forced to move independently. The flow stress tends to increase up to this critical length at which point a sharp decrease in strengths occurs. The location of the peak strength is a function of the degree of order as well as the amount of ordering energy in the system. As the ordering energy is increased, possibly due to a higher thermal excitation, the degree of atomic order must be decreased to maintain superlattice dislocation motion. If the degree of order is constant then the superlattice dislocation motion may be replaced by unit dislocation motion in the form of wavy glide. Also, at relatively high strains cross-slip was observed by Stoloff and Davies due to the breakdown of the superlattice dislocation. The resulting behavior was similar to that of the disordered state.

Stoloff and Davies have studied the influence of order on the type of dislocation motion in iron-cobalt alloys [37]. At temperatures ranging from 173 K to 673 K ordered iron-cobalt exhibits planar glide dislocation motion while the disordered state deforms by wavy glide. Planar glide of the ordered state is explained as occurring predominantly on the {110} planes which possess the lowest amount of energy of the antiphase boundaries linking the dislocations.

The fracture behavior of three compositions of FeCo alloys was studied by Zhao et al. [38]. He concluded that all three alloys are more ductile in the disordered state than in the ordered state. Also, the stoichiometric alloy had less ductility than the two off-stoichiometric alloys, for both ordered and disordered states. Baker and Schulson [39] have suggested that partially disordered grain boundaries are needed for improved ductility. Glezer et al. [40], report that ordered FeCo-2%V, which is more ductile than FeCo, had a higher impurity concentration along the grain boundaries than reported for FeCo. This finding suggests that ductility of these alloys is improved by grain boundary disordering rather than by decreasing the impurity segregation to the grain boundaries.

Stoloff and Davies report that the ordered state of binary FeCo as well as FeCo-V is significantly stronger than the disordered states. This difference seems to be true at elevated temperatures as well as at room temperature. It has been shown that the ordered phase of the FeCo alloy behaves in accordance with the Petch-Hall relationship [41]. At relatively low temperatures, grain refinement raises the yield stress. As with FeCo-2V [42], partial disordering of the alloy lessens the grain size effect but does not eliminate the effect. Schulson suggests grain refinement below a critical size to improve ductility of ordered alloys [43]. He supports his speculation by citing the observation that the room temperature ductility of FeCo-2V appears to be proportional to the inverse of the square root of the grain size diameter. Also, the ductile to brittle transition temperature falls from 450°C to –50°C coincident with a reduction in grain size from 100 microns to one micron [37]. Analyses of several B2 structured compounds revealed a slip system depending on ordering energy [44]. Farkas reports that <100> slip is preferred for B2 NiAl alloys with higher ordering energy values while lower energy values can be attributed to <111> slip. Compounds possessing intermediate values of ordering energy appear to be influenced by both the <100> and <111> slip systems.

1.3 Basic Creep Phenomena

Creep is a time dependent deformation that results from the application of a constant load. This type of deformation typically occurs above 0.3 to 0.6 times a material's absolute melting temperature. As a specimen is subjected to a constant load at a constant temperature, the straining of the specimen is measured as a function of time. The gradual deformation that occurs with time, after the initial elastic and sometimes plastic deformation, is typically referred to as *creep strain*; the curve itself, is known as a *creep curve*, and the slope of the creep curve is known as the *creep rate*.

Usually creep behavior can be segmented into three stages of deformation when depicted on a plot of strain versus time as shown below in Figure 1.7 [45,46]. The first stage is known as primary creep, or transient creep, and is characterized by a strain rate that begins at a relatively high value, but soon decreases to a much lower and almost constant value. This point marks the end of primary creep and the beginning of secondary creep, or steady-state creep. The end of this second stage is often identified by a deviation from linearity of

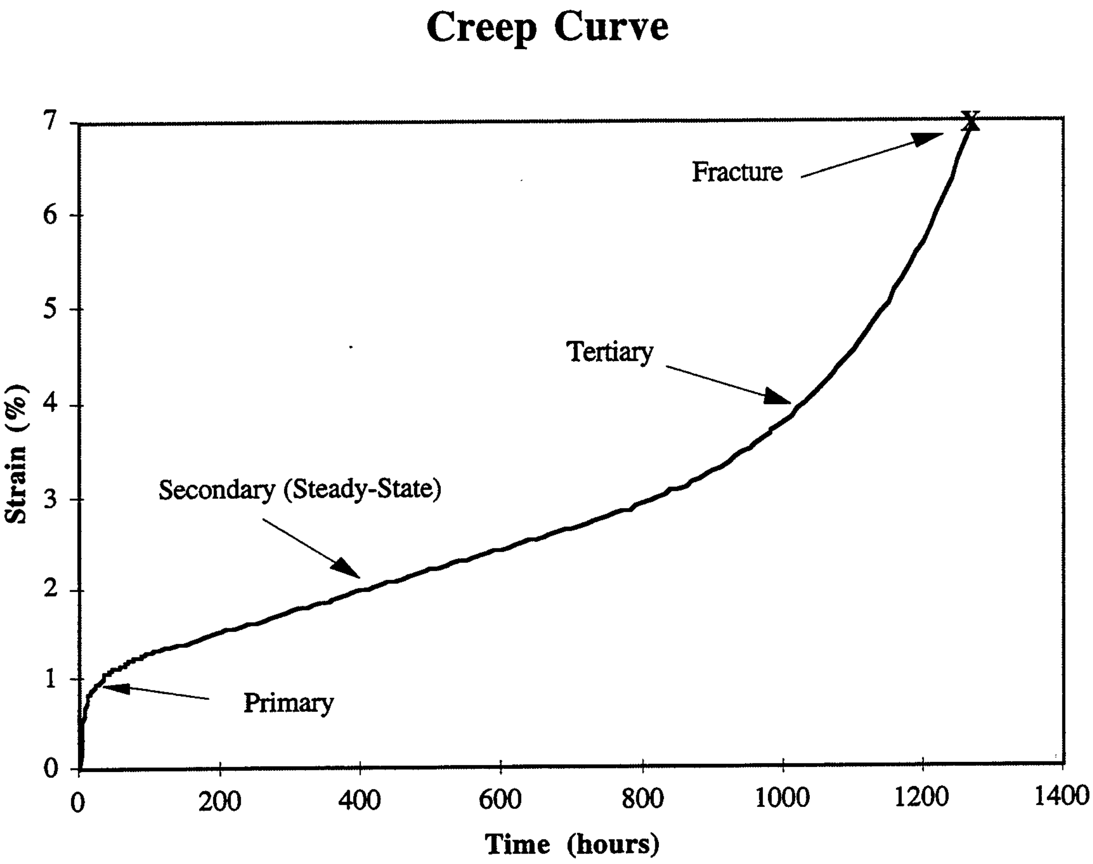

Figure 1.7 Schematic of a Typical Creep Curve.

the strain rate. The third stage of the behavior is referred to as tertiary creep, or unstable creep, and ultimately leads to necking and/or void coalescence and, finally, rupture. In some more recent analyses [47] the traditional tertiary stage is split into a tertiary and a quaternary stage to obtain a closer fit of modeling predictions to experimental data.

The shape of a classical creep curve resulting from a constant load test can be explained by a combination of geometric and material characteristics. The rapidly decreasing slope, characteristic of the first stage, is indicative of the fact that strain hardening is occurring. The degree of strain hardening which occurs is a function of the number, type, and arrangement of dislocations. Simultaneously, processes are occurring in the material to soften it, such as recrystallization and recovery. In addition to these two phenomena a geometric change occurs, due to the reduction in cross sectional area, that causes the stress to increase with a constant load. The strain hardening, softening, and the reduction in area all contribute to the shape of the creep curve. In the primary stage the initial large strain rate decreases rapidly due to the dominant strain hardening that retards the flow process. This strain hardening will be opposed by the increased flow rate due to the necking of the specimen and also by the softening associated with recovery and recrystallization. As these processes reach an equilibrium state the creep behavior is characterized by a steady-state stage of constant slope. The onset of the third stage occurs when grain boundary shearing or intergranular fracture occurs, essentially reducing the load carrying cross sectional area. A rapid recrystallization -- hence, rapid removal of strain hardening - may also initiate this tertiary stage.

Classical creep experiments were carried out by Andrade around 1910 [48, 49]. He developed a test apparatus that he used to apply a varying load that was proportional to the cross sectional area of the deforming specimen during a creep test in order to maintain a constant stress. The curves he documented for lead did not have a tertiary stage. It was suggested that this was due to the fact that he applied a constant stress instead of a constant load. Andrade concluded that at constant stress and constant temperature the length of the specimen could be represented as a function of time by an equation of the form:

$$l = l_0(1 + \beta t^{\frac{1}{3}})e^{kt}. \tag{1.1}$$

By defining strain as the change in length divided by the initial length, the Andrade equation becomes:

$$\varepsilon = (1 + \beta t^{\frac{1}{3}})e^{kt} - 1; \tag{1.2}$$

where β and k are material constants. If kt is small (kt<<1) then $e^{kt} - 1 \approx kt$ and $e^{kt} \approx 1$. By considering these two approximations, Equation 1.2 can be written as:

$$\varepsilon = \varepsilon_1 + \varepsilon_2;$$

where: $\varepsilon_1 = \beta t^{\frac{1}{3}}$, which accounts for the transient creep, while $\varepsilon_2 = kt$ and represents the steady-state creep portion of the curve.

Strain rate is then given as:

$$\dot{\varepsilon} = \frac{1}{3}\beta t^{\frac{-2}{3}} + k. \tag{1.3}$$

From this equation, it is easy to see the decreasing strain rate of the primary region that eventually levels off at a constant value of k for relatively long durations. For many materials, however, this initial modeling done by Andrade is not sufficient and more complex modeling is necessary.

In order to analyze the stress versus strain behavior of a material subjected to creep conditions, the time dependency must be incorporated into the appropriate relationships. The simplest relationship involving stress, strain, and time is one in which, for a constant time, there is a linear proportionality between stress and strain. Rheological models can be used to develop strain versus time equations for a constant applied stress. Dowling [50] shows a set of such linear viscoelastic rheological models and their corresponding equations. One such equation is given as:

$$\varepsilon = \frac{\sigma}{E_1} + \frac{\sigma t}{\eta_1} + \frac{\sigma}{E_2}(1 - e^{\frac{-E_2 t}{\eta_2}}). \tag{1.4}$$

The steady-state portion of this linear viscoelastic equation is represented by $\frac{\sigma t}{\eta_1}$, while $\frac{\sigma}{E_1}$ is the instantaneous strain occurring at loading. The transient, or primary stage portion of the curve is represented by $\frac{\sigma}{E_2}(1 - e^{\frac{-E_2 t}{\eta_2}})$. This linear relationship best depicts the creep behavior that is dominated by diffusional flow, such as Nabarro-Herring or Coble creep mechanisms [51-53]. Dislocation creep, however, does not exhibit this simple proportionality and behaves in a nonlinear manner. In this type of nonlinear creep, the characteristic equation incorporates the stress raised to some power, usually in the range of 3 to 5 [54, 55]. Some sources [56] even report stress exponent values ranging from 7 to 75. One such nonlinear relationship is given as:

$$\varepsilon = \varepsilon_i + B\sigma^n t + D\sigma^\alpha (1 - e^{-\beta t}); \tag{1.5}$$

where ε_i is the instantaneous strain, $B\sigma^n t$ is the steady-state strain portion and $D\sigma^\alpha(1 - e^{-\beta t})$ represents the transient strain. Hence, the strain rate equation corresponding to this relation is:

$$\dot{\varepsilon} = B\sigma^n + D\sigma^\alpha \beta e^{-\beta t}. \tag{1.6}$$

It is apparent that the second term of Equation 1.6 is the limiting term of the transient creep stage.

A great deal of work has been dedicated to the area of the steady-state creep behavior. Efforts are usually conducted to study the creep mechanisms associated with this stage [51-54, 57] or they involve the development and use of a life predicting time-temperature parameter such as the Sherby-Dorn [58], Larson-Miller [59], or Manson-Haferd [60] parameters [61, 62]. This makes sense, since the majority of a component's creep life is spent in this secondary stage. This stage can be represented as a thermally activated process and may be characterized by a set of creep constants consisting of an activation energy, $\boldsymbol{Q}$ (cal/mol), a dimensionless stress exponent, $\boldsymbol{n}$, and a kinetic factor, $\boldsymbol{A}$ [63].

Arrhenius developed a relation governing the rate of a time dependent, thermally activated process [64]. This equation is applicable to steady-state creep behavior with the rate being the corresponding strain rate and Q representing the activation energy [50]. This equation, as it applies to creep is:

$$\dot{\varepsilon}_{SC} = Ae^{-\frac{Q}{RT}}. \tag{1.7}$$

For Q in units of cal/mole and absolute temperature, T, in Kelvin's (K), R is then defined as the universal gas constant with units of cal/(K*mole). With temperature dependency accounted for by the Arrhenius rate equation, this relationship can now be combined with a grain size dependency and substituted into the nonlinear strain rate equation, Equation 1.6, for B. Now the most general form of the nonlinear steady-state creep equation can be written as:

$$\dot{\varepsilon}_{SC} = A_1\sigma^n d^{-p} e^{-\frac{Q}{RT}}; \tag{1.8}$$

where: A_1 is a constant, σ is the applied engineering stress, n is the stress exponent, d is the grain size, p is the grain size exponent, Q is the activation energy, R is the universal gas constant, and T is the absolute temperature.

Beginning an analysis with this equation would enable the determination of the values of n, p and Q for the specific material. These values could then be compared with one of the more readily accepted versions of the Arrhenius rate equation such as Nabarro-Herring [51, 52], Coble [53], or dislocation [54] creep equations. These common relationships are obviously derivations of the common rate equation; however, in each one, an inverse dependence on temperature has been incorporated to better represent actual data.

As described by Dowling, diffusional creep is effected by vacancy gradients which develop at the transverse and longitudinal grain boundaries [50]. If an external stress is applied to a polycrystalline material, the grain boundaries perpendicular to the applied stress are generally subjected to tensile strains normal to their surfaces. Grain boundaries that are parallel to the applied stress are usually subjected to compressive strains. Atom and vacancy motions result, as vacancies are more accommodating along the compressive boundaries and the atoms have a greater propensity towards the tensile boundaries [25]. At lower temperatures this continued transfer of material is maintained primarily by the external loading and causes the grain to deform. At higher temperatures, the vacancy gradient tends to even out and become slightly less dependent on the applied stress; hence, a slight inverse proportionality to temperature is predicted [65]. Comparisons of actual test data support the inverse test temperature dependency of steady-state strain rates for diffusional as well as dislocation creep.

The values of these exponents help to characterize the dominant creep deformation mechanism. Typical values and the associated mechanisms are listed in Table 1.1. Nabarro [51] and Herring [52] theorized that under relatively low stresses and relatively high temperatures vacancies would migrate through the crystal lattice, causing the grains to deform in a time dependent diffusional process. Further development of this theory has resulted in an equation for the steady-state creep rate. Also, comparisons with actual creep data support the inverse dependency on test temperature, which is extracted from the coefficient of the Arrhenius rate equation [50]. The Nabarro-Herring creep equation is given as:

$$\dot{\varepsilon}_{SC} = \frac{A\sigma}{d^2 T} e^{-\frac{Q_{LAT}}{RT}} ; \qquad (1.9)$$

where A is a new material constant and Q_{LAT} is the activation energy associated with self diffusion through the crystal lattice.

Table 1.1 Typical Values of Exponents Used in the Steady-State Creep Equation.

Creep Mechanism	n	p	Q
Diffusional Creep			
Nabarro-Herring, sliding accommodated by volume diffusion [51, 52, 57]	~1	2	Lattice
Coble, sliding accommodated by grain boundary diffusion [53, 57]	~1	3	Grain Boundary
Sliding accommodated by intragranular flow across the grains [66]	1	1	Grain Boundary
Sliding with a continuous glassy phase at the boundary [67]	1	1	Grain Boundary Phase
Sliding accommodated by the formation of grain boundary cavities without a glassy phase [68]	2	1	Lattice
Dislocation Creep			
Dislocation glide & climb, controlled by climb [54]	4.5	0	Lattice
Dislocation glide & climb, controlled by glide [55]	3	0	Chemical interdiffusion
Dispersion Hardening [56]	7-75	0	2 to 3 times self diffusion value

Coble [53] described the other diffusional creep process to be one where the diffusion of vacancies is along the grain boundaries. As expected, Coble creep is even more dependent on grain size than Nabarro-Herring creep. Development of the Coble creep theory also indicates an inverse dependency on temperature. The Coble creep equation is:

$$\dot{\varepsilon}_{SC} = \frac{A\sigma}{d^3 T} e^{-\frac{Q_{G.B.}}{RT}}; \tag{1.10}$$

where A is a new material constant and $Q_{G.B.}$ is the activation energy associated with self diffusion along the grain boundaries.

Weertman [53] proposed that creep occurring in the middle to high stress regime and at temperatures above 0.5 times the absolute melting temperature was controlled by edge dislocation climb away from dislocation barriers. Still accounting for the inverse temperature dependence, a dislocation creep equation is given as:

$$\dot{\varepsilon}_{SC} = \frac{A\sigma^n}{T} e^{-\frac{Q_{LAT}}{RT}}; \tag{1.11}$$

where A is a material constant, the activation energy is associated with lattice diffusion and the stress exponent, n, is typically in the range of 3-5.

Grain boundary sliding is another form of creep deformation. This mechanism, however, must be accompanied by other deformation mechanisms, such as diffusion. Raja and Ashby [57] claimed that Nabarro-Herring and Coble creep could both be described as a grain boundary sliding type deformation in conjunction with diffusional flow.

1.4 Problem Statement

The Air Force need for high-power-density power generation capabilities has dictated the utilization of advanced soft magnetic materials in high temperature, high stress environments. Therefore, a thorough understanding of the materials' magnetic, electrical, and mechanical properties is crucial for the successful development of these starters and generators. While related efforts are exploring the magnetic and electrical behaviors, it is the goal of this effort to provide a better understanding of the mechanical behavior within the desired operating environment. It is the opinion of the author that creep deformation of soft magnetic materials will be a design parameter that must be carefully considered for the advancement of military and commercial aircraft. Specifically, there is a widespread need for tensile data, as well as for a characterization of the creep behavior of candidate iron-cobalt alloys. An understanding of the stress versus strain behavior is required to properly investigate and analyze the time dependent plastic deformation of a material subjected to a constant load at elevated temperatures. An investigation and understanding of the creep strain versus time response is needed to properly model the starter and generator rotor laminates, as they are subjected to high stress and high temperature operating conditions.

1.5 Approach

The author will attempt to add to the body of understanding of creep deformation of this soft magnetic iron-cobalt alloy by undertaking the following tasks:

Tensile Testing

A preliminary investigation of the stress and strain response is made as a function of orientation to the sheet rolling direction, annealing parameters, test temperature and specimen geometry. A more comprehensive follow-on study is conducted, with emphasis on yield point phenomena, Lüders elongation and the Portevin-LeChatelier effect. This analysis provides the necessary foundation for a thorough creep analysis.

Constant Strain Rate Testing

Specific study is made to further identify the relationship between upper and lower yield strengths and the applied strain rate. By employing two different temperatures, comparisons are made of the elastic strains and the maximum and minimum serration stresses as a function of the applied strain rate. The range of strain rates considered bridge the information from the quickly generated tensile data to the relatively slowly generated creep data.

Creep Testing

A thorough investigation of the material creep response is made at a variety of stress and temperature combinations. Data are presented and analyzed in the forms of isochronous stress-strain relations and as times required to attain a specific strain level. Double linear regression analyses of the strain versus time data are utilized to generate a power law creep model capable of predicting the strain rate response within the desired operating environment. The regime of power law breakdown is also investigated. Microstructural and X-ray diffraction analyses are conducted to examine the specimens in an attempt to better predict the associated deformation mechanisms.

Air Force Application

The strain rate model, developed under this effort, along with the linear elastic and nonlinear, time-dependent deformation characteristics, are used in order to predict the mechanical behavior of a rotor laminate. The elastic deformation analysis includes four different sets of boundary conditions and examines both, the plane strain and plane stress conditions. The creep deformation analysis examines one rotor configuration under the condition of plane stress. Comparisons are made between the elastic and creep deformation predictions and an approach for determining the rotor displacement is suggested.

Chapter 2. Material

2.1 Material Description

Iron-cobalt alloys are the only candidates for this high strength, high temperature application. According to Cullity [66], cobalt is the one alloying element that substantially increases the Curie temperature as well as the saturation magnetization of iron. Along with a high saturation magnetization and a high Curie temperature, a promising soft magnetic material must also possess a high permeability, which is defined as the maximum slope of a line from the origin to a particular point on the induction versus applied field curve. This material property can be thought of as quantifying the ease of magnetizing a material. The initial permeability and the maximum permeability are two specific values often used to evaluate a material. Although an iron alloy containing only 36% cobalt has the largest saturation magnetization of any material at room temperature, the iron alloy containing 50% cobalt has nearly as high magnetization values plus the added benefit of much higher permeabilities.

The optimal design of switched reluctance starter/generator rotors and stators must consider the mechanical and electrical properties as well as the magnetic behavior. Rotor geometry directly influences mechanical behavior as well as aerodynamic pumping, or windage, losses. Core losses associated with a particular design can be separated into hysteretic and eddy current components [70, 71]. The hysteretic loss is a material property that can be represented by the area enclosed by an induction versus applied field loop when tested under direct current conditions. The eddy current losses are inversely proportional to the material's resistivity and are proportional to the laminate thickness and square of the frequency. Specific constituents are sometimes added to candidate materials to increase the resistivity, and quite often as thin a laminate as practical is used. These laminates that make up a rotor core must be electrically insulated from each other to prevent gross eddy current circulation and undesirably high losses. In some instances the sheets are coated with an organic varnish, but this insulating layer typically will not withstand the necessary final annealing [69]. One manufacturer of iron cobalt motor laminates has chosen to coat its sheet with magnesium oxide prior to the final heat treating [72]. This process combines with the silicon dioxide (from the silicon in the alloy) to form a glassy magnesium silicate. Most often, however, the iron-cobalt alloy is simply annealed in an oxidizing atmosphere such as air. The iron-cobalt alloy used in this study was first annealed in an oxidation free, dry hydrogen environment and subsequently oxidized at a lower temperature in air to form a deep blue, tightly adhered, iron oxide. Based on the color, the coating is estimated to be approximately 50 nanometers thick. Reference to Appendix A may be made for the complete details of the heat treating specification. The oxidation process is similar to that used for the bluing of gun barrels.

The specific soft magnetic, iron-cobalt, intermetallic alloy of interest for this rotor application is known as Hiperco® Alloy 50HS (the letters HS are used to indicate high strength). All of the material used in this study was manufactured and provided as evaluation samples by Carpenter Technology Corporation in rolled sheet 0.006 inches thick. This magnetic material typically exhibits high magnetic saturation and a unique combination of high yield strength and moderate core loss. As advertised on the Carpenter Technology Corporation data sheet, the melting and Curie temperatures of HA50HS are approximately 1500°C and 940°C, respectively. The saturation induction is advertised to be 23,500 Gauss at an applied field of 200 Oersteds [73]. This value is supported by the findings of Fingers and Kozlowski [74].

The family of Hiperco® Alloys (HA), which includes HA50 and HA50A, has been used in a variety of applications, with the most appropriate alloy being a function of the magnetic and mechanical design requirements. Motor and generator applications typically involve high stresses and sometimes high temperature environments. Although a very low core loss is desirable from a machine efficiency perspective, this attribute is sometimes compromised in order to obtain an improvement in mechanical behavior. To date, HA50 has been used primarily for motor and generator applications. In a case where a very low core loss is the primary design parameter and mechanical properties are a lesser concern, such as in a high efficiency transformer, HA50A is more suitable.

Extensive magnetic and mechanical studies of Hiperco® Alloys 50 and 50A by Carpenter Technology Corporation [75] clearly show that grain size is a primary factor affecting the material properties. In particular, it was shown that variations of the grain growth kinetics resulted in different properties for these alloys. HA50, which contains a deliberate addition of niobium, exhibits reduced grain growth rates presumably due to the growth-impeding influence of niobium carbo-nitrides. Hence, HA50 creates and retains relatively small grain sizes, which favors application where strength is important. In contrast, HA50A exhibits larger grain sizes after undergoing the same heat treating process, resulting in a better magnetic performance. As can be seen in Table 2.1, HA50HS contains an even larger addition of niobium than that of the HA50 in order to retard grain growth during mill processing and final heat treating. This grain refinement results in higher yield strengths

Table 2.1 Chemical Composition (wt%) of Carpenter's Fe-Co Alloys.

Hiperco® Alloy	Co	Fe	V	Nb	Si	Mn	C
HA50	48.71	Balance	1.93	0.05	0.03	0.02	0.007
HA50A	48.85	Balance	2.03	<0.002	0.03	0.06	0.003
HA50HS	48.75	Balance	1.90	0.30	0.05	0.05	0.01

than those of the more conventional HA50 and HA50A materials with little deleterious effect on the magnetic performance.

2.2 Constituents and Microstructure

The HA50HS is categorized as a near 50-50 weight percent iron-cobalt alloy and may be characterized by a microstructure which is commonly referred to in literature [36,76] as a B2, or $L2_0$, ordered structure. Alloys of this type transform, at an order/disorder transition temperature, from a random body centered cubic solid solution to a structure which can be visualized as two interpenetrating cubic lattices with A atoms on one lattice and B atoms on the other. This ordered microstructure is depicted in Figure 2.1. The order/disorder transition temperature for HA50HS is approximately 730°C.

Ordered alloys are often brittle when subjected to tensile loading. A relatively small percentage of vanadium, as seen in Table 2.1, is a significant constituent of this alloy. The addition of vanadium (V) to ordered iron-cobalt alloys has been shown to increase ductility [77]. It was suggested by Kawahara [78], as a way of explaining this ductility improvement, that the added vanadium combines with the cobalt to form a Co_3V precipitate. The formation of this precipitate results in a surrounding region with a composition that is inadequate to sustain the inherent B2 ordering. Results from the work done by Kawahara reveal that these Co_3V precipitates, and their corresponding zones of disordered microstructure, are formed by a diffusion process which allows for them to be dispersed finely and homogeneously throughout the alloy.

As well as containing vanadium for improved ductility, the HA50HS contains 0.30% (wt) niobium (Nb). The purpose of this constituent is to inhibit grain growth during processing and final heat treating, thereby keeping the grain size relatively small and resulting in a higher strength, according to the Petch-Hall relationship. HA50HS was compared to Hiperco® alloys containing less niobium [74], and it was determined through scanning electron micrographs after the final heat treating that the HA50HS was indeed comprised of smaller grains. The grain size of each alloy increased with anneal time and temperature, but in all comparable cases, the higher niobium content alloys had smaller grains. Also apparent were very obvious precipitates, determined to be a laves phase with a hexagonal close packed structure with lattice parameters of a=4.7 Angstroms and c=7.72 Angstroms and a composition of $Nb(Fe,Co)_2$. These precipitates are responsible for the inhibition of grain growth during recrystallization. The precipitates, as well as the actual grains, can be seen in the micrograph illustrated in Figure 2.2. Although there was not a magnification or

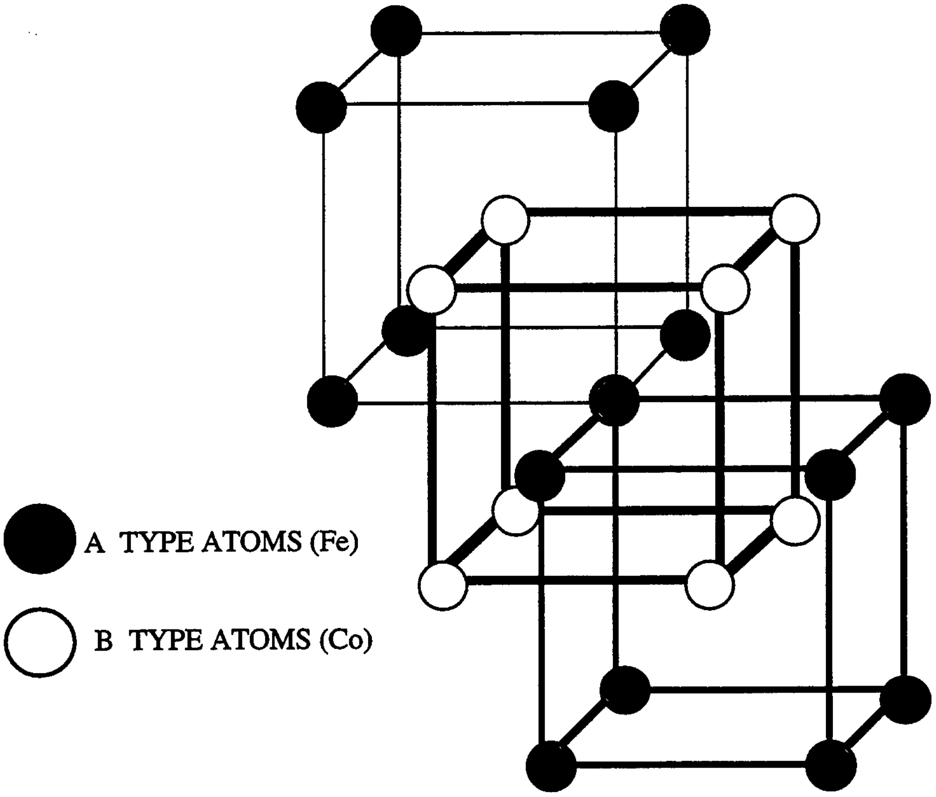
A TYPE ATOMS (Fe)
B TYPE ATOMS (Co)

Figure 2.1 B2 Ordered Microstructure.

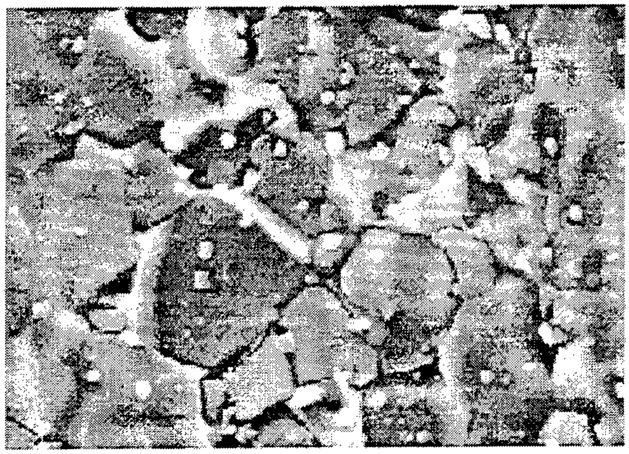

Figure 2.2 SEM Micrograph of HA50HS Annealed for One Hour at 1300°F [74].

scale pertaining to this particular micrograph in the reference, the average grain diameter was reported to be 1.13 microns.

2.3 Manufacturing Process

The HA50HS, as manufactured by Carpenter Technology Corporation [75], begins as raw materials are combined in a vacuum induction furnace. Alloys processed in these furnaces are melted and poured in the absence of atmospheric contaminants. The melting step is precisely controlled to ensure uniformity and optimal properties. Samples are periodically drawn from the molten stage to ensure and adjust the alloy composition. The next step is to hot work the large ingots into smaller, somewhat more manageable, billets. This process is done by properly heating and then rolling the alloy through a series of progressive reductions. This process is known as cogging. The four foot long billets are now transformed into a single strip on a hot rolling mill. As the red hot alloy travels through the rollers, reducing its thickness, the front end of the strip continues to pick up speed until the entire billet has been transformed into hundreds of feet of coiled strip material. After hot rolling, it is necessary to disorder the alloy to permit further processing. This disordering is done by heating the coil to a relatively high temperature (above the order-disorder temperature) then rapidly quenching the strip. The details of this process and the equipment used are proprietary. The quenched strip is then cleaned, surface ground, and cold rolled to a specified thickness on computer controlled mills, which continuously monitor the sheet thickness to within 0.0001 inches. The final step is to trim the strip to the appropriate width.

Even though the addition of small amounts of vanadium has improved the ductility of the originally developed iron-cobalt alloys, optimal manufacturing processes rely on the order/disorder phenomena associated with this type of structure. The ordering parameter is a very important design consideration as related to the manufacturing and subsequent forming processes of ordered alloys. B2 alloys, which possess a high degree of ordering, tend to exhibit a brittle behavior and are difficult to roll or shape into thin strips. As the material is heated, however, it accumulates sufficient thermal energy to disorder and allow forming and reductions in thickness. As the material is cooled relatively quickly, the disordered state remains, providing for more ductile deformations; hence, enabling subsequent cold rolling to a final thickness. After the strip is trimmed to the desired width, fabrication of the actual laminates is often accomplished, while still in the ductile condition, by either electric discharge machining or punching. Lastly, a final heat treating is done to remove the effects of cold rolling and to re-instill the ordering necessary to achieve the desired magnetic properties, and an oxidation step is added to provide for an electrically insulating layer. The laminates are now ready for assembly into an electrical machine.

Chapter 3. Experimental Techniques

3.1 Specimen Preparation

The HA50HS soft magnetic material was received from Carpenter Technology Corporation in strip form approximately six inches wide and 0.006 inches thick. Electric discharge machining and punching were the two cutting methods considered for the fabrication of the test specimens. The method used in a large scale production of laminates for any of the rotor applications would most likely involve a punching process. However, the number of laminates required for the first few engineering prototype units would preclude the relatively high initial cost associated with punching or stamping processes. Also, the burr edge usually created by this process would need to be removed in a subsequent fabrication step. Discussions with Air Force machinists resulted in the decision to electric discharge machine the specimens. This technique was most cost effective for the few hundred test specimens required and will likely be the method used for the first few demonstration and prototype units.

The heat treating of the specimens could have been done in a tightly controlled laboratory furnace. However, an industrial heat treating company, Wall Colmonoy Corporation, was contracted to anneal the batches of specimens throughout the study. As an industrial heat treater, Wall Colmonoy does a great deal of heat treating for the auto industry. For this study, they were able to provide a capability of heat treating large quantities of specimens, as would be needed for production of a large number of power generating units. One of the available furnace racks can be seen in Figure 3.1. The furnace illustrated in the figure is forty inches in diameter and forty inches deep. Although a laboratory furnace would have provided sufficient heat treating capacity, this type of furnace would not be employed for large scale utilization. In fact, the high quality work performed by Wall Colmonoy resulted in a tight tolerance well within the temperature requirements for this study.

It is important to avoid any contamination of the rotor laminates during the heat treatment. All of the specimens were cleaned thoroughly to remove any surface contaminants and handled with gloves prior to annealing. Although thoroughly degreased and cleaned laminations can usually be stacked without a separating insulation, the availability of the large furnace enabled each specimen to be totally exposed to the heat treatment.

A dry hydrogen atmosphere or high vacuum is recommended by Carpenter Technology Corporation [73] to minimize the oxide contamination of the laminates during annealing.

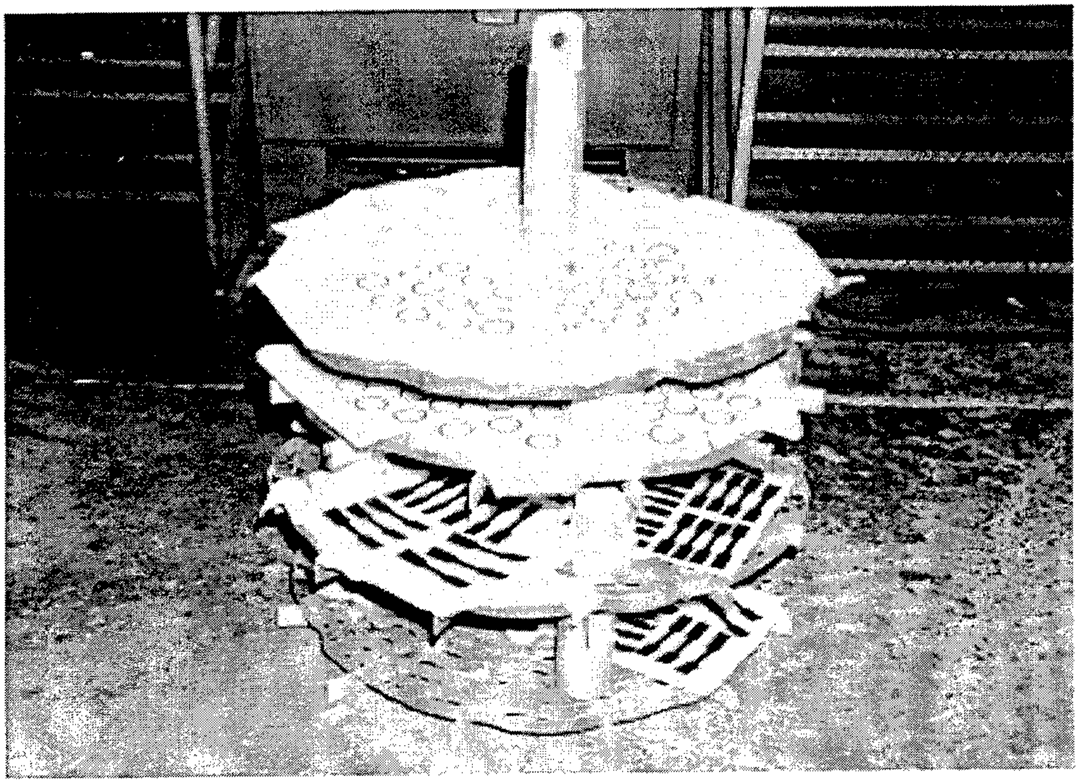

Figure 3.1 Furnace Rack Used by Wall Colmonoy to Heat Treat Various Iron-Cobalt Test Specimens.

When a dry hydrogen approach is used, the entry dew point should be less than -60°F and the exit dew point should be dryer than about -40°F. The exact heat treating temperature employed depends upon the desired application and the acceptable compromises among the magnetic and electrical and mechanical properties. Carpenter recommends heat treating for one to four hours at temperatures ranging from 1300°F to 1400°F. As the anneal temperature or time is increased, the magnetic and electrical properties also increase. However, the tensile strength is inversely related to the anneal time and temperature.

An alternating current or switched reluctance motor or generator application requires a consideration for the reduction of core losses. The eddy current component of the core loss may be reduced by creating a thin layer of oxide on the laminated surfaces. This surface oxide can be achieved by heating in an oxygen bearing atmosphere, such as air, for about thirty to sixty minutes at temperatures ranging from 600°F to 900°F.

3.1.1 Tensile Specimens

The tensile specimens were electric-discharge machined from rolled sheets in the longitudinal, transverse, and 45° orientations with respect to the manufacturer's rolling direction. Three different specimen geometries were used in the screening phase of this investigation. The specimens initially used for tensile testing had a 1.25 inch gage length and 0.5 inch gage width with a gage end blend radius of 0.5 inches. This configuration will be referenced as T1. The transversely oriented specimens were then randomly divided into three groups, and each group was heat treated at a different temperature; 1300°F, 1328°F, and 1350°F, in a dry hydrogen environment for one hour with a dew point less than -60°F and cooled at a rate of approximately 200°F per hour. The 45° and longitudinally oriented specimens were heat treated at 1328°F. A second batch of tensile specimens was electric-discharge machined in the transverse orientation with a 0.625 inch gage length, 0.333 inch gage width and a gage end blend radius of 1.0 inch. These specimens will be referenced as T2. An additional lot of HA50HS specimens was prepared with an even larger blend radius of 2.0 inches. The dimensions of the gage section were the same as for the T2 specimens. These specimens were machined in the three orientations with respect to the rolling direction and then heat treated for two hours at 1328°F. These specimens will be referenced as T3. All three configurations of these tensile specimens were reheated in an air environment for 45 minutes at 750°F to generate an electrically insulating oxidation layer that would be required in an application of rotor laminates. Refer to Appendix A for the exact heat treating specifications. The edges of the specimens were then hand sanded with 600-grit paper to remove any edge defects that may have acted as fracture initiation sites. Finally, the specimens were examined under an optical microscope to verify acceptable surface and edge conditions. All three of the screening phase specimen configurations are illustrated in Figure 3.2.

The T3 geometry was used in the more comprehensive second phase of this study, however, the annealing process was different than that of the T3 specimen of the screening phase. All of the characterization phase specimens were electric discharge machined in the 45° orientation from the rolling direction. They were annealed at a temperature of 1328°F for only one hour in the dry hydrogen environment and subsequently oxidized in air for 45 minutes at 750°F.

3.1.2 Creep Specimens

The specimens used for creep testing have a 1.25 inch gage length and a 0.5 inch gage width with a gage end blend radius of 0.5 inches. This specimen configuration is the same as the T1 tensile specimen as illustrated in Figure 3.2. The specimens were electric discharge machined from the 0.006 inch thick material in the 45° orientation with respect to the manufacturer's rolling direction. The specimens were then heat treated for one hour at 1328°F in a dry hydrogen environment and subsequently reheated and oxidized in air at 750°F to provide an electrically insulating layer. Refer to Appendix A for the exact heat treating specifications. The specimen edges were then hand sanded with 600 grit paper and inspected for surface defects under an optical microscope to verify acceptable surface and edge conditions.

3.2 Tensile Testing

Tensile testing was performed in accordance with ASTM Standard E 8 [79] for the room temperature tests and ASTM Standard E 21[80] for the elevated temperature tests. The tests were conducted on the Instron 4507 Tensile Machine at a crosshead speed of 0.04 inches per minute. These tests were performed at temperatures ranging from -65°F up to 1100°F utilizing Class B-2 extensometers and bolt loaded compression grips with serrated faces. For the elevated temperature tests, the entire specimen and its grips were enclosed in a three zone resistive heating furnace and soaked at test temperature for 15 minutes prior to loading.

The small thicknesses and cross-sectional areas of the specimens required particular attention to the measuring devices. A telescoping extensometer frame was attached to the specimen to translate the displacement outside of the furnace where the extensometer could

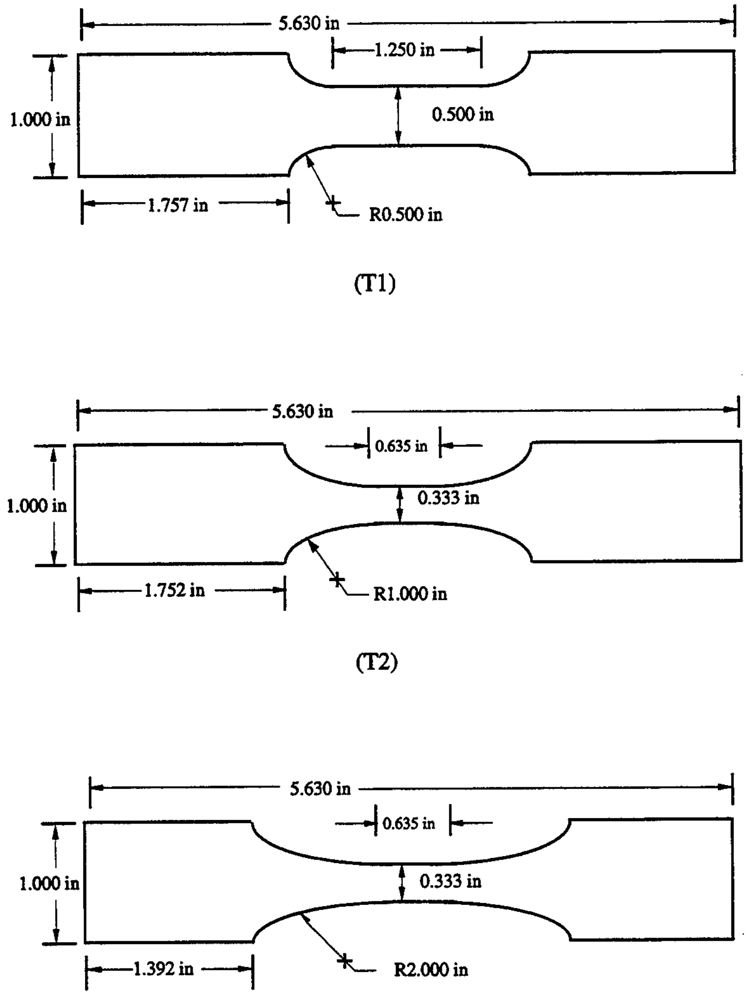
5.630 in
1.250 in
1.000 in
0.500 in
1.757 in
R0.500 in
5.630 in
0.635 in
1.000 in
0.333 in
1.752 in
R1.000 in
5.630 in
0.635 in
1.000 in
0.333 in
1.392 in
R2.000 in

(T1)

(T2)

(T3)

Figure 3.2 Tensile and Creep Specimen Configurations.

be utilized. As an addition to the extensometer reading, crosshead displacement was also recorded for a series of room temperature tests. This additional measurement allowed for a conversion factor to be determined for converting crosshead displacement to strain. Conversion factors were required for each of the three different strain regimes: elastic strain, Lüders strain, and the strain associated with work hardening. Three Type K thermocouples were used to measure the specimen temperature at the center of the gage length and approximately 0.625 inches above and below the center. A loaded specimen can be seen in Figure 3.3. The specimen temperature was controlled with an Applied Test Systems, 3-Zone temperature controller, maintaining a tolerance of ±2°F. The test results were recorded electronically and/or graphically.

3.3 Constant Strain Rate Testing

The T3 configuration tensile test specimens, designed for the characterization phase, were also used in the constant strain rate tests. This elevated temperature testing was done in accordance with ASTM standard E 21[80] at 800 and 900°F. The series of eight tests was conducted on an Instron 4506 tensile test machine at four different crosshead speeds varying from 0.0167 in/min to 0.0000167 in/min at order of magnitude intervals. The specimens were mounted, utilizing an alignment rig, into bolt loaded compression grips with serrated faces. A telescoping extensometer frame was attached to the specimen to translate the change in length of the gage section outside of the furnace where the class B2 extensometer could be used. The entire specimen and grip unit was placed inside a three zone resistive heating furnace and soaked at test temperature for at least fifteen minutes prior to loading. Three type K thermocouples were used to measure the specimen temperature at the center of the gage length and approximately 0.625 inches above and below the center. The temperature was controlled with an Applied Test Systems, three zone temperature controller maintaining a tolerance of ±2°F. All eight of the tests were recorded electronically.

3.4 Creep Testing

Creep testing was performed in accordance with ASTM Standard E 139 [81] at Metcut Research Inc., located in Cincinnati, Ohio. SATEC, Model LD, creep rupture testers were used with a 5:1 lever arm ratio. SATEC Power Positioning furnaces were also used and controlled with West 2810 power controllers. The furnace is a series wound tube furnace, typically known as the “F6 furnace.” The heating element consists of four sections coiled around the tube and wound in series. The total power applied is shunted, allowing for a variation of the power at each section for temperature control.

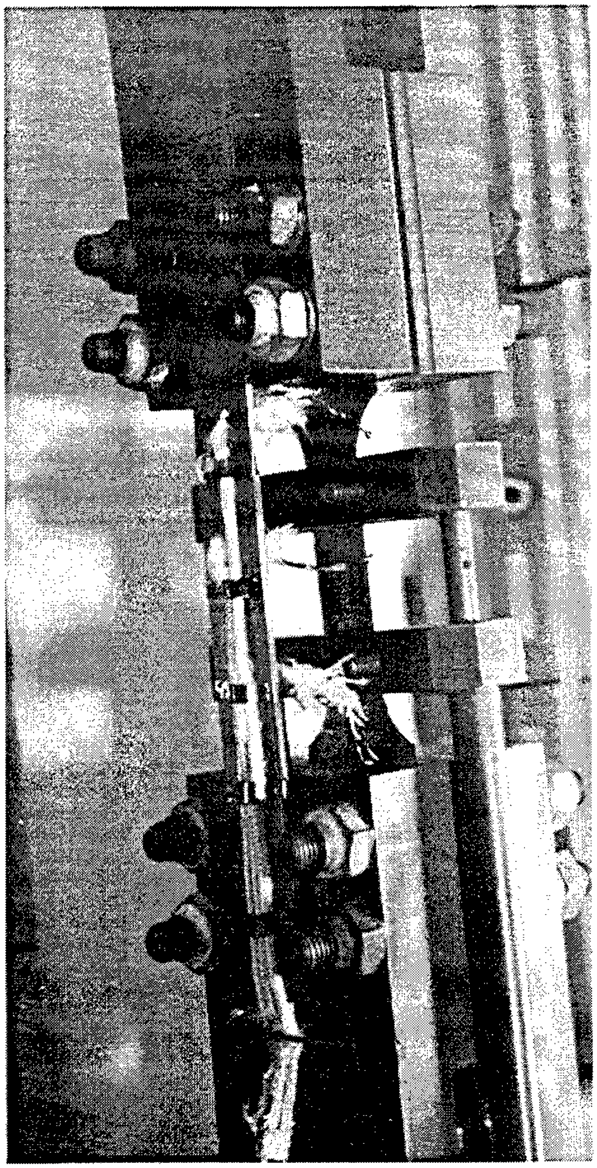

Figure 3.3 Tensile Specimen Inserted in Grips and Exstensometer Frame With Thermocouples in Place.

An alignment fixture was used to clamp the high temperature grips in place while the specimens were inserted in order to prevent damage to the specimens. Also, alignment pins were incorporated into the bolt loaded compression grips, in order to ensure proper alignment of the specimen. The grip faces are serrated and the grip bolts were tightened to approximately 70 inch pounds. This torque was found to be sufficient to prevent slipping without crushing the specimen tab or causing a failure initiation site at the grip front.

Two Type K thermocouples were used to measure the specimen temperature at approximately one half inch above and below the center of the gage length. Flat nickel-chrome (NiChrome) wire was used to bind the thermocouple in position along the specimen edge at each location. The entire specimen and its grips were enclosed in the furnace and soaked for one hour prior to final loading. Ten percent of the test load was applied at the start of this warm up and soak period. The remainder of the test load was incrementally applied at the end of the soak time, with only a few seconds occurring between steps.

The actual displacement was measured with a linear variable differential transformer (LVDT), which consists of a primary and two secondary coils wound around a common core. The primary coil is located between the two secondary coils. During operation of the LVDT a voltage is applied to the primary winding. As the iron core moves (due to an external force) along the axis of the coils, the magnetic core induces a voltage in the secondary windings. The ratio of the voltages of each secondary winding is used to determine the core displacement.

As shown in Figure 3.4, aluminum arms are horizontally attached to the pull train six inches above and below the top and bottom of the furnace, respectively. The end of the top aluminum arm holds a 24 inch long, vertically mounted, quartz rod. The bottom arm holds in place an LVDT in line with the quartz rod to measure its displacement with respect to the lower aluminum arm. Strain versus time data points were recorded electronically at the first of the following three events: ±3°F temperature excursion, 0.001 in/in change in strain, or a three hour time interval.

3.5 Microstructural Analysis

To determine grain size, the samples were first embedded into a Conductomet mold and then sequentially polished using a series of diamond suspension solutions on a texmet cloth. Final polishing was done by using an aluminum slurry on a microcloth. Next, the

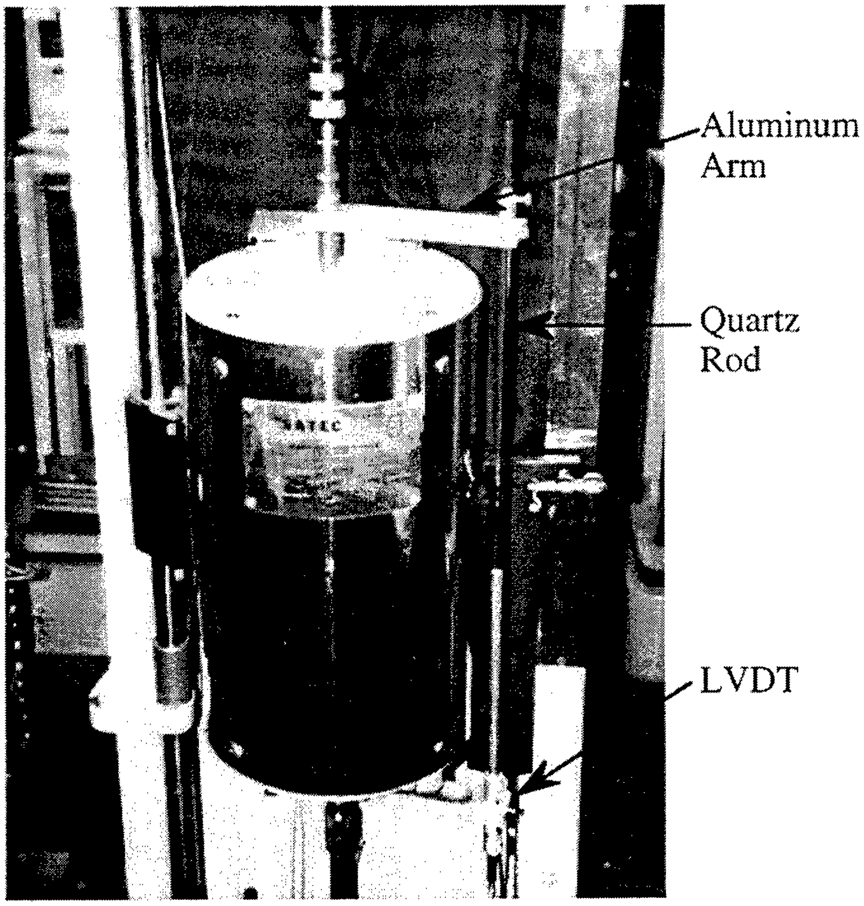
Aluminum Arm
Quartz Rod
LVDT

Figure 3.4 Creep Test Frame and Furnace with Aluminum Arms, Quartz Rod, and LVDT.

samples were chemically etched at room temperature in a nitrated picric acid solution consisting of 100 milliliters of ethanol, 5 grams of picric acid and 5 milliliters of nitric acid. The etching time was a few seconds. A final observation of the microstructure was performed with a scanning electron microscope.

3.6 X-Ray Diffraction Analysis

In an attempt to determine atomic ordering, X-ray diffraction was conducted on multiple HA50HS specimens. Rectangular specimens were manually cut to a size of approximately 0.5 inches by 0.4 inches. They were then chemically cleaned in trychloroethylene and then acetone for a few minutes each to remove any surface contaminants. The samples were held in place on glass slides with a small amount of grease. The prepared slides were then placed in the vacuum chamber of the Rigaku Rotoflex X-Ray Powder Diffractometer. This particular X-ray diffractometer, which can be used for both powder and bulk samples, operates with a copper source. Scans were conducted at 2θ angles ranging from 25 degrees to 90 degrees. The data scans were recorded electronically.

Chapter 4. Results and Discussion

4.1 Tensile Testing

The tensile behavior portion of this study was conducted in two phases. The first phase explored the stress versus strain response as a function of annealing process and orientation to the manufacturer's rolling direction of the supplied sheet. Testing was conducted at room temperature and 900°F only. The second phase focused solely on one anneal and the 45° orientation, however, multiple tests were conducted at temperatures ranging from -65°F up to 1100°F. Constant strain rate testing was also conducted as part of this comprehensive phase.

4.1.1 Screening Phase

Based on the tests of the first phase, one can conclude that the strengths of the HA50HS specimens are certainly a function of both the heat treatment parameters and the orientation to the rolling direction. As depicted in Figure 4.1, specimens annealed at 1300°F had the highest strength, while those annealed at 1350°F produced the lowest strengths. Also, the specimens cut at a 45° orientation to the manufacturer's rolling direction exhibited the lowest strengths when compared to those corresponding to the longitudinal and transverse orientation. This trend is illustrated in Figure 4.2 for the room temperature tests, as well as the 900°F tests.

It is suggested that even the 1300°F heat treatment for one hour is sufficient to fully anneal the HA50HS material [75]. Although tensile data is not available for the as rolled, unannealed condition of the HA50HS, it is available for the closely related HA50 alloy. The as cold rolled yield strength for the HA50 material is reported to be 185 ksi, while the ultimate strength is 195 ksi. Discussions with Carpenter Technology Corporation representatives [75], along with microstructural investigations of the influence of annealing parameters [74], and the lower measured strengths from this screening phase, indicate that a specimen of HA50HS alloy that is heat treated for one hour at 1328°F would be fully annealed.

All of the T1 specimens tested at room temperature fractured at the fillet; therefore, the second specimen design, T2, was developed. This new specimen had a larger blend radius and a smaller cross-sectional area in the gage section. It was calculated that reducing the gage area and increasing the blend radius would result in lower stress concentrations in the blend radii, hence more fractures would occur in the gage section [82]. Room temperature

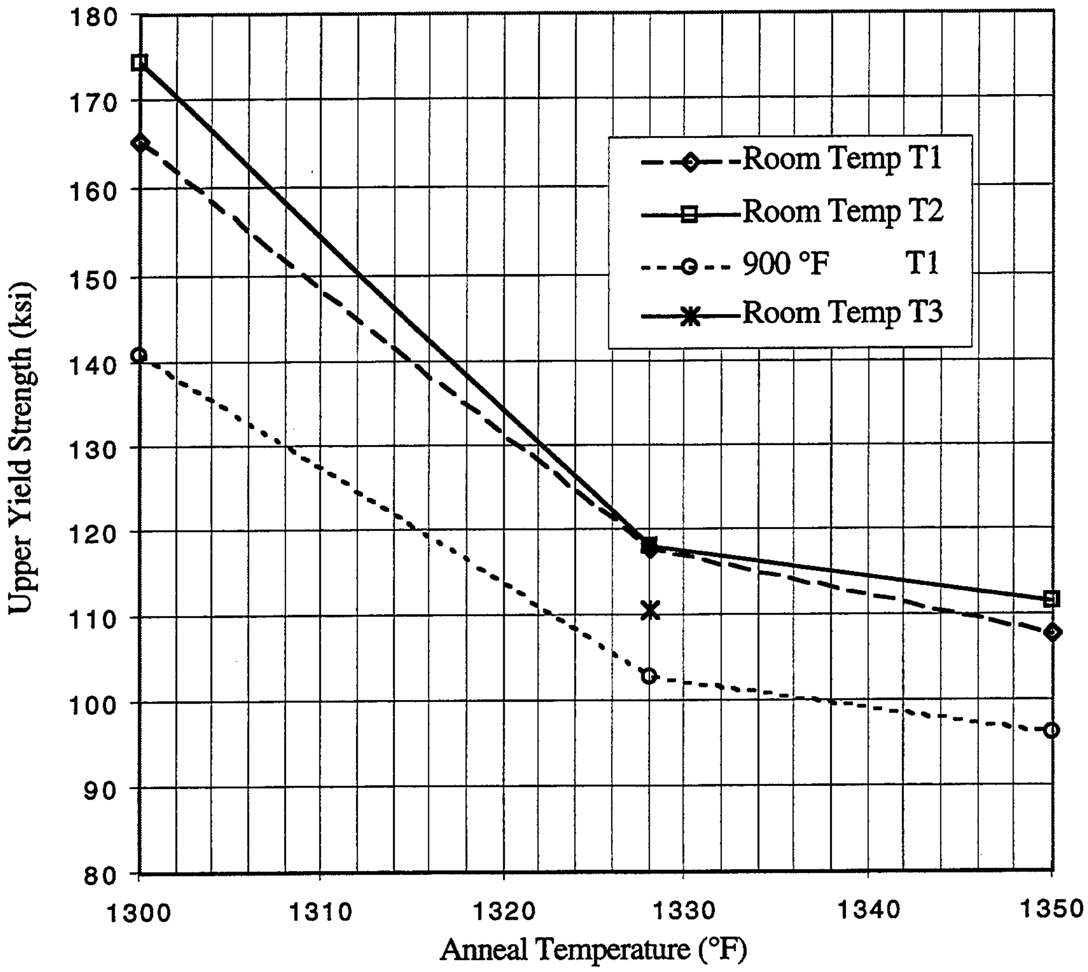

Figure 4.1 Upper Yield Strength of HA50HS Specimens Tested in the Transverse Orientation as a Function of Anneal Temperature.

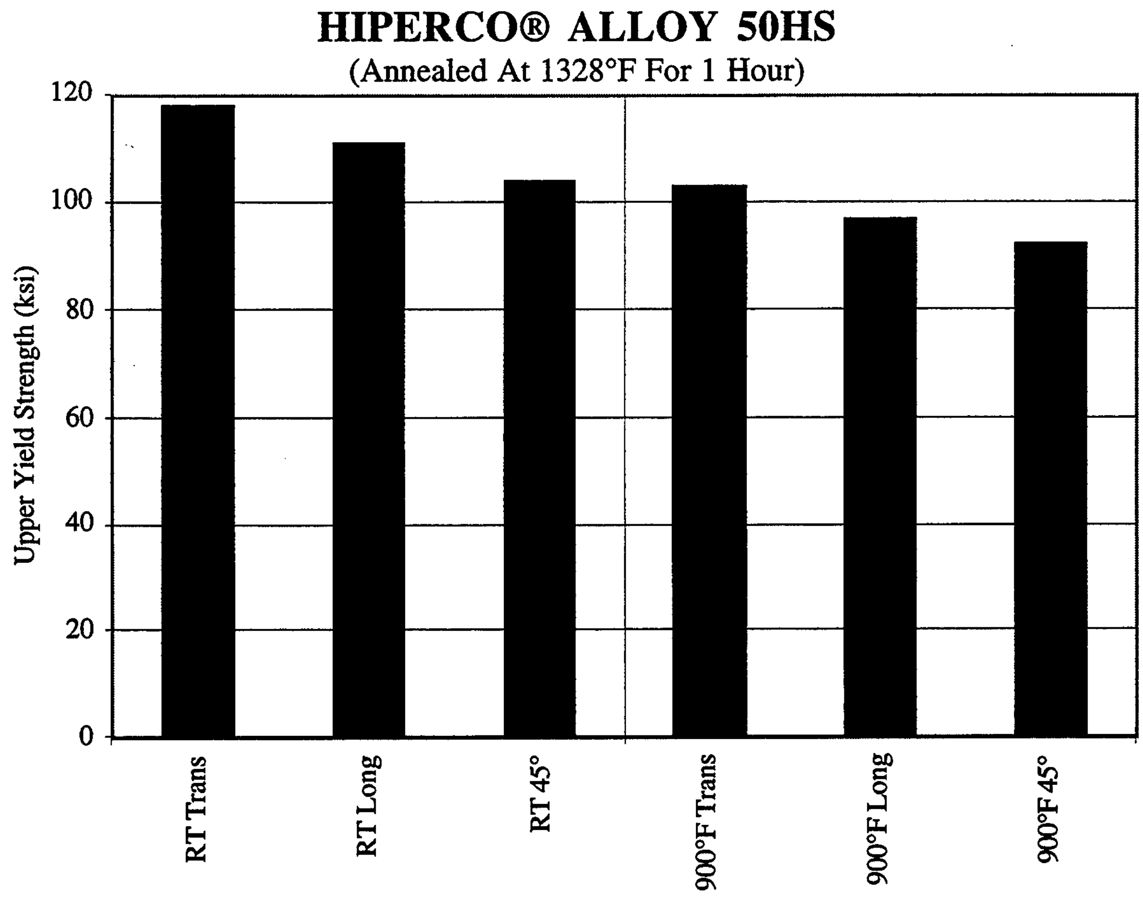

Figure 4.2 Upper Yield Strength of HA50HS T1 Specimens Tested as a Function of the Orientation to Rolling Direction.

fractures of the T2 specimens typically occurred in the gage area; however, they were often at either end of this region. Even though fractures of these specimens did not occur at the center of the gage length, yield strength and ultimate strength had higher average values than those associated with the T1 specimens. The data from the T2 testing relative to T1 data suggest that true strength values may even be slightly higher, resulting in a conservative representation of the true material strengths. The T3 specimens, which had the same gage dimensions but a larger blend radius than the T2 configuration, typically fractured in the center of the test section. If they had been heat treated with the same process as the T2 specimens, they most likely would have had a slightly greater yield strength; however, this was not the case since they were annealed at 1328°F for two hours instead of one hour. The longer anneal time was the dominant parameter, resulting in a lower yield strength by about 9%.

The data obtained by the conclusion of this first phase was preliminary in nature; however, it was sufficient to provide material behavioral trends and a starting point for the more comprehensive phase of the study. An analysis of variations (ANOVA) was performed on the T1 strength data. The ANOVA indicated that for any comparison between the three heat treatments and between the three orientations to rolling direction, there existed at least a 99.95% certainty that each anneal temperature and each orientation would produce a significantly different yield strength average.

Along with these preliminary mechanical results, consideration was made of results from ongoing magnetic and electrical studies, in order to develop the desired specimen configuration. The 45° orientation was selected in order to obtain data associated with the weaker orientation, and the one hour anneal at 1328°F was the selected heat treatment. Also, the T3 specimen geometry was selected for the second phase of the tensile study, thereby reducing the stress concentrations.

4.1.2 Characterization Phase

The tensile testing of the second phase of this study consisted of 48 uniaxial tensile tests of the T3 specimen configuration annealed at 1328°F for one hour in a dry hydrogen environment. The typical stress-strain curves recorded in both phases of testing, as represented in the curves of Figure 4.3, clearly indicate a yield point at lower temperatures, which is identified and referred to in this study as the upper yield strength, a heterogeneous deformation that proceeded at a slightly lower average stress level, and most often, a section of homogeneous deformation that concluded with necking and fracture. At the

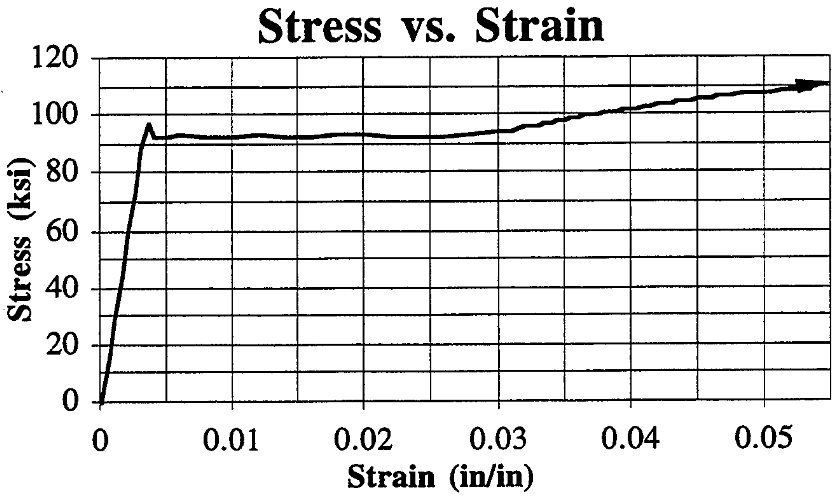

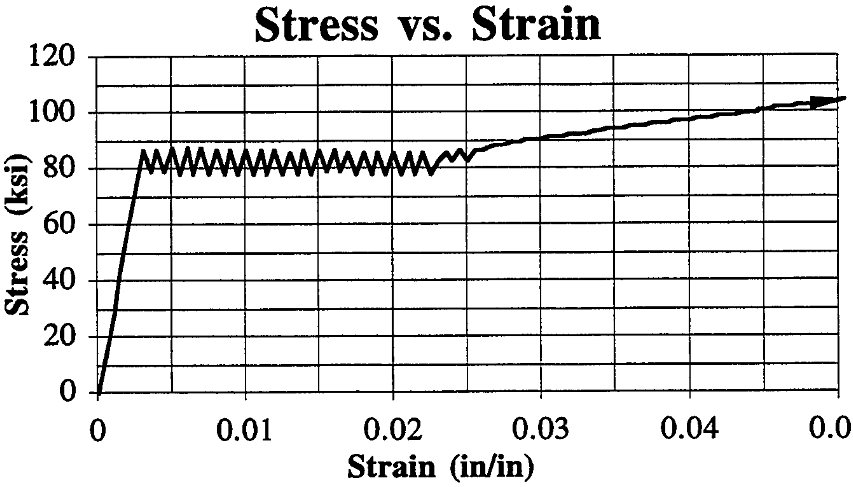

Figure 4.3 Typical Stress Versus Strain Response for a HA50HS Iron-Cobalt Alloy Tested in the 45° Orientation to the Rolling Direction at (Top) Room Temperature, and (Bottom) at 1000°F.

upper yield point a discrete band of deformation, known as a Lüders band, could be seen on the test section of the specimen, usually at about 45° to the loading axis. Figure 4.4 shows Lüders bands that have initiated at a stress concentration site created by the mounting of the extensometer frame. The formation of the Lüders band would initiate the typical load drop of approximately 5% to 10%. During this heterogeneous yielding stage, additional bands formed at this lower stress level and propagated through the entire gage region of the specimen.

This propagation is known as yield point elongation and is represented by an increasing strain at a relatively constant stress level. At elevated temperatures the constant stress required to propagate the bands was gradually replaced by the serrated portion of the stress-strain curve, as can be seen in the bottom plot of Figure 4.3. The serration fluctuated between maximum and minimum stress levels as the strain continued to increase and eventually covered the entire test section of the specimen. This behavior was more apparent in the elevated temperature tests at 600°F and above than during the lower temperature tests. In some tests the specimen fractured during the yield point elongation. For this type of response the upper yield strength was documented as the ultimate strength. An ultimate strength greater than the upper yield strength was indicative of the specimen deforming through the yield point elongation region and into the homogeneous portion of the curve where load increased with strain until fracture occurred.

It can be seen from Figure 4.5 that the elastic modulus is similar to that of iron and steel, about $30\text{x}10^6$ psi at room temperature [19]. The crosshead derived data points are those which were determined from a crosshead displacement measurement and subsequently converted by a previously determined factor. The measured strain data points were determined by measuring the gage length displacement with a telescoping frame and an extensometer. As one would expect, the elastic modulus decreases as the test temperature is increased. This decrease in modulus is due to the increased amount of stretching or distortion of the atomic bonds enabled by the thermodynamic weakening of the atomic bonds. Since the elastic modulus is defined as the change in stress over the change in strain, or the slope of the linear elastic portion of the stress versus strain response, an increase in the amount of relative strain or a decrease in the yield strength would result in a reduced modulus. Figures 4.6 and 4.7 indicate that both an increase in elastic strain as well as decrease in yield strengths occur as test temperature is raised. At 1100°F linear elastic data from four tests resulted in an average modulus of approximately $15.3\text{x}10^6$ psi. A linear fit of all data from -65°F to 1100°F could be employed. However, a distinct shift

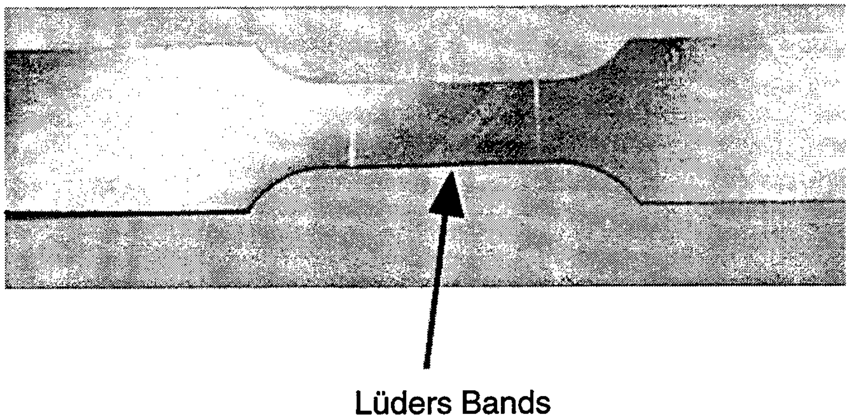
Lüders Bands

Figure 4.4 Formation of Lüders Bands on a HA50HS Tensile Specimen Tested in the 45 Degree Orientation at 800°F.

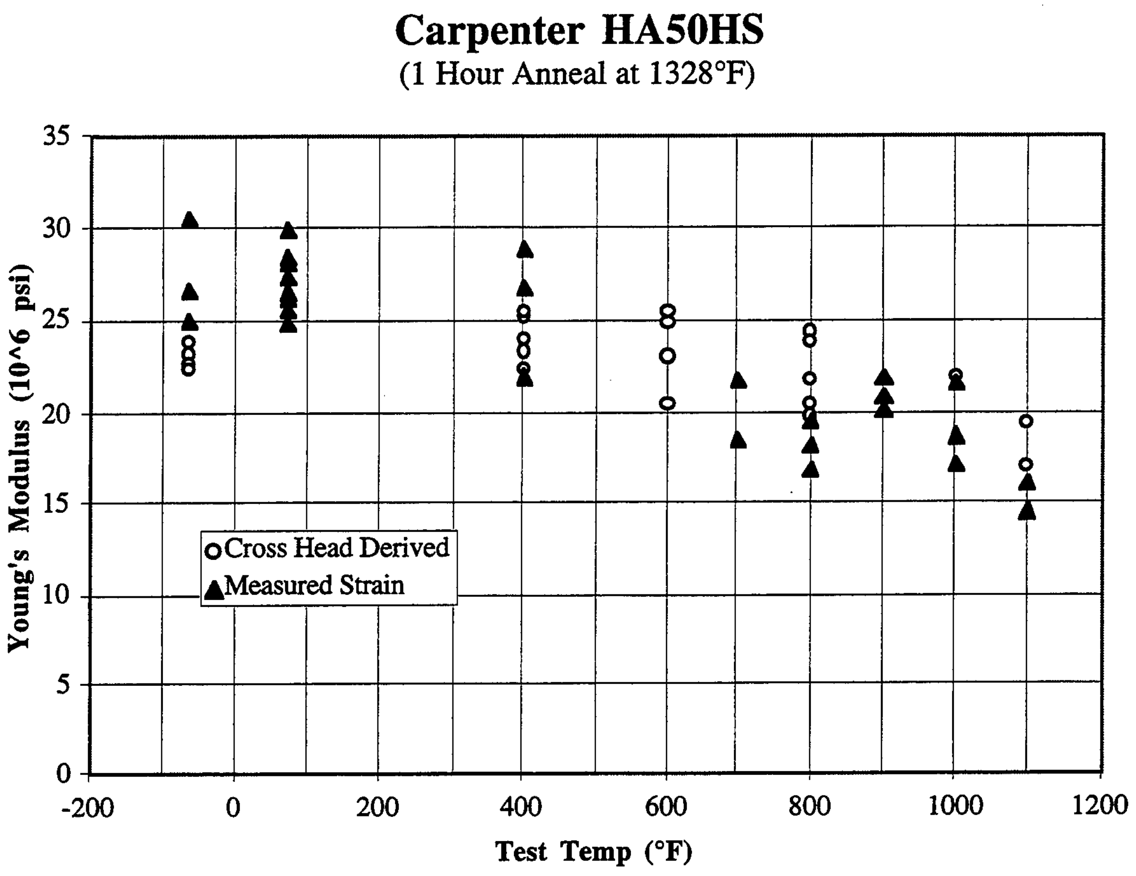

Figure 4.5 Elastic Modulus Versus Temperature for Hiperco® Alloy 50HS as Determined for the 45 Degree Orientation to Rolling Direction.

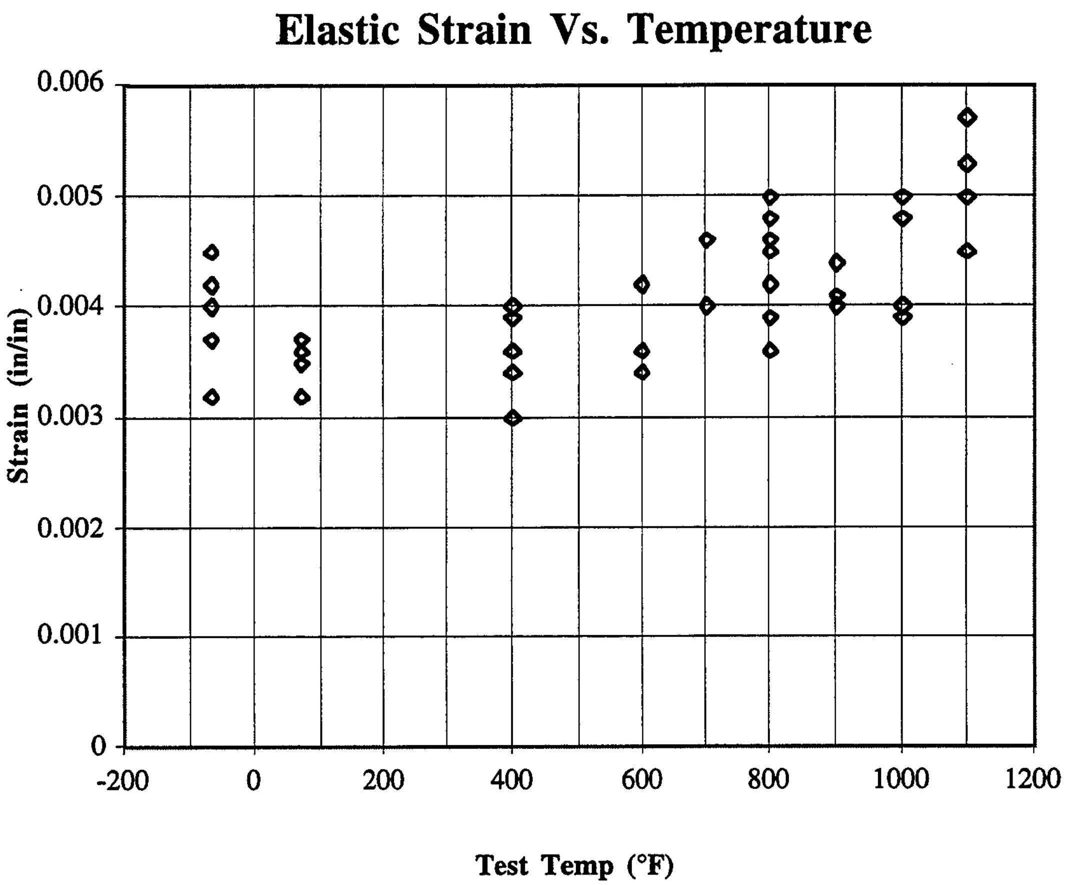

Figure 4.6 Elastic Strain Versus Test Temperature of HA50HS Specimens Tested in the 45 Degree Orientation.

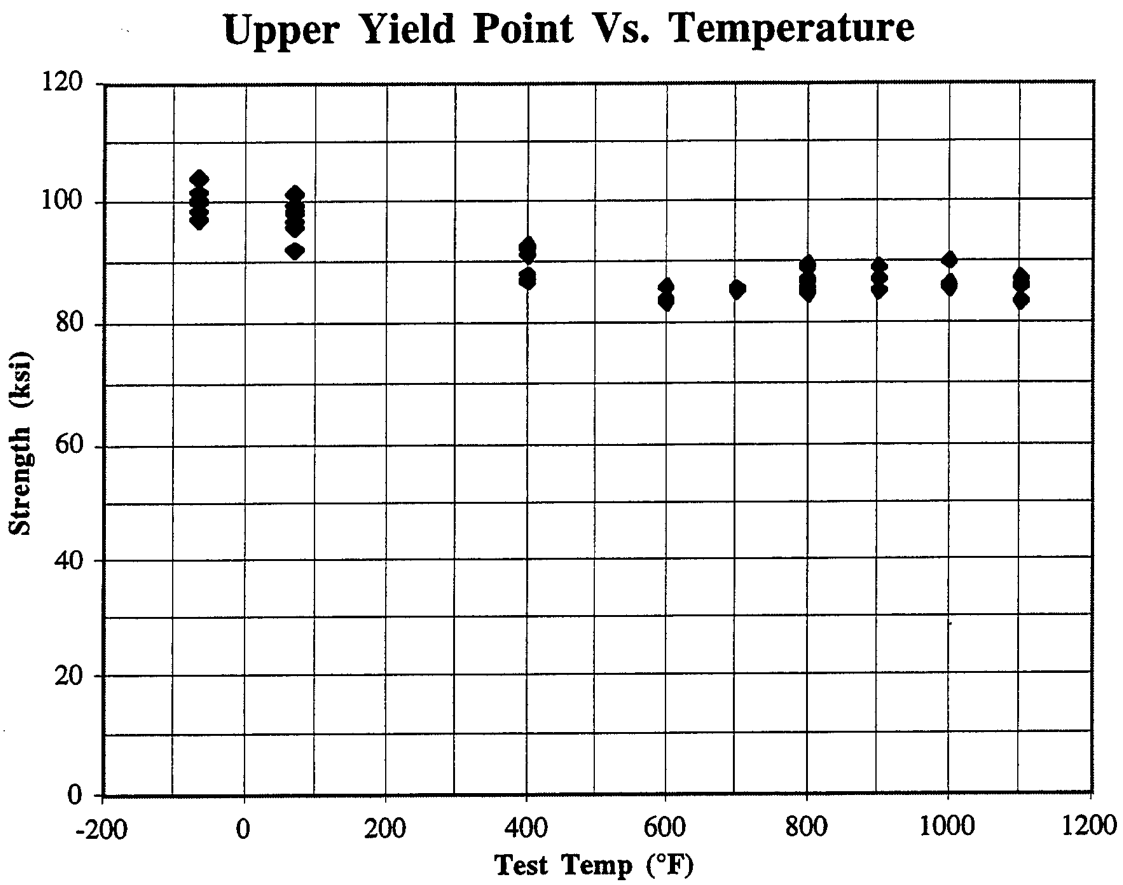

Figure 4.7 Upper Yield Strength Versus Test Temperature of HA50HS Specimens Tested in the 45 Degree Orientation.

in the trend of the modulus variation can be visualized as occurring between 400 and 600°F. This shift is also evidenced by the elastic strain data and the yield strength represented in Figures 4.6 and 4.7, respectively.

Due to the yield phenomenon associated with the tensile deformation of this material, it was necessary to document the upper yield point, the lower yield point, and the mid serration flow stress to fully describe and characterize the deformation response of each test. The upper yield point is defined as the abrupt drop in the applied stress coincident with the formation of the first Lüders band. The lower yield point is the level to which the stress falls immediately after the upper yield point. This lower stress level is typically the stress required to propagate the Lüders band the entire length of the gage section. This single yield point behavior is illustrated in Figures 1.5 and 4.3. At elevated temperatures, however, the distinct upper and lower yield points are replaced by the serrated stress versus strain response characteristic of dynamic strain aging, or the Portevin-LeChatelier effect. The average stress value located between the repeated upper and lower points is registered in this study as the mid serration flow stress. This serrated behavior is illustrated in Figure 1.6 and 4.3.

In the lower regime of the test temperatures, from -65°F up to 400°F, there were no serrated flow responses, therefore, the average mid serration flow stress was coincident with the lower yield point. This value was indeed the stress required to propagate the Lüders band through the specimen. Figure 4.8 illustrates this behavior. Although the average upper yield point decreases as temperature increases, the magnitude of this point increases with respect to the lower yield point with an increase in temperature. At -65°F, room temperature, and 400°F the yield point drops are approximately 1.7%, 2.4%, and 3.1% of the upper yield point, respectively. Although these percentage drops indicate relatively small yield points, the test data were very consistent with every test.

At 600°F the yield point begins to be replaced with the serrated flow that is indicative of dynamic strain aging. Also, the mid serration flow stress average rises above the lower yield point average with an increase in test temperature. At 600°F the average yield point drop is only 2.0% and the average mid serration flow stress is only slightly above the lower yield point. However, as the single yield point has essentially been eliminated at 700°F, the magnitude of the repeated drops are approximately 5%. At 800°F through 1100°F the drops are essentially constant with a magnitude of about 8%. Not only is the serration magnitude relatively constant in this elevated temperature range, but the mid-

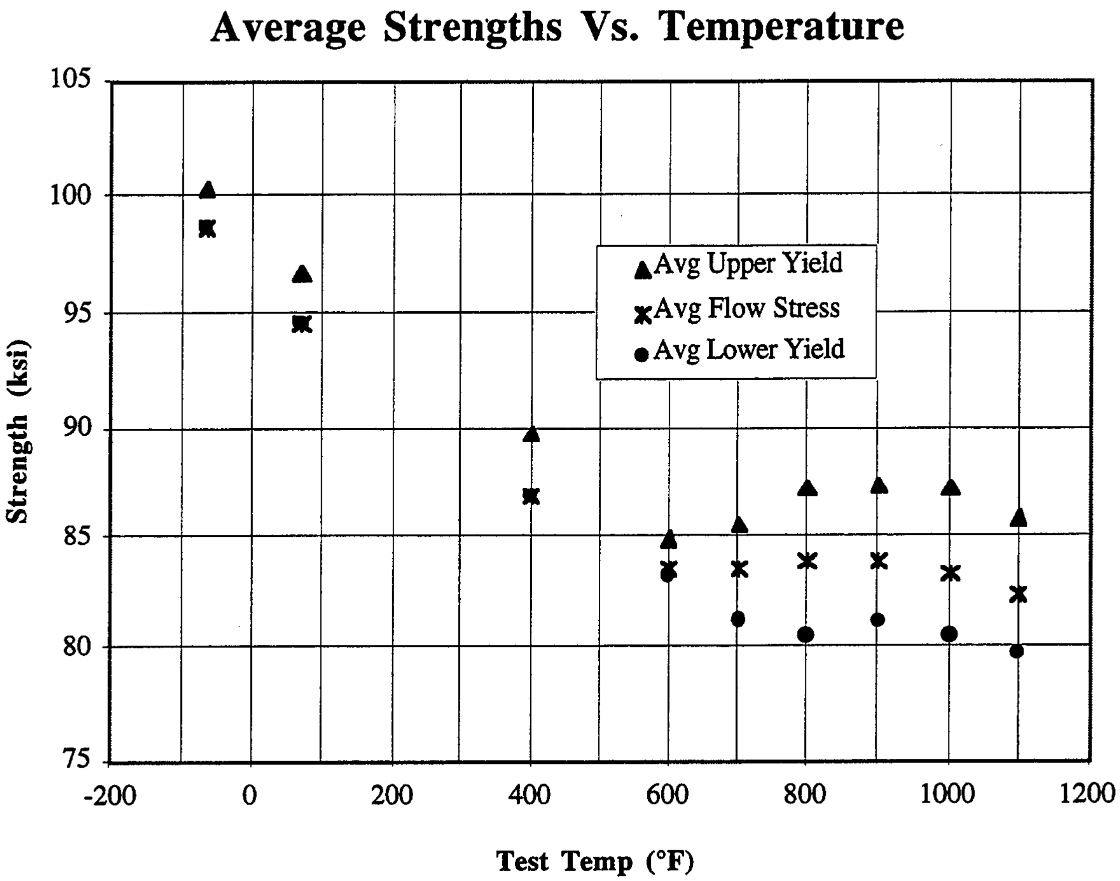

Figure 4.8 Average Yield Strengths of HA50HS Specimens Tested in the 45 Degree Orientation.

serration flow stress is also. The fact that the yield stress becomes independent of temperature in the same temperature range as the dynamic strain aging serrated flow is supported in related literature. Reed-Hill states that an interesting aspect of dynamic strain aging is that the strengths of metals expressing this behavior become independent of temperature [18].

Studies pertaining to the temperature dependence of yield strength for body centered cubic alloys have been documented by Johnston and Gilman [21]. Their investigation of the influence of long range order of an iron-cobalt-vanadium alloy revealed a flow stress versus temperature trend very similar to the behavior documented for the HA50HS studied under this research effort. The actual flow stress values for the ordered HA50HS are approximately three times the values documented by Johnston and Gilman for their FeCo-V; however, the similarity in behavior is obvious [21]. According to Stoloff and Davies [37] the temperature dependence of yielding is markedly reduced upon ordering. Data are presented for disordered material, which show a substantial decrease in flow stress as temperature is increased from 73 K to 473 K. Over the same temperature range, the behavior of ordered material begins at a much lower flow stress but the temperature dependency is also reduced. The different behaviors result in a crossing of strength trends with the ordered state remaining almost unaffected by temperature increases up to nearly 870 K [37].

The elastic strain, as documented for this study in Figure 4.6, is the strain which corresponds to the stress of the upper yield point. The average elastic strains range from the lowest value of 0.36% at room temperature up to 0.56% at 1100°F. The trend between these two temperatures is approximately linear. At -65°F, an average value of 0.4% strain was recorded. When dealing with materials that deform without a yield point, it is usual to select a stress to be the yield stress which corresponds to a strain of 0.002 or 0.2%. Yield point phenomena, however, will typically increase the elastic strain by maintaining the linear elastic behavior for a longer duration [26]. Values such as those obtained under this study are not unreasonable.

The amount of deformation which occurs from the upper yield point to the initiation of work hardening is known as yield point elongation [16]. Since the yield point is coincident with the development of the first Lüders band, this elongation region at a constant stress is also known as Lüders strain [83]. Obviously, Lüders strain is a function of the specimen geometry and can only be accurately measured if the Lüders band, or bands, propagate the entire gage length of the specimen. As can be interpreted from Figure 4.9, some of the specimens tested fractured during this near perfectly plastic deformation. Multiple specimens at -65°F and one at room temperature failed during this heterogeneous deformation. The specimens in which the Lüders band successfully propagated the entire gage length indicate a consistent Lüders strain of approximately 2 to 2.5%.

Following the yield point and the Lüders elongation region, the HA50HS material undergoes a work hardening process. The stress required to continue deformation increases with increasing strain. The maximum amount of engineering stress a material can withstand without fracture in a tensile test is known as the ultimate tensile strength. The corresponding strain represents the maximum strain for which plastic deformation is uniform along the specimen gage length. As strain is increased the engineering stress begins to decrease as a result of nonuniform deformation, or necking, of the specimen.

Figure 4.10 illustrates the temperature dependence of the ultimate strength. The ultimate strengths measured at -65°F and room temperature are about the same. There is a shift in behavior, however, at some temperature between room temperature and 400°F. The strength begins to increase as test temperature is increased. A maximum value of approximately 148 ksi is attained at 700°F. Above this temperature the ultimate strength begins to decrease linearly with increasing temperature. The lowest ultimate strength, 84 ksi, was registered at a test temperature of 1100°F. It is speculated that the ultimate strength behavior is proportional to the increase in the rate of work hardening associated with dynamic strain aging. The maximum ultimate strengths then correspond to a maximum amount of dislocation immobilization by the segregating solute atoms.

Another material property that may be obtained from a tensile test is the strain to fracture, or the percent elongation. This value of the total strain is often used as an indication of a material's ductility. It must be emphasized, however, that the total strain measurement typically involves deformation beyond the point of specimen necking. As necking occurs, the rest of the specimen gage length stops deforming and may even relax as the deformation is localized in the necked region. Still, a point of comparison for most materials is the percent elongation. This mechanical characteristic is included in this study as well.

As determined in this study the total strain is comprised of the initial elastic strain, the Lüders strain, and the work hardening strain. For some of the -65°F tests the elastic strain is the only valid strain measurement, since the specimen failed during the Lüders elongation

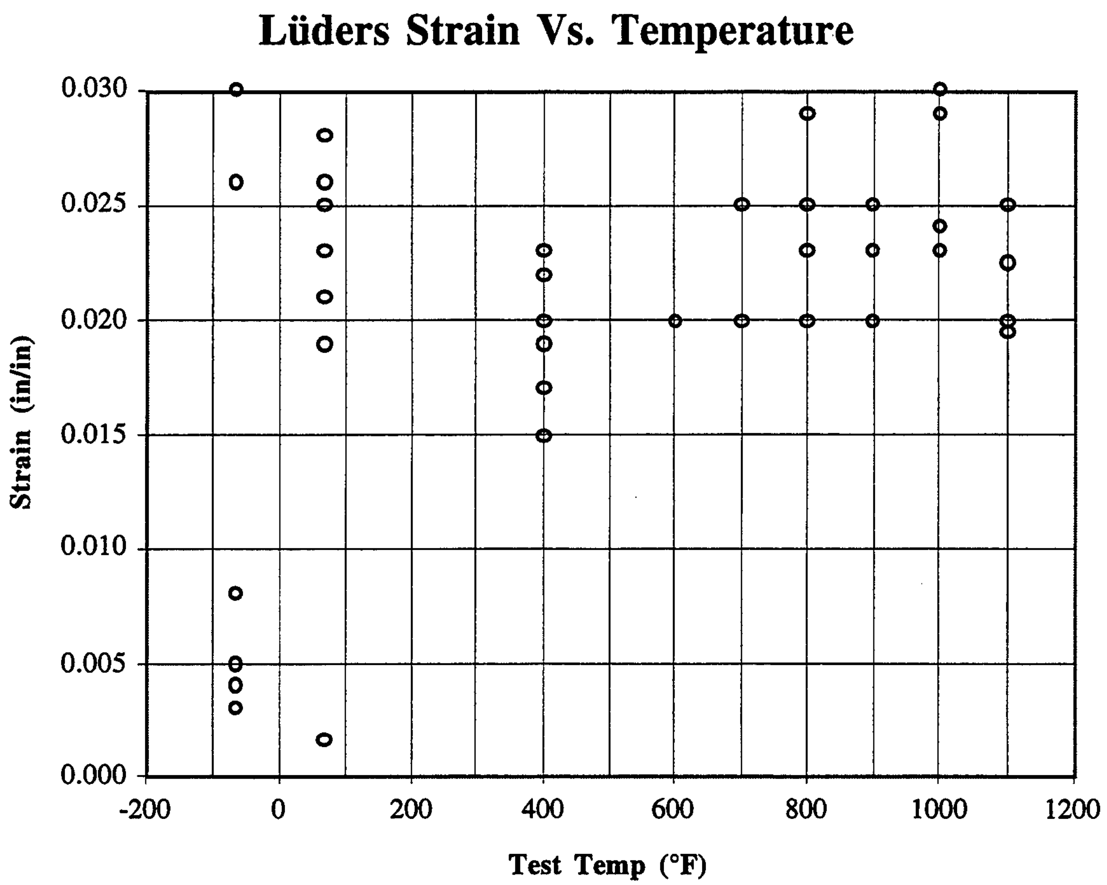

Figure 4.9 Lüders Strain (Yield Point Elongation) Versus Test Temperature of HA50HS Specimens Tested in the 45 Degree Orientation.

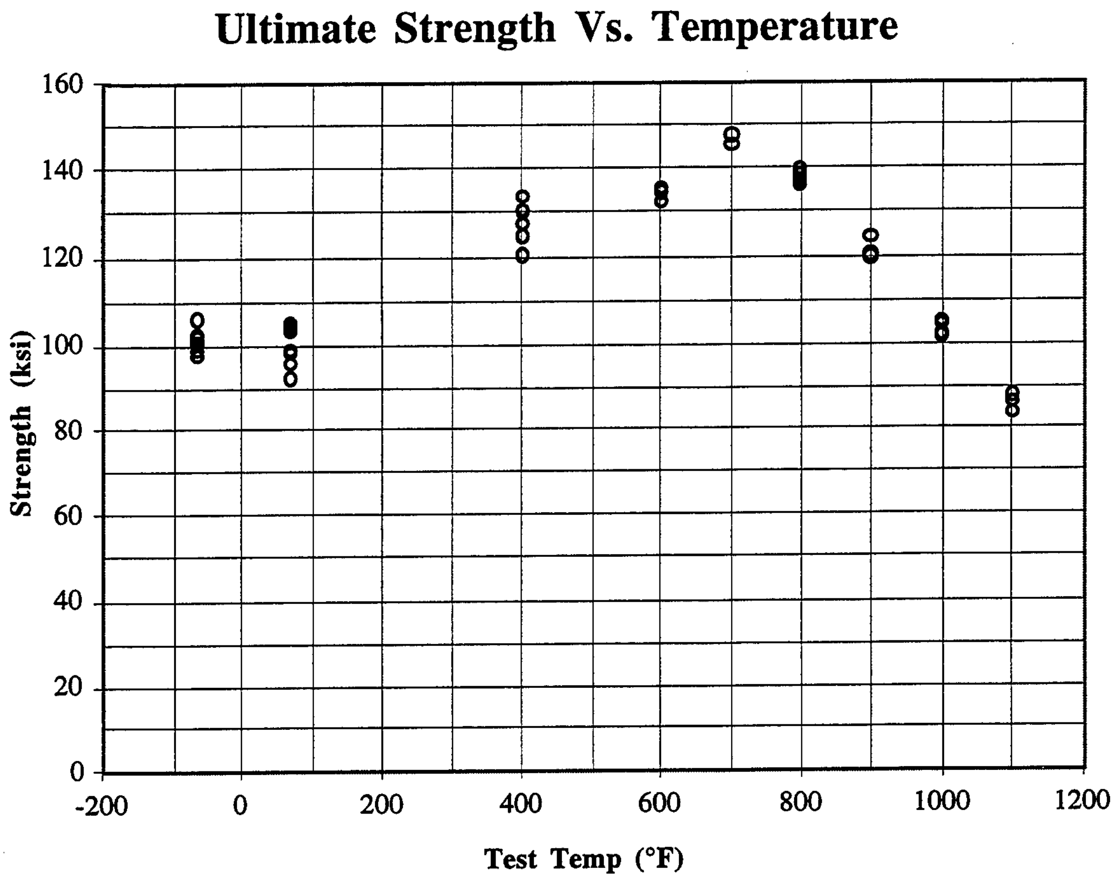

Figure 4.10 Ultimate Tensile Strength Versus Test Temperature of HA50HS Specimens Tested in the 45 Degree Orientation.

region. Only one of these low temperature tests deformed into the work hardening regime. As can be seen from Figure 4.11, a total strain of approximately 5% was recorded from this test. All but one of the room temperature tests progressed through the Lüders elongation region but none of them reached a point where necking became obvious. Typical total strain values for these tests ranged from approximately 4 to 6%. The fracture surface of one of the room temperature tensile specimens is depicted in Figure 4.12 The SEM micrograph shows a cleavage fracture surface, which is indicative of brittle behavior. This particular specimen deformed to a total strain of only 5.3%. The elevated temperature tests all registered a decrease in the stress required to continue straining; therefore, the total elongation measurement included the deformations associated with necking. At 400°F the total strains recorded ranged from about 11 to 15%. The total strains increased linearly with respect to temperature up to a value of 25% at 1100°F. The only exception to this proportional relationship occurs at 800°F where the highest total strain, 31%, was measured.

4.1.3 Constant Strain Rate Testing

It is theorized that the abrupt change in strain rate, as illustrated on many of the creep curves, is related to yielding as registered on the stress versus strain response. The abrupt strain rate change seems to occur when the applied creep stress is in the proximity of the yield stress as determined by tensile data. To properly relate tensile test data to creep behavior, a bridge of strain rate sensitivity data must be determined between the two strain rates. Tensile tests were conducted at a constant crosshead speed of 0.05 in/min. This rate translated to an elastic strain rate of approximately 1.0 in/in/hr. Creep tests, on the other hand, were conducted at a constant load which led to strain rates as low as 10^{-7} hr^{-1}. Most creep strain rates, however, were on the order of 10^{-5} hr^{-1}.

A series of four tensile tests were conducted at 800°F at constant crosshead speeds ranging from 0.0167 in/min to 0.0000167 in/min at order of magnitude intervals. These speeds corresponded to initial strain rates between 0.28 in/in/hr and 0.00028 in/in/hr. The entire process was repeated at 900°F. As discussed previously there was no evidence of a single yield point. There was a serrated flow of repeated maximum and local minimum stresses, typically associated with dynamic strain aging. These maximum and minimum points of the serration were analyzed as a function of strain rate.

A decreased strain rate generally decreases the flow stress of a material. The magnitude of this influence is known as the strain rate sensitivity, and it is a function of temperature for a

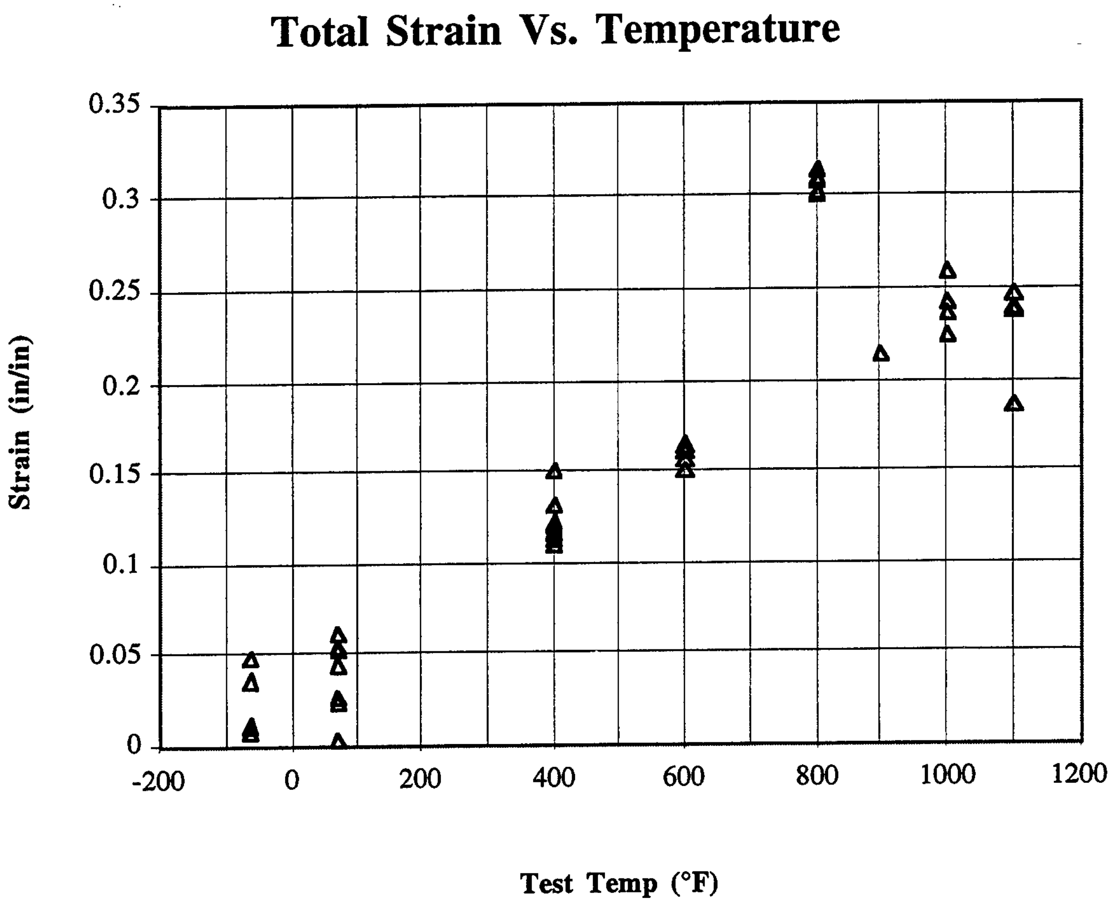

Figure 4.11 Total Elongation Versus Test Temperature of HA50HS Specimens Tested in the 45 Degree Orientation.

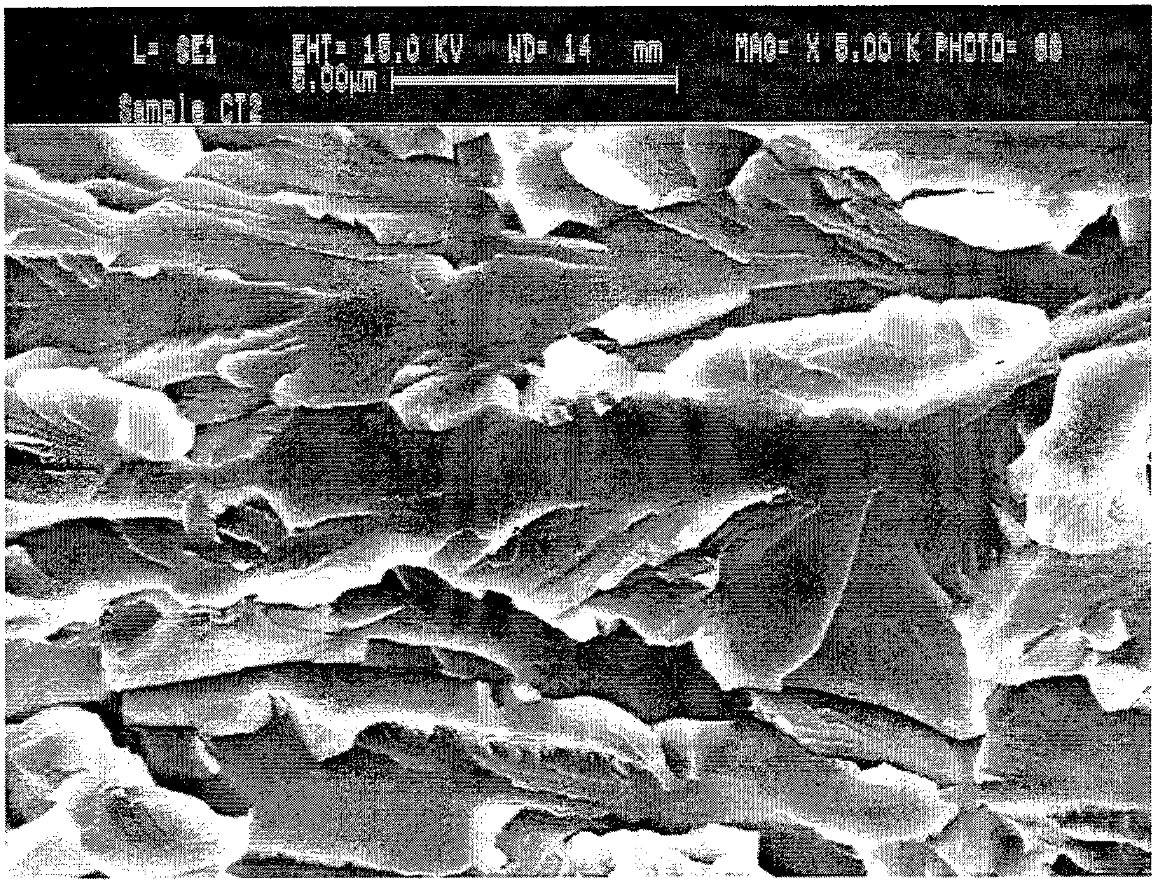
L= SE1
EHT= 15.0 KV
WD= 14 mm
MAG= X 5.00 K
PHOTO= 88
5.00µm
Sample CT2

Figure 4.12 SEM Micrograph of Fracture Surface of HA50HS Tensile Specimen Tested at Room Temperature in the 45 Degree Orientation to the Rolling Direction.

given material. The strain rate sensitivity varies between zero and unity. A value of zero indicates that the material is not strain rate sensitive and a measured stress will be the same at any of the considered strain rates. A strain rate sensitivity of one indicates that the measured stress increases linearly with strain rate. Most metals and alloys exhibit low strain rate sensitivities between zero and 0.10 at room temperature; they can, however, increase significantly at elevated temperatures [25].

There typically exists a linear relationship between the natural logarithm of strain rate and the yield stress. The relationship can be expressed as:

$$\dot{\varepsilon} = k\sigma^m, \tag{4.1}$$

where σ is either the upper or lower yield point. By taking the natural logarithm of both sides, Equation 4.1 becomes:

$$\ln\dot{\varepsilon} = \ln k + m\ln\sigma. \tag{4.2}$$

The slope of the $\ln(\dot{\varepsilon})$ versus $\ln(\sigma)$ curve is the strain rate sensitivity. This relationship can now be used to predict the yield points, at strain rates which correspond to relatively slow creep deformation, based on tensile test measurements.

The strain rate sensitivity analysis, conducted under this study, indicated a sensitivity that was nearly equal to zero when determined for both the maximum and the local minimum serration stresses. The independence of yield stress on strain rate was not surprising when considering the two elevated test temperatures. According to Reed-Hill, the strain rate sensitivity becomes very low in the temperature range of dynamic strain aging as the flow stress becomes nearly independent of the strain rate [18]. As reported earlier, dynamic strain aging is apparent between 600°F and 1100°F for this material. Figures 4.13 and 4.14 illustrate the near zero strain rate sensitivity for both the maximum and local minimum serration stresses.

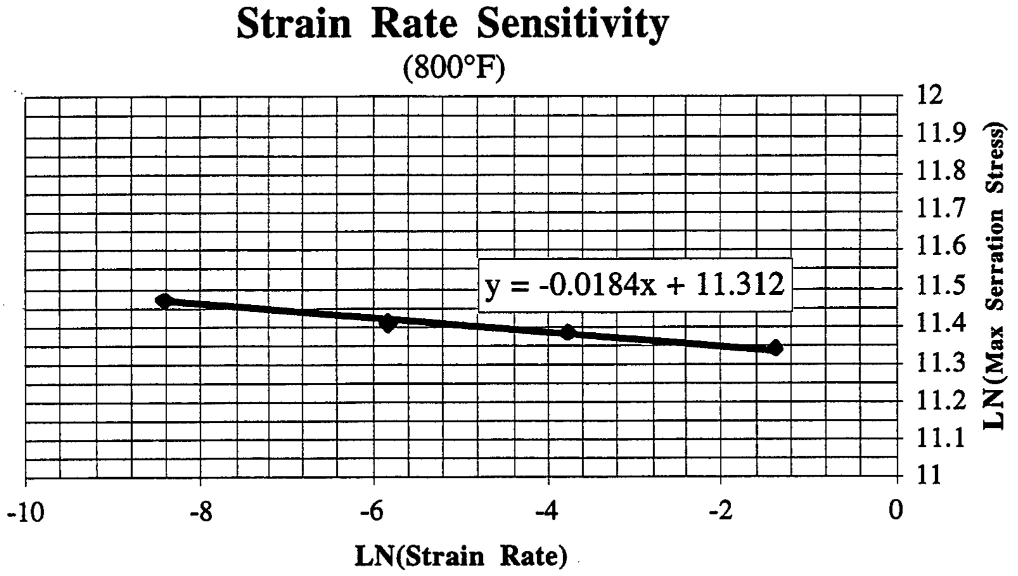

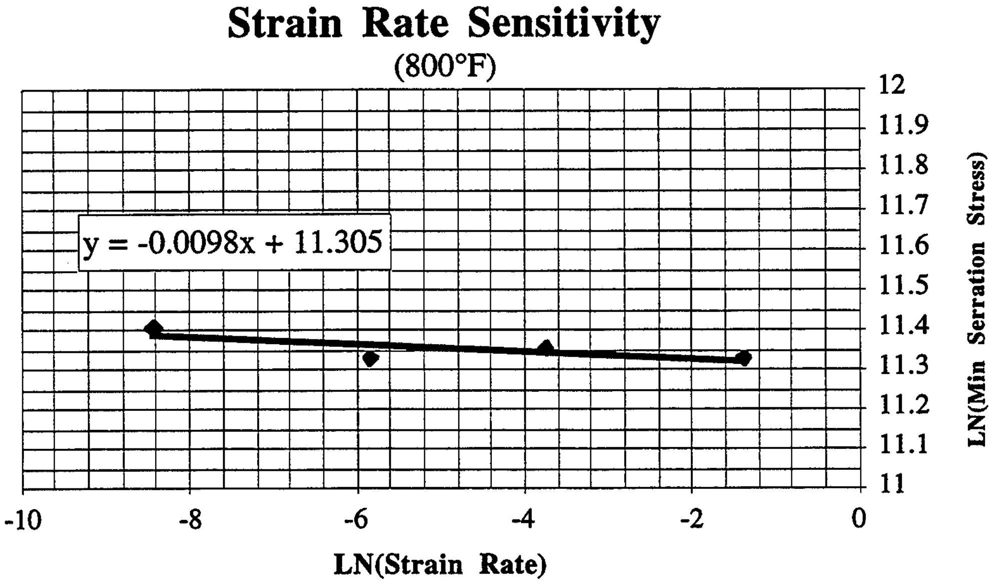

Figure 4.13 Strain Rate Sensitivity Curves at 800°F Corresponding to the Maximum and Minimum Serration Stress Levels.

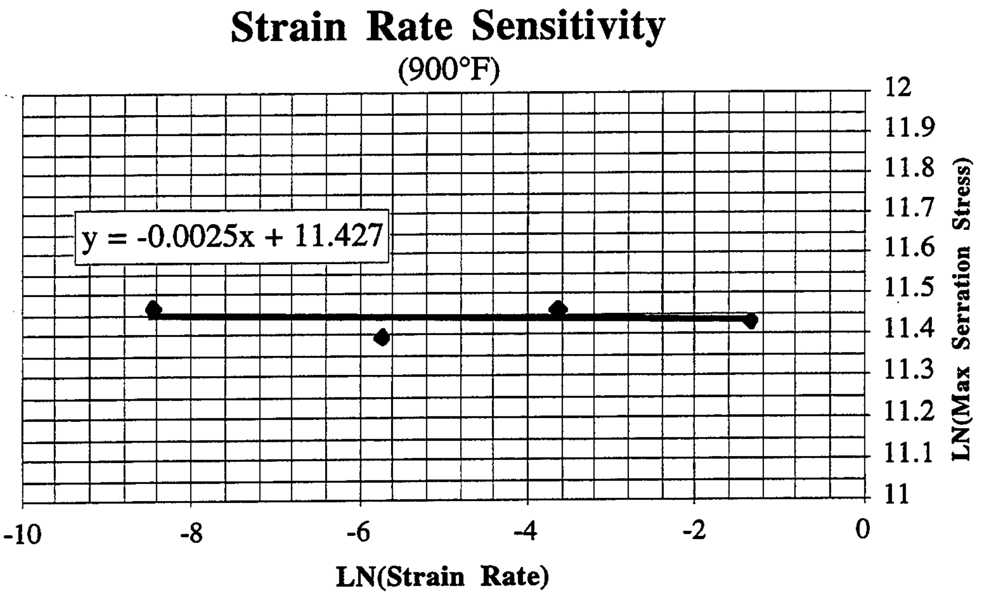

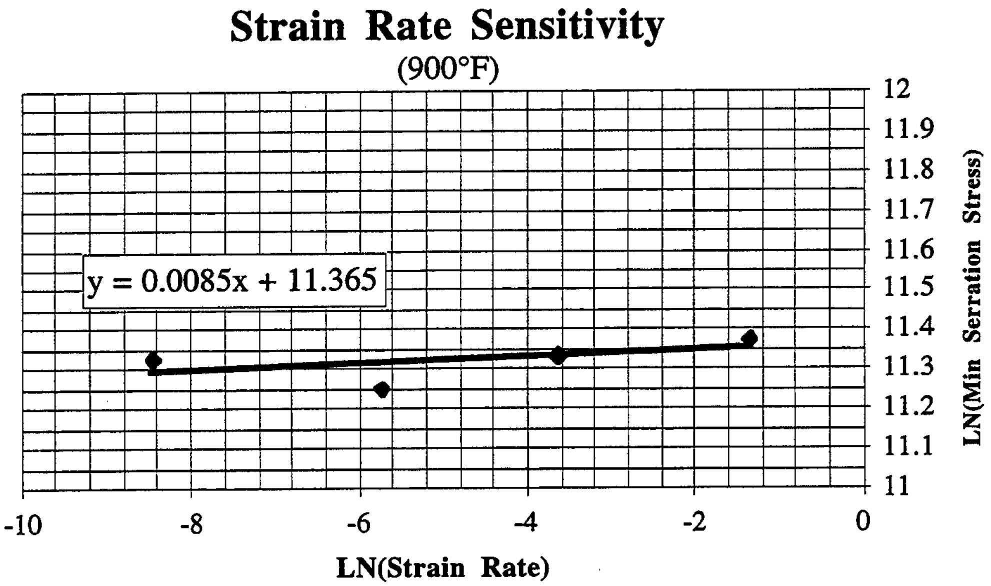

Figure 4.14 Strain Rate Sensitivity Curves at 900°F Corresponding to the Maximum and Minimum Serration Stress Levels.

4.2 Creep Testing

4.2.1 Creep Test Results

The Air Force requirement for an advanced soft magnetic material, capable of maintaining structural integrity in high temperature and high stress environments is the motivation behind the focus of this study: creep deformation. The high magnetic and electrical requirements dictate the use of an ordered intermetallic alloy, specifically one comprised of iron and cobalt. As mentioned previously, the iron-cobalt alloy possesses a B2 ordered crystal structure when it is annealed as a soft magnet. There is some information available in the literature on the mechanical properties of ordered intermetallics; however, most of the studies relate to the titanium alluminides, which are not typically B2 crystal structures [37]. There is even less data published that pertain to the mechanical behavior of iron-cobalt alloys. Although information can be found which pertains to Hiperco®50 and Hiperco®27 [84], there is very little information pertaining to Hiperco® Alloy 50HS. As far as this author knows, there has been only one publication which pertains to the creep behavior of HA50HS [85].

A comprehensive test matrix was developed and periodically modified throughout this study. After consultation with various Air Force Research Laboratory researchers and discussions with multiple Department of Defense contractors an initial set of test parameters was selected. The temperature range included a relatively low creep temperature of 700°F, which is a likely condition for an application currently in development, up to the maximum test temperature of 1100°F. The 700°F and the 1100°F test temperatures correspond to homologous temperatures of 0.36 and 0.49, respectively. There are currently no known plans for an 1100°F application, however, a desire for a 1000°F operating temperature has already been proposed. The intermediate test temperatures, between 800°F and 1000°F, were established at 50°F intervals. The test stresses were selected at each temperature in an attempt to achieve a variation in the deformation behavior and the times to failure. Some specific stresses range from 30 ksi at 1100°F up to 130 ksi at 700°F. The final creep test matrix is representative of the stresses and temperatures that may be expected in various Department of Defense and commercial applications.

Two tests were conducted at 700°F. The first applied load corresponded to a stress of 120 ksi, while the second load equated to 130 ksi. Both of these stresses are well above the average upper yield point of 86 ksi as determined in the tensile portion of this study. With a strain rate sensitivity of nearly zero, the applied stress corresponds to plastic deformation beyond the Lüders elongation region. As can be seen in Figure 4.15, the life of the 120 ksi test specimen was dominated by steady-state creep. Approximately 300 hours were in this region while the final 100 hours represented the tertiary creep stage. There was no evidence of primary creep at this relatively high stress. A steady-state region was present in the 130 ksi test also. Its strain rate was estimated to be 3.25 x 10^{-3} in/in/hr, and it represented about 40 hours of this test followed by a final 10 hour period of tertiary deformation. The 120 ksi test duration was 409 hours at a final creep strain of about 17%. The 130 ksi test duration was only 48 hours at a creep strain of approximately 22%. According to the 700°F tensile test data, the 120 ksi specimen should have experienced approximately 12% plastic deformation upon loading while the 130 ksi test specimen should have plastically deformed about 17%. The fit-back method revealed total plastic deformations of 29.8% and 40.4% for the 120 and 130 ksi test specimens, respectively.

Since the strain measured during the creep test is totally plastic deformation beyond the elastic and plastic strain due to loading, the sum of the creep strain measured and the estimated plastic deformation from the tensile tests should equal the total elongation as determined by the fit-back method. This theory is supported by the recorded data and specimen measurements associated with the specimens tested at 700°F.

Five tests were conducted at 800°F. Constant stresses of 85, 90, 100, 110, and 120 ksi were applied. Although each stress increment varied by only about 10%, or less, three very distinguishable responses were documented. As can be seen in Figure 4.16, the 85 and 90 ksi tests resulted in essentially the same creep strain versus time behavior. Neither of these two tests indicated a substantial amount of creep strain up to nearly 1200 hours. The steady-state strain rates associated with the 85 and 90 ksi creep test are approximately 4.27 x 10^{-7} in/in/hr and 3.61 x 10^{-7} in/in/hr, respectively. Due to the technique used to record strain, the very small strains and very slow strain rates corresponding to these two tests may have been influenced by the laboratory environment. As discussed in the procedures for this study, a strain versus time data point was recorded when a temperature excursion of 3 degrees Fahrenheit, or a period of 3 hours, or when a change in strain of 0.1% occurs. A review of the raw data easily shows that there were no changes in strain of 0.001 between any two data points. Also, there were no temperature excursions greater than 3 degrees F reported. The fact that the measuring instrument relied on a fused quartz rod located outside of the furnace made it subject to environmental conditions. The rod is 24 inches long and it was attached to the horizontal arm of the pull train 21.5 inches from the LVDT interface. The coefficient of thermal expansion for this type of quartz is given as

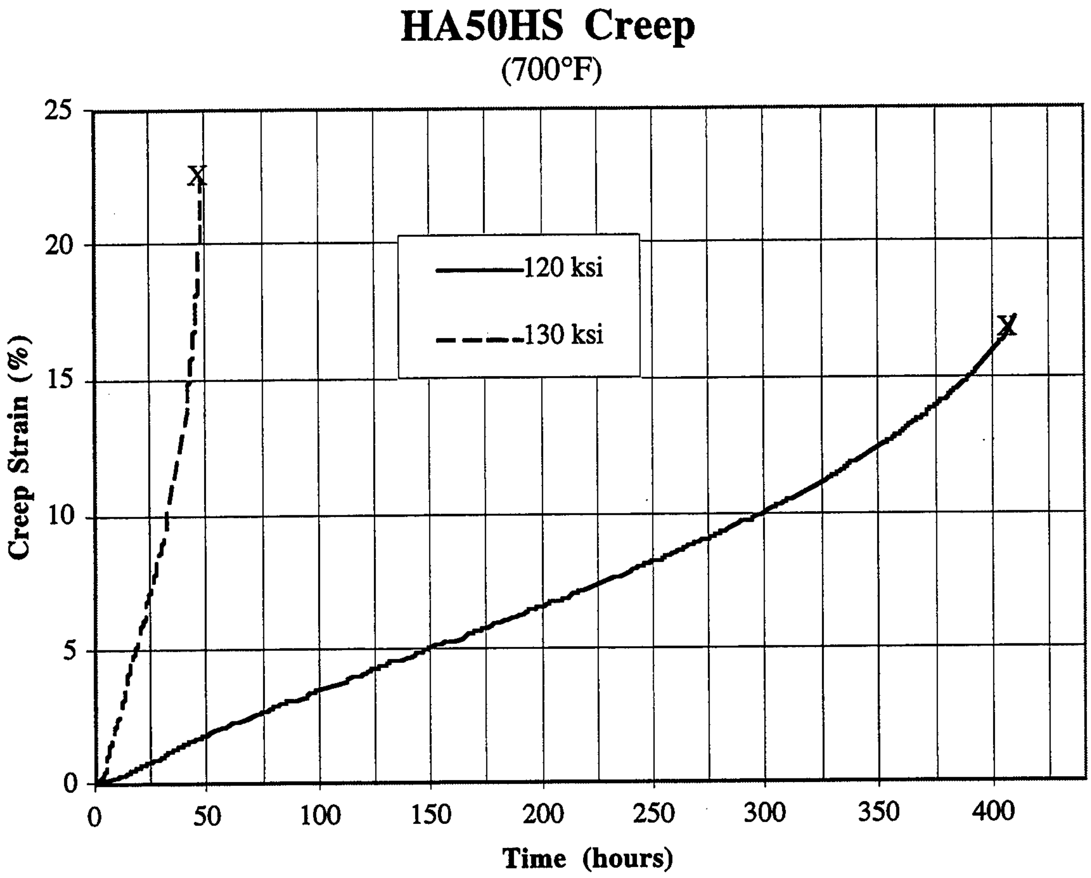

Figure 4.15 Creep Strain Versus Time Response of HA50HS Specimens Tested at 700°F.

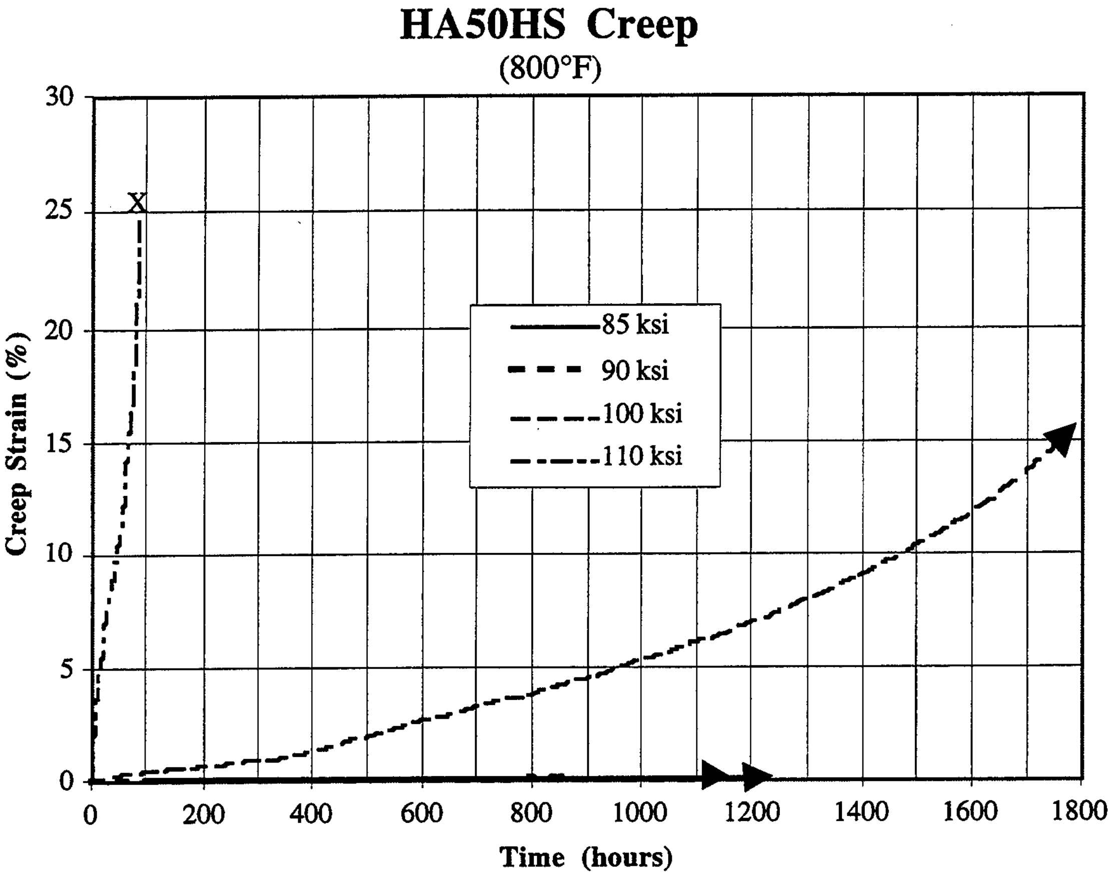

Figure 4.16 Creep Strain Versus Time Response of HA50HS Specimens Tested at 800°F.

5.5 x 10^{-7} per degree Celsius from 20-320°C. A maximum temperature variance of 6 degrees C is estimated due to the laboratory air conditioning system. This temperature change could result in a displacement measurement of approximately 7 x 10^{-5} inches. Assuming a gage length of 1.25 inches, this displacement translates to a 0.0057% change in strain. This environmental influence represents about one fourth of the recorded data scatter for these two tests.

An increase of only 10 ksi resulted in a significant increase in the initial steady-state strain rate of 2.2 x 10^{-5} in/in/hr for about 240 hours followed by a gradual increase to 6.44 x 10^{-5} in/in/hr. This increase, which occurred at about 0.8% creep strain, led to the second steady-state region of about 500 hours in length. At approximately 1752 hours the test was stopped. The response was in the tertiary region and it is speculated that fracture was imminent. A creep strain of 14.8% was recorded at the test termination. Upon unloading of the specimen it was determined that the total elongation was approximately 22.7 percent. The difference of 7.9% between these two values is indicative of the amount of initial plastic deformation due to loading. Tensile test data indicate that a stress of 100 ksi should result in a plastic deformation of about 6.5%.

The 110 ksi test was one of the first tests to illustrate a well defined primary creep region. This traditionally shaped creep curve illustrates all three stages of creep deformation, although the tertiary stage corresponds to nearly half of the total life. The specimen fractured at approximately 80 hours and 25% creep strain. A total plastic elongation of 32.5% was calculated for this specimen. This value implies that 7.6% plastic deformation was induced into the specimen as a result of loading. Based on the 800°F tensile data, a stress of 110 ksi should result in a plastic deformation of about 8%.

The 120 ksi test duration was only about 3.7 hours. The corresponding creep curve was not included in the summary of the 800°F curves due to the extremely short life as compared to the other curves. The response at this high stress indicated no primary stage and a steady-state strain rate of 3.8 x 10^{-2} in/in/hr for about 2.5 hours, followed by an approximately one hour tertiary response prior to fracture. The plastic deformation due to the initial loading is estimated to be 17.2%. This value was calculated based on a final creep strain measurement of 21.4% and a final elongation after unloading of 38.6%. The tensile data indicated that for an applied stress of 120 ksi a plastic deformation of approximately 14% should result.

Again, at 850°F, two very distinct behaviors were registered while being caused by a change in stress of only 10 ksi. As illustrated in Figure 4.17, at 90 ksi a steady-state strain rate of 4.3 x 10^{-6} in/in/hr was registered for the first 600 hours of the test. At approximately 680 hours and 0.6% creep strain, an abrupt change in the behavior resulted in a strain rate of 4.0 x 10^{-4} in/in/hr that relatively quickly leveled off to a second steady-state strain rate of 2.0 x 10^{-4} in/in/hr. This second steady-state region progressed for nearly 400 hours, followed by a tertiary region and, finally, fracture at 1362 hours and a creep strain of about 15.6%.

An increase in the applied stress of only 10 ksi significantly altered the deformation response. This response, due to the higher stress of 100 ksi, resembled a traditional curve including all three stages of creep deformation. The steady-state strain rate of 1.2 x 10^{-3} in/in/hr of the second stage was preceded by a short primary stage and followed by tertiary stage of about 20 hours' duration. The total creep strain resulting from this test was approximately 27.7% occurring at about 109 hours.

The total elongation measured for the 90 ksi test specimen upon unloading was 16.8%, while the elongation of the 100 ksi test specimen was 34.3%. There were no tensile tests conducted at 850°F; however, by interpolating the data shown in Figure 4.8, the upper yield point can be estimated to be 87.3 ksi and the mid-serration flow stress is approximately 84 ksi. Both of these interpolated yield points are about the same as those corresponding to the 800 and 900°F data. Based on the stress versus strain curves for the 800 and 900°F tensile tests, approximately 1 to 3% plastic deformation should occur at 90 ksi. The proximity of the applied load to the upper yield point, along with the yield point elongation phenomena, creates a noticeable amount of data scatter at this stress level. A stress level of 100 ksi, however, is high enough above the average upper yield point to allow for a consistent measure of plastic deformation. The correlating stress versus strain behavior indicates a plastic deformation of 6.5% resulting from an applied stress of 100 ksi. This estimated initial plastic deformation upon loading, plus the measured creep strain, is approximately equal to the total elongation measurement.

Chronologically, the first three creep tests conducted were at a temperature of 900°F. One proposed Air Force application required a soft magnetic material to maintain its structural integrity at temperatures up to 900°F and localized stresses up to 85 ksi. This set of maximum operating conditions was used as the center set of test parameters, from which the rest of the surrounding creep test matrix was developed. Stresses of 80, 85, and 90 ksi

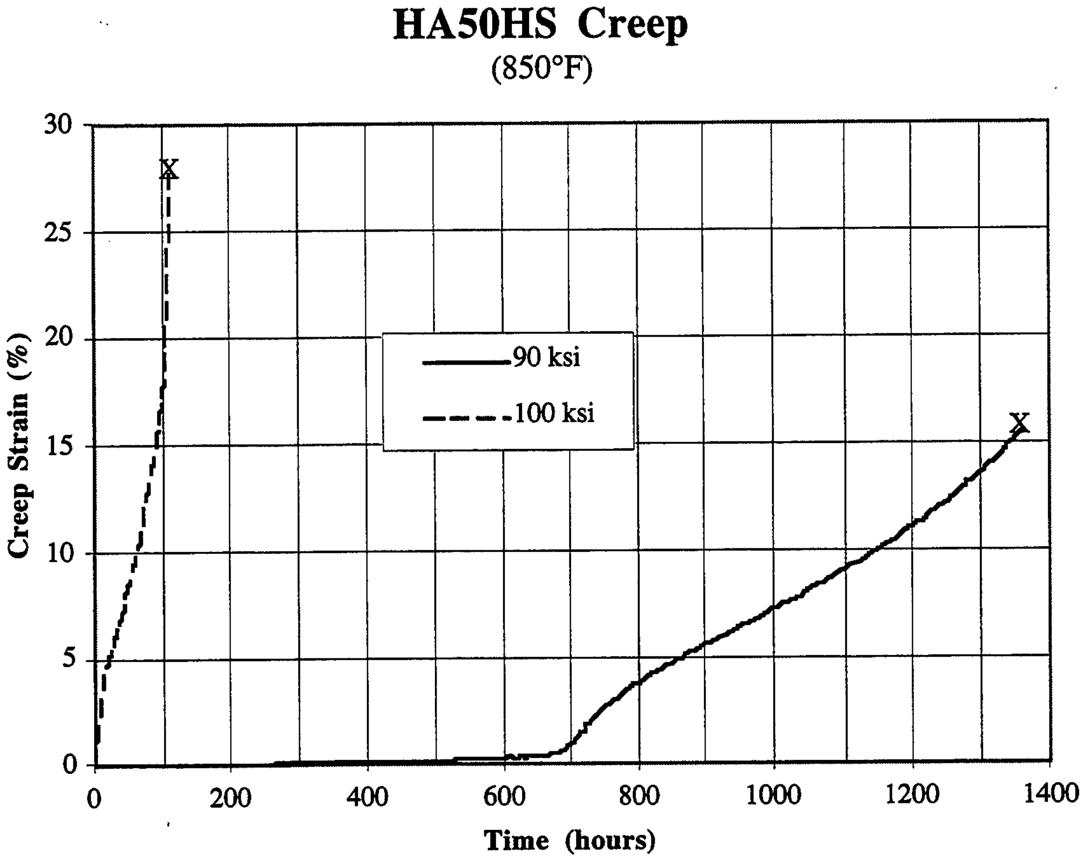

Figure 4.17 Creep Strain Versus Time Response of HA50HS Specimens Tested at 850°F.

were applied, and three distinct creep strain versus time responses were recorded. As an attempt to better locate the threshold stresses segregating the various responses, three additional tests were conducted at 82.5, 87.5 and 95 ksi. All six of these responses are illustrated in Figure 4.18.

Beginning with the lower applied stress of 80 ksi, a slight primary creep stage can be detected of only 2 or 3 hours' duration. This region of decreasing strain rate is followed by a 260 hour long steady-state region with a strain rate of about 1.7 x 10^{-5} in/in/hr. At about 0.7% creep strain and between 260 and 300 hours, a gradual transition of increasing strain rate occurred. It is difficult to detect the precise end points of this region because the end of the steady-state region is not abrupt and the beginning of the tertiary stage is not obvious. The total creep life for this specimen was 856 hours, and fracture occurred at a creep strain of 19.6%. According to the corresponding tensile data, the upper yield point at this temperature is 87.3 ksi; therefore, there should have been no plastic deformation occurring from the initial loading. A final elongation of 20.0% was measured. This slight variation in the amount of plastic deformation may be due to the inherent deviations associated with the fit-back method of measuring total plastic deformation.

An increase of only 5 ksi, bringing the applied stress up to 85 ksi, resulted in a significantly different creep response. A short duration of primary creep lasted for only one or two hours before transitioning to the steady-state region. This first steady-state region continued for approximately 117 hours at a constant rate of 3.1 x 10^{-5} in/in/hr. The end of this linear response occurred at approximately 0.6% creep strain and was marked by an abrupt increase in rate. From about 120 hours up to 240 hours a second linear response was recorded. The strain rate corresponding to this steady-state behavior was approximately 6.5 x 10^{-4} in/in/hr. This rate is greater than twenty times that of the first steady-state region. The specimen began a gradual transition to the tertiary stage and finally fractured at about 304 hours and 14.9% creep strain. The applied stress of 85 ksi is below the average upper yield stress at this temperature, yet it is above the average lower yield point and the mid-serration flow stress. Hence, no initial plastic deformation should have occurred as a result of loading the specimen. The final elongation of the specimen was measured to be 14.6%.

An additional increase of only 5 ksi resulted in a third type of creep strain versus time response. This response, for the 90 ksi applied stress, resembled that of a traditional creep response. Although spanning a relatively short life, the response included all three stages

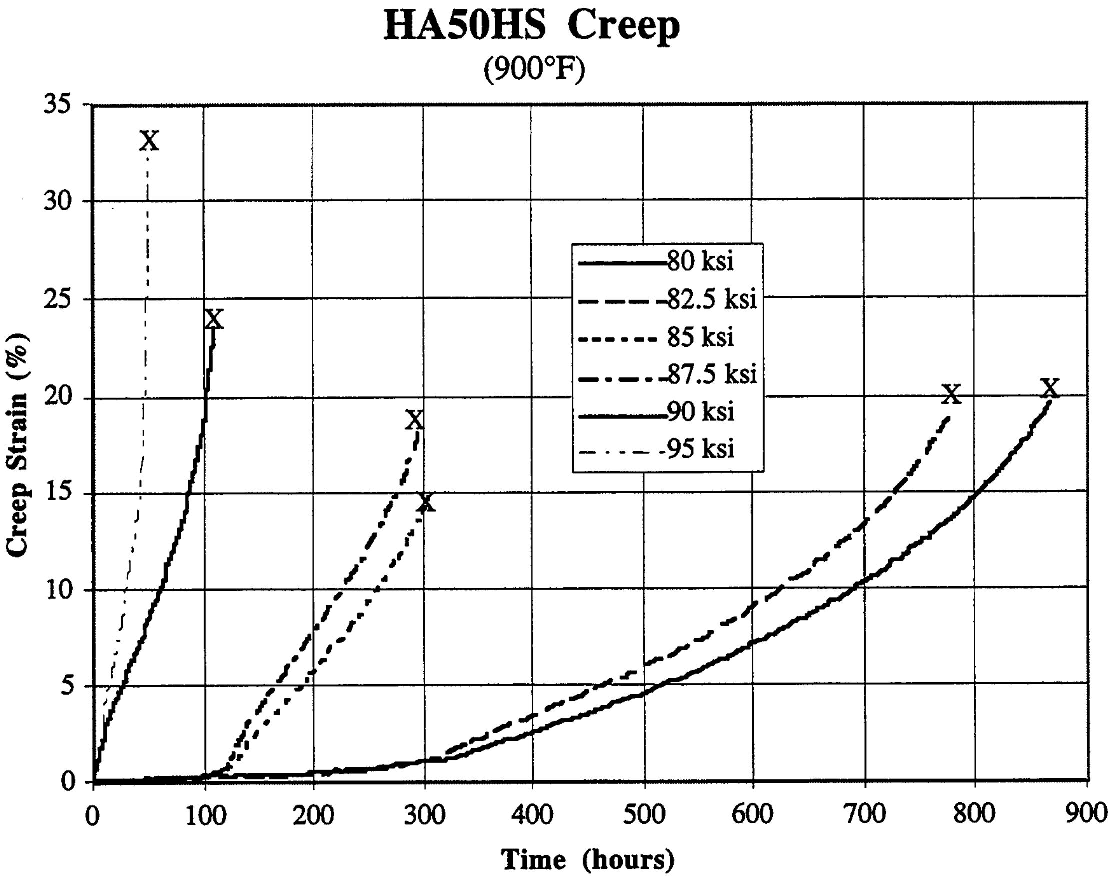

Figure 4.18 Creep Strain Versus Time Response of HA50HS Specimens Tested at 900°F.

of creep deformation. The decreasing strain rate associated with primary creep began to level off, after about 10 hours, to a constant strain rate of 1.5×10^{-3} in/in/hr, defining the steady-state region. This linear creep strain versus time response continued for about sixty hours before transitioning to an unstable tertiary deformation and finally fracturing at about 109 hours. The final creep strain measurement was 23.6%. Since the applied stress is slightly above the average upper yield point determined for this temperature, some plastic deformation can be expected during the final steps of the loading sequence. The corresponding tensile data indicate that an applied stress of 90 ksi should plastically deform the specimen by approximately 4%. This value correlates well to a total elongation measurement of 28.6%.

Preliminary reviews of these three distinct creep responses led to the attempt to pinpoint the threshold of applied stress at which the behaviors vary. Stress levels of 82.5 ksi and 87.5 ksi were applied. The creep response due to the 82.5 ksi stress better resembled that of the 80 ksi test than the 85 ksi test. As can be seen in Figure 4.18, the most obvious differences are the creep life and the better defined second linear portion of the curve. A short primary creep region was detectable for a few hours before quickly transitioning to a steady-state creep region. This steady-state region continued at a rate of 2.0×10^{-5} in/in/hr until it reached 0.65% creep strain at about 240 hours. The abrupt change in strain rate, which occurred at this point, was more apparent than the rate change of the 80 ksi test, yet it was not nearly as obvious as the increase in rate depicted on the 85 ksi response curve. The second linear portion of the response continued from about 300 to 560 hours at a rate of 2.65×10^{-4} in/in/hr. Tertiary deformation followed this region and eventually the specimen fractured at a creep strain of 19.4% and at a time of 778 hours. A final elongation measurement of 20.4% indicates that there may have been some non-recoverable plastic deformation upon loading. All of the tensile tests at this temperature indicated an upper yield point above 82.5 ksi with an average value of 87.3 ksi. It is possible that there was some plastic deformation occurring due to the step loading sequence with a final load being above the lower yield point.

The creep versus strain response due to an 87.5 stress is shown in Figure 4.18 to more closely resemble the 85 ksi behavior rather than the 90 ksi behavior. There were no indications of primary creep and although the final creep life was almost the same as the 85 ksi life, the final creep strain was about 5% greater. The creep deformation began with a steady-state response of 3.55×10^{-5} in/in/hr and continued at this rate for about 110 hours at which point a creep strain of 0.6% was attained. At this transition point a change in strain rate of more than two orders of magnitude occurred, increasing the strain rate to 1.2 x 10^{-3} in/in/hr, before leveling off after thirty hours to a minimum strain rate of 8.12 x 10^{-4} in/in/hr. This rate continued from about 140 to 240 hours before unstable deformation appeared as the tertiary stage and finally fracture at 295 hours. The final creep strain recorded at this stress and temperature was 18.1%, while the final elongation measured after unloading was 18.6%. As this applied stress is approximately equal to the upper yield point determined from the corresponding stress versus strain data, an initial plastic deformation of 0.5% is certainly possible.

One final test was conducted at 900°F. A stress of 95 ksi was applied and resulted in the behavior documented in Figure 4.18. There was no primary creep depicted from this set of test parameters. The initial deformation recorded was steady-state and it continued through the majority of the specimen life. A constant strain rate of 3.2 x 10^{-3} in/in/hr continued from the start of the test up to about 40 hours and 14% strain. The tertiary strain rate increased rapidly with fracture occurring at about 50 hours and 32.7% creep strain. Since the applied stress is above the average upper yield point, as determined by corresponding stress versus strain behavior, plastic deformation should occur upon loading. These corresponding tensile data indicate that an applied stress of 95 ksi should result in approximately 5% plastic strain. This amount of initial plastic deformation plus the time dependent creep deformation corresponds well with the final elongation measurement of 38.3%.

Five tests were conducted at a temperature of 950°F ranging in applied stress from 65 to 90 ksi. These tests are depicted in Figure 4.19. As would be expected, the initial steady-state strain rates increase as the applied stress is increased. The strain rate variation between the 65 and 90 ksi tests is greater than two orders of magnitude. The constant strain rates corresponding to the intermediate applied stresses of 75, 80, and 85 ksi, however, vary by less than 75%. There is no apparent step increase in strain rate associated with the 65 and 75 ksi tests. However, a transition can be detected for the 80 ksi test and the abrupt increase in steady-state strain rate is very obvious for the 85 ksi stress condition.

An applied stress of 65 ksi ultimately resulted in a creep life of 723 hours and a final creep strain of 21.7%. There was no indication from the recorded strain versus time data of a primary region. The constant strain rate began at the initiation of the test and proceeded at a value of 5.65 x 10^{-5} in/in/hr up to about 1.0% creep strain and 160 hours. The remainder of the response is best described as tertiary and dominates the creep test duration. Even

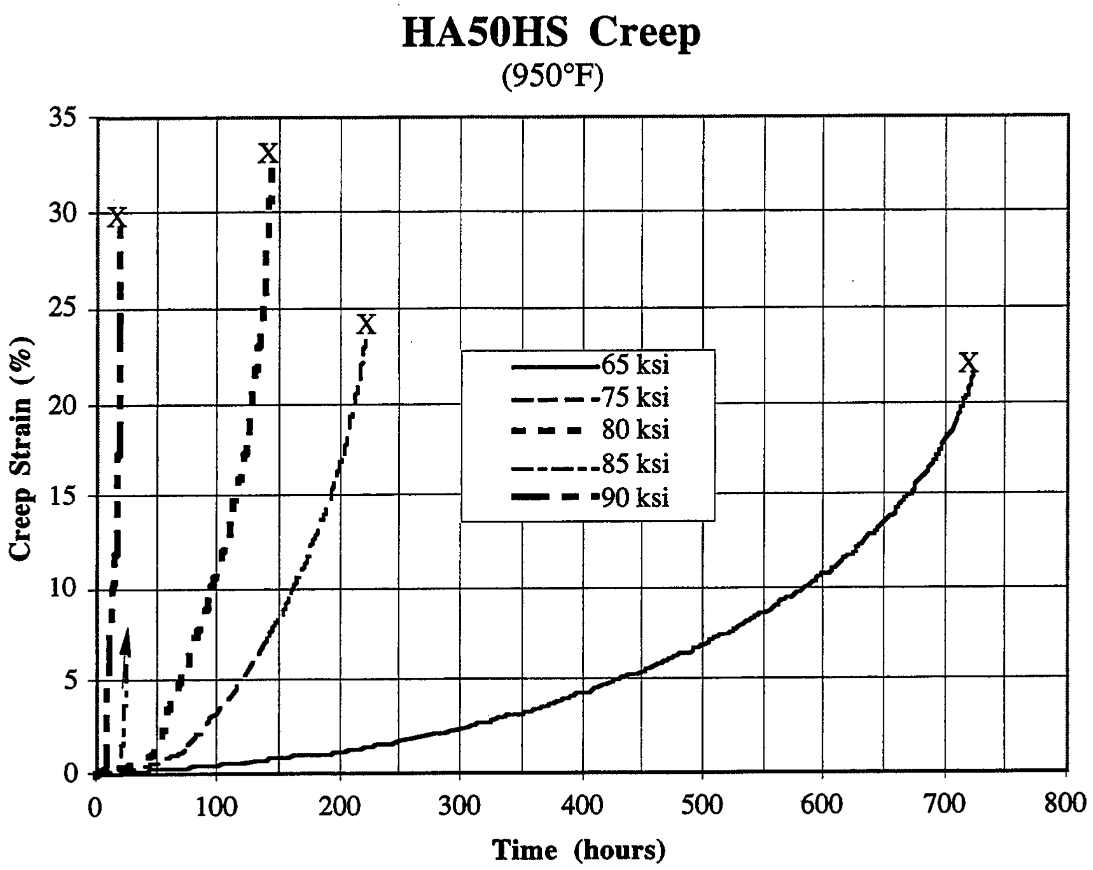

Figure 4.19 Creep Strain Versus Time Response of HA50HS Specimens Tested at 950°F.

though there were no tensile tests conducted at 950°F, it is likely that the upper yield point is well above 65 ksi. It is speculated, based on 900 and 1000°F stress versus strain data, that the upper yield point at 950°F is approximately 87.2 ksi. Obviously, this speculation implies that there should not be any plastic deformation occurring simultaneously with loading. The final elongation was measured as 22.2%. This 0.5% difference is likely a result of the creep strain measuring technique or measurement error associated with the fit-back method used to derive the total gage length elongation.

The creep strain versus time response correlating to an applied stress of 75 ksi at 950°F resulted in a total creep life and strain of 220 hours and 23.3%, respectively. The recorded data did not indicate a primary creep region. The initial behavior was steady-state deformation that continued from the start of the test at a strain rate of approximately 1.15×10^{-4} in/in/hr up to a strain of 0.7% and a corresponding time of about 50 hours. The end of the steady-state response marked the initiation of a transition period from about 50 hours to approximately 80 hours. As with the 80 ksi at 900°F test, it is difficult in this test to determine the precise beginning and ending of this region. The change in strain rate is apparent but the transition is gradual and the beginning of the tertiary stage is less obvious as well. As with the 65 ksi test, there were no tensile data available for direct comparison. It is again speculated that the upper yield points are well above the applied stress of 75 ksi; hence, no plastic deformation at loading should occur. An elongation measurement of 24.0% suggests a derived difference of 0.7%.

An increase of only 5 ksi effected a substantial difference in behavior as compared to the 75 ksi response. Although the lack of a primary region and a similar steady-state strain rate are illustrated, the marked transition to the second steady-state region is much better defined. The initial strain rate is estimated to be 1.6×10^{-4}. This rate continues for approximately 40 hours, which corresponds to about 0.7% creep strain. The transition to the second linear response takes place over about a 12-hour period. The second steady-state region spans approximately 48 hours from 52 to 100 hours at a rate of 1.8×10^{-3} in/in/hr. At this point the unstable deformation associated with the tertiary creep stage begins and continues until the specimen fractures at 142 hours. The final creep strain recorded is 32.6% and the final plastic elongation is measured as 32.4%. This statistical equivalency is supported by the speculation that the upper yield point at 950°F is still above 80 ksi; hence, no plastic deformation should occur as a result of the initial loading at the start of the test.

An applied stress of 85 ksi resulted in a similar initial response, however, the change in strain rate is significantly more abrupt than that of the 80 ksi test. Not only does the transition between strain rates span a shorter time, it also occurs sooner in the creep life. The creep deformation began with a strain rate of approximately 2.0 x 10^{-4} in/in/hr and continued at this rate until a strain of 0.65% was reached. This strain was attained at a time of 19 hours. At this transition point a change in strain rate of almost two orders of magnitude occurred, increasing to 1.3 x 10^{-2} in/in/hr, before apparently leveling off. As in a few other tests with relatively high strain rates, this specimen elongated beyond the maximum extension limit of the LVDT and then fractured before the LVDT could be properly reset. The last valid creep strain measurement was approximately 6.8% at about 28 hours into the test. The strain rate appeared to be leveling off to predicate a second steady-state region as shown in other creep curves. It is speculated that this constant rate region was short lived in order to allow a quickly deforming tertiary stage prior to fracture. A total elongation of the specimen gage length was determined to be 25.5% using the fit-back method. Based on corresponding tensile data shown in Figure 4.8, the upper yield point at 950°F is estimated to be 87.2 ksi. Since the applied stress in this creep test is nearly equal to the upper yield point, it is difficult to claim with certainty an amount of plastic deformation due to the initial loading. It is speculated, however, that the range of possible permanent deformation spans the Lüders strain. At 950°F the Lüders strain is estimated to be between 2.0 and 3.0%. It is, therefore, reasonable to speculate that during the last 20 hours of the creep test, the specimen deformed between 15.7 and 18.7%, to attain the final elongation determined after fracture.

Although the creep strain versus time response for the 90 ksi test is not easily seen, due to the scaling of Figure 4.19, some curve peculiarities are evident. The recorded response indicates no primary creep stage. The behavior begins with the initial constant strain rate of approximately 3.6 x 10^{-3} in/in/hr. This rate is almost twenty times the rate associated with an applied stress of 85 ksi. A tertiary stage becomes prevalent and the specimen eventually fractures at a time and creep strain of 19.6 hours and 29.2%, respectively. The total plastic elongation measured after fracture was 34.7%. This 5.5% difference between the final creep strain and the total elongation is comparable to the estimated amount of plastic strain resulting from initial loading above the upper yield point of 87.2 ksi.

Six creep tests were conducted at a temperature of 1000°F, ranging in applied stress from 45 to 85 ksi. As can be seen in Figure 4.20, creep strain versus time responses associated with the three lower stresses are comprised primarily of unstable tertiary deformation. The

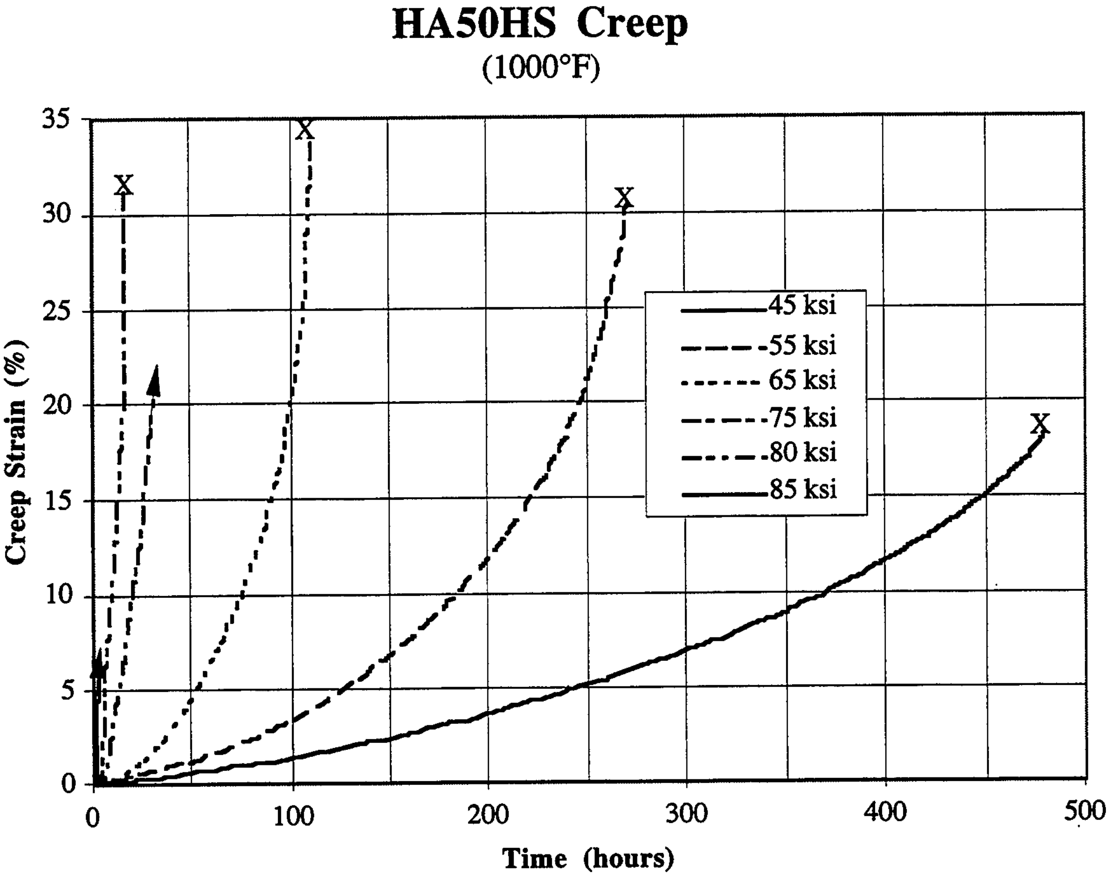

Figure 4.20 Creep Strain Versus Time Response of HA50HS Specimens Tested at 1000°F.

three higher stressed tests exhibit two steady-state stages separated by an abrupt increase in strain rate. Both the 75 and 85 ksi tests deformed to the maximum LVDT range and then fractured before the LVDT was reset. Hence, the time to fracture is accurate but there was no accurate recording of the final creep strain for these two tests. The initial steady-state strain rates increased as the applied stress was increased. The overall initial strain rate increase from the 45 ksi test to the 85 ksi test was more than an order of magnitude. The average upper yield strength, as illustrated in Figure 4.8, is 87.2 ksi and the lower yield point is about 80.6 ksi.

The lowest applied stress at 1000°F, 45 ksi, ultimately resulted in a creep life of about 479 hours and a corresponding creep strain of 18.4%. There was no indication of a primary creep stage and only a relatively short secondary creep stage. The initial linear response continued from the start of the test to approximately 50 hours at a rate of 1.3×10^{-4} in/in/hr. At this point the linear response was replaced by an exponential type curve which defined the tertiary creep stage and proceeded for the remainder of the test. The final elongation was measured to be 18.5%, which is within an acceptable margin of error to support the estimate that no plastic deformation would occur coincident with loading 45 ksi.

The creep strain versus time response registered from an applied stress of 55 ksi at 1000°F resulted in a total creep life and strain of 270.2 hours and 30.4%, respectively. The recorded data did not indicate a primary creep stage. The initial behavior was linear only up to about 40 hours at a strain rate of approximately 2.4×10^{-4} in/in/hr. The end of the steady-state, or secondary, stage marked the beginning of the tertiary stage. This final stage is represented by an exponential type curve spanning more than 200 hours and dominating the creep life. The final gage length elongation was 29.9%. This derived measurement should theoretically equal the final creep strain measurement when there is no plastic deformation due to the initial loading. According to the corresponding stress versus strain data at 1000°F, there should not have been any permanent deformation coincident with the application of the test load. The apparent 0.5% difference is likely a result of the apparatus used to measure creep strain or error associated with the fit-back method used to measure the gage length total elongation.

An increase of 10 ksi, bringing the applied stress up to 65 ksi, resulted in a response very similar to those generated by the 45 and 55 ksi tests. Two obvious differences, depicted in Figure 4.20, are the decreased time to fracture and the increased final creep strain. The specimen exhibited a total creep strain of approximately 33.8% at the end of a creep life of

111 hours. As with the two previous tests conducted at this temperature, there was no indication of primary creep. A secondary creep region was evident followed by a proportionally large tertiary stage prior to fracture. The first twenty hours of the response was linear, characterized by a constant strain rate of approximately 4.7 x 10^{-4} in/in/hr. The end of this linear response marked the beginning of the tertiary stage, which continued until the specimen fractured. When considering the yield points determined from the corresponding tensile data, the initial load should not have resulted in any plastic deformation at the start of the test. A final permanent strain of 34.3% was measured and supports the speculation that no initial deformation occurred coincident with the application of the final load increment.

The applied stress of 75 ksi is the lowest stress tested that resulted in the abrupt increase in strain rate between two steady-state regimes. Also, this plot of the behavior does not illustrate a final creep strain. This deficiency is due to the change in length of the specimen being greater than the maximum displacement of the LVDT. The LVDT displacement reached a maximum and the specimen fractured during the night before the LVDT could be reset. The time to fracture and the final elongation measurement are still valid. The initial recorded deformation was steady-state and continued at a constant rate of 8.9 X 10^{-4} in/in/hr up to about 6 hours and 0.7% strain. A two hour period followed, which transitioned the behavior to a second linear region characterized by a constant strain rate of 7.1 X 10^{-3} in/in/hr. This response continued for about another ten hours before an increasing strain rate became evident as the tertiary stage began to dominate. Based on the corresponding tensile data, a stress of 75 ksi should not cause any permanent deformation. The total elongation measured after the test was concluded was 29.8%. This value corresponds to the final recorded creep life of 34.2 hours. The last creep strain measurement of 20.3% was taken at approximately 30.5 hours. Since the deformation was well established as an unstable tertiary response, it is entirely possible that the final 3.7 hours of unrecorded creep strain resulted in an additional strain of 9.5%.

An applied stress of 80 ksi combined with a test temperature of 1000°F resulted in a creep life of only 16.8 hours and a total creep strain of 31.3%. As with the other tests conducted at this temperature, there was no indication of a primary stage. The initial response, although very short, was linear and defined by a constant strain rate of 1.9 x 10^{-3} in/in/hr. At approximately 3 hours into the test the creep strain measured 0.65% and the behavior began to transition over a period of not more than 2 hours to a second steady-state response. This linear behavior proceeded for nearly 8 hours at a rate of 1.5 x 10^{-2} in/in/hr until the strain rate began to increase as an indication of the onset of the tertiary stage. The applied stress generating this response is nearly equivalent to the lower yield point as determined by the corresponding stress versus strain response. Although the upper yield point is about 7 ksi greater, some plastic deformation may be evident as a result of the proximity of the applied stress to the yield points. The final elongation was measured to be 33.4%. A portion of this permanent deformation may be due to plastic deformation upon loading.

The 85 ksi creep test conducted at 1000°F was one of the shortest duration tests completed. Also, as with the 75 ksi test at this temperature, the specimen deformed to a greater displacement than the travel limit of the LVDT. The LVDT extended to its limit as the specimen continued to deform. The specimen then fractured prior to the LVDT being reset for continued measurements, however, the time to fracture and the final elongation measurements are still valid. The initial recorded behavior was steady-state and continued at a constant rate of 2.3×10^{-3} in/in/hr up to about one hour and 0.25% creep strain. At this transition point a change in strain rate of nearly two orders of magnitude occurred, increasing to a maximum of 1.4×10^{-1} in/in/hr before leveling off to a minimum constant value of 2.8×10^{-2} in/in/hr. This strain rate continued until the change in creep strain was no longer being measured. It is speculated that a tertiary stage soon developed after the last accurate creep strain reading of 9.7%. Assuming the upper yield point is approximately equal to the applied stress, a plastic deformation due to the initial loading could vary significantly. The specimen may deform only slightly beyond the elastic regime, or it may deform through the entire Lüders elongation region. According to the tensile data at 1000°F, this variation could be as large as 3.0%. The total elongation of the gage length was measured to be 40.0%. It is then speculated that the creep strain corresponding to a life of only 5.6 hours would be at least 37%.

Four tests were conducted at a temperature of 1100°F ranging in applied stress from 30 to 60 ksi at 10 ksi increments. As illustrated in Figure 4.21, this set of creep strain versus time curves differed from all of the lower temperature sets, in that there was no evidence from any test of two distinguishable steady-state regions separated by an abrupt increase in strain rate.

The creep strain versus time response corresponding to test parameters of 30 ksi applied stress and a temperature of 1100°F resulted in a total creep life of 123 hours and a final creep strain of 49.5%. The recorded data indicated a steady-state region starting at the

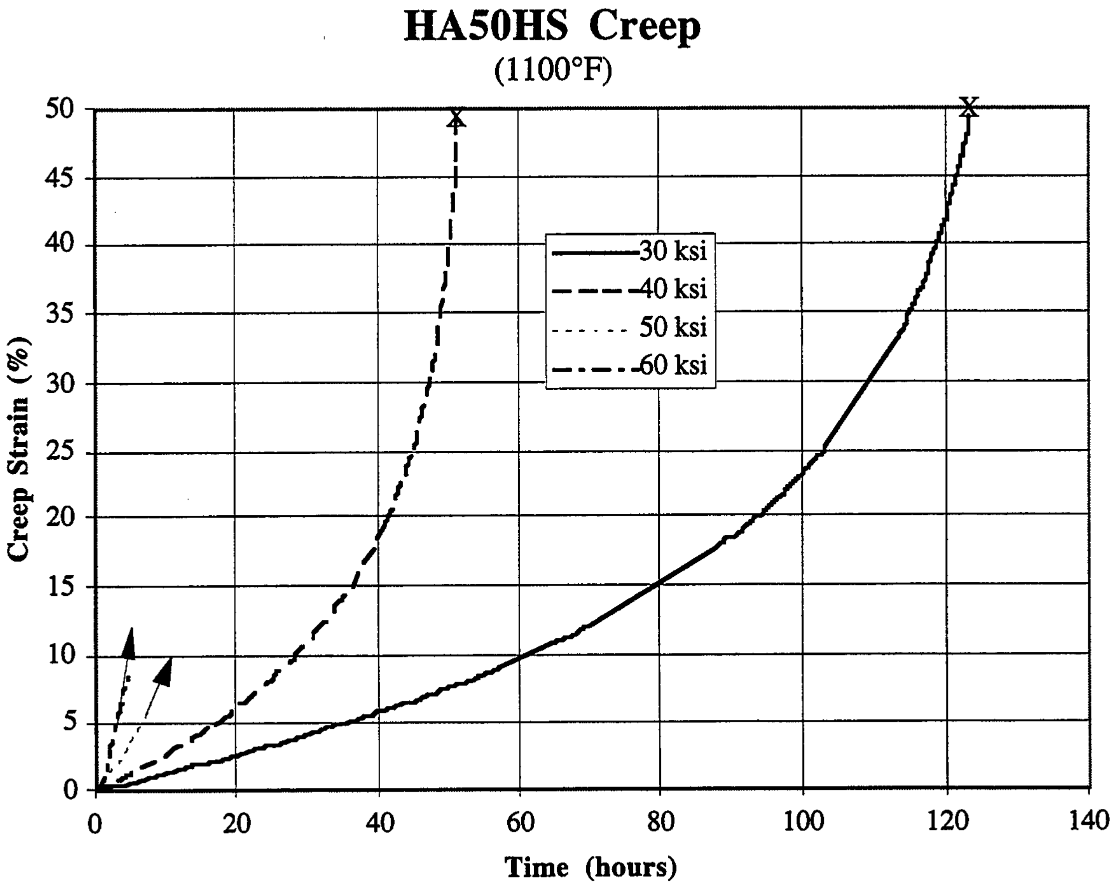

Figure 4.21 Creep Strain Versus Time Response of HA50HS Specimens Tested at 1100°F.

beginning of the test and continuing at a rate of 1.55 x 10^{-3} in/in/hr. This minimum strain rate proceeds for about 50 hours, at which time tertiary deformation becomes evident until the specimen fractures. At this relatively low stress, initial plastic deformation is not expected. This speculation is supported by the total elongation measurement of 50.6%. The 1.1% difference between final creep strain and the final elongation may be due to the strain measuring apparatus or possibly error associated with the fit-back method to determine elongation of the gage length.

It appears, from the next test, that final creep strain is independent of applied stress in this stress vicinity. A 40 ksi stress at 1100°F resulted in a creep life of 51.4 hours at a creep strain of 49.5%. The early creep strain versus time response illustrates a behavior beginning with a steady-state deformation which proceeds at a constant rate of 3.2 x 10^{-3} in/in/hr for only about 11 hours. As with the 30 ksi test, no abrupt strain rate change is evident; there is a gradual transition to the final stage. This tertiary stage spans a strain of more than 40% in as many hours prior to fracture. The total gage length elongation was measured to be 53.8%.

An applied stress of 50 ksi at 1100°F produced a total creep life of 19.5 hours. As in certain previous tests, this specimen elongated beyond the limit of the LVDT and then fractured before the LVDT could be reset. The last valid creep strain measurement was 29.0% and occurred at approximately 18.5 hours. The deformation was well established as tertiary and the strain rate was increasing for the few hours immediately preceding the final creep strain reading. A total elongation of the specimen gage length was measured to be 45.1%. It is certainly within reason to accept that the final hour of straining resulted in an additional 16% of permanent deformation. There was no indication of primary creep during this test. The initial strain was characterized by a constant rate of 8.5 x 10^{-3} in/in/hr, which lasted for about 8.4 hours. At this time the LVDT had reached its maximum extension and remained fully extended until it could be reset the next morning. At approximately 16.4 hours the strain had increased to about 18%. The specimen continued to deform at an increasing rate until the LVDT needed resetting. Unfortunately, the specimen broke before the LVDT could be reset. Based on the related tensile test data, no plastic deformation was expected coincident with the application of the test load.

A final increment of 10 ksi, bringing the applied stress to 60 ksi, at 1100°F also created a data acquisition challenge. As with the previous test, this stress and temperature combination resulted in a specimen strain rate sufficiently fast to deform beyond the LVDT maximum extension and fracture before the LVDT could be reset. Hence, a final creep life was measured but not a corresponding creep strain. No primary deformation was recorded. The initial steady-state response was at a rate of 2.2 x 10^{-2} in/in/hr and continued throughout the entire recorded life. At approximately 4.2 hours and 8.5% creep strain the LVDT reached its maximum limit. The specimen continued to deform until it finally fractured at approximately 8.2 hours. The final gage length elongation was 45.2%. An assumption that a final creep strain is equivalent to the measured elongation requires an accelerated strain rate for the remainder of the test. A simplified linear fit of the estimated deformation is represented by a constant strain of 9.18 x 10^{-2} in/in/hr. Based on the lower stress tests at this temperature it is speculated that the strain rate from this test gradually increases from the constant steady-state rate to a rate even greater than the estimated linear fit. This increase in strain rate characterizes the tertiary creep stage. The data assimilated from the 1100°F tensile tests imply that there would be no initial plastic deformation due to the step loading at the start of the test.

Eighteen different stresses were used in conjunction with the seven different temperatures as creep test parameters. The minimum stress, 30 ksi, was applied with a test temperature of 1100°F. The maximum applied stress was 130 ksi at a test temperature of 700°F. Most of the stress levels involved only a single corresponding test temperature; however, seven stress levels included multiple tests. Although these curves have all been previously illustrated in the common temperature plots, Figures 4.15-4.21, there is significant benefit to viewing the behaviors on a common stress basis.

The lowest stress at which more than one temperature was tested was 65 ksi. The type of deformations present in both the 950°F and the 1000°F responses are similar, as can be seen in Figure 4.22. Neither test showed evidence of a primary region, and after a relatively short steady-state deformation the majority of the creep life and creep strain was recorded as tertiary creep. Another similarity is the creep strain at which steady-state behavior began a gradual transition to tertiary behavior. This value was about 1.0% for both temperatures. The most obvious difference corresponding to the 50°F increase in test temperature is the reduction in creep life of more than 600 hours. Also, an increase in the creep strain at fracture of nearly 0.13 in/in is apparently due to the increase in temperature.

Two test were conducted at 75 ksi. Again, an increase in test temperature from 950°F to 1000°F resulted in a significant shift in the overall specimen response as depicted in Figure 4.23. As would be expected, the steady-state strain rates are higher and better defined for

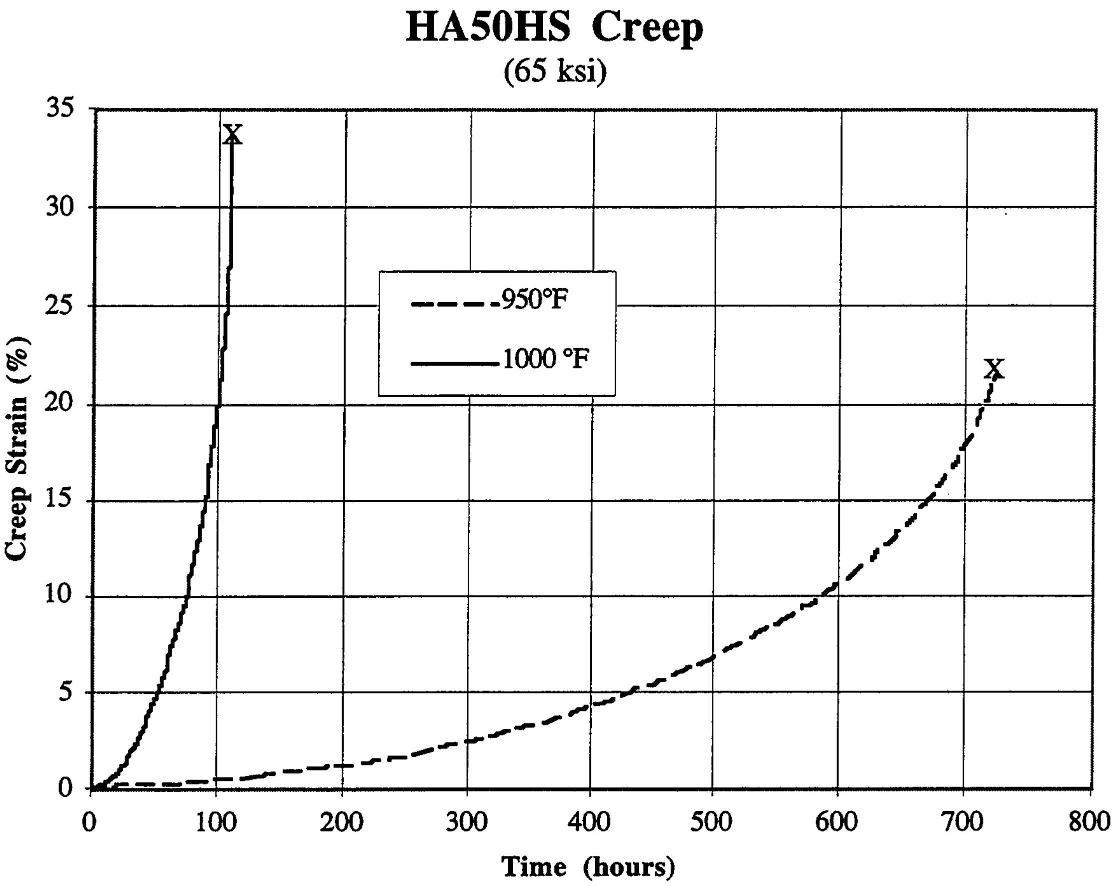

Figure 4.22 Creep Strain Versus Time Response of HA50HS Specimens Tested at 65 ksi.

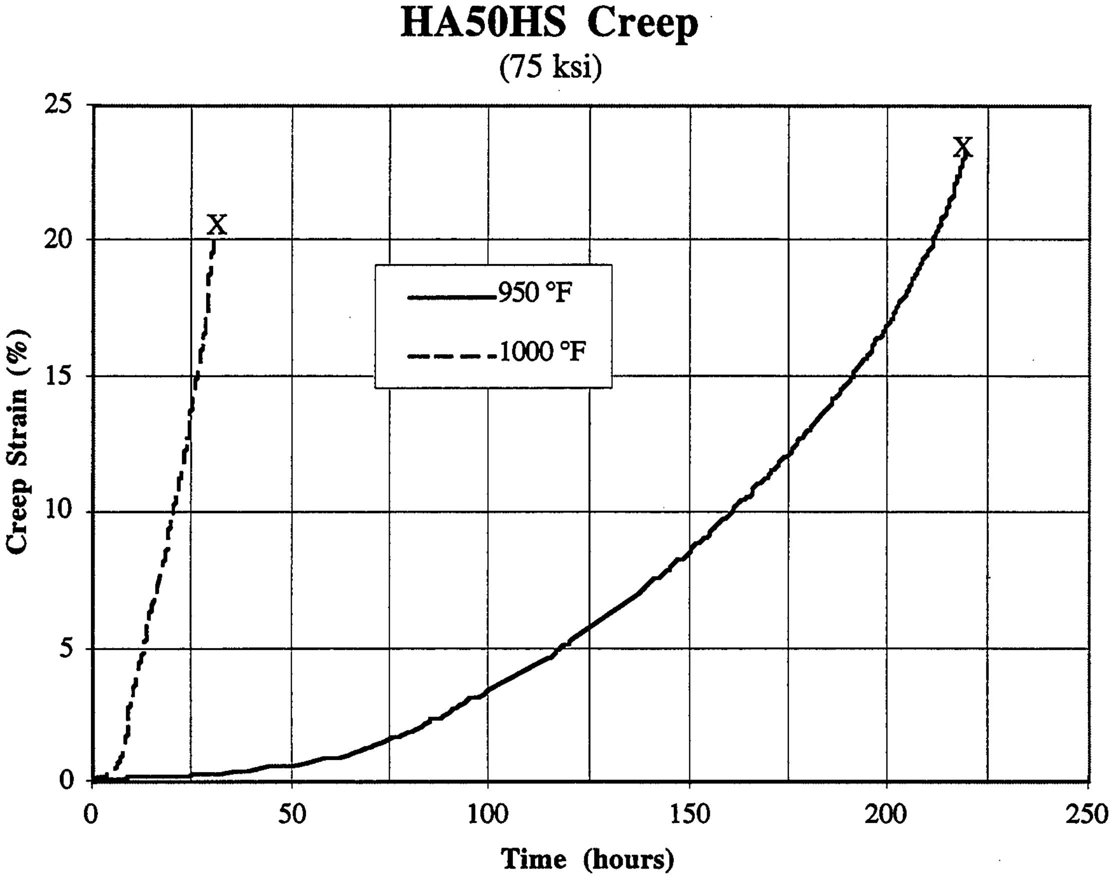

Figure 4.23 Creep Strain Versus Time Response of HA50HS Specimens Tested at 75 ksi.

the 1000°F test than those measured from the 950°F test. The higher temperature test resulted in an abrupt transition between linear regions. The impact of the temperature difference on the final creep strain can not be determined from these curves due to the fact that the 1000°F specimen deformed beyond the LVDT limit and then fractured before the LVDT could be reset. Total elongation, measured after fracture, does indicate that the higher temperature causes a greater creep strain at fracture. Final elongations were measured at 24.0% and 29.8% for the 950°F and the 1000°F tests, respectively.

Three tests were conducted at an applied stress level of 80 ksi. The tests were at 50°F intervals from 900°F to 1000°F. The more significant difference, as illustrated in Figure 4.24, is between the 900°F and the 950°F curves. There is a difference of more than 700 hours and 0.13 in/in final strain between these two temperatures. Also, the increase in test temperature results in better defined steady-state regions with a more abrupt transition from the first to the second. The response due to the highest test temperature at this stress level was similar to that of the 950°F response. They were both comprised of abrupt increases in strain rate and well defined steady-state regions of deformation. The final creep strain measurements and final elongations were also similar. Although it is difficult to detect the precise point at which the transition from a linear response occurs for the 900°F test, all three tests transition at about the same creep strain. The two higher temperature tests begin the rate increase at about 0.65% to 0.7% creep strain, while the 900°F test seems to first deviate from linearity at about 0.65% creep strain.

Figure 4.25 illustrates four tests that were conducted at an applied stress level of 85 ksi. The three higher temperature tests represent similar deformation responses with an abrupt increase in steady-state strain rate between two linear response regions. The transition between the two steady-state regions occurred at a creep strain of about 0.3% for the 1000°F test and at 0.60% and 0.65% for the 900°F and 950°F tests, respectively. Both the 950°F and the 1000°F test deformed beyond the LVDT limit and subsequently fractured prior to the LVDT being reset. Therefore, the temperature dependence on final creep strain is better represented by the final elongation measurements which are 14.6%, 25.5%, and 40.0%, corresponding to the 900°F, 950°F and the 1000°F deformations, respectively. When a test temperature of 800°F was applied with the load of 85 ksi, a totally different response was recorded. The test was conducted for nearly 1200 hours with no indication of an increase in strain-rate above the constant rate on the order of 10^{-7} in/in/hr. The 800°F test was stopped prior to fracture and an elongation of only 0.29% was measured.

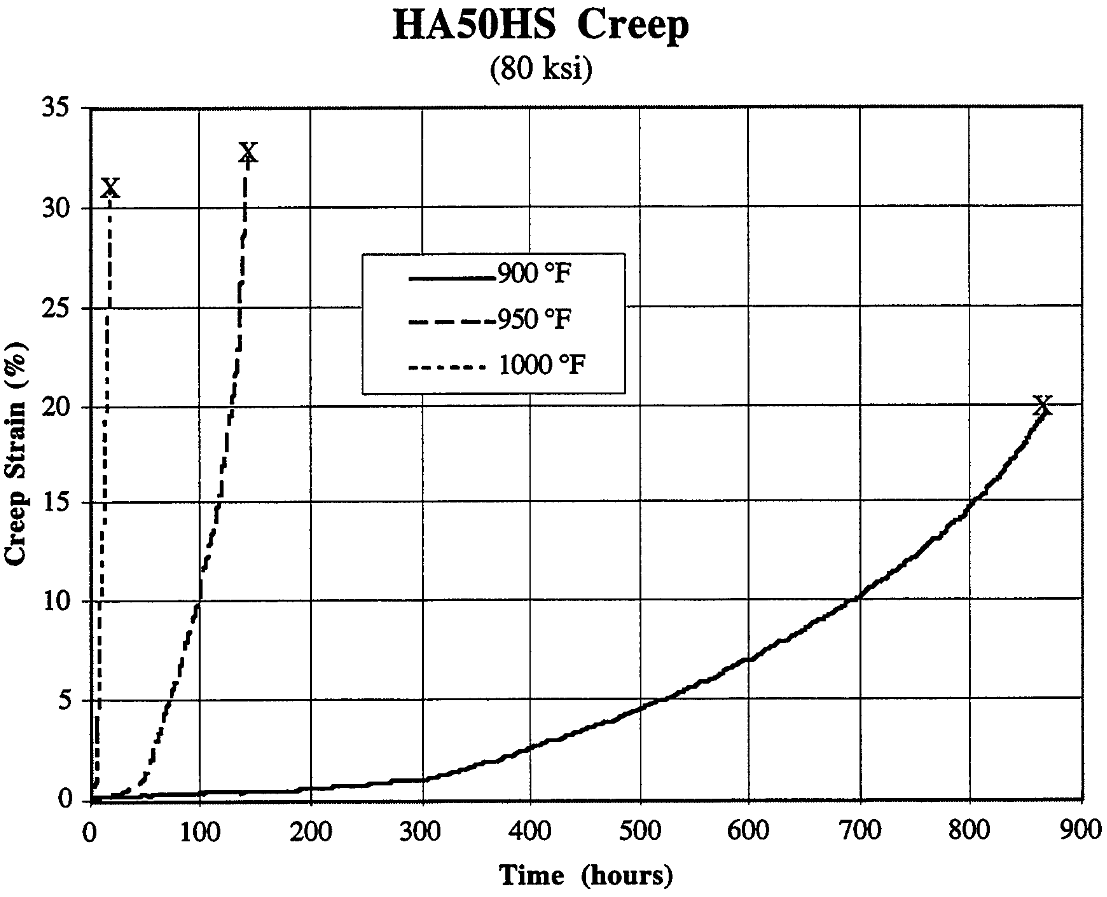

Figure 4.24 Creep Strain Versus Time Response of HA50HS Specimens Tested at 80 ksi.

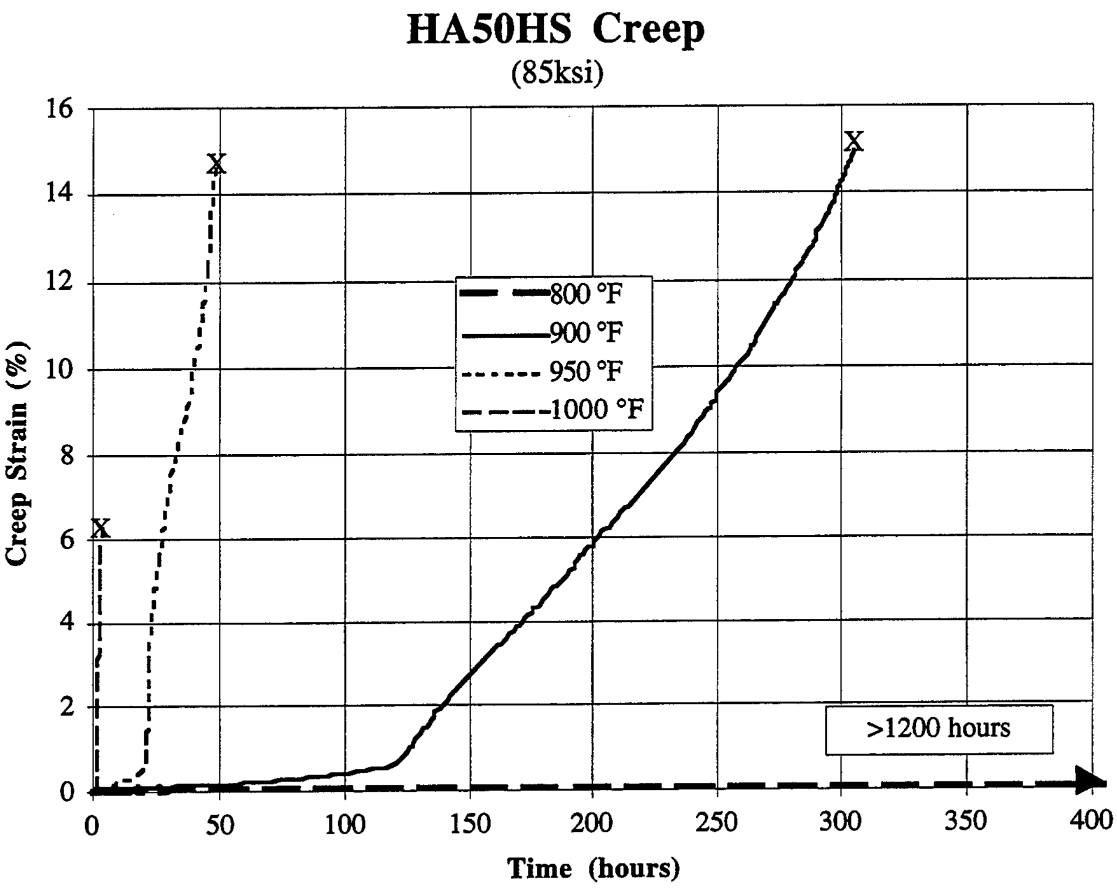

Figure 4.25 Creep Strain Versus Time Response of HA50HS Specimens Tested at 85 ksi.

Four different temperatures were applied in conjunction with a stress level of 90 ksi. Temperatures ranged from 800°F to 950°F at 50°F intervals. The overall responses are illustrated in Figure 4.26 and are similar to those corresponding to a stress level of 85 ksi. The lowest temperature test, 800°F, exhibited essentially no creep deformation even at times beyond 1100 hours. The estimated constant creep strain rate is on the order of 10^{-7} in/in/hr. An increase in temperature of only 50¡F resulted in a significant difference in behavior. At 850°F the creep strain versus time response follows the 800°F response at an order of magnitude higher strain rate for nearly 700 hours. At this point the strain rate increases by approximately two orders of magnitude and the specimen finally fails at about 1360 hours. The higher temperature test exhibits the shorter life and the greater final creep strain. The elongation measurements and the corresponding tensile data indicate that about 5% plastic deformation occurred with loading for both of the higher temperature tests.

Only two tests were conducted at an applied stress level of 100 ksi. The 800°F test was the longest test conducted under this study lasting for more than 1750 hours before the test was stopped. Figure 4.27 illustrates not only a significant difference in creep life but also two different types of responses. The 800°F test indicated the possibility of two linear regions prior to a tertiary stage. The 850°F test represented a more traditional creep behavior including all three stages of deformation. Even though the lower temperature test was stopped prior to fracture, it is speculated that fracture was imminent. This speculation implies that a 50°F increase in test temperature, at 100 ksi, causes an increase in final creep strain of about 0.13 in/in. The final elongation measurements of both of these specimens indicate a plastic deformation upon loading of about 7%. This value corresponds closely with actual and interpolated tensile data.

Similar responses were recorded for the two tests conducted at a stress level of 120 ksi. The 700°F and 800°F curves are similar in that neither response illustrates a primary creep stage and the steady-state stage comprises most of the creep life. The most obvious difference that can be seen in Figure 4.28 is the variation of the total creep lives. The increase of 100°F resulted in a reduction in creep life from over 400 hours to less than 4 hours. Also, this increase effected an increase in final creep strain from about 17% to 21%. Elongation measurements imply that 17% plastic deformation occurred upon loading at 800°F while only 12.5% plastic deformation resulted upon loading at 700°F.

The most significant benefit to the common stress plots, Figures 4.22-4.28, is the ability to visualize the change in response resulting from an increase or decrease in test temperature

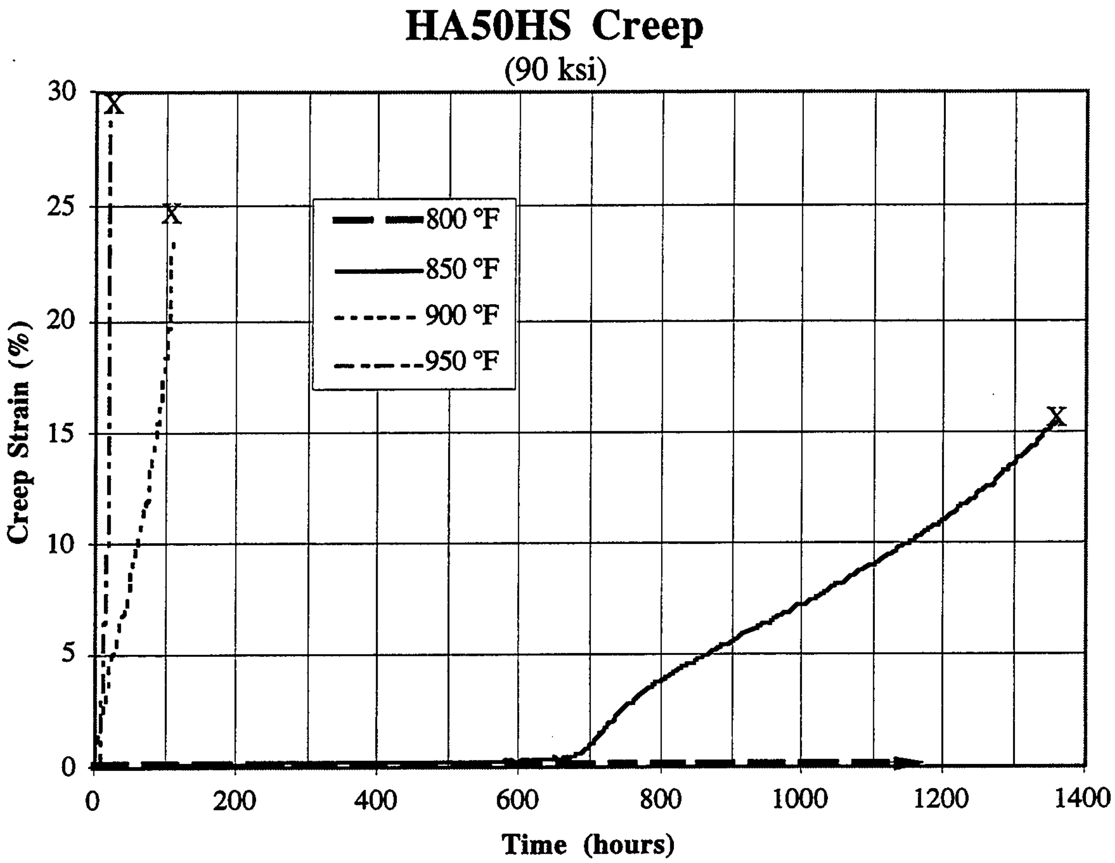

Figure 4.26 Creep Strain Versus Time Response of HA50HS Specimens Tested at 90 ksi.

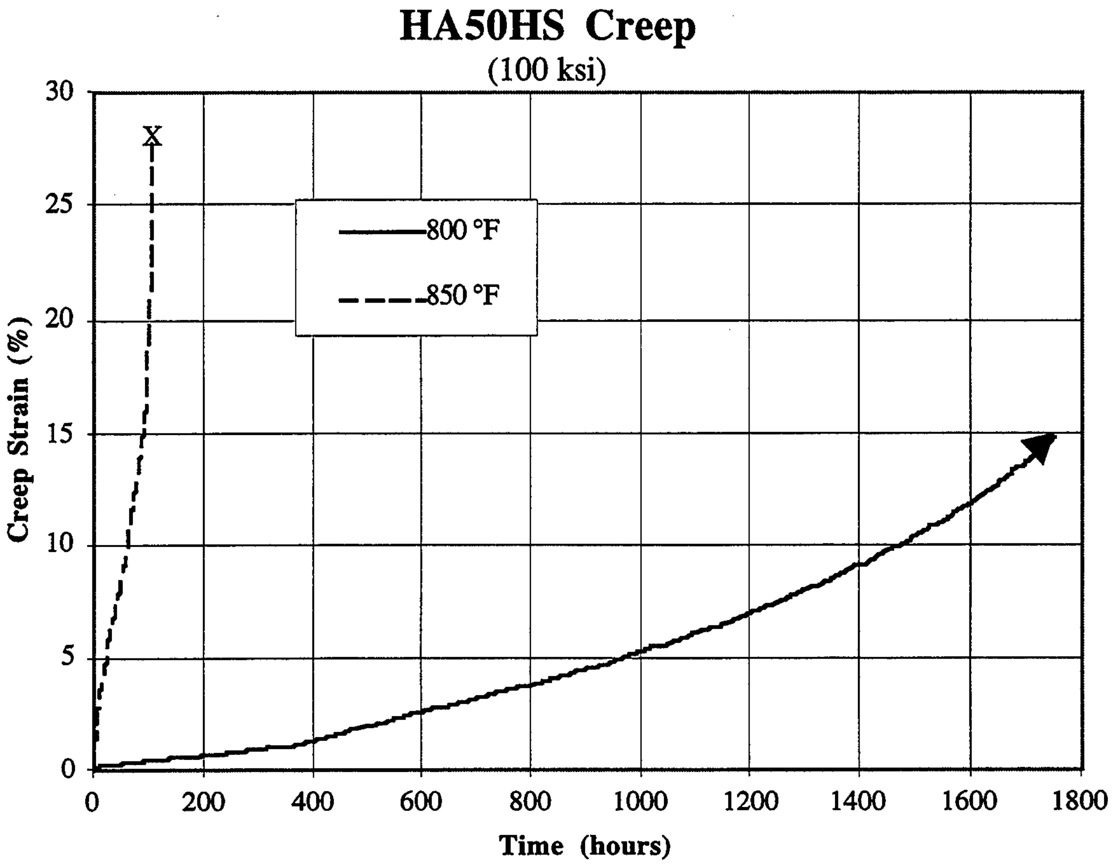

Figure 4.27 Creep Strain Versus Time Response of HA50HS Specimens Tested at 100 ksi.

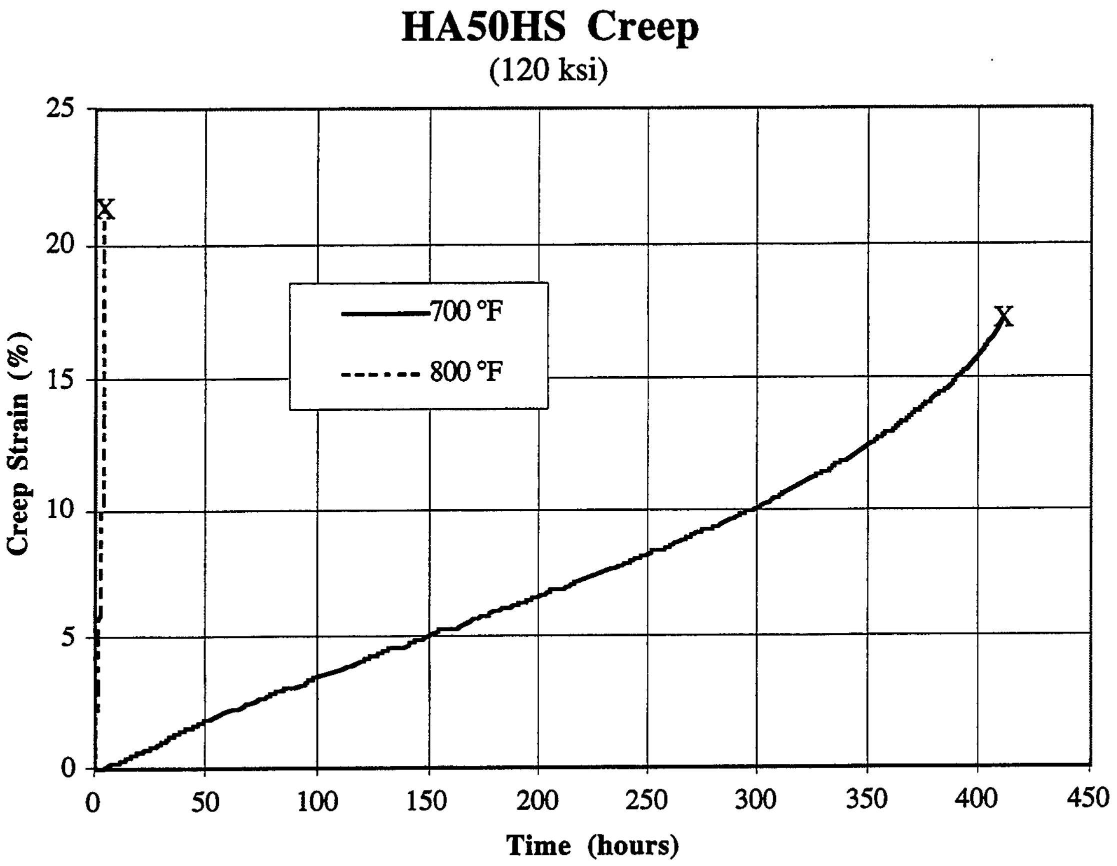

Figure 4.28 Creep Strain Versus Time Response of HA50HS Specimens Tested at 120 ksi.

of only 50°F. In many of the illustrations this change involved a similar type response with a shift in creep life and final creep strain. However, at some of the stress levels an increase of 50°F resulted in a totally different response, as is the case at 90 ksi. The 85 ksi curves show a significant difference in behavior due to a 100°F increase. In all of the constant stress comparisons an increase in temperature resulted in an increase in final creep strain and a decrease in creep life. Comparisons of curves exhibiting the abrupt increase in strain rate show that the actual transition between the two steady-state regions moves closer to the test initiation as the test temperature is increased. Steady-state strain rates are increased as temperature is increased at a constant stress.

The most significant benefit to common temperature plots, Figures 4.15-4.21, is the ability to visualize the change in creep strain versus time response that occurs from a change in applied stress of only 5 or 10 ksi. In some of the constant temperature response plots a variation of stress does not change the prevalent stages of creep deformation. An increase in stress does, however, appear to increase the amount of creep deformation while shortening the creep life. For other families of constant temperature responses a variation of only 5 ksi results in the creep response changing from a traditional creep curve to a response involving two steady-state regions separated by an abrupt increase in strain rate. This influence is easily seen in Figure 4.19 with the 75 and 80 ksi responses. Figure 4.16 depicts three different responses due to 5 or 10 ksi changes in the applied stress level. Comparisons of curves exhibiting the abrupt increase in steady-state strain rate show that the transition between the two linear regions moves closer to the test initiation as the applied stress level is increased. This dependency is easily seen in Figures 4.18 and 4.19.

4.2.2 Isochronous Stress Versus Strain

The results of a single creep test are typically summarized by stress, temperature, steady-state creep rate, and time to rupture. Data generated from one or more creep tests may be presented in a variety of forms. If a sufficient number of creep tests are conducted at various stress levels, the data may be replotted to illustrate stress versus strain curves for various constant values of time. These curves, which are generated at specific temperatures, are known as isochronous stress-strain curves. This method of plotting creep data is equivalent to assuming that the total creep strain is a function of stress and time.

Isochronous stress-strain curves, such as those depicted in Figures 4.29-4.33, are constructed from the standard creep strain versus time curves recorded for several stress

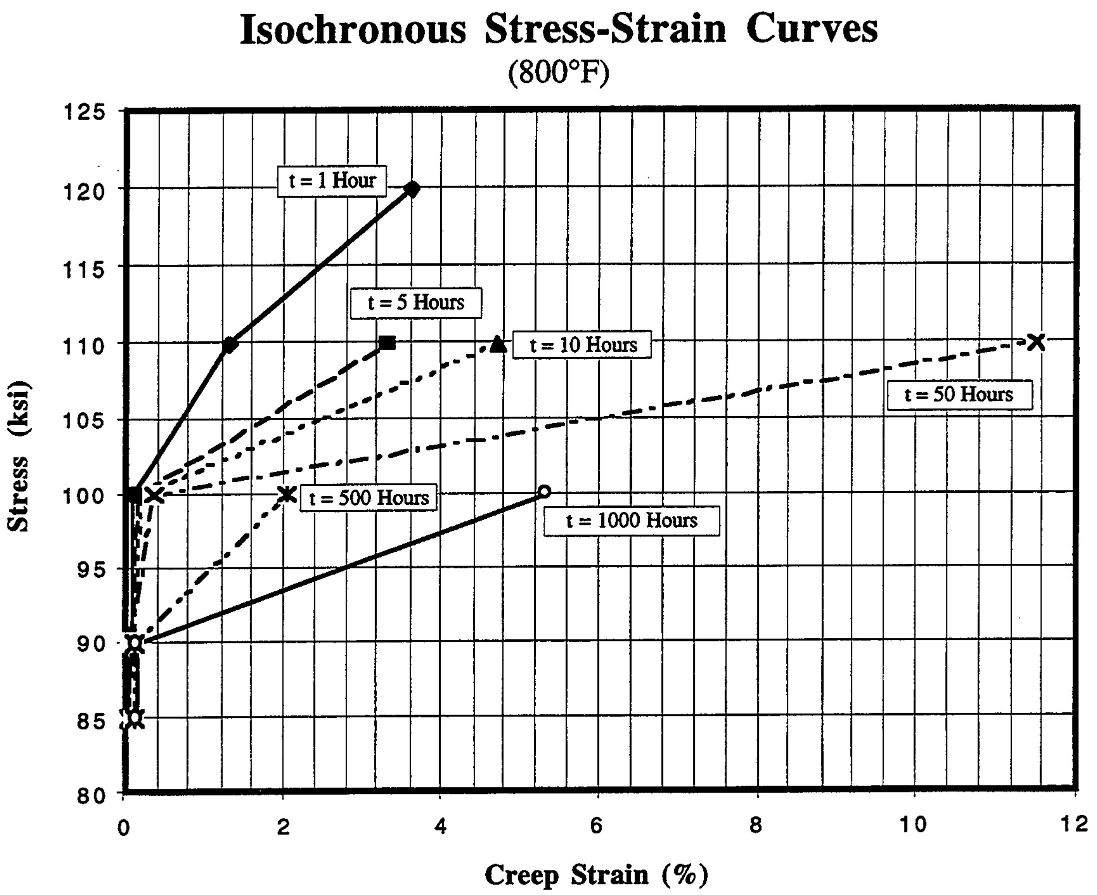

Figure 4.29 Isochronous Stress-Strain Curves of HA50HS Specimens Creep Tested at 800°F.

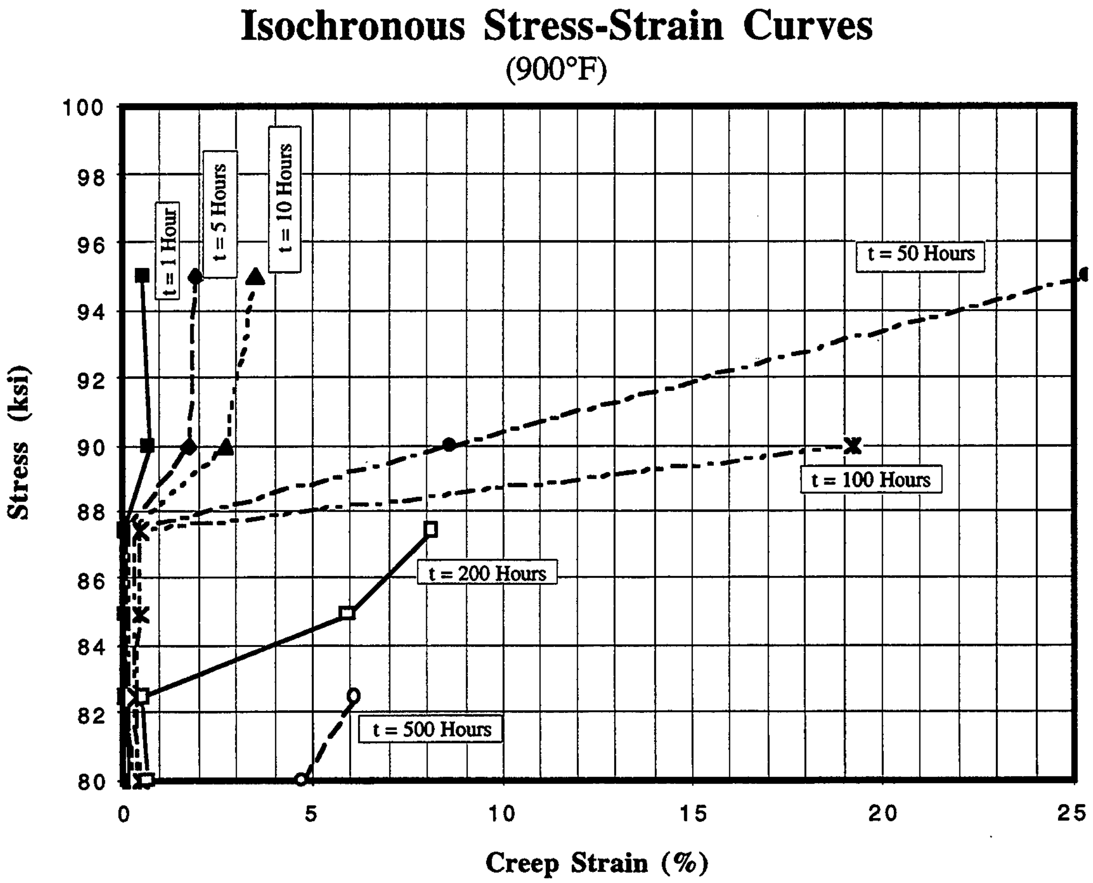

Figure 4.30 Isochronous Stress-Strain Curves of HA50HS Specimens Creep Tested at 900°F.

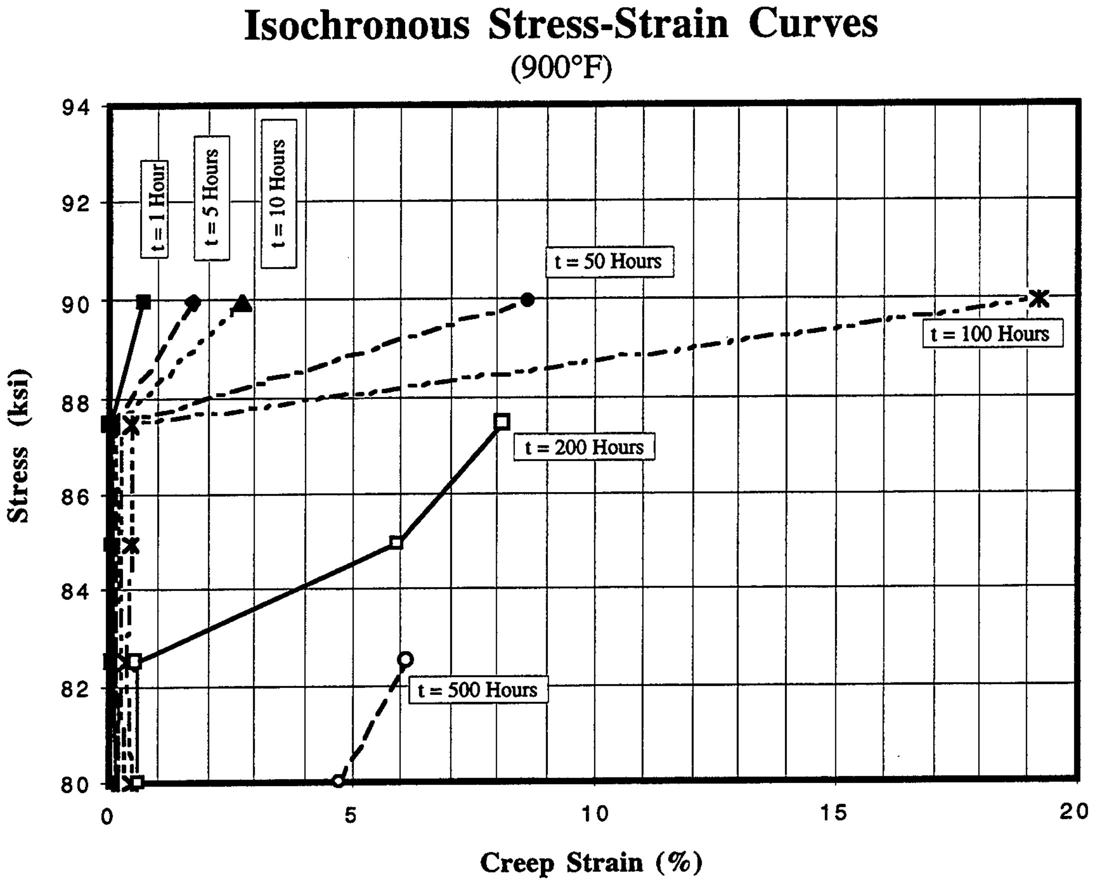

Figure 4.31 Isochronous Stress-Strain Curves (Up to 90 ksi) of HA50HS Specimens Creep Tested at 900°F.

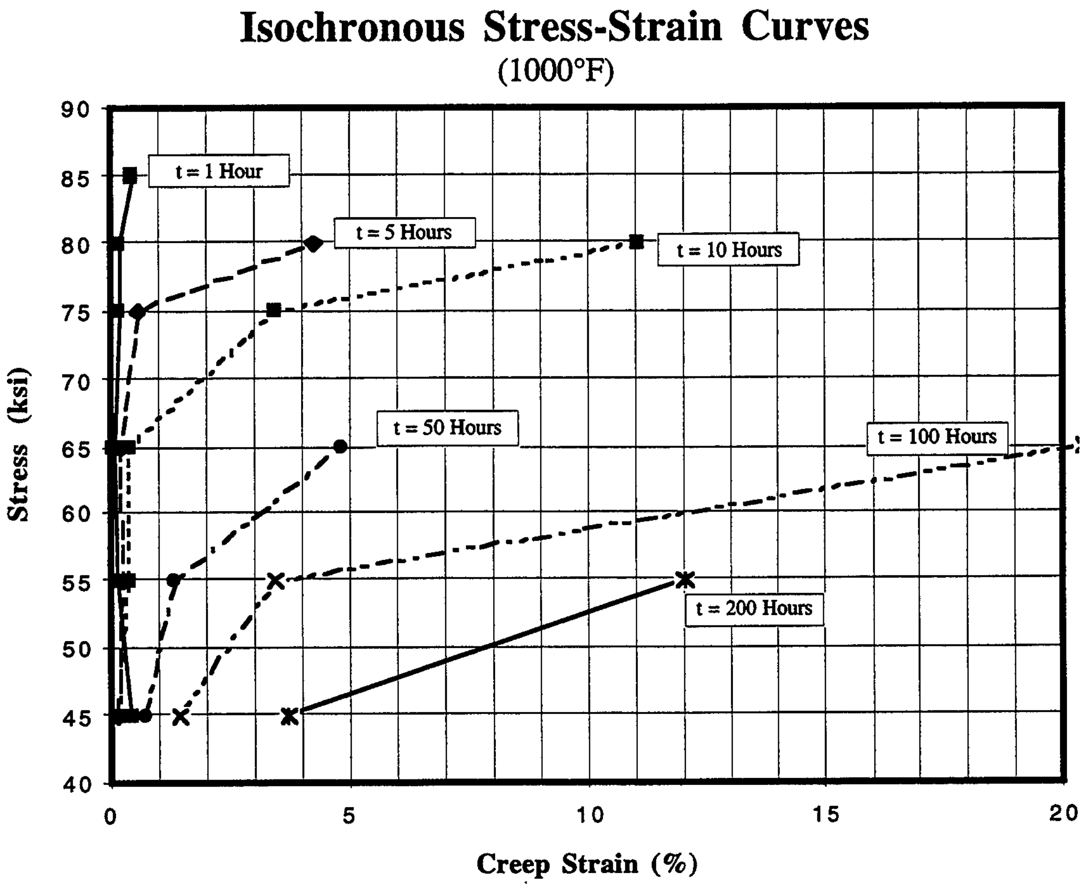

Figure 4.32 Isochronous Stress-Strain Curves of HA50HS Specimens Creep Tested at 1000°F.

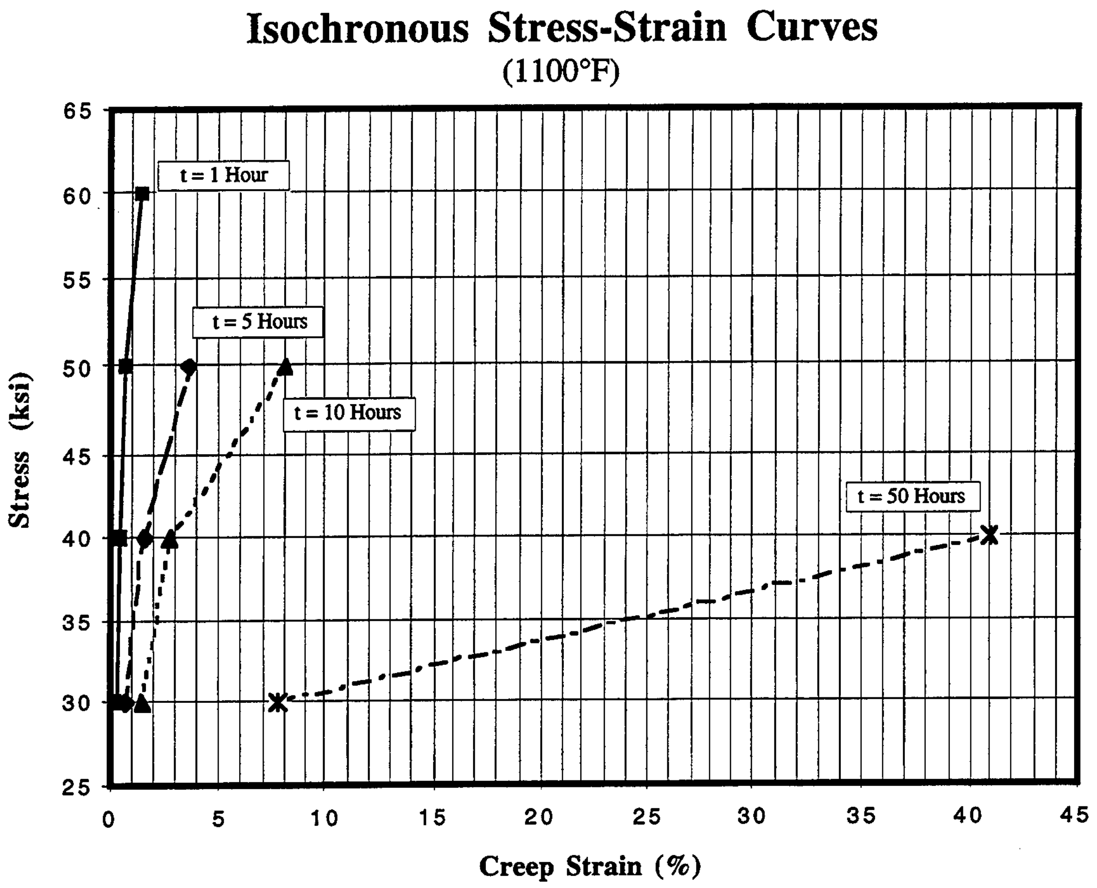

Figure 4.33 Isochronous Stress-Strain Curves of HA50HS Specimens Creep Tested at 1100°F.

levels. Strains corresponding to specific times are replotted versus the corresponding stress levels. Curves are generated for various values of time.

A linear visco-elastic behavior would be indicated by a straight line representation of the stress versus strain relationship for any given value of time. This behavior is typically the case for a material dominated by the low stress, diffusional flow creep behaviors, such as Nabarro-Herring or Coble creep. Dislocation creep of crystalline materials at relatively high stresses and lower temperatures, however, does not exhibit a proportional relationship between strain rates and stress. There is instead a strong power dependence.

The utility of an isochronous stress-strain curve that represents nonlinear behavior, is that an elasto-plastic deformation analysis may be performed without consideration to time dependency [50]. The isochronous stress-strain curve for a specific time may be used as if it were an elasto-plastic stress-strain curve. Shanley pointed out that the use of the isochronous stress-strain curves overestimates the strain in a location where the stress has been increasing and underestimates the strain at locations where the stress is decreasing [86].

Although a significant amount of creep testing was conducted in this study, requiring a substantial amount of time, the generation of smoother isochronous stress-strain curves requires even more data points. These curves were generated from data conducted at 800, 900, 1000, and 1100°F. Each curve can be thought of as a "slice" of stress-strain behavior in time. At relatively low creep strains on the 800°F plot, the time curves are all very similar. As can be seen in Figure 4.29, time dependency becomes more apparent at a creep strain of about 1.0%. Naturally, as the curves corresponding to increasing lengths of time are plotted, the number of data points available is decreased. Hence, the linearity of the behavior is exaggerated. This linear representation should not be thought of as linear visco-elastic behavior. There were five creep tests conducted at 800°F and three very different responses were recorded. The lower two stresses resulted in very little creep deformation up to about 1200 hours when the tests were stopped. The third test was conducted at 100 ksi and generated a point for each curve on the plot before it was stopped at about 1700 hours. The two highest stress tests deformed quickly, generating only three data points for the 100 ksi test and only one data point for the 120 ksi test.

Figure 4.30 illustrates the isochronous stress-strain curve pertaining to tests conducted at 900°F. More creep tests were conducted at this temperature than any other. As with the

800°F curves, the strains which correspond to the lower stresses are nearly coincident to each other. This linear response can be seen on the curves representing a time of one hour up to a time of 100 hours. The behavior at 200 hours indicates an initial elastic response only up to a stress of 82.5 ksi. The 500 hour response does not include data at low enough stress levels to illustrate the elastic behavior. It is speculated that a stress of 70 ksi would result in strains less than 1%, thereby illustrating the elastic behavior for this slice in time as well. The data points associated with a stress of 95 ksi appear to be located at lower than expected strains for the time curves of ten hours and less. The actual creep strain versus time responses generated by the tests show the behavior of the 95 ksi test as being very similar to the behavior associated with the 90 ksi test during the early stages of deformation. Beyond ten hours, however, the strain rate of the higher stressed specimen increases significantly over that of the lower stressed specimen. This trend is obvious from Figure 4.30. Due to the high stress, as compared to the tensile properties, and the fact that each of these data points are based on individual tests and not statistical quantities, it is not unreasonable to disregard the data points corresponding to the 95 ksi test. This exclusion of data is done and the time dependency is nicely illustrated in Figure 4.31. Figure 4.32 also depicts a strong power dependence between strain rates and stress for various times. The set of curves represents the evolution of the stress versus strain response as a function of time as anticipated. The lower strain values, less than 0.4%, and the corresponding stresses are representative of a linear elastic behavior from times of one hour up to nearly 50 hours. At times of 50 hours and above, the stress levels were not low enough to illustrate this elastic response. The behavior at 200 hours is linear only due to the lack of additional data points. The higher stress tests all failed before 200 hours and tests with stresses lower than 45 ksi were not conducted at this temperature.

Isochronous stress-strain curves at 1100°F are shown in Figure 4.33. Naturally, at this elevated temperature the curves are more representative of the lower time and stress behaviors. Only two of the four creep tests lasted longer than 50 hours prior to fracture. The initial linear elastic response is implied by the developing trend at low stresses, but there is still substantial time dependency even at stresses as low as 30 ksi. The behavioral trends of the time curves allow the speculation that a stress level of 20 ksi would be sufficient to demonstrate an elastic response for times up to 10 hours. The 50 hour response would also be much more aligned with the lower times at this stress level.

The isochronous stress-strain representation of multiple creep tests is perhaps the most illustrative way to visualize the time dependency of a material's stress versus strain response. The curves generated under this study also clearly indicate a strong power dependency between strain rates and stress at many of the shorter time curves. It is also speculated that this same relationship exists at longer times, however, insufficient data in some instances preclude a solid conclusion.

4.2.3 Times To A Percent Creep Strain

Quite often data taken from multiple creep tests at various temperatures and stresses are expressed as times required for a specimen to deform to a specific amount of strain [46]. This time may then be used to estimate the life of a part. When referring to creep life, the term failure may be used to specify specimen fracture. However, a part may also fail by reaching a certain amount of deformation, such as the case of an electric motor or generator. The rotor contained within one of these high speed electrical machines may diametrically deform and subsequently reduce the required air gap between the rotor and stator poles. Once contact has been made between the poles, the machine has failed.

Data from all of the creep tests conducted under this study were used to create charts depicting the times required for the creep strain to reach 0.1%, 0.2%, 0.5%, 1.0%, 2.0%, and fracture, as a function of applied stress and test temperature. The relationship between stress and time is assumed to be governed by Equation 4.3, below.

$$\sigma = b\, t^{m}. \tag{4.3}$$

Plots of lines, developed by using least squares curve fitting, are also included in the figures in order to predict the logarithmic trend of the data. The slope, m, of the trend lines relates the natural logarithm of time to the applied stress by the relation:

$$\sigma = m \ln(t) + b. \tag{4.4}$$

Two of the tests conducted did not provide data, even for the time to 0.1% because of the very low strain rates up to the test termination of about 1200 hours. Data scatter associated with the strain measuring technique is apparent in the graphs illustrating the times to lesser creep strains. Also, the apparent difference in the shapes of the creep strain versus time curves adds to a larger deviation between the estimated and actual times. For most of the creep strain behaviors that exhibited an abrupt increase in strain rate, the transition consistently occurred at a creep strain of about 0.65%. However, the time required to reach this strain varies with stress and temperature.

Figure 4.34 illustrates the times required for the test specimens to reach a creep strain of 0.1%. As expected, a significant amount of data scatter is present. This scatter is especially true for the 1000°F data, which has a coefficient of determination of only 0.29. It appears that some of the trendlines have similar slopes, however, on a semilogarithmic plot this similarity may still represent a large variance. Slopes of the logarithmic trendlines range in value from –1.2 to –17.0. Times required to reach a creep strain of 0.2% are depicted in Figure 4.35. It appears, from this representation, that the 950°F, 1000°F, and 1100°F data depict similar slopes of about –14.3. The 800°F, 850°F, and 900°F data also indicate similar behaviors with an average characteristic slope of about –1.89. The 700°F curve is established by only two data points and was not included in the determination of the slopes.

The slopes of the least squared curve fits in Figure 4.36 can be visually separated into two groups. As the data scatter seems to be lessening, the trend lines corresponding to the time required to reach a creep strain of 0.5% may be characterized with average slopes of –1.87 and –11.55 for the 800-900°F and 950-1100°F test temperatures, respectively. The improved estimation of behavior is represented by the increased coefficients of determination corresponding to each individual trend line. The minimum r^2 value for the lower temperature plots is about 0.72 while the minimum r^2 value resulting from the higher temperature curves is approximately 0.94.

The coefficients of determination continue to increase as the trend lines become better estimations of the actual data. The time required to reach a creep strain of 1.0% is illustrated in Figure 4.37. Again, the 800-900°F plots may be segregated into a group with a defining slope of about –2.0. The higher temperature (950-1100°F) curves may be grouped and characterized by a slope of approximately –10.3. Figure 4.38 illustrates the time required for the test specimens to reach a creep strain of 2.0% as a function of applied stress and test temperature. The lower temperature data are estimated by trend lines with r^2 values greater than 0.84. The average slopes of these three curves is approximately –2.37. The higher temperature data series are represented by even better estimations, characterized

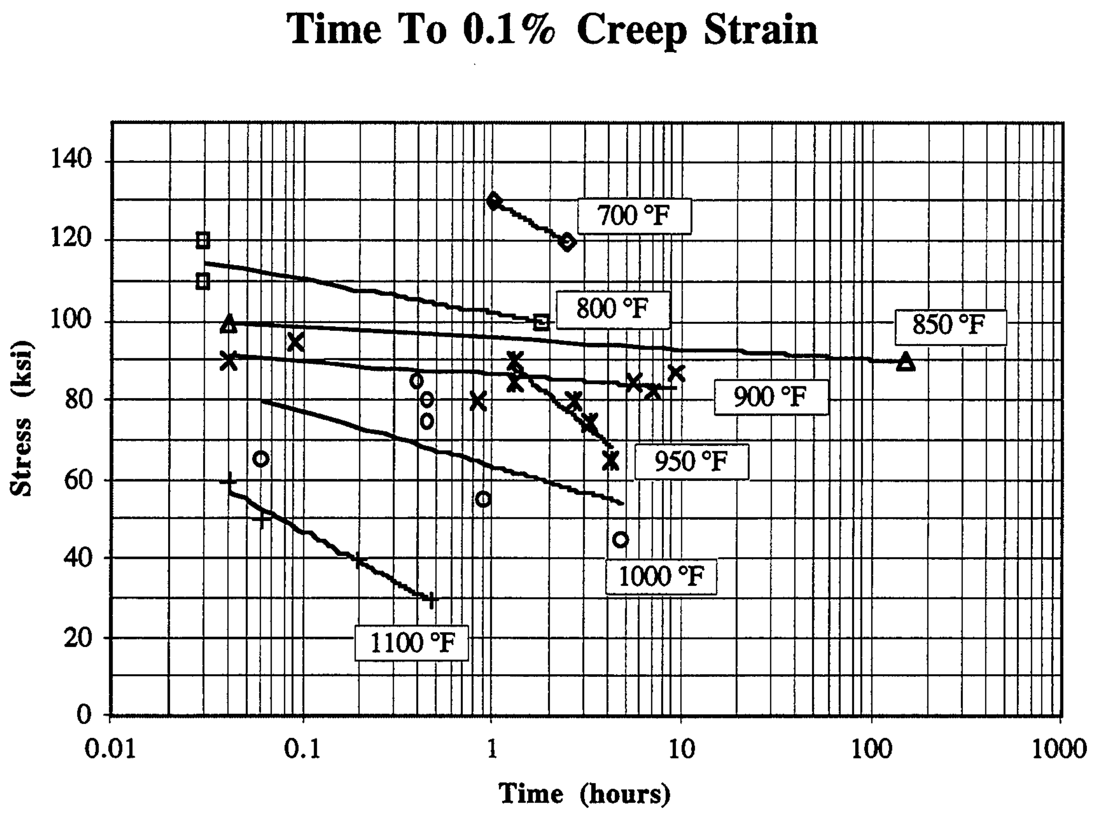

Figure 4.34 Time Required for a HA50HS Specimen to Reach 0.1% Creep Strain as a Function of Applied Stress and Temperature.

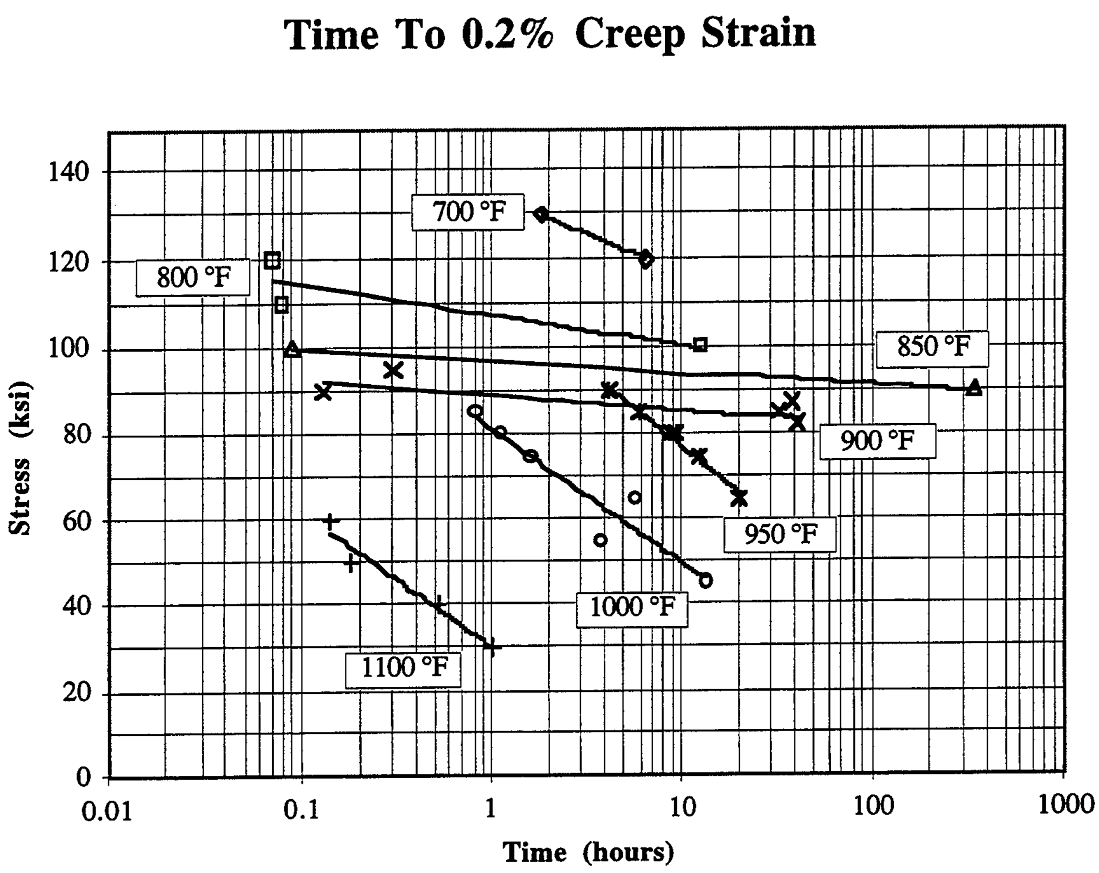

Figure 4.35 Time Required for a HA50HS Specimen to Reach 0.2% Creep Strain as a Function of Applied Stress and Temperature.

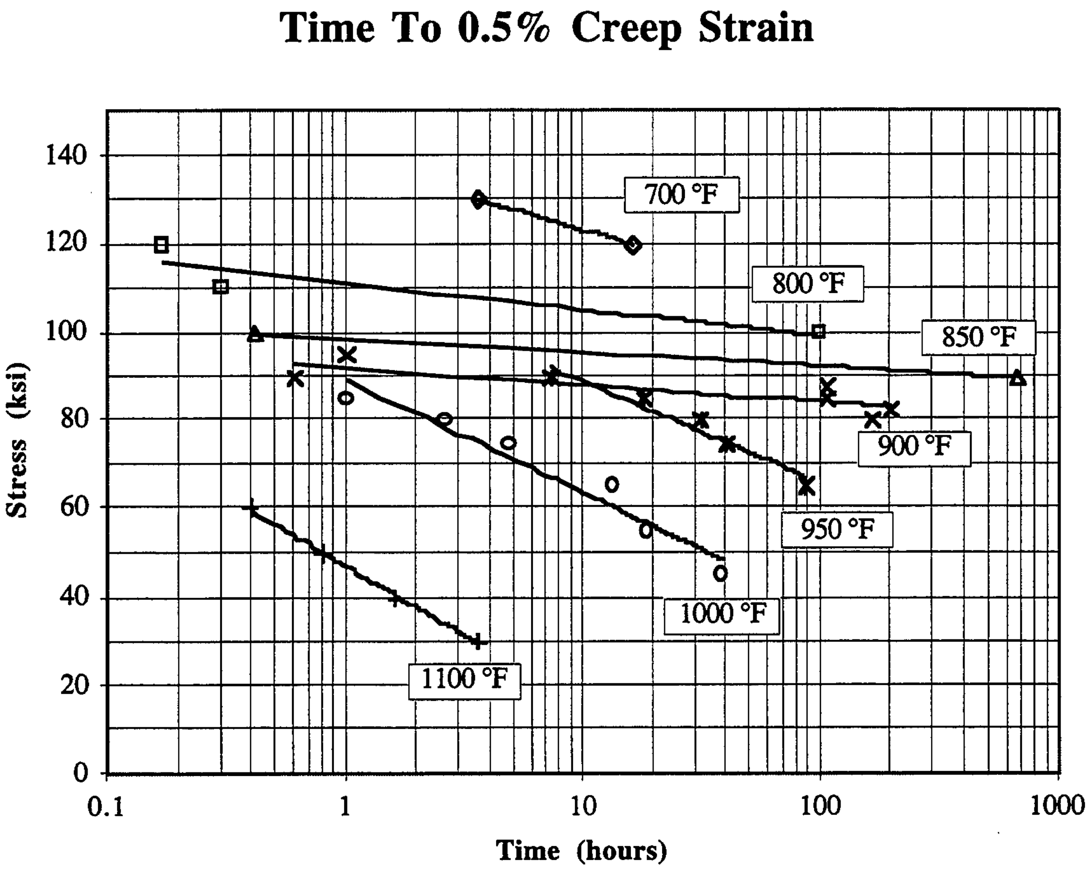

Figure 4.36 Time Required for a HA50HS Specimen to Reach 0.5% Creep Strain as a Function of Applied Stress and Temperature.

Time To 1.0% Creep Strain

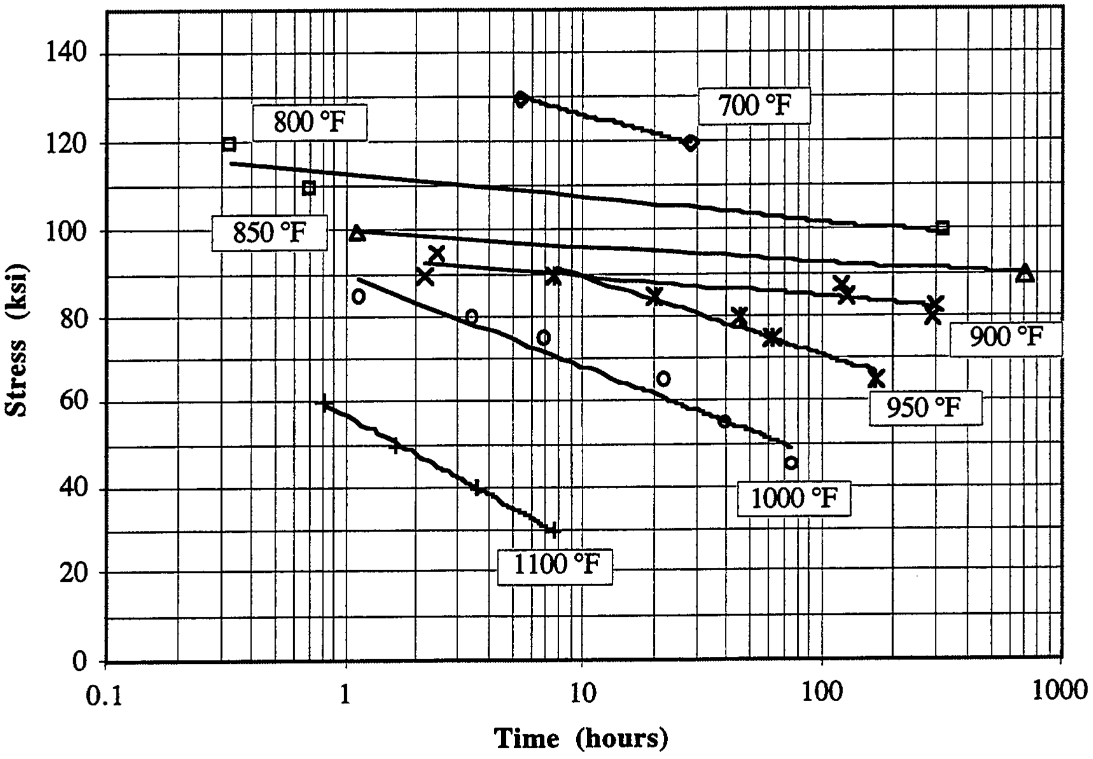

Figure 4.37 Time Required for a HA50HS Specimen to Reach 1.0% Creep Strain as a Function of Applied Stress and Temperature.

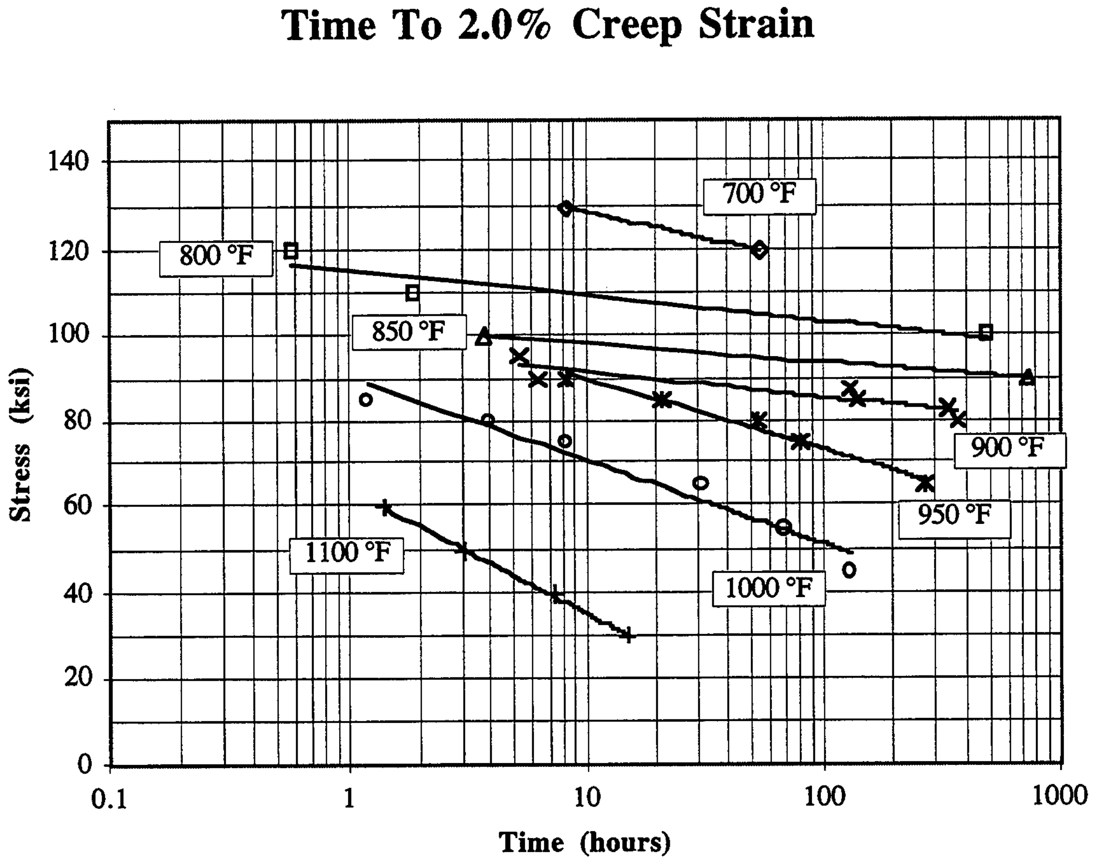

Figure 4.38 Time Required for a HA50HS Specimen to Reach 2.0% Creep Strain as a Function of Applied Stress and Temperature.

by coefficients of determination of better than 0.95. The average slope corresponding to these 950-1100°F data is about –9.37.

Time to creep fracture is perhaps one of the least useful characterizations of this material. The large creep strains coincident with fracture would likely be beyond a component deformation limit. The data, however, are included in Figure 4.39 to provide a more complete description. The two separate groups of temperature plots are less distinguishable, and a gradual decrease in slope from –3.22 to –10.98 corresponds to a temperature increase from 800°F to 1100°F, respectively. The 700°F slope is within this range of slopes. The linear estimations of the data are better for this set of data than for any of the previously described stress versus time to creep responses. The minimum coefficient of determination describing an estimate to fracture is 0.96.

4.3 Creep Behavior Modeling

4.3.1 Power Law Model

The linear regression technique utilizes the least squares method to calculate a straight line that best fits the data to be modeled. The equation of the fitted line is in the form of:

$$y = m_1 x_1 + m_2 x_2 + \ldots m_n x_n + b, \tag{4.5}$$

where the dependent *y*-value is a function of the independent *x*-value. The *m*-values are coefficients corresponding to each of the *x*-values and *b* is a constant. The *m*-coefficients correspond to the slope of a line for a single regression analysis and the constant *b* is the value of the dependent variable at the point where the line crosses the dependent axis. The known dependent values are input into the statistics program along with the known sets of independent values. If there is only one set of independent values, the process is known as single linear regression. Multiple linear regression is conducted for data sets with more then one array of independent variables. Regression statistics may be obtained from the sets of independent and dependent variables. Standard error values for the m-coefficients and for the constant *b* may be determined. The coefficient of determination, known as r^2, compares estimated and actual values of the dependent variable. This coefficient can range in value from 0 to 1. If r^2 equals 1, there is a perfect correlation in the sample. In other words, there is no difference between the estimated and the actual values of the dependent

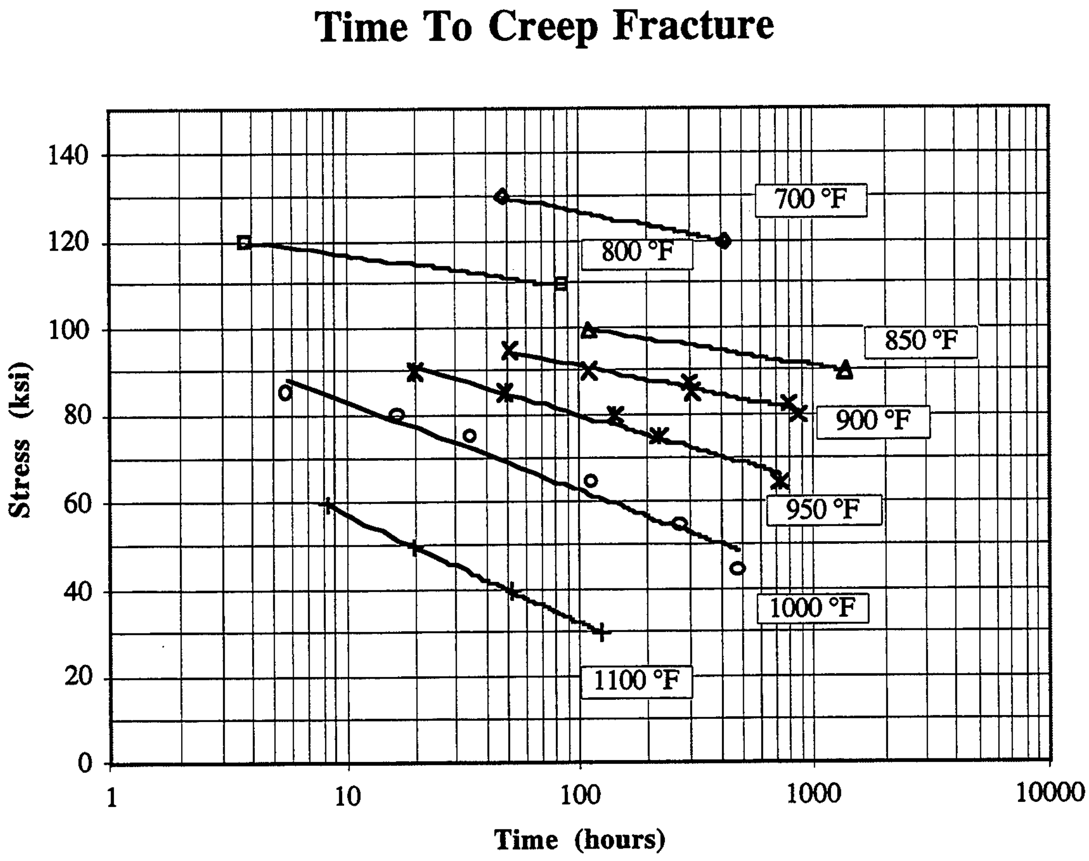

Figure 4.39 Time Required for a HA50HS Specimen to Fracture as a Function of Applied Stress and Temperature.

variable. If the coefficient of determination is equal to zero, however, the calculated regression equation is of no use in predicting the dependent variable.

Another important statistical quantity is known as the F statistic. This value is determined by the calculated relationship between the dependent and independent sets of variables and can be used to determine the probability that the results occurred by chance. A high coefficient of determination would indicate a strong relationship between the independent and dependent variables. There is, however, a possibility that there is no relationship among the variables and that a rare sampling of data caused the statistical analysis to erroneously indicate a strong relationship. If the F statistic is larger than an F-critical value, there exists a certain probability of a relationship among the independent and dependent variables. An F-critical value can be obtained, corresponding to the desired probability, by using the number of data points and the number of independent variables and referring to tables of values listed in many statistics textbooks [87, 88, 89]. An F-critical value that would identify a 5% probability of there being no correlation between the data and the model would be written as $F_{0.05}$.

The form of the steady-state creep strain relation allows a double linear regression analysis to determine the stress exponent as well as the activation energy. The natural logarithm of both sides of Equation 1.11 results in the relation:

$$\ln T\dot{\varepsilon} = n \ln \sigma - \frac{Q}{RT} + \ln A. \tag{4.6}$$

The regression analysis continues by comparing Equation 4.5 to Equation 4.6 and considering $\ln T\dot{\varepsilon}$ as the dependent variable, y, and $\ln \sigma$ and $1/RT$ as two arrays of independent variables, x_1 and x_2, respectively. The two fitting constants, m_1 and m_2, of Equation 4.5 equate to the activation energy, Q, and the stress exponent, n. The exponential of the intercept constant, b, is equal to the creep strain rate coefficient, or kinetic factor, A. The creep test data used in the linear regression analyses are listed in Table 4.1. The dependent variable is the steady-state strain rate corresponding to each test. The two independent variables used in this analysis are absolute test temperature and the applied stress.

Table 4.1 Creep Test Data Used in the Series of Linear Regression Analyses.

DOUBLE LINEAR REGRESSION

DEPENDENT VARIABLE — STRAIN RATE
INDEPENDENT VARIABLES — TEMPERATURE AND STRESS

Temp (K)	Temp (°F)	Stress (psi)	Type	Strain Rate 1 (in/in/hr)	Strain Rate 2 (in/in/hr)	Knee Location Time (hrs)	Knee Location Strain (%)	Life (hours)
644	700	120000	C	N/A	0.000323			410
644	700	130000	C	N/A	0.003245			50
700	800	85000	B or C	4.267E-07	N/A			>1200
700	800	90000	B or C	3.609E-07	N/A			>1200
700	800	100000	B or C	0.000022	0.00006438			>1752
700	800	110000	C	N/A	0.001639			86
700	800	120000	C	N/A	0.0382			4
727	850	90000	B	0.000004303	0.000203	680	0.6	1362
727	850	100000	C	N/A	0.00124			109
755	900	80000	A	0.0000172	N/A			856
755	900	82500	B	0.0000202	0.000265	240	0.65	778
755	900	85000	B	0.0000312	0.000647	117	0.6	304
755	900	87500	B	0.0000355	0.000812	110	0.6	295
755	900	90000	C	N/A	0.00147			109
755	900	95000	C	N/A	0.00321			51
783	950	65000	A	0.0000565	N/A			723
783	950	75000	A	0.000115	N/A			220
783	950	80000	B	0.000162	0.001838	40	0.7	142
783	950	85000	B	0.000199	N/A	19	0.65	48
783	950	90000	C	0.00356	N/A			19
811	1000	45000	A	0.0001345	N/A			479
811	1000	55000	A	0.00024	N/A			270
811	1000	65000	A	0.000471	N/A			111
811	1000	75000	B	0.000886	0.007054	6	0.7	34
811	1000	80000	B	0.001861	0.014556	3	0.65	17
811	1000	85000	B	0.002298	0.028	1	0.27	6
866	1100	30000	A	0.00155	N/A			123
866	1100	40000	A	0.003204	N/A			51
866	1100	50000	A	0.00846	N/A			20
866	1100	60000	A	0.0224	N/A			8

Three distinct behaviors can be identified by the data illustrated in the creep curves. Examples of these behaviors are depicted in Figure 4.40. The first behavior is that of a traditional creep curve and is referenced as Type-A in this study. Type-A creep involves primary, secondary, and tertiary stages of creep deformation. The Type-A responses recorded in this study all resulted from tests at stress levels below the minimum serration stress, as determined by the corresponding tensile tests. The next distinct behavior is characterized by two steady-state regions of deformation separated by an abrupt increase in the strain rate. These particular tests are identified as Type-B in this study, with a Type-B1 response corresponding to the first steady-state region and Type-B2 corresponding to the second steady-state region. All of the responses resulting from creep tests that were conducted at stress levels between the maximum and minimum serration stresses were Type-B behaviors. The third distinguishable response is similar in shape to the Type-A response. This third response, however, is characterized by having the highest strain rates of the three responses. This response, identified as Type-C, resulted from applied stress levels above the corresponding yield strengths.

A matrix containing the three steady-state deformation types is illustrated in Figure 4.41. As can be seen from the figure, all of the Type-A deformations did indeed occur below the minimum serration stress. The region between the minimum and maximum serration stresses contained only Type-B deformations. Four Type-B deformations occurred outside of this region; however, three of them were located on the threshold separating the regions. All eight of the Type-C deformations occurred in the region above the maximum serration stress. The thresholds are determined from the corresponding tensile data. The three asterisks identify tests that did not result in an obvious type of behavior. The 85 and 90 ksi tests conducted at 700K were both stopped prior to fracture. The creep strains versus time responses were linear throughout the test. It is not possible to conclude whether the responses were the first steady-state portions of a Type-B deformation or if they were the only steady-state portions of the Type-C deformation. The 100 ksi test is also questionable since the Type-C deformation was not obvious even though the applied stress was well above the maximum serration stress.

There are a total of ten Type-A responses listed in Table 4.1. The double linear regression analysis applied to these responses resulted in a calculated activation energy of 98,851 cal/mol and a stress exponent of 3.83. The kinetic factor was determined to be approximately 4.94×10^7 for rates in hr^{-1}, stresses in psi, and temperatures in K. These three determined values were incorporated into Equation 1.11 and plotted in Figure 4.42

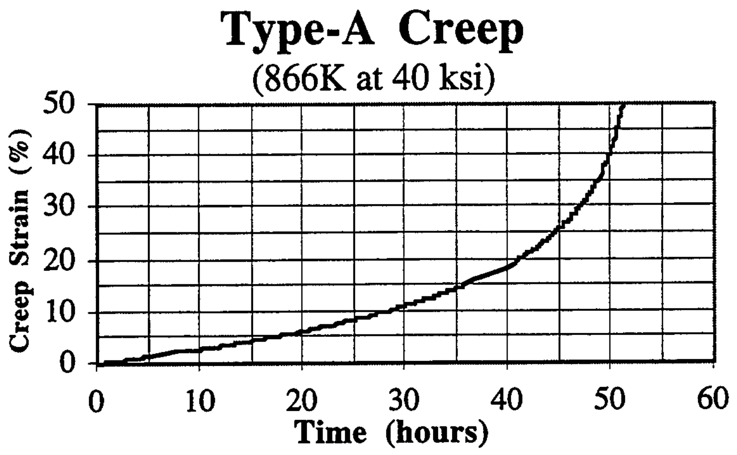

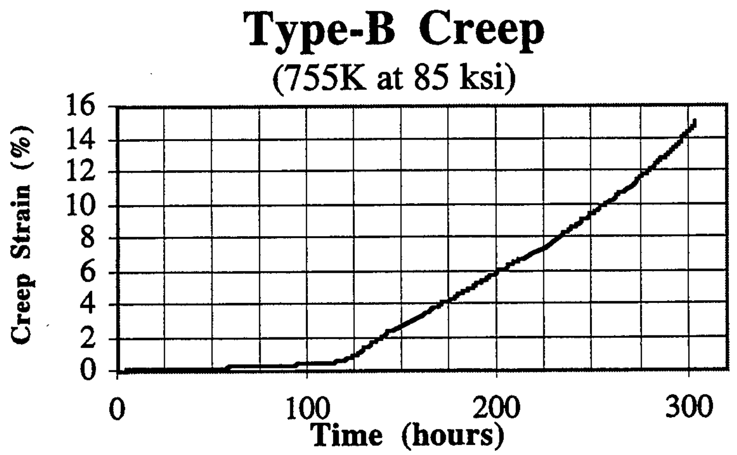

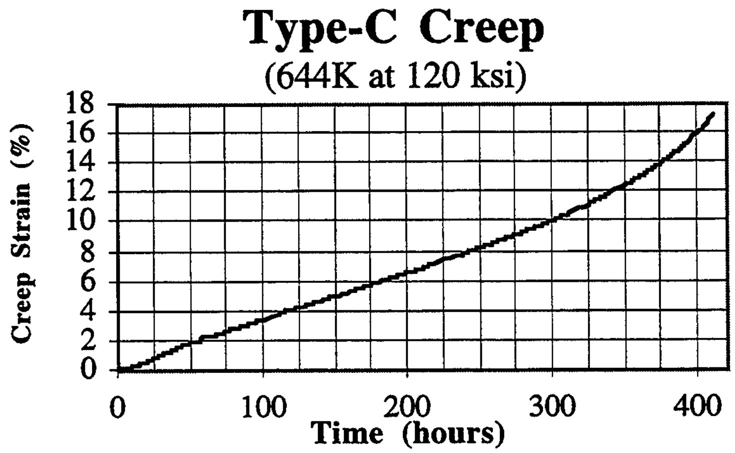

Figure 4.40 Typical Responses of the Three Distinguishable Creep Type Deformations.

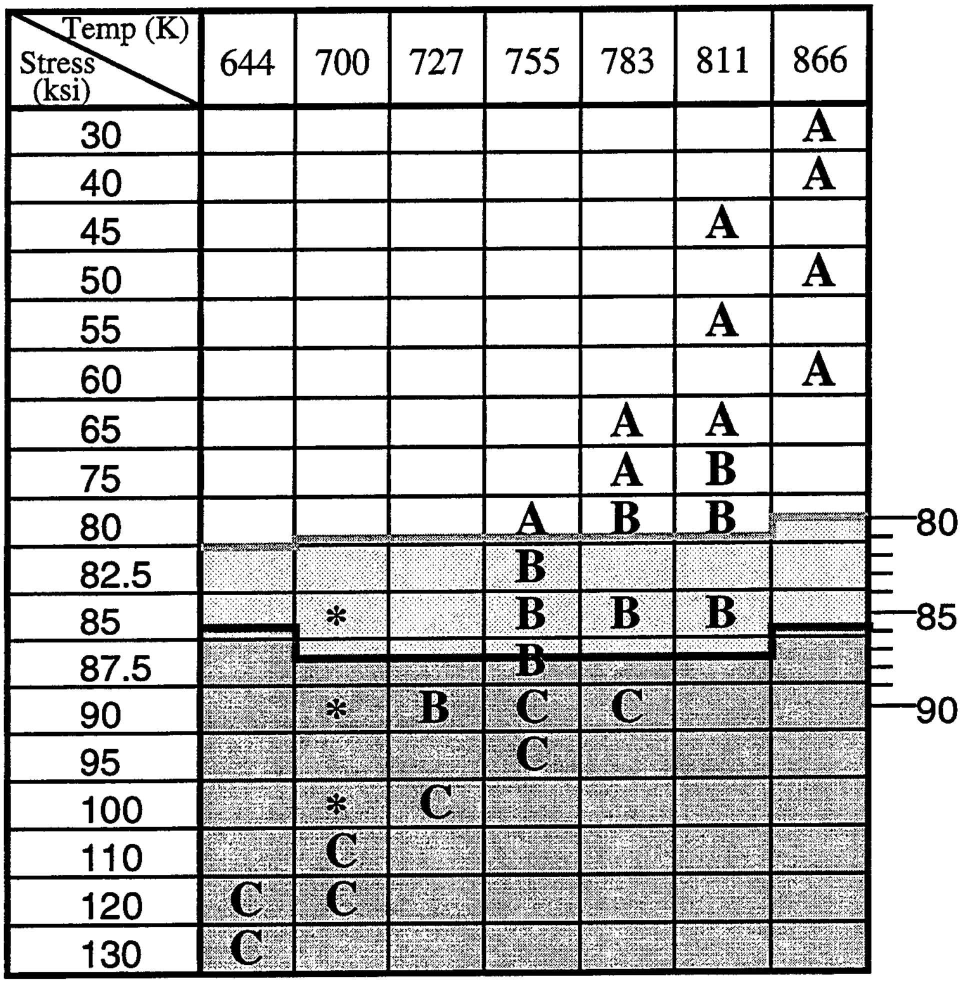

Temp (K) / Stress (ksi)	644	700	727	755	783	811	866
30							A
40							A
45						A	
50							A
55						A	
60							A
65					A	A	
75					A	B	
80				A	B	B	
82.5				B			
85		*		B	B	B	
87.5				B			
90		*	B	C	C		
95				C			
100		*	C				
110		C					
120	C	C					
130	C						

☐ Below Minimum Serration Stress

▨ Between Maximum and Minimum Serration Stresses

▩ Above Maximum Serration Stress

Figure 4.41 Creep Deformation Types of HA50HS Specimens Subjected to Stresses Below the Minimum Serration Stress (Type-A), Between the Minimum and Maximum Serration Stresses (Type-B), and Above the Maximum Serration Stress (Type-C).

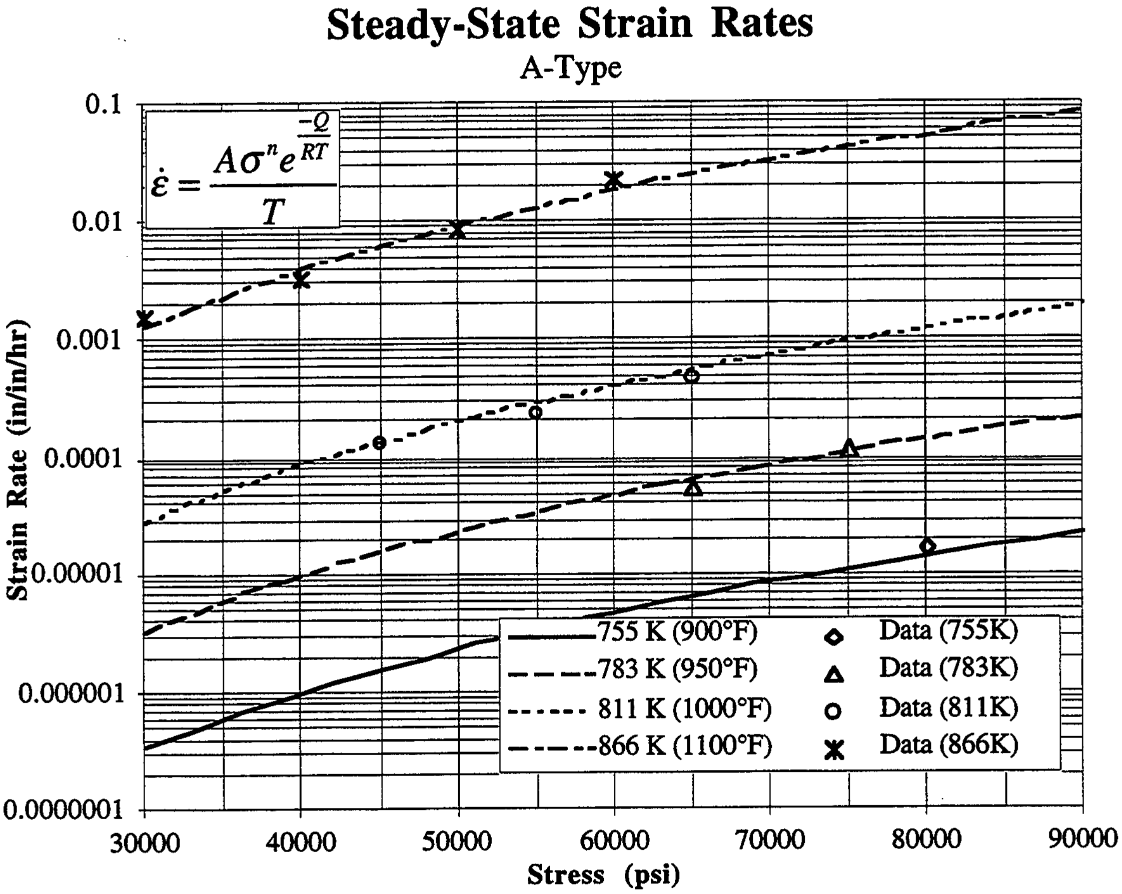

Figure 4.42 Predicted and Actual Steady-State Strain Rates Corresponding to Type-A Creep Behavior of a HA50HS Specimen as a Function of Applied Stress and Temperature.

for constant temperatures. The actual data are also plotted and appear to follow closely the predicted behaviors. The coefficient of determination, r^2, is approximately 0.995 and the F-statistic is 749. The value for $F_{0.01}$ is only 9.55. The nearly perfect coefficient of determination and the large difference between the F statistic and $F_{0.01}$ indicate that the modeled Type A behavior has a better than 99% probability of accurately predicting the creep strain associated with this range of test parameters.

There are a total of nine Type-B responses included in this research effort. Of these nine tests, only eight are included in the Type-B2 regression analysis, while all nine were used in the B1 analysis. One of the Type-B tests conducted at a test temperature of 783K was not used to determine the creep constants describing the second steady-state response due to the fact that the complete response was not recorded. The specimen deformed beyond the maximum extension of the LVDT and subsequently failed before the measuring system could be properly reset. It is likely that the first linear regime was accurately recorded, but the region, which corresponds to the Type-B2 creep regime, was not.

Two of the tests conducted at 700K indicated very little creep strain with a significant amount of data scatter. These two tests were stopped at approximately 1200 hours, and the amount of data scatter allowed only a rough estimate of the steady-state strain rate. It is also unclear as to whether this linear deformation should be characterized as Type-B or Type-C. It is possible that the abrupt increase in strain rate would have eventually occurred if the tests were not stopped. The third questionable test was also conducted at 700K with an applied stress of 100 ksi. The creep strain versus time response illustrates a Type-B behavior; however, the applied stress is well above the measured upper yield strength corresponding to the test temperature. The increase in apparent steady-state strain rate is only threefold instead of at least an order of magnitude, as established by every other Type-B test. It is quite possible that this particular test would be best characterized as a Type-C deformation. The strain rate data pertaining to this specific test were not included in any of the regression analyses. The data resulting from all three of the previously described tests were excluded from further analyses.

The double linear regression analysis of the Type-B1 responses resulted in a calculated activation energy of 99,318 cal/mol and a stress exponent of 8.49. The kinetic factor was determined to be about 1.06 x 10^{-15}. Equation 1.11 can now be plotted for Type-B1 deformation with the appropriate creep constants. Curves of constant temperature are illustrated in Figure 4.43 along with the actual data used in the relevant analysis. The

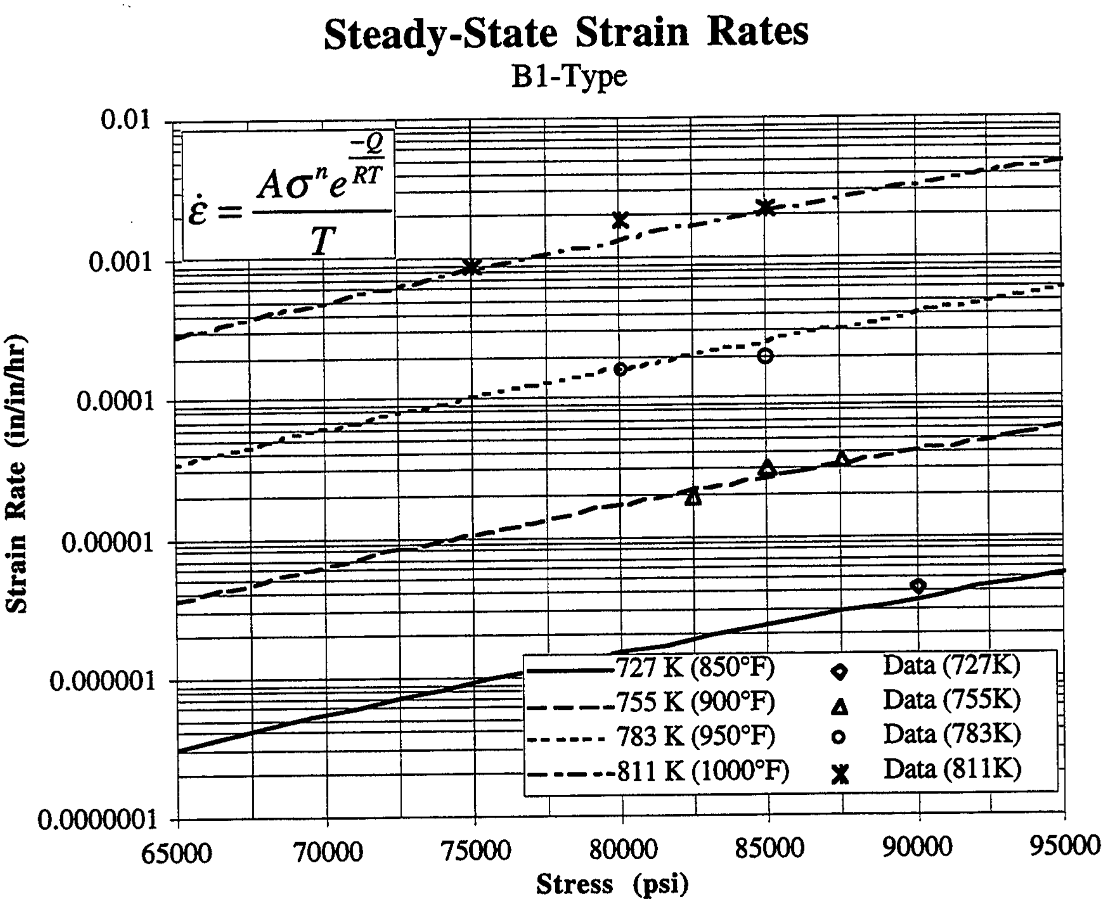

Figure 4.43 Predicted and Actual Steady-State Strain Rates Corresponding to the First Linear Portion of Type-B Creep Behavior of a HA50HS Specimen as a Function of Applied Stress and Temperature.

coefficient of determination, r^2, is approximately 0.995 and the F statistic is calculated to be about 1119. The value for $F_{0.01}$ is only 10.92. Again, the nearly perfect correlation of predicted and actual test data and the large difference between the F statistic and $F_{0.01}$ indicate that the modeled Type B1 behavior has a better than 99% probability of accurately predicting the creep strain associated with this range of test parameters.

The double linear regression analysis, corresponding to the Type-B2 creep deformation, resulted in a calculated activation energy of 87,259 cal/mol. A stress exponent of 13.54 was determined as well as a kinetic factor of 1.02×10^{-42}. The coefficient of determination and the F-statistic were calculated to be 0.985 and 164.8, respectively. The modeled rate equation, with the appropriate creep rate constants incorporated, is illustrated in Figure 4.44. The actual data used in the analysis are plotted along with the predicted curves at constant temperatures. An $F_{0.01}$ value of 13.27 implies that the close correlation between actual and predicted strain rates did not occur due to chance sampling. The near perfect correlation shows a high degree of usefulness of the predictive model.

There are only eight tests characterized as Type-C responses in this research effort. As mentioned previously, all of these tests were subjected to an applied stress, which was above the upper yield point, as determined by the tensile data at corresponding temperatures. The fact that these tests correlate to large amounts of initial plastic deformation makes the results of little practical importance to the aerospace equipment designers. Also the high stress level most likely will be affected by a breakdown of the power law assumption of creep deformation. Although a more appropriate relation could be used, a regression analysis was employed to determine the assumed constant values needed for Equation 1.11.

The double linear regression applied to the eight Type-C responses resulted in a calculated activation energy of 73,737 cal/mol. A stress exponent of 25.4 was determined and, as would be expected, a very small kinetic factor of 1.18×10^{-105} resulted. These three values are incorporated into Equation 1.11 and plotted for constant temperatures in Figure 4.45. The actual data are also plotted to allow a visual comparison of the modeling predictions. The coefficient of determination for this data set is approximately 0.915 and the observed F-statistic is calculated to be about 21.41. The value for $F_{0.01}$ is 13.27. The relatively low coefficient of determination and the small difference between the observed F statistic and the $F_{0.01}$ value indicate that the resulting equation, with the determined creep strain rate constants incorporated, is of less use in predicting strain rates than the other predictive

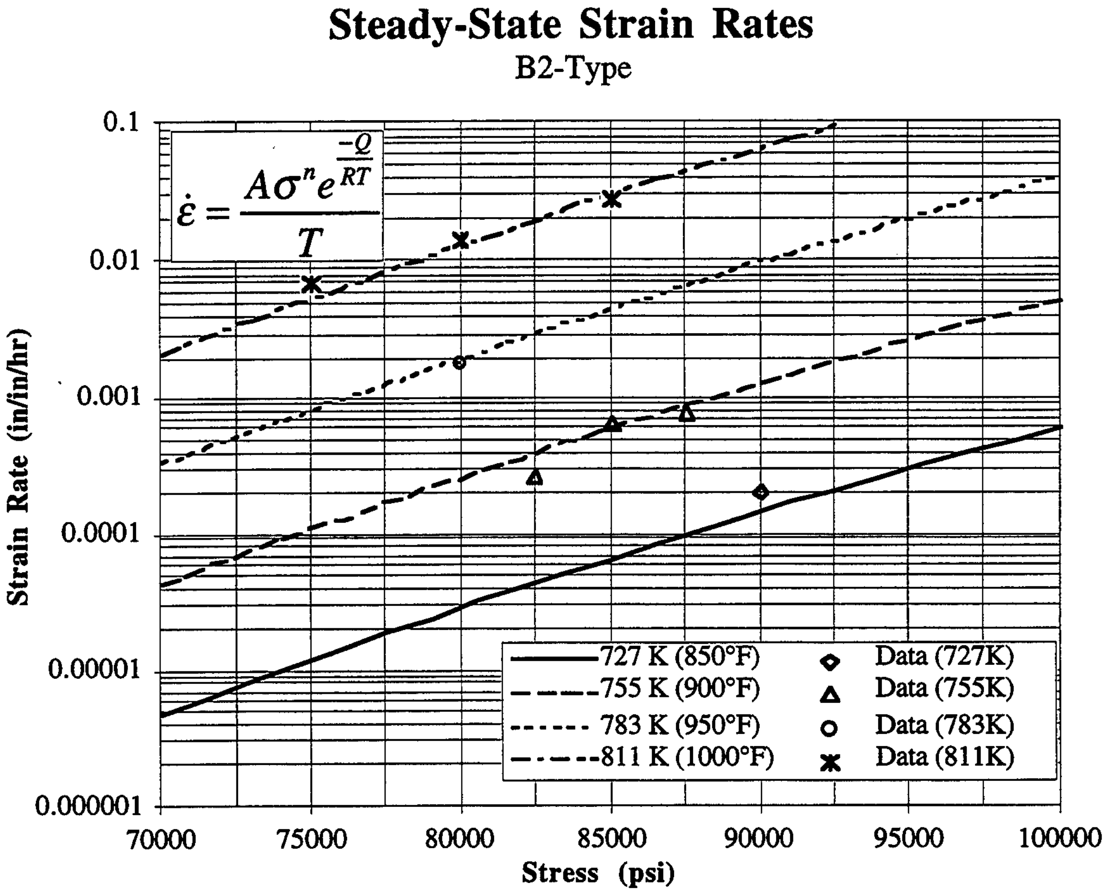

Figure 4.44 Predicted and Actual Steady-State Strain Rates Corresponding to the Second Linear Portion of Type-B Creep Behavior of a HA50HS Specimen as a Function of Applied Stress and Temperature.

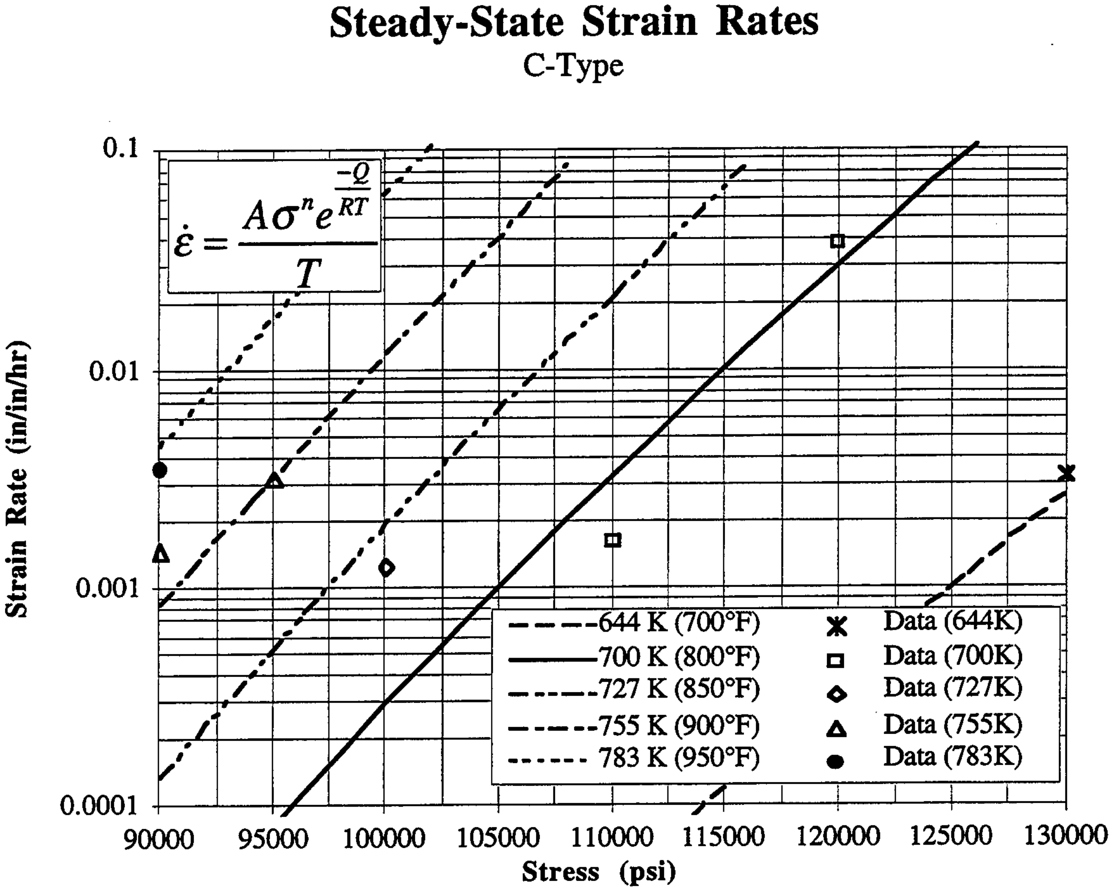

Figure 4.45 Predicted and Actual Steady-State Strain Rates Corresponding to Type-C Creep Behavior of a HA50HS Specimen as a Function of Applied Stress and Temperature.

equations. The activation energy value is not surprising. The high strain rates resulting from such high stresses require a low value for the activation energy. The high stress exponent is indicative of a large dependence on applied stress and the very small kinetic factor is needed to counter the large stress influence.

A comparison of the creep constants and statistical data for each of the four steady-state responses is needed to help understand the possible deformation mechanisms. A consolidation of this data is shown in Table 4.2. The Type-A response correlates very well to creep data published by Stoloff and Davies for a very similar material [37]. This traditional response is well represented by the power law relations between stress and steady-state strain rate of the form of Equation 1.11. The near perfect coefficient of determination and the other regression statistics are also strong indications of an appropriate model.

The regression analysis of the Type-B1 responses show about the same activation energy as determined for the Type-A responses. The stress exponent, however, is more than twice the value associated with the lower strain rate, Type-A, response. Again, the near perfect coefficient of determination and other statistical values indicate an appropriately configured model.

The nearly coincident activation energies of the Type-A and B1 responses led to speculation that perhaps the same deformation mechanism was dominant in each of the responses. Hence, the data from both responses were combined into another regression analysis. An activation energy of 95,501 cal/mol was calculated along with a stress exponent of 4.06. The kinetic factor, A, was determined to be approximately 5.28×10^5. With these new creep constants, Equation 1.11 is plotted for constant temperatures in Figure 4.46. The actual data are also plotted and closely follow the predicted strain rates. The r^2 value for this estimation is 0.990 and the F-statistic is calculated to be about 763. The critical value of $F_{0.01}$ is only 6.23. Therefore, the close correlation between actual and predicted strain rates implies a high degree of usefulness of the corresponding model.

The statistics from this combined data set show a slight degradation in accuracy of the model from the two separate sets of variables, which suggests that there is indeed a difference between the deformation regimes. It is speculated that the nearly equal activation energies suggest only a slight dependency on test temperature while the high stress

Table 4.2 Creep Constants and Statistical Values for HA50HS as Determined by Multiple Linear Regression Analysis.

Creep Type	Q (cal/mol)	n	A $\left(\frac{K}{hr\,(psi)^n}\right)$	r^2	F-Statistic	$F_{0.01}$
A	98,851	3.83	4.94E(7)	0.995	749.1	9.95
B1	99,318	8.49	1.06E(-15)	0.998	1119	10.92
B2	87,259	13.54	1.02E(-42)	0.985	164.8	13.27
C	72,596	25.33	1.56E(-105)	0.913	26.2	13.27
AB1	95,329	4.02	7.21E(5)	0.990	793.4	6.23

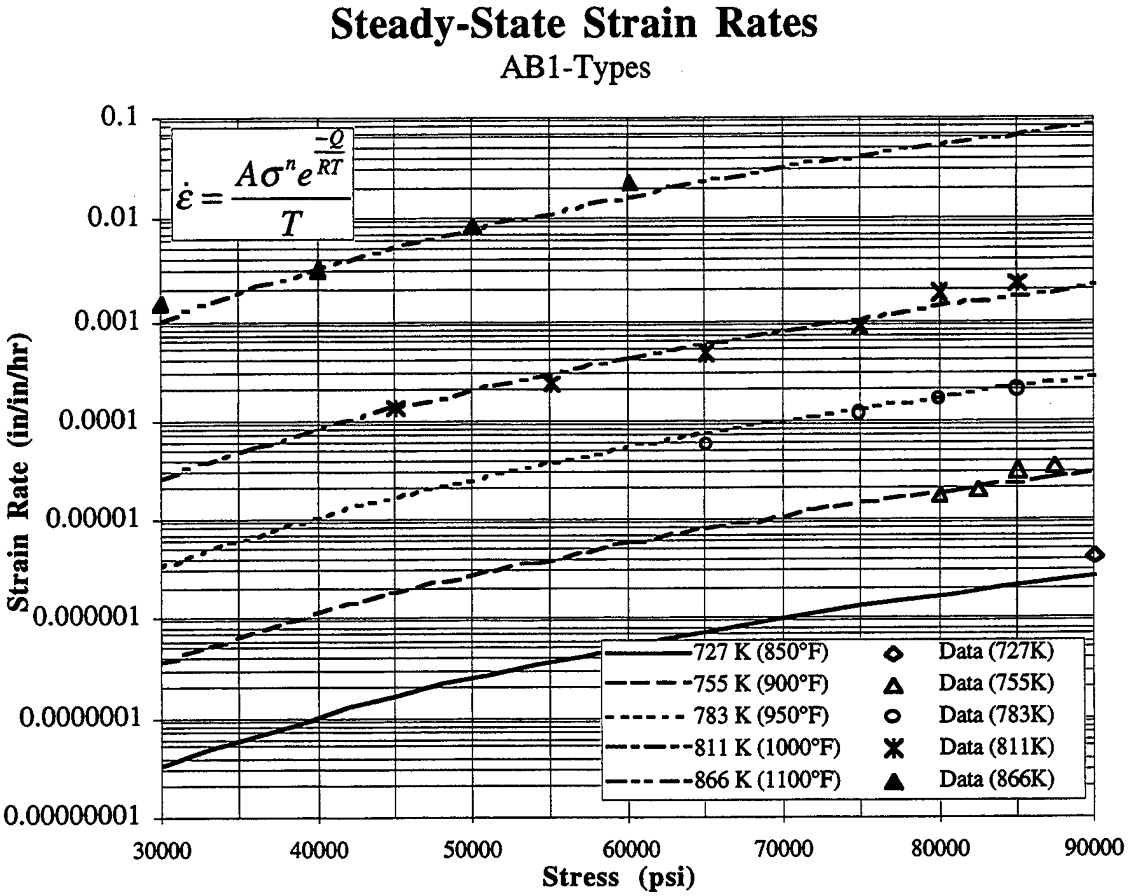

Figure 4.46 Predicted and Actual Steady-State Strain Rates Corresponding to a Consolidation of Type-A and the First Linear Portion of Type-B Creep Behaviors of a HA50HS Specimen as a Function of Applied Stress and Temperature.

exponent of the Type-B1 deformation suggests a much larger dependency on stress. This speculation is supported by the fact that the Type-A stress levels are all below the lower yield strengths while the Type-B1 stress levels are all between the maximum and minimum serration stress levels. It is therefore concluded that creep tests conducted below the lower yield strength should not be modeled with tests conducted above this level.

4.3.2 Power Law Breakdown

The use of Equation 1.11 implies the activation energy, stress exponent, and kinetic factor are all constant throughout the regime of interest. Large ranges of temperature and especially stresses often result in the crossing from one deformation mechanism to another. It is these intermechanism ranges that often cause discrepancies in predictive relations. Many of the creep tests conducted under this study involved stresses near or above the corresponding yield strengths. This regime of deformation usually depicts a breakdown of the power law relations between stress and strain rate and often requires a totally new expression to predict creep behavior.

The power-law expression, used in the regression analyses, is used with the assumption that the stress exponent, the kinetic factor, and the activation energy all remain constant throughout the range of modeled conditions. This assumption is not always valid and the power-law relation sometimes breaks down. At high stresses, above about 10^{-3} of the shear modulus of a material, the measured strain rates are typically above those predicted by power-law expressions [63]. An attempt to model too large a temperature range may also lead to invalid predictions and erroneous strain rates. Various empirical relationships have been developed in order to predict strain rates spanning many orders of magnitude and crossing multiple deformation mechanism boundaries [90]. One such equation, suggested by Jonas et al. [91] and Garafalo [92], and discussed briefly by Hosford and Caddell [93] is:

$$\dot{\varepsilon} = A[\sinh(\alpha\sigma)]^{\frac{1}{m}} e^{\frac{-Q}{RT}}, \tag{4.7}$$

where $\frac{1}{m}$ is a measure of the stress sensitivity and is equivalent to the stress exponent, n. The stress factor, α, is related to the activation volume, which appears in the original rate equation analyses. The product of the activation volume, v, and stress, σ, represents the energy (e.g., N*m=J) required to overcome a stress-influenced thermal activation barrier. The probability of overcoming such a barrier, according to classical rate theory, would be:

$$\text{probability} \propto (e^{\frac{v\sigma}{kT}} - e^{-\frac{v\sigma}{kT}}) \tag{4.8}$$

where v equals the activation volume, σ is the applied stress, k is Boltzmann's constant, and T is the absolute temperature [65]. It can be seen that the right hand side of Equation 4.8 is twice $\sinh(\frac{v\sigma}{kT})$; hence, the variable α is related to, or perhaps even equal to $\frac{v}{kT}$. Even though this quantity is a function of both temperature and the mechanism of deformation (the latter through the specific value of v), in practice it is nonetheless treated as a constant with typical values of 1×10^{-3} for many engineering alloys [65]. This value for α has been used in the present study.

The utility of the relation described by Equation 4.7 is its applicability to a wide range of applied stresses. For relatively low stresses, $\sinh(\alpha\sigma) \approx \alpha\sigma$; therefore,

$$\dot{\varepsilon} = A(\alpha\sigma)^n e^{-\frac{Q}{RT}} \tag{4.9}$$

Equation 4.9 is simply the creep equation with the α term separated out of the kinetic factor, A. When modeling relatively high stresses, Equation 4.7 can be reduced to:

$$\dot{\varepsilon} = A' e^{\alpha\sigma n'} e^{-\frac{Q}{RT}}, \tag{4.10}$$

where A' is equal to half of A and n' is equal to $\frac{1}{m}$ from Equation 4.7. Equation 4.10 indicates a strong rate sensitivity on stress.

It is speculated that the high stresses and the relatively high strain rates corresponding to the Type B-2 and Type-C creep deformations would be more appropriately represented by the steady-state strain rate relation governed by Equation 4.7. A double linear regression analysis was conducted on the Type-B-2 and Type-C data in order to fit Equation 4.7. First, the relation is manipulated into the following form:

$$\ln \dot{\varepsilon} = \ln A + \frac{1}{m}\ln[\sinh(\alpha\sigma)] - \frac{Q}{RT}. \qquad (4.11)$$

The regression analysis of the Type-B2 data resulted in a value for m of 5.95 and an activation energy of 86,355 cal/mol. Also, the kinetic factor, A, is approximately 2.85 x 10^{15}. The corresponding statistical analysis resulted in a value for the coefficient of determination of 0.987 and an F-statistic of 185. The critical $F_{0.01}$ value for this data set is only 10.92. The Type-C analysis provided similar results with a value for m of 4.15, an activation energy of 72,643 cal/mol, and a kinetic factor of 3.11 x 10^{8}. The coefficient of determination and the F-statistic are 0.945 and 43.0 respectively. Again, the critical $F_{0.01}$ for the Type-C data set is about 13.27. Although both types of deformation appear to be well characterized by the resulting constants, the statistical data implies that the Type-B2 is actually a better representation. The predicted strain rates and the actual data are illustrated in Figures 4.47 and 4.48.

4.4 Microstructural Analysis

Microstructural investigations were conducted on three different creep specimens. As can be seen, and compared in Figures 4.16 and 4.27, a decrease of only 10 ksi resulted in a creep life increase of more than twenty times. A decrease of only 50°F resulted in a creep life increase of nearly seventeen times. Initially, after conducting only a few creep tests, it was thought that a behavioral threshold existed between 800°F and 850°F at a stress level of 100 ksi. Also, a threshold was anticipated between 100 ksi and 110 ksi at a temperature of 800°F. The relatively small changes in the test parameters resulted in significant changes in creep life. An SEM was used to examine and compare the microstructures of these three specimens. All of the SEM micrographs showed very similar microstructures characterized as having fine equiaxed grains on the order of 2 microns in diameter. The micrograph of the specimen tested at 110 ksi and 800°F is typical of the three samples, and is shown in

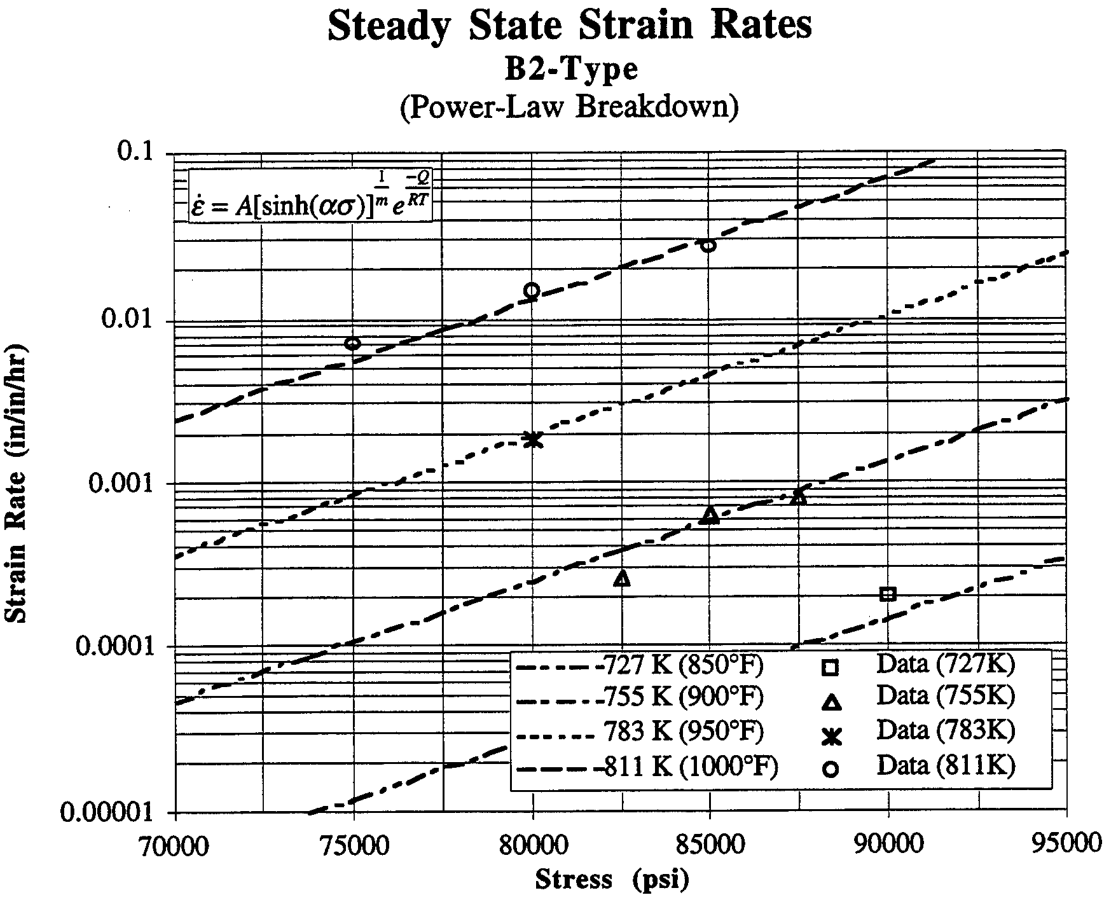

Figure 4.47 Predicted and Actual Steady-State Strain Rates Corresponding to Type-B2 Creep Behavior in the Power-Law Breakdown Regime of a HA50HS Specimen.

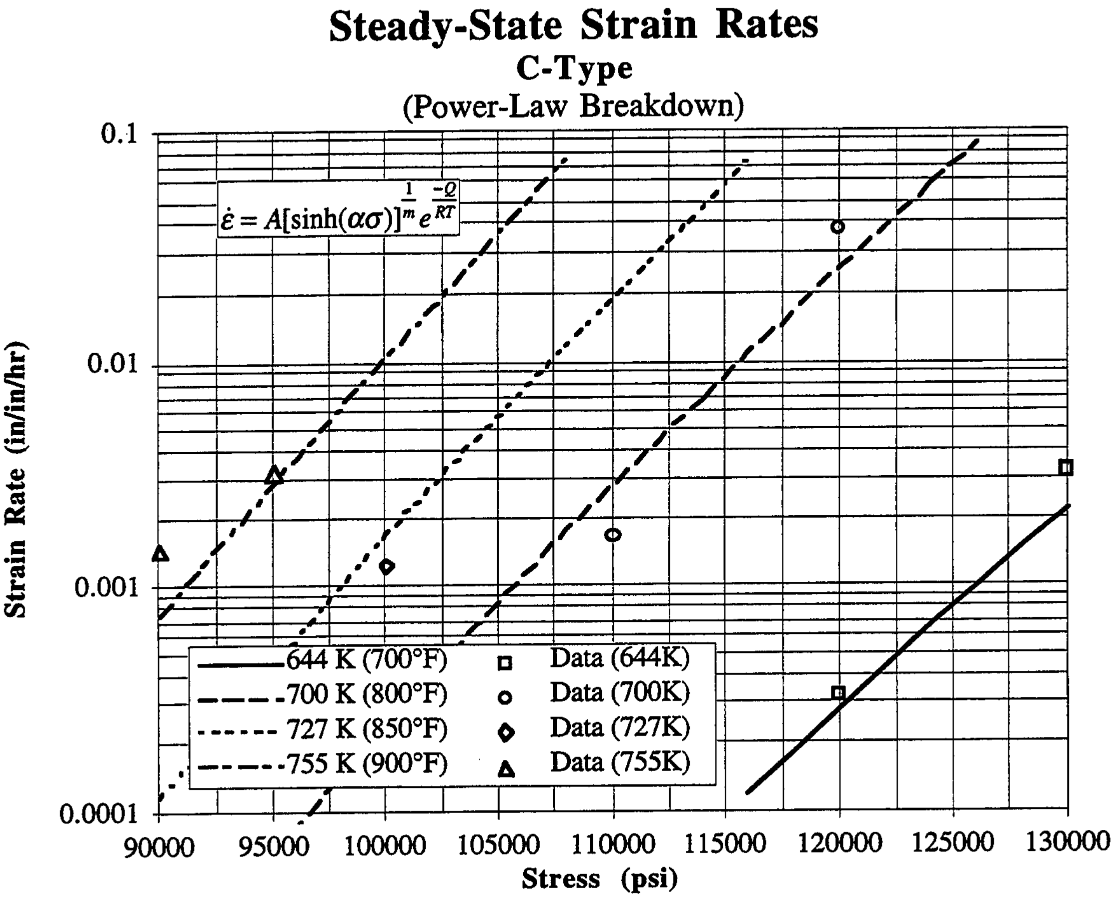

Figure 4.48 Predicted and Actual Steady-State Strain Rates Corresponding to Type-C Creep Behavior in the Power-Law Breakdown Regime of a HA50HS Specimen.

Figures 4.49 and 4.50. Also apparent in all of the samples are finely dispersed precipitates thought to be an HCP Laves phase of $Nb(Fe,Co)_2$. These precipitates are located along the grain boundaries as well as within the grains. As mentioned in Chapter 2, the niobium constituent is included to act as a grain refiner in order to increase the mechanical strength. The SEM findings show some of the grain boundaries bending around some of the precipitates, which indicates a pinning action, thus validating the grain refinement intent.

With the completion of a greater portion of the creep test matrix, it is more apparent that the natural deformation thresholds occur as a function of the proximity to yield stress. This relationship is discussed in Section 4.3 and illustrated in Figure 4.41. All three of the specimens examined with the SEM were in the Type-C regime. In retrospect, it is not surprising that all three were characterized by very similar post-deformation microstructures. Perhaps a better microstructural investigation would include four specimens, each identified as one of the four types of creep deformation: Types A, B1, B2, and C.

4.5 X-Ray Diffraction Analysis

In an attempt to support the speculation that the abrupt increase in the steady-state creep strain rate is caused by disordering of the atomic structure, X-ray diffraction testing was conducted on creep tested specimens. Two specimens were tested at 1000°F with an applied constant load of 80 ksi. The first specimen was tested for about 3.7 hours and is described as the post-knee specimen. The initial steady-state strain rate was approximately 1.9×10^{-3} in/in/hr and ended at about 2.2 hours with a sudden increase in strain rate to nearly 2.4×10^{-2} in/in/hr. The specimen was unloaded at a creep strain of nearly 7%. The second specimen was tested for only 1.5 hours when it was unloaded, prior to reaching the knee in the curve. The final creep strain attained by this specimen was only 0.3%. As expected, the measured steady-state strain rate was approximately 1.9×10^{-3} in/in/hr. This specimen is referenced as the pre-knee specimen.

To properly use X-ray diffraction as an indication of atomic ordering an understanding of the possible crystal structures is necessary. The X-ray diffraction technique is thoroughly explained by Cullity [94]. As described in Chapter 2 of this document, the HA50HS material used in this study possesses a B2 crystal structure when in the ordered state. In the disordered state this alloy is characterized as having a body-centered-cubic (BCC) crystal structure. The B2 structure, as illustrated in Figure 2.1, is not a BCC structure. The different atom in the center of a cubic acts as a corner atom of the cubic structure of the

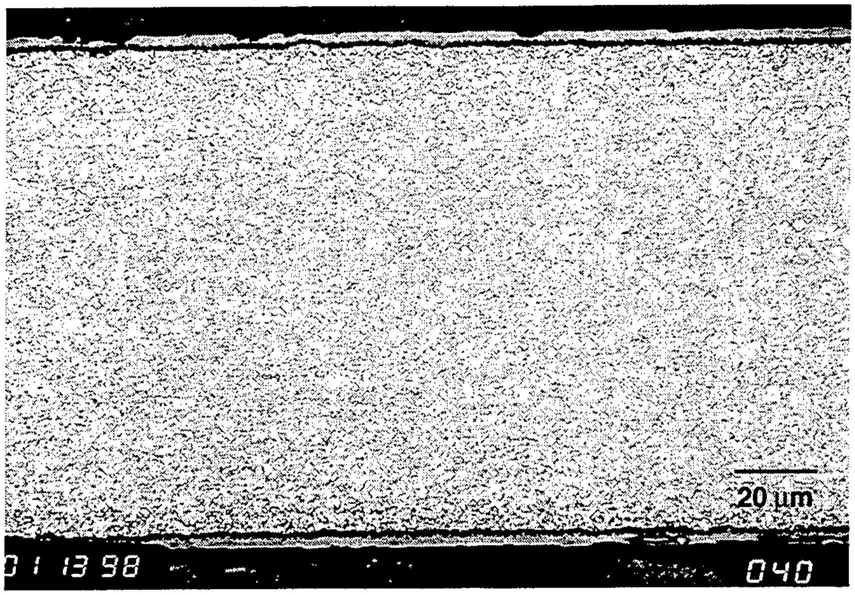

(a)

(b)

Figure 4.49 Optical Micrographs of a HA50HS Creep Specimen Tested at 110 ksi and 800°F in the 45 Degree Orientation to the Rolling Direction: (a- 500x, b-1000x).

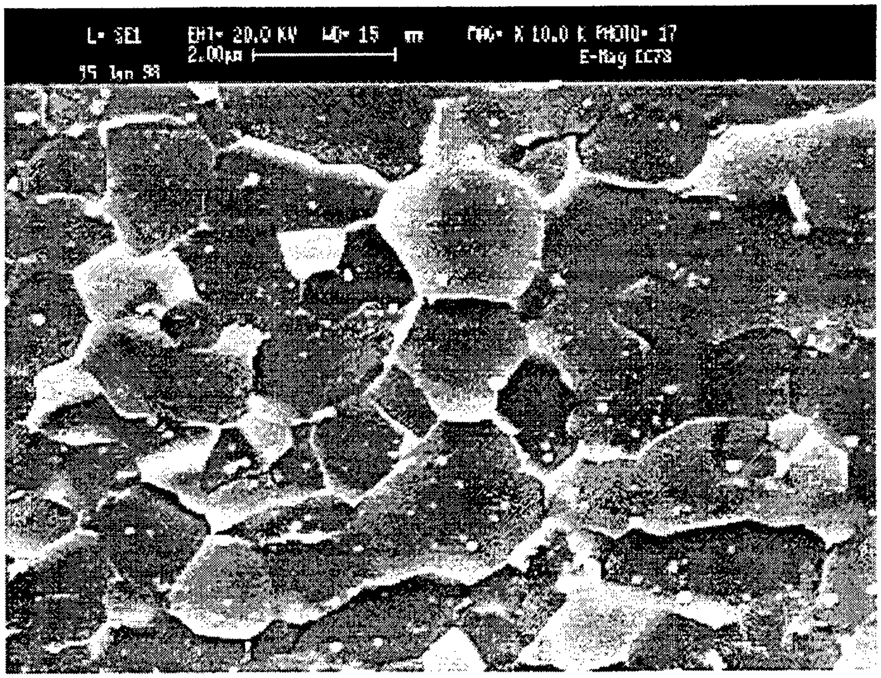
L= SE1
EHT= 20.0 KV
WD= 15 mm
MAG= X 10.0 K
PHOTO= 17
2.00µm
E-Mag CC78
15 Jan 98

Figure 4.50 SEM Micrograph (10,000x) of a HA50HS Creep Specimen Tested 110 ksi and 800°F in the 45 Degree Orientation to the Rolling Direction.

companion element. Hence, a B2 structure is simple cubic and should generate X-ray reflections accordingly.

X-ray reflections of a simple cubic structure should be detectable off of every possible plane as shown in Table 4.3. The BCC structure, however, does not reflect off of every plane. Reflections off of the odd planes (those planes where the indices sum to an odd number) are canceled out due to destructive interference. Bragg's law is used to determine the location of the reflection peaks in the form of :

$$2d\sin\theta = \lambda; \tag{4.12}$$

where: θ = diffraction angle, λ = wavelength, and d = atomic spacing.

The wavelength used is that of the X-ray generated by a specific source. A wavelength of 1.54178 Angstroms corresponds to the K_α radiation generated by the copper source used in this study. The atomic spacing is defined for a cubic lattice as:

$$d = \frac{a}{\sqrt{h^2 + k^2 + l^2}}; \tag{4.13}$$

where: a is the lattice parameter, and h, k, and l are diffraction indices.

A lattice parameter of 2.8664 Angstroms, which describes iron, was used in this analysis. The reflected angle measured by the X-ray diffractometer is twice the angle of Bragg's law, therefore Table 4.3 provides 2θ angles which correspond to specific planes. An estimate of the ordering parameter can be made from the ratio of the peak intensities of the (200) reflection over the (100) reflection. Since these two planes are parallel, any crystallographic texture will have identical contributions to peak intensities and, therefore, will be inconsequential.

Since the specimens were annealed to instill ordering, it was anticipated that the post-knee specimen would be disordered or, at least, indicate a lessor degree of ordering than the pre-

Table 4.3 Calculated X-Ray Diffraction Peak Locations.

B2 (Simple Cubic) Structure		BCC Structure	
(h, k, l)	2θ (degrees)	(h, k, l)	2θ (degrees)
(1, 0, 0)	31.20	(1, 1, 0)	44.71
(1, 1, 0)	44.71	(2, 0, 0)	65.08
(1, 1, 1)	55.52	(2, 1, 1)	82.41
(2, 0, 0)	65.08	(2, 2, 0)	99.05
(2, 1, 0)	73.94	(3, 1, 0)	116.52
(2, 1, 1)	82.41	(2, 2, 2)	137.38
(2, 2, 0)	99.05		
(2, 2, 1)	107.57		
(3, 0, 0)	107.57		
(3, 1, 0)	116.52		
(3, 1, 1)	126.24		
(2, 2, 2)	137.38		

knee specimen. Unfortunately, the X-ray diffraction scans did not provide conclusive evidence. A scan from 2θ angles of 25 to 90 degrees should have resulted in six peaks for the B2 ordered structure and only three peaks if the specimens were disordered. Both pre-knee and post-knee scans provided at least 18 separate peaks. It is speculated that the oxides developed during the oxidation and testing of the specimens are the cause for all of the extra peaks. Also, a recent investigation of the aging effects of Hiperco® Alloy 50 has shown that the ordering parameter actually increases with time at elevated temperatures [95]. This finding challenges the speculation of an atomic disordering phenomenon being the cause of the increase in strain rate. Due to the limited access of the X-ray diffractometer and the uncertainty of detectable ordered peak intensities, additional X-ray diffraction tests were not pursued in this study.

Chapter 5. Research Application

The ultimate goal of this research effort is to impact the designs and manufacturing processes of switched reluctance starter/generator rotor laminates. A component failure due to creep deformation may be avoided if a designer has an understanding of not only material properties, but also the mode of loading, the failure criterion, and the optimization objective [96]. The investigation of the soft magnetic alloy resulted in a set of constants that describe the creep behavior of the uniaxial test specimen. In order to effectively utilize this data and associated predictive methodologies, a mechanics analysis must be done for the specific application of interest. This chapter includes an elastic deformation analysis for four different sets of boundary conditions that may be applied to the rotor configuration shown in Figure 5.1. It also includes an analysis and discussion pertaining to power law creep deformation for one of the possible rotor configurations.

The elasticity problem consists of determining the stress and displacement profiles in an elastic body subjected to surface forces, surface displacements, and body forces. At each point within the elastic body there exists a state of stress which is defined by six components. Requiring each point to be in equilibrium provides for three equations, which is not enough to obtain a solution. In order to solve the elasticity problem six stress-strain relations and six strain-displacement relations are introduced along with the three equilibrium equations. These fifteen equations are now sufficient to solve for the fifteen stress, strain, and displacement unknowns. It is also possible to place restrictions on the strain-displacement relations in order to obtain a solution to the six partial differential equations. The imposed restrictions are known as the compatibility conditions. If the compatibility and equilibrium conditions can be satisfied, then a solution may be obtained for the desired stresses and displacements.

5.1 Equilibrium Element

In order to determine the appropriate governing equations, the equilibrium condition must be examined for an element of a constant thickness, rotating disk subjected to radial and tangential stresses. This equilibrium element is depicted in Figure 5.2. Let the stress vectors acting on the faces *OADE*, *OGFE*, and *OABG* be denoted by σ_{y_1}, σ_{y_2}, and σ_{y_3}, respectively.

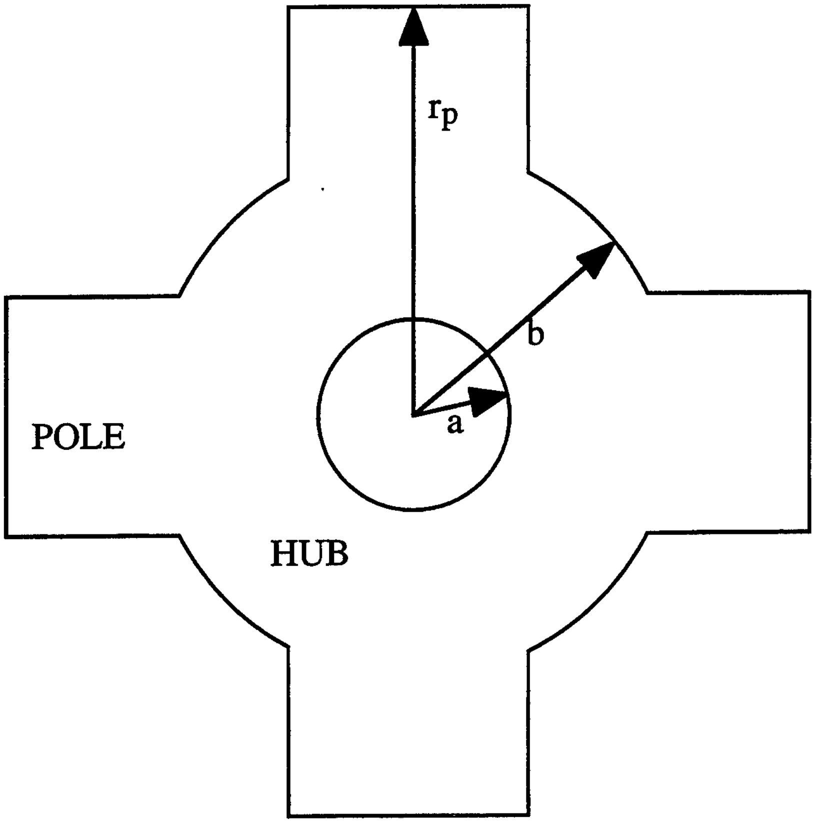
r_p
b
a
POLE
HUB

Figure 5.1 Possible Integrated Power Unit Rotor Geometry.

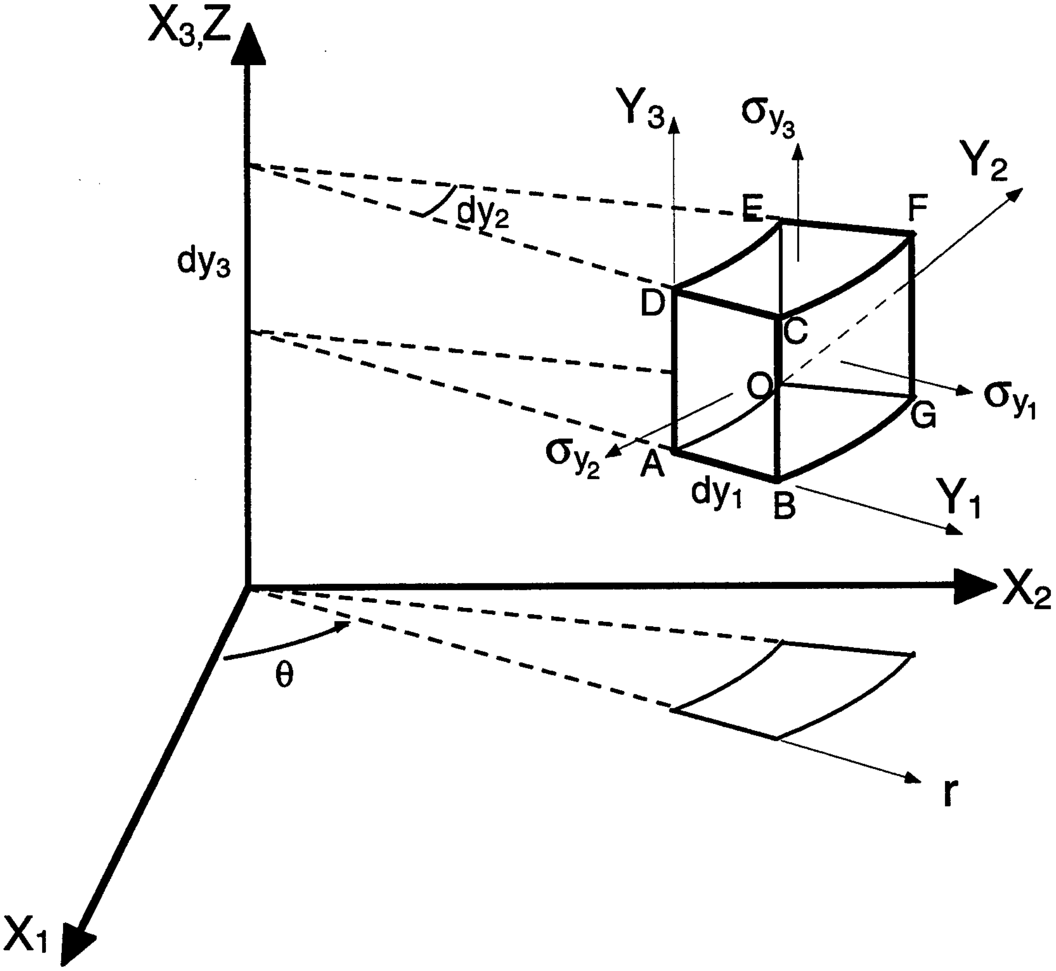
X3,Z
Y3
σy3
Y2
E
F
dy2
dy3
D
C
O
σy1
G
σy2
A
dy1
B
Y1
X2
θ
r
X1

Figure 5.2 Equilibrium Element of a Constant Thickness, Rotating Disk Subjected to Radial and Tangential Stresses.

The force acting on face *BCFG* of the differential element is described as the total stress acting on the face in the y_1 direction times the area of the face. The total stress, then, is the stress vector in that direction plus the change in the y_1 stress with respect to the y_1 direction times the length of the element in the y_1 direction. The area of the face is simply the area, which incorporates the scale factors required for the coordinate transformation, plus the change in area with respect to the y_1 direction times the length of the element in that direction. The force is perhaps better described in the following equation form.

$$F_{BCFG} = \left[\sigma_{y_1} + \frac{\partial \sigma_{y_1}}{\partial y_1} dy_1\right]\left[h_2 h_3 dy_2 dy_3 + \frac{\partial}{\partial y_1}(h_2 h_3) dy_2 dy_3 dy_1\right] \qquad (5.1)$$

Carrying out the multiplication of the right hand side of Equation 5.1 expands it to:

$$\sigma_{y_1} h_2 h_3 dy_2 dy_3 + \sigma_{y_1} \frac{\partial}{\partial y_1}(h_2 h_3) dy_1 dy_2 dy_3 + h_2 h_3 \frac{\partial \sigma_{y_1}}{\partial y_1} dy_1 dy_2 dy_3 + \frac{\partial \sigma_{y_1}}{\partial y_1} \frac{\partial (h_2 h_3)}{\partial y_1} (dy_1)^2 dy_2 dy_3 . \qquad (5.2)$$

The last term in the above expression is a fourth order term and infinitesimal; therefore, it is negligible. The second and third terms may be combined to reduce Equation 5.1 to:

$$F_{BCFG} = \sigma_{y_1} h_2 h_3 dy_2 dy_3 + \frac{\partial}{\partial y_1}\left(\sigma_{y_1} h_2 h_3\right) dy_1 dy_2 dy_3 . \qquad (5.3)$$

Since the outward force on face *BCFG* was taken to be positive, the outward force on the opposite face *OADE* must be negative and is simply described as:

$$F_{OADE} = -\sigma_{y_1} h_2 h_3 dy_2 dy_3 . \qquad (5.4)$$

The same steps can be repeated to determine the forces on the remaining four faces of the element. The elemental body force vector is $Fh_1h_2h_3dy_1dy_2dy_3$ and the elemental inertia force vector is $A\rho h_1h_2h_3dy_1dy_2dy_3$.

The summation of all of the forces acting on the element becomes the equilibrium equation as written below:

$$\begin{aligned}\frac{\partial}{\partial y_1}(\sigma_{y_1}h_2h_3)dy_1dy_2dy_3+\frac{\partial}{\partial y_2}(\sigma_{y_2}h_1h_3)dy_1dy_2dy_3+\frac{\partial}{\partial y_3}(\sigma_{y_3}h_1h_2)dy_1dy_2dy_3\\+Fh_1h_2h_3dy_1dy_2dy_3-A\rho h_1h_2h_3dy_1dy_2dy_3=0.\end{aligned}\tag{5.5}$$

Each one of the stress vectors $\sigma_{y_1},\sigma_{y_2},\sigma_{y_3}$ can be written in terms of its corresponding components along the y_1,y_2,y_3 axes as:

$$\begin{aligned}\sigma_{y_1}&=e_1\sigma_{11}+e_2\sigma_{12}+e_3\sigma_{13}\\\sigma_{y_2}&=e_1\sigma_{21}+e_2\sigma_{22}+e_3\sigma_{33}\\\sigma_{y_3}&=e_1\sigma_{31}+e_2\sigma_{32}+e_3\sigma_{33}\end{aligned}\tag{5.6}$$

where σ_{ij} is the stress component acting on a plane normal to the y_i axis and aligned with the y_j direction.

By substituting these expressions for the stress vectors into the equilibrium equation, the following expression is derived:

$$\begin{aligned}\frac{\partial}{\partial y_1}[h_2h_3(e_1\sigma_{11}+e_2\sigma_{12}+e_3\sigma_{13})]+\frac{\partial}{\partial y_2}h_1h_3(e_1\sigma_{21}+e_2\sigma_{22}+e_3\sigma_{33})]+\\\frac{\partial}{\partial y_3}h_1h_2(e_1\sigma_{31}+e_2\sigma_{32}+e_3\sigma_{33})]+(F-A\rho)h_1h_2h_3=0.\end{aligned}\tag{5.7}$$

Now, by expanding the partial derivatives in Equation 5.7 and then factoring out the unit vectors, e_1, e_2, and e_3, the following independent expressions are revealed:

$$\begin{aligned}&\frac{\partial}{\partial y_1}(\sigma_{11}h_2h_3)+\frac{\partial}{\partial y_2}(\sigma_{21}h_1h_3)+\frac{\partial}{\partial y_3}(\sigma_{31}h_1h_2)+\sigma_{12}h_3\frac{\partial h_1}{\partial y_2}+\\&\sigma_{13}h_2\frac{\partial h_1}{\partial y_3}-\sigma_{22}h_3\frac{\partial h_2}{\partial y_1}-\sigma_{33}h_2\frac{\partial h_3}{\partial y_1}+h_1h_2h_3(F_1-A_1\rho)=0\end{aligned} \tag{5.8a}$$

$$\begin{aligned}&\frac{\partial}{\partial y_1}(\sigma_{12}h_2h_3)+\frac{\partial}{\partial y_2}(\sigma_{22}h_1h_3)+\frac{\partial}{\partial y_3}(\sigma_{32}h_1h_2)+\sigma_{23}h_1\frac{\partial h_2}{\partial y_3}+\\&\sigma_{21}h_3\frac{\partial h_2}{\partial y_1}-\sigma_{33}h_1\frac{\partial h_3}{\partial y_2}-\sigma_{11}h_3\frac{\partial h_1}{\partial y_2}+h_1h_2h_3(F_2-A_2\rho)=0\end{aligned} \tag{5.8b}$$

$$\begin{aligned}&\frac{\partial}{\partial y_1}(\sigma_{13}h_2h_3)+\frac{\partial}{\partial y_2}(\sigma_{23}h_1h_3)+\frac{\partial}{\partial y_3}(\sigma_{33}h_1h_2)+\sigma_{31}h_2\frac{\partial h_3}{\partial y_1}+\\&\sigma_{32}h_1\frac{\partial h_3}{\partial y_2}-\sigma_{11}h_2\frac{\partial h_1}{\partial y_3}-\sigma_{22}h_1\frac{\partial h_2}{\partial y_3}+h_1h_2h_3(F_3-A_3\rho)=0\end{aligned} \tag{5.8c}$$

In order to obtain the equilibrium equations in a more applicable form for a rotating disk analysis a coordinate transformation to a cylindrical (r,θ,z) coordinate system must be done. A transformation from the Cartesian coordinate system to any other system requires functional relations between the two. For this particular transformation the relations are illustrated as a projection of the equilibrium element onto the X_1X_2 plane as shown in Figure 5.2 and described as follows:

$$\begin{aligned}y_1&=r\cos\theta,\\y_2&=r\sin\theta,\\y_3&=z.\end{aligned}$$

By definition the squares of the scale factors for each coordinate system are equal. Hence,

$$h_1^2 = h_r^2 = (\frac{\partial x}{\partial r})^2 + (\frac{\partial y}{\partial r})^2 + (\frac{\partial z}{\partial r})^2 = \cos^2\theta + \sin^2\theta + 0 = 1 \Rightarrow h_1 = 1,$$

$$h_2^2 = h_\theta^2 = (\frac{\partial x}{\partial \theta})^2 + (\frac{\partial y}{\partial \theta})^2 + (\frac{\partial z}{\partial \theta})^2 = (-r\sin\theta)^2 + (r\cos\theta)^2 + 0 = r^2 \Rightarrow h_2 = r,$$

$$h_3^2 = h_z^2 = (\frac{\partial x}{\partial z})^2 + (\frac{\partial y}{\partial z})^2 + (\frac{\partial z}{\partial z})^2 = 0 + 0 + 1 = 1 \Rightarrow h_3 = 1.$$

To carry out the transformation the following substitutions are made into the three independent equilibrium expressions, Equation 5.8, as shown below.

$$\begin{array}{lll} 1 \rightarrow r & \partial y_1 \rightarrow \partial r & h_1 = 1 \\ 2 \rightarrow \theta & \partial y_2 \rightarrow \partial \theta & h_2 = r \\ 3 \rightarrow z & \partial y_3 \rightarrow \partial z & h_3 = 1 \end{array}$$

$$\frac{\partial}{\partial r}(\sigma_{rr} r) + \frac{\partial}{\partial \theta}\sigma_{\theta r} + \frac{\partial}{\partial z}(\sigma_{zr}) + 0 + 0 - \sigma_{\theta\theta} - 0 + r(F_r - A_r \rho) = 0$$

$$\frac{\partial}{\partial r}(\sigma_{r\theta} r) + \frac{\partial}{\partial \theta}\sigma_{\theta\theta} + \frac{\partial}{\partial z}(r\sigma_{z\theta}) + 0 + 1 - 0 - 0 + r(F_\theta - A_\theta \rho) = 0$$

$$\frac{\partial}{\partial r}(\sigma_{rz} r) + \frac{\partial}{\partial \theta}\sigma_{\theta z} + \frac{\partial}{\partial z}(\sigma_{zz} r) + 0 + 0 - 0 - 0 + r(F_z - A_z \rho) = 0$$

These equilibrium expressions can now be simplified to their final form. From this point, the elemental inertia force terms are neglected.

$$\frac{\partial \sigma_{rr}}{\partial r} + \frac{1}{r}\frac{\partial \sigma_{\theta r}}{\partial \theta} + \frac{\partial \sigma_{zr}}{\partial z} + \frac{1}{r}(\sigma_{rr} - \sigma_{\theta\theta}) + F_r = 0 \qquad (5.9a)$$

$$\frac{\partial \sigma_{r\theta}}{\partial r} + \frac{1}{r}\frac{\partial \sigma_{\theta\theta}}{\partial \theta} + \frac{\partial \sigma_{z\theta}}{\partial z} + \frac{2}{r}\sigma_{\theta r} + F_\theta = 0 \qquad (5.9b)$$

$$\frac{\partial \sigma_{rz}}{\partial r} + \frac{1}{r}\frac{\partial \sigma_{\theta z}}{\partial \theta} + \frac{\partial \sigma_{zz}}{\partial z} + \frac{1}{r}\sigma_{rz} + F_z = 0 \qquad (5.9c)$$

The IPU rotor geometry may be analyzed by considering a thin disk of uniform thickness rotating with a constant angular velocity. The assumptions of plane elasticity and circular symmetry imply $F_z = 0$ and that Equation 5.9c is identically satisfied. For this analysis the resulting centrifugal force is treated as the body force in the radial direction. The body force in the radial direction for a rotating disk is given as:

$$F_r(r) = \rho\omega^2 r.$$

Since the rotation of the rotor is at a constant angular velocity, $F_\theta = 0$. Also, due to the assumption of circular symmetry and plane elasticity conditions, $\frac{\partial\sigma_{\theta\theta}}{\partial\theta} = 0$. The remaining equilibrium equation can now be written as:

$$\frac{d\sigma_{rr}}{dr} + \frac{1}{r}(\sigma_{rr} - \sigma_{\theta\theta}) + \rho\omega^2 r = 0; \qquad (5.10)$$

Since the derivation of this equilibrium equation did not involve material properties, it is then applicable to both elastic and plastic deformation analyses.

5.2 Estimation of Elastic Deformation of an Integrated Power Unit Rotor Laminate

To properly conduct an elastic analysis, boundary conditions must be satisfied such that the stresses and displacements due to the external influences are coincident with the body surface values. There are three variations of boundary conditions possible. The first problem is one with known body forces and prescribed surface forces. The second problem is one with known body forces and prescribed surface displacements. The third type of problem is one with a mixture of boundary conditions, such as: prescribed displacements on one boundary and prescribed stresses on another. The boundary conditions included in the following elastic analysis are of the first and third types.

The relevant compatibility equation is known as the Beltrami-Michell [97] equation and is expressed as:

$$(\frac{d^2}{dr^2}+\frac{1}{r}\frac{d}{dr})(\sigma_{rr}+\sigma_{\theta\theta})=-(1+k_2)(\frac{dF_r}{dr}+\frac{F_r}{r}); \tag{5.11}$$

where k_2 is as defined below [98]. Note that the first terms in parentheses are simply the Laplacian operator expressed in orthogonal curvilinear coordinates.

This analysis is done in such a way that both plane strain and plane stress conditions may be evaluated. Terms identified as k_1 and k_2 are used throughout the derivations and may be replaced by elastic quantities as indicated below.

$$\text{For plane stress conditions: } k_1=\frac{1}{E} \text{ and } k_2=\nu.$$

$$\text{For plane strain conditions: } k_1=\frac{1-\nu^2}{E} \text{ and } k_2=\frac{\nu}{1-\nu}.$$

E is the modulus of elasticity and ν is Poisson's ratio of the material. Equations 5.10 and 5.11 are rewritten to better prepare for the subsequent manipulations. Equation 5.10 is transformed to:

$$\frac{1}{r^2}\frac{d}{dr}(r^2\sigma_{rr})=\frac{1}{r}(\sigma_{rr}+\sigma_{\theta\theta})-F_r. \tag{5.12}$$

Equation 5.11 is manipulated to:

$$\frac{1}{r}\frac{d}{dr}\{r[\frac{d}{dr}(\sigma_{rr}+\sigma_{\theta\theta})+(1+k_2)F_r]\}=0. \tag{5.13}$$

Now, integrating Equation 5.13 with respect to r results in the following relation:

$$\sigma_{rr} + \sigma_{\theta\theta} = A \ln r + B - (1 + k_2) \int_{r_o}^{r} F_r(\xi) d\xi, \qquad (5.14)$$

where r_o is defined as a fixed value of r (inner radius), and A and B are constants of integration. $\int_{r_o}^{r} F_r(\xi) d\xi$ correlates to the body forces and is represented as *H(r)* for simplicity. By substituting Equation 5.14 into Equation 5.12 and integrating the resulting relationship, an expression for the radial stress can be derived as:

$$\frac{1}{r^2}\frac{d}{dr}(r^2 \sigma_{rr}) = \frac{1}{r}[A \ln r + B - (1 + k_2) H(r)] - F_r(r);$$

$$\sigma_{rr} = \frac{C}{r^2} + \frac{A}{4}(2 \ln r - 1) + \frac{B}{2} - \frac{1 + k_2}{2} H(r) + \frac{k_2 - 1}{2} I(r); \qquad (5.15)$$

where C is a new integration constant and *I(r)* corresponds to the body forces and is equal to $\frac{1}{r^2}\int_{r_o}^{r} \xi^2 F_r(\xi) d\xi$. A comparison of Equations 5.14 and 5.15 reveals an expression for tangential stress as:

$$\sigma_{\theta\theta} = -\frac{C}{r^2} + \frac{A}{4}(2 \ln r + 1) + \frac{B}{2} - \frac{1 + k_2}{2} H(r) + \frac{1 - k_2}{2} I(r). \qquad (5.16)$$

Two constants of integration have come about so far in this elastic analysis. Next, expressions for the displacements are derived. Beginning with the appropriate strain-displacement and stress-strain relations, which govern an elastic analysis in a polar coordinate system, general expressions for the radial and tangential displacements can be determined. The series of equations are:

$$e_{rr} = \frac{\partial u_r}{\partial r} = k_1(\sigma_{rr} - k_2\sigma_{\theta\theta}); \tag{5.17}$$

$$e_{\theta\theta} = \frac{u_r}{r} + \frac{1}{r}\frac{\partial u_\theta}{\partial \theta} = k_1(\sigma_{\theta\theta} - k_2\sigma_{rr}); \tag{5.18}$$

$$e_{r\theta} = \frac{1}{2}\left[\frac{1}{r}\frac{\partial u_r}{\partial \theta} + r\frac{\partial}{\partial r}\left(\frac{u_\theta}{r}\right)\right] = \frac{1+\nu}{E}\sigma_{r\theta}. \tag{5.19}$$

The radial displacement is determined by first integrating Equation 5.17 with respect to the radius:

$$\begin{aligned} u_r = k_1\{-(1+k_2)\frac{C}{r} + \frac{A}{4}[2(1-k_2)\ln r - (3-k_2)]r + \frac{(1-k_2)}{2}Br - \\ \frac{(1-k_2^2)}{2}r[H(r) - I(r)]\} + f(\theta), \end{aligned} \tag{5.20}$$

where $f(\theta)$ is an unknown function of θ only. To determine tangential displacement, Equation 5.19 is rewritten with the appropriate substitutions and integrations to arrive at:

$$r\frac{\partial}{\partial r}\left(\frac{u_\theta}{r}\right) = \frac{2(1+\nu)}{E}\sigma_{r\theta} - \frac{1}{r}\frac{\partial u_r}{\partial \theta}. \tag{5.21}$$

Since $f(\theta)$ is the only term of the radial displacement equation that is a function of θ, $\frac{\partial u_r}{\partial \theta}$ can be replaced by $\frac{\partial f}{\partial \theta}$. Equation 5.21 can now be simplified as:

$$r\frac{\partial}{\partial r}\left(\frac{u_\theta}{r}\right) = -\frac{1}{r}\frac{\partial f}{\partial \theta}; \text{ or,}$$

$$u_\theta = \frac{\partial f}{\partial \theta} + rg(\theta); \tag{5.22}$$

where $g(\theta)$ is another unknown function of θ only. The general expression for the radial and tangential displacements are incorporated into Equation 5.18 to obtain:

$$\frac{1}{r}\left(\frac{d^2 f}{d\theta^2} + f\right) + \frac{dg}{d\theta} = AK_1. \tag{5.23}$$

A like term comparison of this equation with respect to r results in the following two equalities:

$$\frac{d^2 f}{d\theta^2} + f = 0 \tag{5.24}$$

and

$$\frac{dg}{d\theta} = Ak_1. \tag{5.25}$$

Equation 5.24 is a harmonic equation which has the solution of $f(\theta) = M\cos\theta + N\sin\theta$. Equation 5.25 can be directly integrated to determine $g(\theta) = Ak_1\theta + L$, where M, N, and L are all constants. The functions of θ can now be incorporated into the displacement equations. At this point the constants M, N, and L are all equal to zero since there is no rigid body displacement or rotation.

$$u_r(r,\theta) = k_1\{-(1+k_2)\frac{C}{r} + \frac{A}{4}[2(1-k_2)\ln r - (3-k_2)]r + \frac{(1-k_2)}{2}Br - \frac{(1-k_2^2)}{2}r[H(r) - I(r)]\} \tag{5.26}$$

By specifically addressing the spinning rotor application, non-integral expressions for *H(r)* and *I(r)* can be determined.

$$H(r) = \int_a^r F_r(\xi)d\xi = \frac{1}{2}\rho\omega^2(r^2 - a^2) \tag{5.27}$$

$$I(r) = \frac{1}{r^2}\int_a^r \xi^2 F_r(\xi)d\xi = \frac{1}{4}\rho\omega^2\frac{1}{r^2}(r^4 - a^4) \tag{5.28}$$

Also, due to the fact that the disk has a single value displacement, the constant A must equal zero in the displacement equations. The next step is to apply the appropriate boundary conditions. Four different sets of conditions are considered. The first set of boundary conditions describes a rotating disk without poles with a hole in the center. The second case is one which describes a rotating disk without poles and fixed to a shaft through the center of the hole. The third set of boundary conditions pertains to a rotating disk with a hole in the center and poles at the outer hub radius. The fourth configuration considered is a rotating disk fixed to a central shaft and subjected to peripheral loading due to the rotor poles.

5.2.1 Elastic Configuration #1

Boundary conditions for the first case describe a rotor that is free to deform at both the inner and outer radii. At the inner and outer radii the radial stress is equal to zero.

$$\sigma_{rr}\big|_{r=a} = 0 \quad \text{and} \quad \sigma_{rr}\big|_{r=b} = 0 \tag{5.29}$$

Application of the boundary conditions at the inner and outer radii to Equation (5.15) results in two expressions that can be solved simultaneously to determine the constants *B* and *C* for this particular set of boundary conditions.

At the inner radius:

$$\sigma_{rr} = 0 = \frac{C}{a^2} + \frac{B}{2}. \tag{5.30}$$

At the outer radius:

$$\sigma_{rr} = 0 = \frac{C}{b^2} + \frac{B}{2} - \frac{1}{4}\rho\omega^2(b^2 - a^2)(1 + k_2) + \frac{\rho\omega^2}{8b^2}(k_2 - 1)(b^4 - a^4). \tag{5.31}$$

The simultaneous solution of Equations 5.30 and 5.31 results in the following expressions for *B* and *C*:

$$B = \frac{1}{4}\rho\omega^2[2b^2(1 + k_2) - (k_2 - 1)(b^2 + a^2)]; \tag{5.32}$$

$$C = \frac{\rho\omega^2 a^2}{8}[(k_2 - 1)(b^2 + a^2) - 2b^2(1 + k_2)]. \tag{5.33}$$

The expressions for the constants *B* and *C* can now be substituted back into Equations 5.15, 5.16, and 5.26, to derive equations for the radial and tangential stresses as well as the radial displacement. These three relations describe the stress and displacement conditions for this specific set of boundary conditions. After rigorous algebraic manipulation, the following common expressions remain:

$$\sigma_{rr} = \frac{3+k_2}{8}\rho\omega^2(b^2 + a^2 - \frac{a^2b^2}{r^2} - r^2); \quad (5.34)$$

$$\sigma_{\theta\theta} = \frac{3+k_2}{8}\rho\omega^2[b^2 + a^2 + \frac{a^2b^2}{r^2} - \frac{(1+3k_2)}{(3+k_2)}r^2]; \quad (5.35)$$

$$u_r = \frac{\rho\omega^2 r(3+k_2)(1-k_2)}{8}k_1[b^2 + a^2 + \frac{(1+k_2)}{(1-k_2)}\frac{a^2b^2}{r^2} - \frac{(1+k_2)}{(3+k_2)}r^2]. \quad (5.36)$$

The same expressions were derived by Sada [97] with a stress function approach for a thin disk of uniform thickness rotating with a constant angular velocity. The body force is the centrifugal force and is derived from a potential. Sada defined the stress function, ϕ, by:

$$r\sigma_{rr} = \phi$$

and (5.37)

$$\sigma_{\theta\theta} = \frac{d\phi}{dr} + \rho\omega^2 r^2;$$

and showed that it satisfied the equilibrium equation as simplified by the circular symmetry consideration. By using the appropriate compatibility and strain-displacement relations, an expression for the stress function is determined. Sada then applied the boundary conditions of radial stress being equal to zero at both the inner and outer radii to achieve Equations 5.34-5.36.

5.2.2 Elastic Configuration #2

Boundary conditions for the second case describe a rotor that is free to deform at the outer radius but fixed at the inner radius. At the outer radius the radial stress is equal to zero and at the inner radius the displacement is equal to zero.

$$u_r\big|_{r=a} = 0$$

and (5.38)

$$\sigma_{rr}\big|_{r=b} = 0$$

The radial stress at *r=b* is written as:

$$\sigma_{rr} = 0 = \frac{C}{b^2} + \frac{B}{2} - \frac{1+k_2}{2}\frac{1}{2}\rho\omega^2(b^2 - a^2) + \frac{k_2 - 1}{2}\frac{1}{4}\rho\omega^2\frac{1}{b^2}(b^4 - a^4); \text{ or,}$$

$$\sigma_{rr} = 0 = \frac{C}{b^2} + \frac{B}{2} - \frac{\rho\omega^2}{8}\frac{(b^2 - a^2)}{b^2}[(3+k_2)b^2 + (1-k_2)a^2]. \tag{5.39}$$

At the inner radius, *r=a*, the displacement must equal zero for the disk to remain fixed to the shaft. In addition to the radial displacement equaling zero, the tangential displacement must also equal zero at the inner radius. This is important only if the angular velocity is not constant. Since there is no rigid body translation involved in the straining of the disk, Equation 5.26 is written as:

$$u_r = 0 = -(1+k_2)\frac{C}{a} + \frac{(1-k_2)}{2}Ba; \tag{5.40}$$

Now, Equations 5.40 and 5.39 are easily solved simultaneously to find the expressions for the constants *B* and *C*.

$$\frac{1}{2}B = \frac{1+k_2}{8}\rho\omega^2 k \tag{5.41}$$

$$C = \frac{1-k_2}{8}\rho\omega^2 a^2 k \tag{5.42}$$

$$\text{where } k = \frac{(b^2 - a^2)[(3+k_2)b^2 + (1-k_2)a^2]}{(1+k_2)b^2 + (1-k_2)a^2}$$

Now that expressions for the constants A, B, C, and D have been determined specifically for this set of boundary conditions, the corresponding stress and displacement relations may be finalized.

$$\sigma_{rr} = \frac{\rho\omega^2}{8}\{[1+(\frac{a}{r})^2]k - [1-(\frac{a}{r})^2][(3+k_2)r^2 + (1-k_2)a^2 - k_2 k]\} \tag{5.43}$$

$$\sigma_{\theta\theta} = \frac{\rho\omega^2}{8}\{[1+(\frac{a}{r})^2]k_2 k - [1-(\frac{a}{r})^2][(1+3k_2)r^2 - (1-k_2)a^2 - k]\} \tag{5.44}$$

$$u_r = \frac{\rho\omega^2(1-k_2^2)}{8}k_1 r[1-(\frac{a}{r})^2][k - (r^2 - a^2)] \tag{5.45}$$

5.2.3 Elastic Configuration #3

Boundary conditions for the third configuration evaluated describe a spinning rotor with a centrally located hole that is free to deform and is subjected to peripheral loading due to the rotor poles at the outer radius. At the inner radius the radial stress is equal to zero, and at the outer radius the radial stress is equal to the loading estimated from the pole contribution.

$$\begin{gathered} \sigma_{rr}\big|_{r=a} = 0 \\ \text{and} \\ \sigma_{rr}\big|_{r=b} = \sigma_{ro} \end{gathered} \tag{5.46}$$

Again, at the inner radius Equation 5.15 becomes:

$$\sigma_{rr} = 0 = \frac{C}{a^2} + \frac{B}{2}. \tag{5.47}$$

Equation 5.15 at the outer radius is written as:

$$\sigma_{rr} = \sigma_{ro} = \frac{C}{b^2} + \frac{B}{2} - \frac{(1+k_2)}{4}\rho\omega^2(b^2 - a^2) + \frac{(k_2 - 1)}{8b^2}\rho\omega^2(b^4 - a^4);\text{ or,}$$

$$\sigma_{ro} = \frac{C}{b^2} + \frac{B}{2} - \frac{\rho\omega^2}{8}\frac{(b^2 - a^2)}{b^2}[(3+k_2)b^2 + (1-k_2)a^2]. \qquad (5.48)$$

The periphery loading condition, $\sigma_r = \sigma_{ro}$, is approximated by proportionally distributing the body forces associated with the poles over the entire disk circumference. Obviously, the greater the pole arclength or, the greater the number of individual poles, the better the approximation of the loading.

$$\sigma_{ro} = \frac{\text{Number of Poles } * \text{ Pole Arclength}}{2\pi b}\int_b^{r_p} \rho\omega^2 r dr$$

$$(5.49)$$

$$\sigma_{ro} = \frac{\text{Number of Poles } * \text{ Pole Arclength}}{4\pi b}\rho\omega^2(r_p^2 - b^2)$$

where r_p is the radius to the pole tip from the center of the rotor hole.

Equations 5.47 and 5.48 can now be solved simultaneously to determine the constants B and C. The resulting expressions are:

$$B = \frac{\rho\omega^2}{4}[2b^2(1+k_2) - (a^2 + b^2)(k_2 - 1)] - \frac{2\sigma_{ro}b^2}{(a^2 - b^2)}; \qquad (5.50)$$

$$C = \frac{a^2\rho\omega^2}{8}[(k_2 - 1)(a^2 + b^2) - 2b^2(1+k_2)] + \frac{\sigma_{ro}a^2b^2}{(a^2 - b^2)}. \qquad (5.51)$$

The expressions for the constants B and C can now be incorporated back into the radial stress, tangential stress, and radial displacement equations. After a great deal of algebraic manipulation, Equations 5.15, 5.16, and 5.26 are now in the proper form to completely describe the stress and displacement conditions as a function of radial position.

$$\sigma_{rr} = \frac{\sigma_{ro} b^2 (1 - \frac{a^2}{r^2})}{(b^2 - a^2)} + \frac{\rho\omega^2}{8}(3 + k_2)(a^2 + b^2 - \frac{a^2 b^2}{r^2} - r^2) \tag{5.52}$$

$$\sigma_{\theta\theta} = \frac{\sigma_{ro} b^2 (1 + \frac{a^2}{r^2})}{(b^2 - a^2)} + \frac{\rho\omega^2 b^2}{8}(3 + k_2)[1 + \frac{a^2}{b^2} + \frac{a^2}{r^2} - \frac{r^2(3k_2 + 1)}{b^2(3 + k_2)}] \tag{5.53}$$

$$\begin{aligned} u_r = k_1(1 - k_2)\{&\frac{\rho\omega^2}{8}(3 + k_2) r[a^2 + b^2 + \frac{(1 + k_2)}{(1 - k_2)}\frac{a^2 b^2}{r^2} - \\ &\frac{(1 + k_2)}{(3 + k_2)} r^2] - \frac{\sigma_{ro} b^2}{(a^2 - b^2)}[\frac{a^2}{r}\frac{(1 + k_2)}{(1 - k_2)} + r]\} \end{aligned} \tag{5.54}$$

5.2.4 Elastic Configuration #4

Boundary conditions for the final case describe a rotor that is fixed at the inner radius and is subjected to peripheral loading due to the rotor poles. At the outer radius the radial stress is equal to the loading estimated from the pole contribution, and at the inner radius the displacement is equal to zero.

$$\begin{gathered} u_r\big|_{r=a} = 0 \\ \text{and} \\ \sigma_{rr}\big|_{r=b} = \sigma_{ro} \end{gathered} \tag{5.55}$$

With the outer radius boundary condition, Equation 5.15 is written as:

$$\sigma_{rr} = \sigma_{ro} = \frac{C}{b^2} + \frac{B}{2} - \frac{1+k_2}{2}\frac{1}{2}\rho\omega^2(b^2-a^2) + \frac{k_2-1}{2}\frac{1}{4}\rho\omega^2\frac{1}{b^2}(b^4-a^4); \text{ or,}$$

$$\sigma_{ro} = \frac{C}{b^2} + \frac{B}{2} - \frac{\rho\omega^2}{8}\frac{(b^2-a^2)}{b^2}[(3+k_2)b^2 + (1-k_2)a^2]. \tag{5.56}$$

The boundary condition at the inner radius is now considered. This condition is the same as described by Equation 5.40 and can be rewritten as an expression for the constant *B* as:

$$B = \frac{2C}{a^2}\frac{(1+k_2)}{(1-k_2)}. \tag{5.57}$$

Equations 5.56 and 5.57 are now solved simultaneously to determine expressions for the constants *B* and *C*.

$$C = \frac{\sigma_{ro}a^2b^2(1-k_2)}{a^2(1-k_2)+b^2(1+k_2)} + \frac{(1-k_2)}{8}\rho\omega^2 k \tag{5.58}$$

$$B = 2(1+k_2)[\frac{\sigma_{ro}b^2}{a^2(1-k_2)+b^2(1+k_2)} + \frac{\rho\omega^2}{8}k] \tag{5.59}$$

$$\text{where } k = \frac{(b^2-a^2)[(3+k_2)b^2+(1-k_2)a^2]}{(1+k_2)b^2+(1-k_2)a^2}$$

The expressions for the constants *B* and *C* pertaining to this set of boundary conditions can now be put back into the general expressions for radial and tangential stresses as well as for the radial displacement. After rigorous algebraic manipulation, the following equations result:

$$\sigma_{rr} = \frac{\sigma_{ro} b^2}{a^2(1-k_2)+b^2(1+k_2)}[\frac{a^2}{r^2}(1-k_2)+(1+k_2)]+$$
$$\frac{\rho\omega^2}{8}[\frac{a^2}{r^2}(1-k_2)(k+a^2)+(1+k_2)(k+2a^2)-(3+k_2)r^2]; \qquad (5.60)$$

$$\sigma_{\theta\theta} = \frac{\sigma_{ro} b^2}{a^2(1-k_2)+b^2(1+k_2)}[\frac{a^2}{r^2}(k_2-1)+(k_2+1)]+$$
$$\frac{\rho\omega^2 a^2}{8}\{(k+a^2)[\frac{(k_2-1)}{r^2}+\frac{(k_2+1)}{a^2}]-\frac{(3k_2+1)}{a^2}r^2\}; \qquad (5.61)$$

$$u_r = k_1(1-k_2^2)\{\frac{\sigma_{ro} b^2 (r-\frac{a^2}{r})}{[a^2(1-k_2)+b^2(1+k_2)]}+\frac{\rho\omega^2}{8}[k(r-\frac{a^2}{r})-r^3-a^2 r(\frac{a^2}{r^2}-2)]\}. \qquad (5.62)$$

5.3 Estimation of Creep Deformation of an Integrated Power Unit Rotor Laminate

Large stresses require the consideration of possible deformations beyond the elastic regime. Budiansky and Mangasarian investigated the plastic deformation of an infinite sheet, subjected to biaxial tension, with a circular hole [99]. The analysis resulted in the determination of plastic stress concentration factors and uniaxial Ramberg-Osgood stress-strain curves. In a related effort, Mangasarian investigated elastic and plastic deformations of an infinite sheet with a normally loaded circular hole [100]. A follow-on effort by Budiansky incorporated a modification of the Ramberg-Osgood relation which allowed for an exact analytical solution for the stress concentration factor over a full range of applied stresses [101]. Although these researchers suggest valuable methodologies for investigating plastic deformations of circular holes in infinite sheets, the problem needs to be refined to specifically address the rotor configuration and time dependency.

To better estimate deformation caused by high temperature, high stress environments of the spinning rotor, an analysis was done that incorporates analytical modeling with empirical data. This analysis is based on a series of papers written by A. M. Wahl from 1961 through 1964 [102-106]. To begin the analysis the following assumptions are made.

1) Creep rate at any given temperature is a function of stress multiplied by a function of time as represented in the expression:

$$\dot{\varepsilon} = F(\sigma) f(t).$$

2) Stresses at any radius are constant with time. This statement implies that the initial transient condition is neglected.

3) The stress-strain rate relation is a power function of stress in the form of:

$$\dot{\varepsilon} = k\sigma^n f(t).$$

4) A biaxial state of stress (plane stress) exists and is comprised only of tangential and radial stresses ($\sigma_{zz} = 0$).

Based on empirical data generated by the creep tests performed within this study, assumptions 1) and 3) appear to be valid. The consequence of assumption 2) is that the transient conditions due to starting and stopping of the power units are neglected. The time required to accelerate from zero to full power is approximately two seconds in an emergency operating mode, while the time taken for normal starting is only slightly longer. Neglecting these short durations of changing stresses with respect to time should have little impact on the analysis when comparing the transient times to the much longer steady-state durations. Assumption 4) is valid for the thin laminate. A state of plane strain is more appropriate if the entire rotor is analyzed as a unit.

The tangential, radial, and axial strain rates may be expressed, for plane stress conditions, in the following forms [102]:

$$\dot{\varepsilon}_{\theta\theta} = \frac{\dot{u}}{r} = kS^n f(t)[\frac{\sigma_{\theta\theta} - \frac{1}{2}\sigma_{rr}}{S}];$$

$$\dot{\varepsilon}_{rr} = \frac{d\dot{u}}{dr} = kS^n f(t)[\frac{\sigma_{rr} - \frac{1}{2}\sigma_{\theta\theta}}{S}]; \tag{5.63}$$

$$\dot{\varepsilon}_{zz} = kS^n f(t)[\frac{-(\sigma_{rr} + \sigma_{zz})}{2S}].$$

where S is an equivalent stress that varies with the particular yield criterion chosen for the application.

If the von Mises yield strength criterion is used, then:

$$S = \sqrt{\sigma_{\theta\theta}{}^2 + \sigma_{rr}{}^2 + \sigma_{\theta\theta}\sigma_{rr}}\,. \tag{5.64}$$

If the Tresca (maximum shear) yield criterion is used, then:

$$S = \sigma_{\theta\theta}. \tag{5.65}$$

The Tresca criterion is used to continue the analysis. Wahl considered both the Tresca and von Mises criterion as well as combinations of the two [103]. He concluded that the Tresca criterion better represented the data generated from rotating disk experiments. An additional advantage of the Tresca approach is that it is simpler than the von Mises approach, and it allows for closed form solutions. The strain rate relations associated with the Tresca yield criterion for plane stress conditions become:

$$\dot{\varepsilon}_{\theta\theta} = k\sigma_{\theta\theta}{}^{n}(1-\frac{1}{2}\frac{\sigma_{rr}}{\sigma_{\theta\theta}})f(t);$$

$$\dot{\varepsilon}_{rr} = k\sigma_{\theta\theta}{}^{n}(\frac{\sigma_{rr}}{\sigma_{\theta\theta}}-\frac{1}{2})f(t); \tag{5.66}$$

$$\dot{\varepsilon}_{zz} = -(\dot{\varepsilon}_{\theta\theta}+\dot{\varepsilon}_{rr}).$$

Use of the Tresca yield criterion implies the middle principal stress has no effect on yielding; therefore it is also reasonable to assume that there would be no plastic deformation in the corresponding direction [107]. For the rotating disk with peripheral loading the maximum stress will always be the tangential stress [108]. The principal stress in the Z direction is assumed to be zero due to the plane stress condition. This zero stress is the minimum stress at all radial locations other than the hole edge where the radial stress is also equal to zero. Therefore, the radial stress is the middle stress at all locations other than the hole edge. Hence, it is assumed that the plastic deformation rate would be zero in the radial direction ($\dot{\varepsilon}_{rr} = 0$).

Equations 5.66 can now be rewritten as:

$$\dot{\varepsilon}_{\theta\theta} = \frac{\dot{u}}{r} = k\sigma_{\theta\theta}{}^{n}(1-\frac{1}{2}\frac{\sigma_{rr}}{\sigma_{\theta\theta}})f(t);$$

$$\dot{\varepsilon}_{rr} = 0; \tag{5.67}$$

$$\dot{\varepsilon}_{zz} = -\dot{\varepsilon}_{\theta\theta}.$$

Wahl has experimentally shown that the assumption of $\dot{\varepsilon}_{rr} = 0$ is approximately fulfilled throughout the rotor, except at the inner and outer diameters [103]. This assumption does not imply a strain of zero at these locations, only that the value of strain is not changing with time. A configuration which includes peripheral loading, as is the case for the spinning rotor, would satisfy the assumption of $\dot{\varepsilon}_{rr} = 0$ at the outer diameter. Wahl subsequently investigated the creep deformation of a disk with a central hole that was uniformly loaded at the periphery [104].

Since the radial stress is equal to zero at the hole edge, the first relation of Equations 5.67 can be written as:

$$\dot{\varepsilon}_{\theta\theta} = \frac{\dot{u}_a}{r} = k\sigma_{\theta\theta}{}^n f(t); \text{ at } r = a \tag{5.68}$$

where $\dot{u}_a$ equals the radial deformation rate at the inside diameter. Equation 5.68 can now be solved for the tangential stress.

$$\sigma_{\theta\theta} = [\frac{\dot{u}_a}{rkf(t)}]^{\frac{1}{n}} = [\frac{\dot{u}_a}{kf(t)}]^{\frac{1}{n}} r^{\frac{-1}{n}} \tag{5.69}$$

Returning to the equilibrium equation, Equation 5.10 is integrated from the inner radius to the outer radius of the rotor hub.

$$r\sigma_{rr}\Big|_{r=a}^{r=b} = \int_a^b \sigma_{\theta\theta} dr - \rho\omega^2 \int_a^b r^2 \text{, or,}$$

$$r\sigma_{rr}\Big|_{r=a}^{r=b} = \int_a^b \sigma_{\theta\theta} dr - \frac{1}{3}\rho\omega^2(b^3 - a^3) \tag{5.70}$$

The particular IPU rotor configuration includes poles extending from the outer diameter of the rotor hub. The poles act as peripheral loads on the rotor, therefore at the inner radius $\sigma_{rr} = 0$, while at the outer radius $\sigma_{rr} = \sigma_{ro}$. Equation 5.70 can now be expressed as:

$$b\sigma_{ro} = \int_a^b \sigma_{\theta\theta} dr - \frac{1}{3}\rho\omega^2(b^3 - a^3). \tag{5.71}$$

Equation 5.69 can now be incorporated into Equation 5.71 to get:

$$b\sigma_{ro} = \int_a^b [\frac{\dot{u}_a}{kf(t)}]^{\frac{1}{n}} r^{-\frac{1}{n}} dr - \frac{1}{3}\rho\omega^2(b^3 - a^3),$$

$$b\sigma_{ro} = [\frac{\dot{u}_a}{kf(t)}]^{\frac{1}{n}} \frac{1}{1-\frac{1}{n}} r^{1-\frac{1}{n}}\Big|_a^b - \frac{1}{3}\rho\omega^2(b^3 - a^3),$$

and finally,

$$b\sigma_{ro} = [\frac{\dot{u}_a}{kf(t)}]^{\frac{1}{n}} (\frac{n}{n-1})(b^{\frac{n-1}{n}} - a^{\frac{n-1}{n}}) - \frac{1}{3}\rho\omega^2(b^3 - a^3). \tag{5.72}$$

A rearrangement of Equation 5.72 results in:

$$[\frac{\dot{u}_a}{kf(t)}]^{\frac{1}{n}} = (\frac{n-1}{n})[b\sigma_{ro} + \frac{1}{3}\rho\omega^2(b^3 - a^3)]\frac{1}{b^{\frac{n-1}{n}} - a^{\frac{n-1}{n}}}. \tag{5.73}$$

The substitution of the right hand side of Equation 5.73 into Equation 5.69 results in the following equation for tangential stress as a function of radial position.

$$\sigma_{\theta\theta} = (\frac{n-1}{n})[b\sigma_{ro} + \frac{1}{3}\rho\omega^2(b^3 - a^3)][b^{\frac{n-1}{n}} - a^{\frac{n-1}{n}}]^{-1} r^{-\frac{1}{n}} \tag{5.74}$$

It can be shown that the average tangential stress for a peripherally loaded rotating disk with a central hole is given as:

$$\sigma_{\theta\theta Avg} = \frac{b\sigma_{ro}}{b-a} + \frac{1}{3}\rho\omega^2(\frac{b^3-a^3}{b-a}) \tag{5.75}$$

This average stress is defined as the summation of the inertial force components, due to the spinning rotor, acting normal to, and evenly distributed over the net cross-sectional area. By definition, this average tangential stress is constant at any radial position from the inner to the outer radii. Incorporation of Equation 5.75 into Equation 5.74, along with allowing $\frac{n-1}{n} = \alpha$, greatly simplifies the expression to:

$$\sigma_{\theta\theta} = \alpha\frac{\sigma_{\theta\theta Avg}(b-a)}{b^\alpha - a^\alpha}r^{-\frac{1}{n}}. \tag{5.76}$$

An expression for the radial stress can now be determined by re-evaluating the equilibrium equation with the expression for the tangential stress. Equation 5.10 is manipulated in the following manner:

$$\frac{d}{dr}(r\sigma_{rr}) - \alpha\frac{\sigma_{\theta\theta Avg}(b-a)}{b^\alpha - a^\alpha}r^{-\frac{1}{n}} + \rho\omega^2 r^2 = 0;\ \text{or,}$$

$$r\sigma_{rr} = \alpha\frac{\sigma_{\theta\theta Avg}(b-a)}{b^\alpha - a^\alpha}\int_a^r r^{-\frac{1}{n}}dr - \rho\omega^2\int_a^r r^2 dr. \tag{5.77}$$

The derivation is continued by carrying out the integrations and solving for the radial stress.

$$\sigma_{rr} = \frac{\sigma_{\theta\theta Avg}(b-a)}{r}[\frac{r^{\alpha} - a^{\alpha}}{b^{\alpha} - a^{\alpha}}] - \frac{\rho\omega^2}{3r}(r^3 - a^3) \tag{5.78}$$

Complete expressions for the stress distributions enable the formation of an expression for the tangential strain rate based on Equation 5.67. The tangential strain rate is then represented by the relation:

$$\dot{\varepsilon}_{\theta\theta} = (1 - \frac{\sigma_{rr}}{2\sigma_{\theta\theta}})k\sigma^n_{\theta\theta}f(t). \tag{5.79}$$

Test data from the creep tests conducted in this research effort indicate that the constant *k* can be represented as:

$$k = \frac{Ae^{-\frac{Q}{RT}}}{T}; \tag{5.80}$$

where: *A* is a material constant, *Q* is the activation energy, *R* is the universal gas constant, and *T* is the absolute temperature.

The expression for *k* was determined from the steady-state responses of the individual creep tests. Corresponding to a steady-state condition the function of time can be included as: *f(t)*=1. Therefore, the strain in the tangential direction is expressed as:

$$\varepsilon_{\theta\theta} = (1 - \frac{\sigma_{rr}}{2\sigma_{\theta\theta}})\frac{Ae^{-\frac{Q}{RT}}}{T}\sigma^n_{\theta\theta}t. \tag{5.81}$$

In order to determine the displacement of the rotor at a specific radial position, the strain-displacement equation is used.

$$u_r = r\varepsilon_{\theta\theta} \tag{5.82}$$

5.4 Analysis Impact

Stress and displacement profiles corresponding to the appropriate relations derived in Sections 5.2 and 5.3 are illustrated in the figures of this section. Plane strain and plane stress considerations are included in the elastic analyses. The representative curves are a result of rotor geometry, material properties and operating conditions. Computer programs developed under this study, and used to determine the stresses and deformations, were written such that the variables may be changed to describe various geometries and operating conditions. The curves shown in subsequent figures correspond to a rotor with a geometry as shown in Figure 5.1, spinning at 55,000 rotations per minute (rpm). The operating temperature is accounted for by the use of an elastic modulus appropriate for that temperature. A modulus of 20×10^6 psi corresponds to a temperature of 1000°F.

Stress and displacement profiles of the first rotor configurations are illustrated in Figures 5.3 and 5.4. The tangential stress is about 46 ksi at the hole edge and gradually decreases to about 13 ksi at the outer diameter. The radial stress satisfies the imposed boundary conditions by being equal to zero at the inner and outer radii, while attaining a maximum stress of approximately 9.7 ksi at a radial position of 0.85 inches. The tangential stress is substantially greater than the radial stress at all radial locations.

The plane strain and plane stress conditions result in nearly the same radial stress profile while a slight difference is apparent for the tangential stress and a significant difference is illustrated for the radial displacement. These differences make sense. The assumption defined by the plane stress condition implies a geometry that is free to deform in the Z-direction in order to avoid a corresponding stress. At the hole edge, where the tangential stress is greatest, this condition allows for larger radial and tangential deformations. As the deformation travels outward along the radius, both tangential and radial stresses decrease. This change causes the outer portion of the disk to act as a containment of the inner portion of the disk, resulting in a thickness increase at the outward radial positions. As it becomes

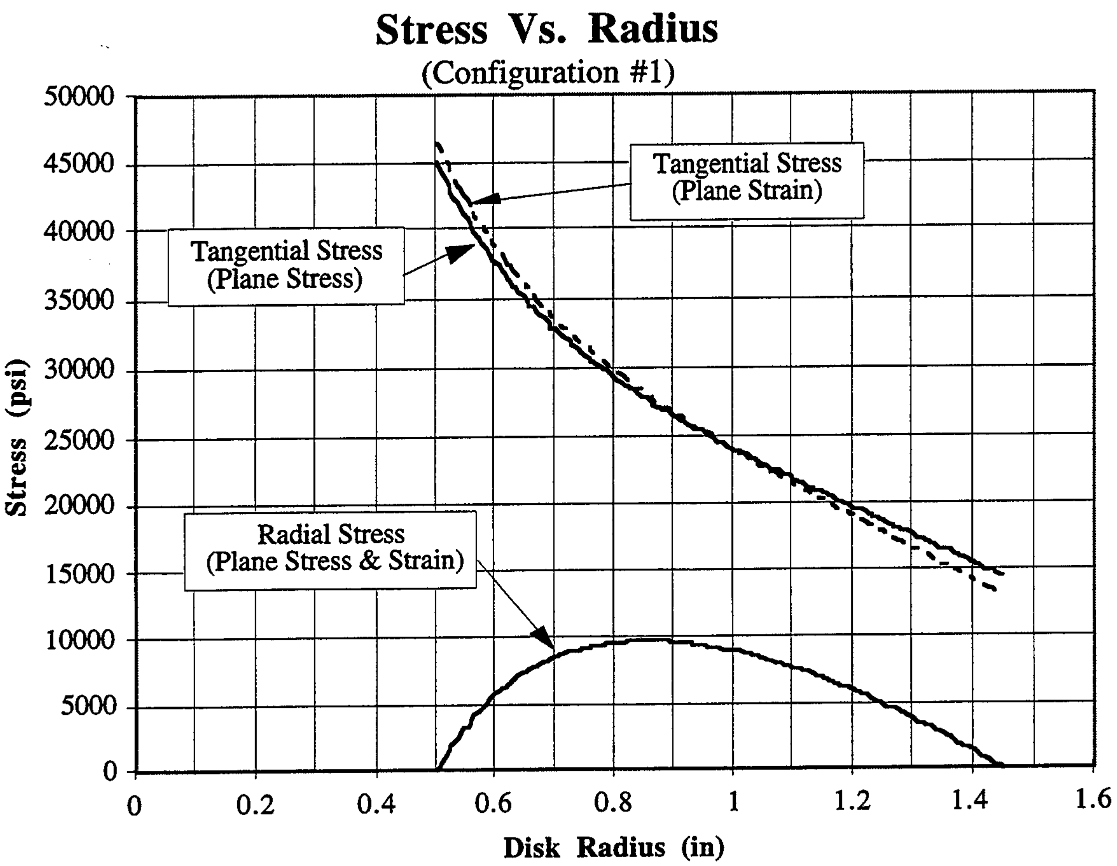

Figure 5.3 Elastically Determined Stress Profiles For Rotor Configuration #1 Tested at 1000°F, While Spinning at 55,000 RPM.

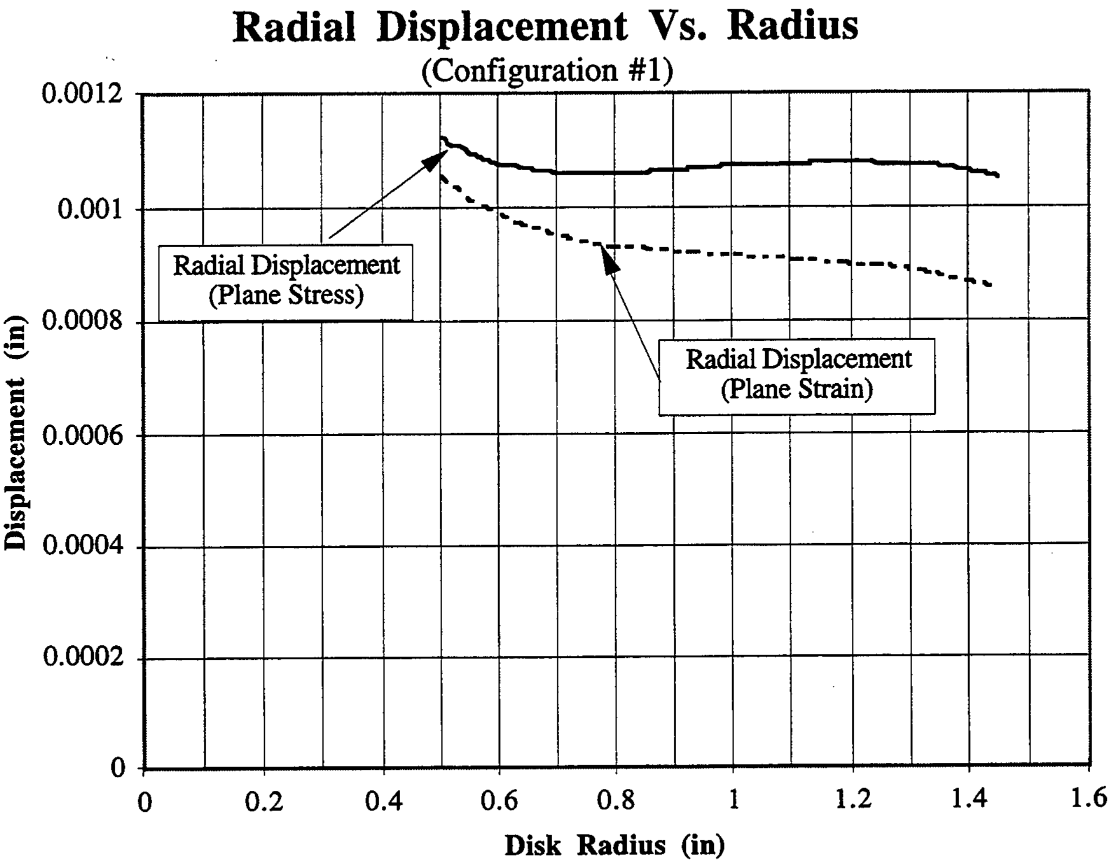

Figure 5.4 Elastically Determined Displacement Profiles For Rotor Configuration #1 Tested at 1000°F, While Spinning at 55,000 RPM.

more difficult to deform the spinning disk tangentially and radially, the required stress must increase above that which corresponds to a plane strain condition.

Configuration #2 is represented by the stress and displacement profiles shown in Figures 5.5 and 5.6. The condition of the unconstrained outer edge of the spinning disk is satisfied by the radial stress equaling zero at this point. The fixed displacement at the hole edge is seen in Figure 5.6. For the plane stress condition the radial stress gradually decreases from a maximum stress of 28 ksi at the hole edge to a minimum stress of zero at the disk outer radius. The radial stress governed by the plane strain condition begins with a slightly lower maximum stress of 27 ksi at the hole edge and becomes nearly coincident with the plane stress profile at a radial position of about 0.85 inches. The plane stress condition results in a tangential stress of only 8 ksi at the hole edge. After reaching a maximum stress of 12.5 ksi, at about 0.82 inches, the tangential stress decreases to a value of about 7 ksi. The tangential stress, as governed by the plane strain conditions, begins at approximately 12 ksi, rises to a maximum of 14 ksi at a radial position of 0.7 inches, before crossing the plane stress profile at about 1.13 inches and ending at 6 ksi at the outer radius. The plane stress radial displacement at the outer radius is nearly 0.0005 inches. This displacement is about 35% greater than the corresponding plane strain displacement. Again the difference is due to the Poisson effect and the assumed deformation in the Z-direction.

Figures 5.7 and 5.8 illustrate the stress and displacement profiles associated with the third analyzed configuration. The profiles are similar to those of the first configuration except that the effect due to the rotor poles is incorporated into this illustration. The maximum tangential stress occurs at the hole edge with a value of approximately 85 ksi and decreases to a minimum value of about 37 ksi at the hub radius. The significance of the difference between the tangential stresses described by plane strain and plane stress conditions is reduced due to the increased stress magnitudes caused by the rotor poles. The radial stress begins at zero, as dictated by the boundary condition and increases to a maximum of about 23 ksi at a radial position of 1.0 inch. As the pole contribution is incorporated into the analysis, the radial stress is equal to the peripheral load at the hub radius. Not only does the peripheral loading increase the magnitudes of the displacements, it also changes the displacement profiles. The pole contribution to the radial displacement is obvious when Figure 5.8 is compared to Figure 5.4.

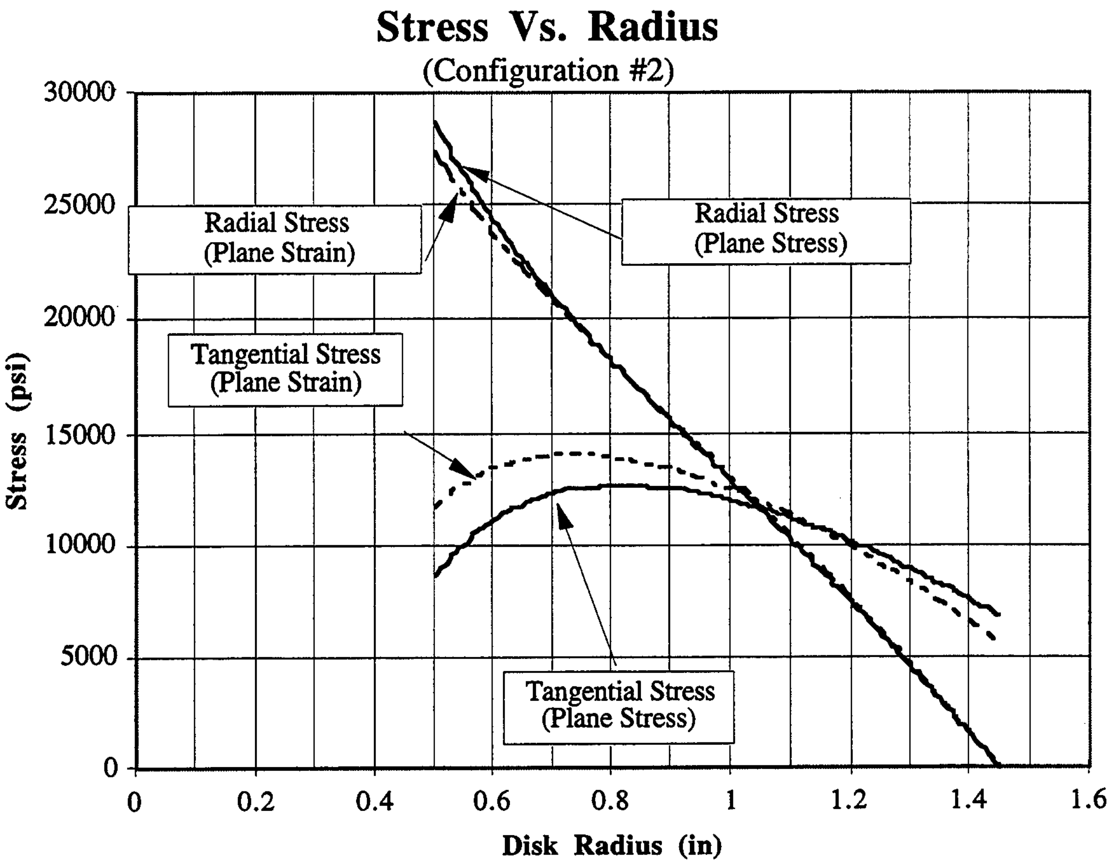

Figure 5.5 Elastically Determined Stress Profiles For Rotor Configuration #2 Tested at 1000°F, While Spinning at 55,000 RPM.

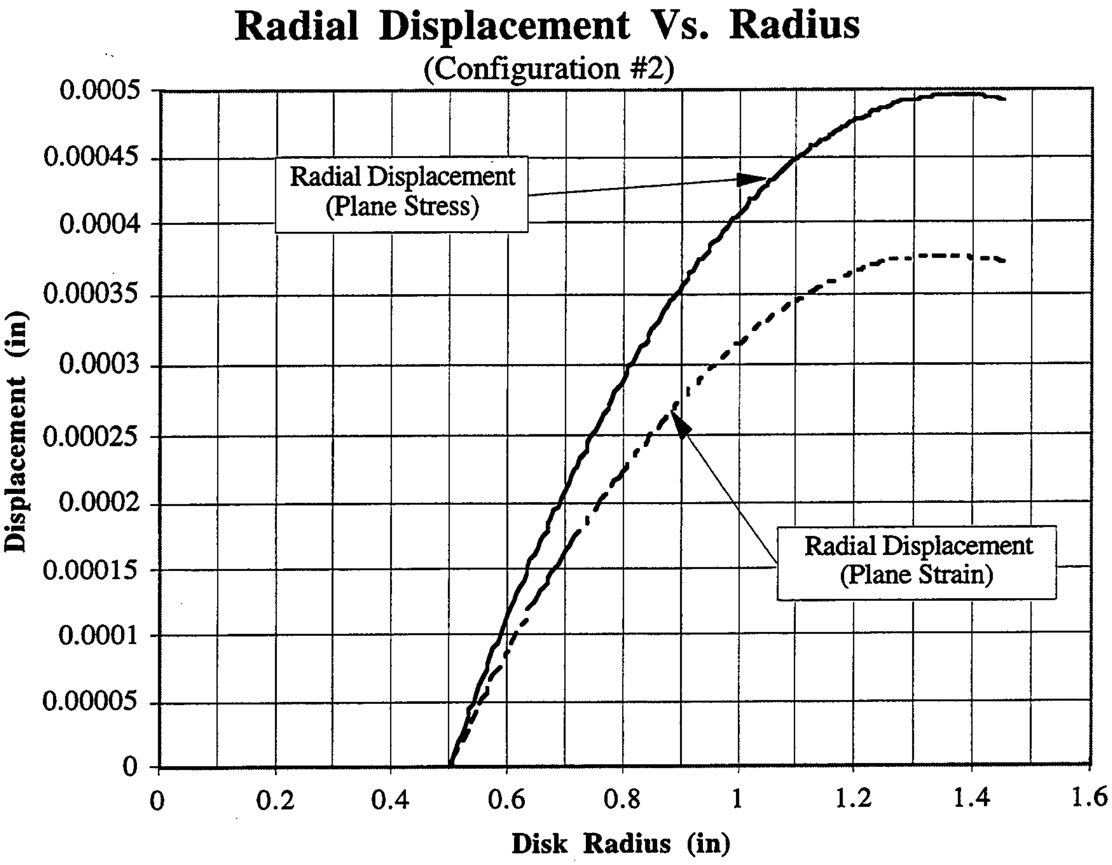

Figure 5.6 Elastically Determined Displacement Profiles For Rotor Configuration #2 Tested at 1000°F, While Spinning at 55,000 RPM.

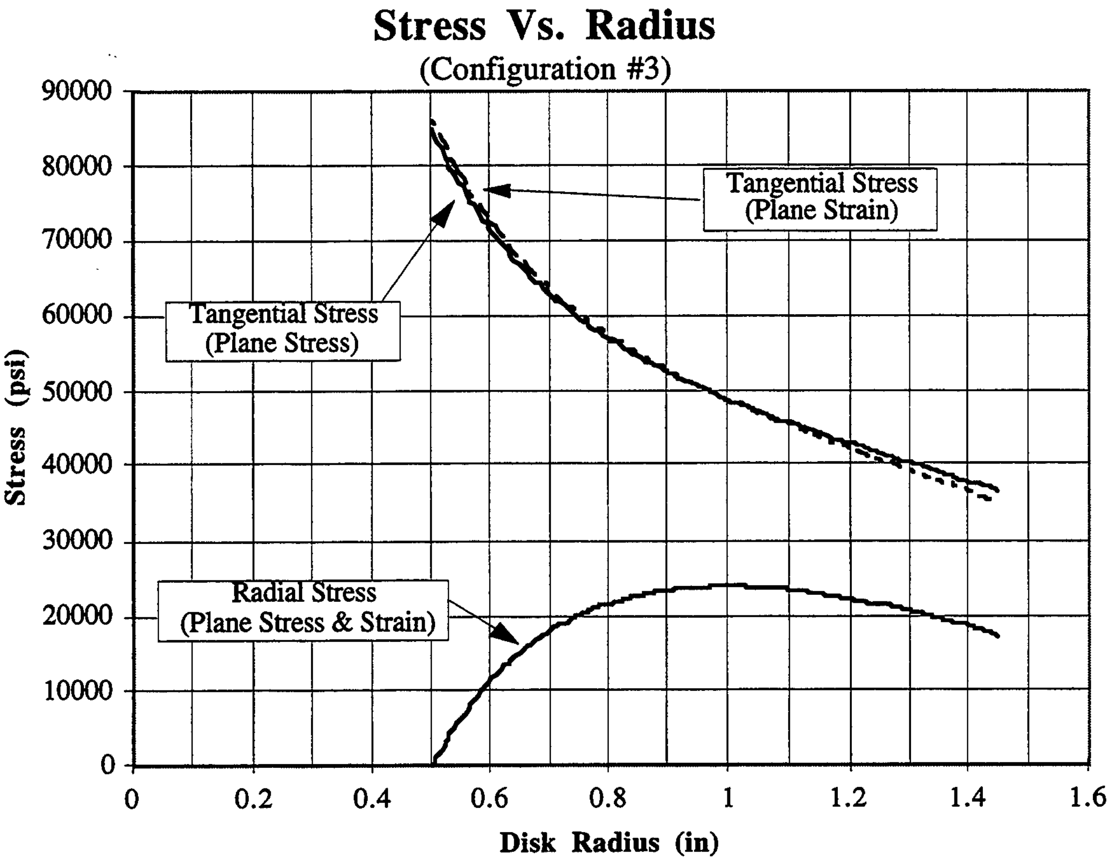

Figure 5.7 Elastically Determined Stress Profiles For Rotor Configuration #3 Tested at 1000°F, While Spinning at 55,000 RPM.

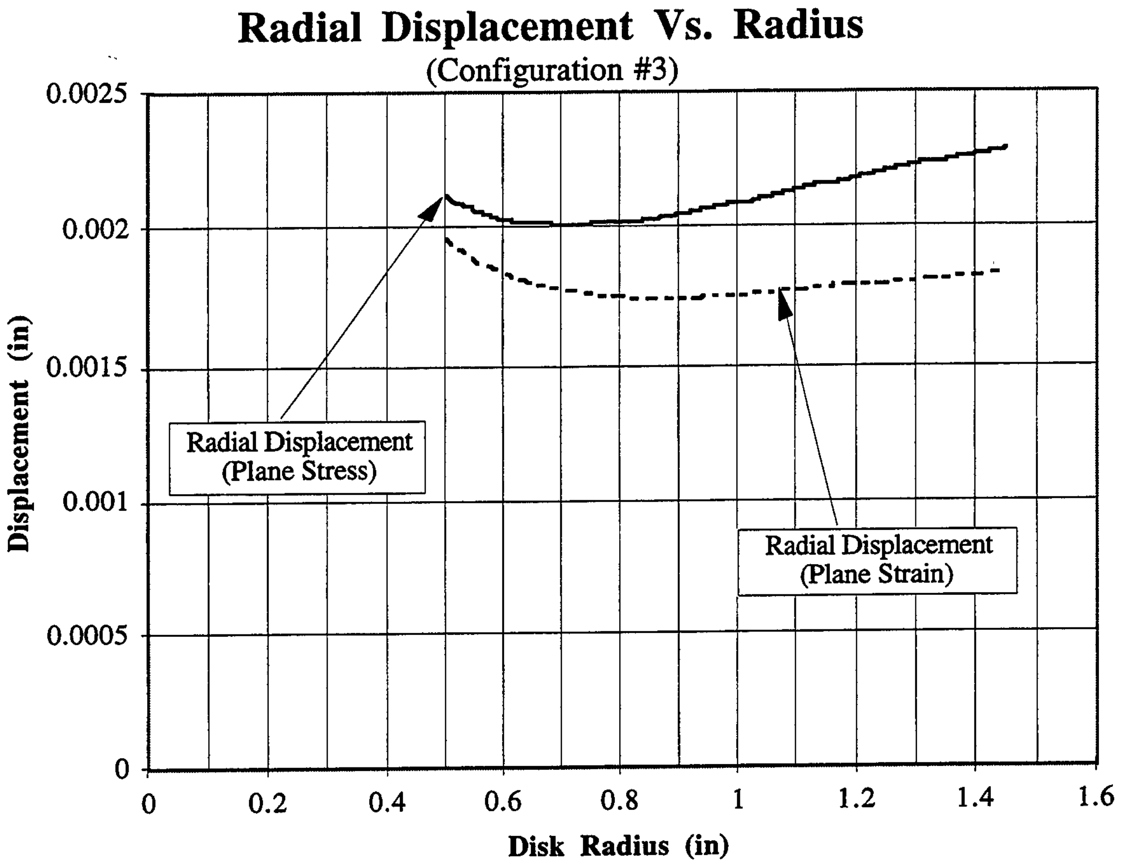

Figure 5.8 Elastically Determined Displacement Profiles For Rotor Configuration #3 Tested at 1000°F, While Spinning at 55,000 RPM.

The stress and displacement profiles depicted in Figures 5.9 and 5.10 illustrate the elastic conditions of rotor Configuration #4. All of the profiles are very similar in shape to those representing Configuration #2. The impact of the pole loading on the periphery is seen as an increase in magnitude of all of the stresses and displacements. The radial stresses at the hole edge are estimated to be 51 ksi and 54 ksi for plane strain and plane stress conditions, respectively. The two radial stress profiles merge and decrease to approximately 17 ksi at the hub radius. The tangential stresses at the hole edge are estimated to be 21 ksi and 15 ksi for plane strain and plane stress conditions, respectively. These two profiles cross at a radial position of about 1.25 inches and vary only slightly at the outer radius. The radial displacement profiles satisfy the boundary condition at the hole edge. The poles, however, cause an outer displacement that is more than twice the displacement associated with Configuration #2.

The creep deformation analysis requires empirically derived data as well as geometrical and mechanical property data. Boundary conditions are equivalent to those evaluated in the elastic analysis of Configuration #3 with the hole free to deform and the outer radius subjected to peripheral loading. Also, the assumption of a plane stress condition is used to simplify the creep analysis. As derived in Section 5.3, the radial and tangential stresses, along with the tangential strain and radial displacement are functions of the empirically determined creep constants. The most likely loading condition would be one resulting in Type-A deformation as defined in Chapter 4. A rotor is not likely to be intentionally loaded to a stress which approaches the flow stress. Based on this assumption, the creep constants determined from the ten Type-A creep responses are used to predict the creep stresses and displacements.

A stress exponent, n, of 3.83 is incorporated into Equations 5.76 and 5.78 in order to determine the corresponding tangential and radial stresses. The resulting stresses, along with a kinetic factor, A, of 4.94×10^7, and an activation energy, Q, of 98,851 cal/mol are also used to predict radial displacements from Equations 5.81 and 5.82. For this analysis an operating temperature of 1000°F was chosen. Figures 5.11 and 5.12 illustrate the predicted behavior due to creep. The radial stress satisfies the boundary conditions by equaling zero at the inner radius and the peripheral stress at the hub radius. The maximum radial stress is approximately 20.8 ksi, located at a radial position of about 1.08 inches from the center of the rotor. The tangential stress begins with a maximum value of 61 ksi at the hole edge and continues to decrease to a minimum value of 48 ksi at the hub radius. The radial displacement, as seen in Figure 5.12, represents the deformation as a function of

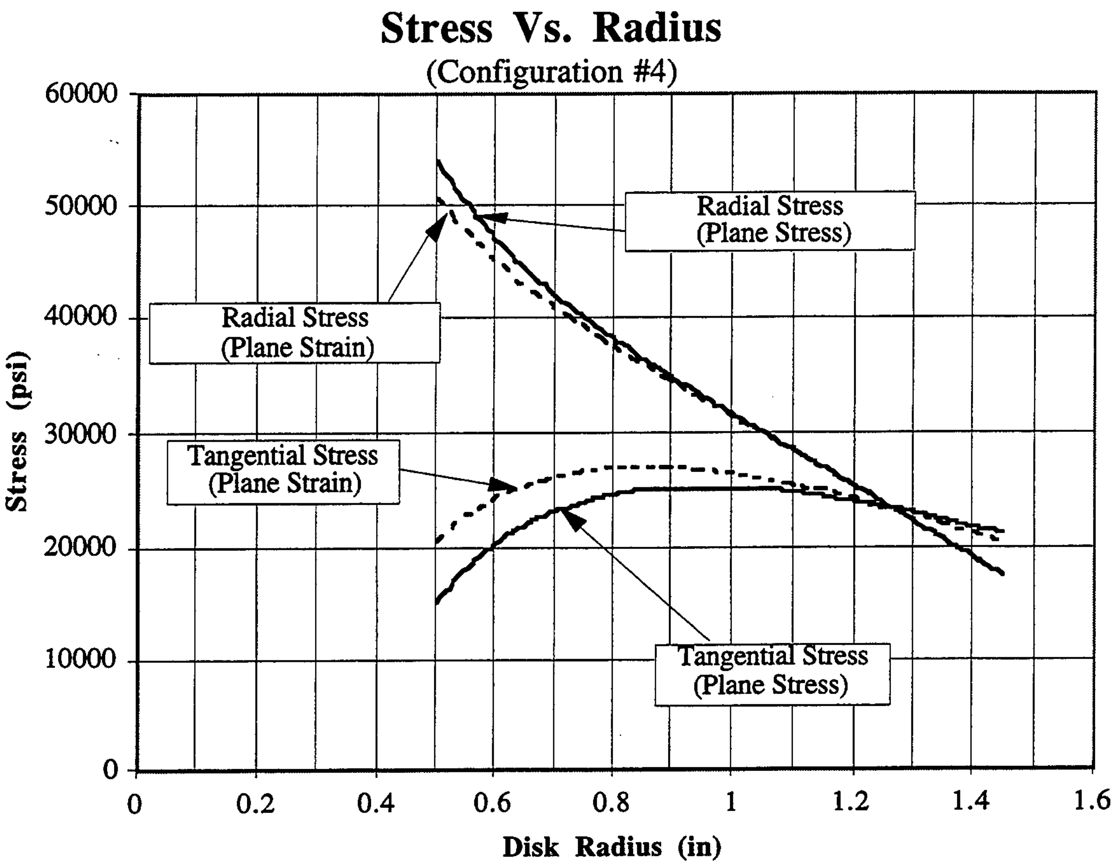

Figure 5.9 Elastically Determined Stress Profiles For Rotor Configuration #4 Tested at 1000°F, While Spinning at 55,000 RPM.

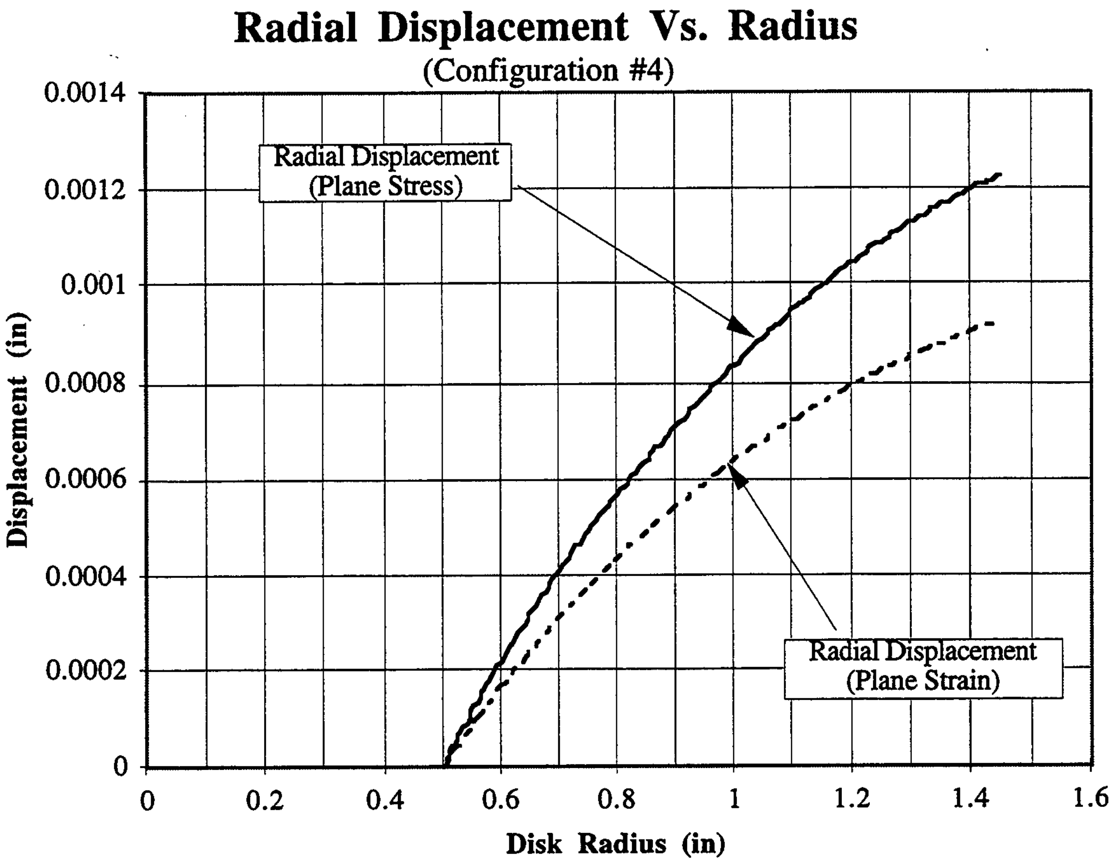

Figure 5.10 Elastically Determined Displacement Profiles For Rotor Configuration #4 Tested at 1000°F, While Spinning at 55,000 RPM.

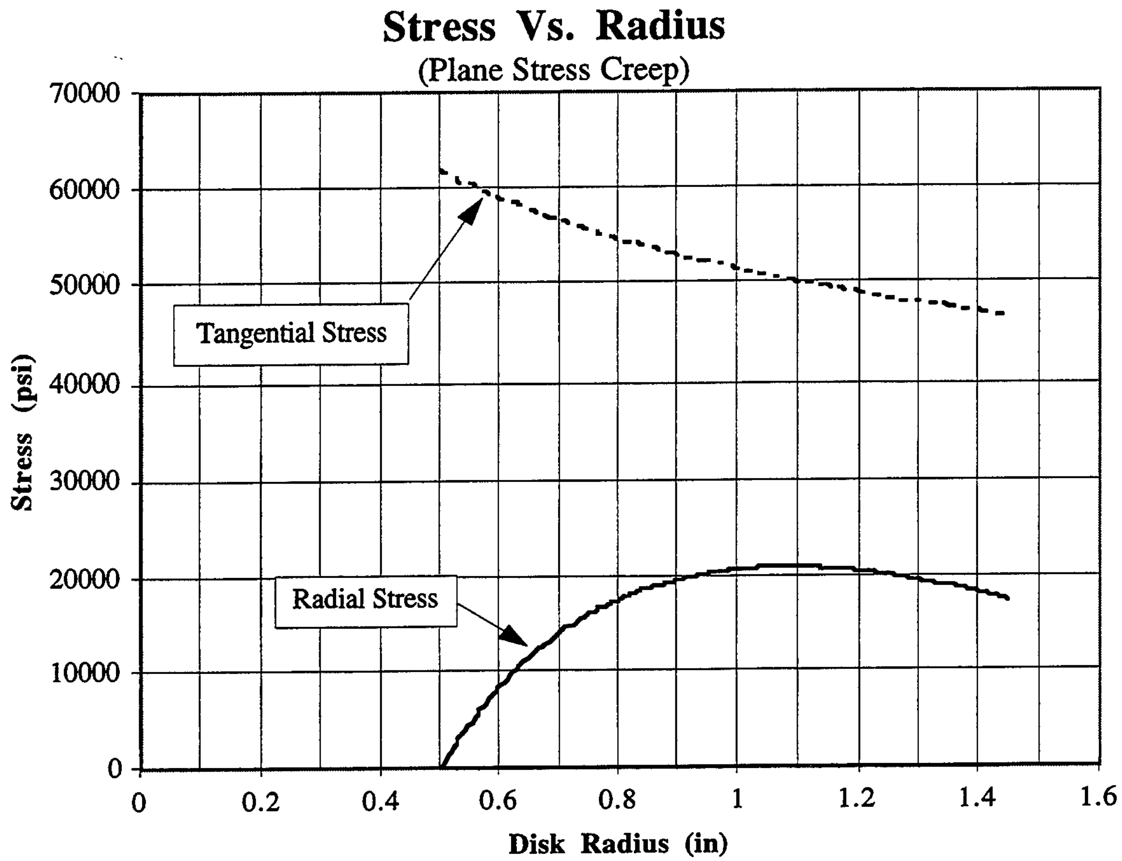

Figure 5.11 Creep Stress Profiles For Rotor Configuration #3 Tested at 1000°F (800K), While Spinning at 55,000 RPM.

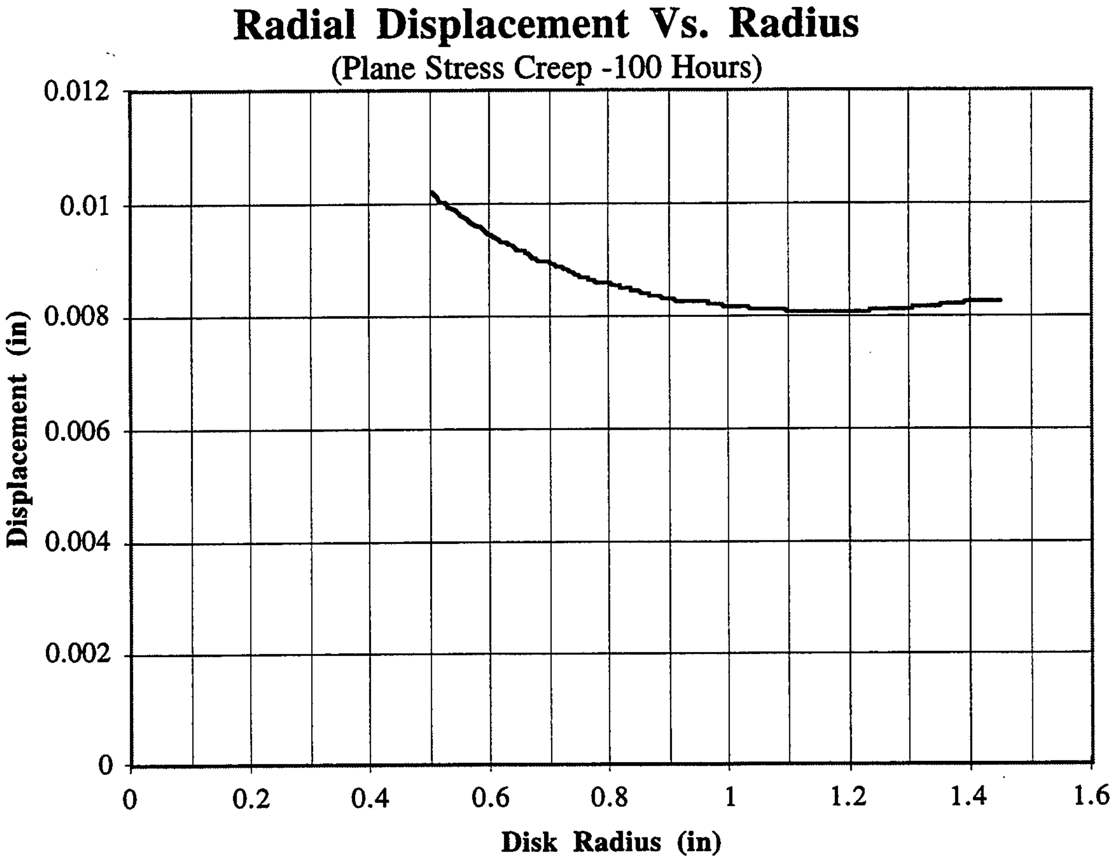

Figure 5.12 Creep Displacement Profiles For Rotor Configuration #3 Tested at 1000°F (800K), While Spinning at 55,000 RPM.

radius at a time of 100 hours. It can be seen from this plot that the hole edge has the greatest radial displacement of 0.0103 inches. After passing through a minimum value at about 1.2 inches, the displacement increases slightly to 0.0084 inches at the hub radius. The linear proportionality of radial displacement with time manifests itself in the displacement plots as identically shaped curves varying only in magnitude. For instance, from Figure 5.12, it can be determined that a displacement due to creep at the hole edge would be 0.102 at a time of 1000 hours and 0.00102 at a time of 10 hours.

The elastic and creep analyses may be used to predict the overall rotor deformation behavior. Various assumptions are made with each approach and it is not readily obvious if an elastic or creep deformation approach is best suited to describe the resulting displacements. One method is to calculate both the elastic and creep behaviors, at a specific radius for a specific set of operating parameters. This type of comparison is made in Figures 5.13 and 5.14. Figure 5.14 shows the radial deformation of the rotor hub as a function of disk rotations per minute. Calculated creep deformations at various times are shown as well as the predicted elastic response. Once the desired rotor speed has been selected the maximum hub displacement may be determined as a function of the strain contributions of both elastic and creep deformations. For instance: Figure 5.15 shows the calculated elastic displacement of the hub radius as well as the calculated creep displacement, corresponding to a time of 100 hours. Stresses associated with lower speeds result in essentially elastic deformation only. It is not until above 30,000 rpm that a deformation due to creep, at a time of 100 hours, becomes a substantial portion of the total deformation. The simplest approach to obtain the total deformation is to simply add the elastic and creep components together for a specific value of time. This approach was followed to estimate the total deformation curve illustrated in Figure 5.15. A more rigorous method for estimating total rotor displacement may be similar to the approach demonstrated by Dowling [50], which involves a Ramberg-Osgood stress-strain relation. Dowling analyzes a moment versus strain relationship for a beam of rectangular cross-section made from a material having a particular Ramberg-Osgood stress-strain curve. A similar technique could be employed for the rotor configurations, which would incorporate the elastic and creep deformations for a specific value of time. The resulting Ramberg-Osgood type curve would approach the limiting case of the elastic solution for relatively low rotor speeds and another limiting case, corresponding to the time dependent creep deformation, for higher rotor speeds. Although not exact, the total deformation corresponding to intermediate rotor speeds may be approximated as the sum of the elastic and creep displacements.

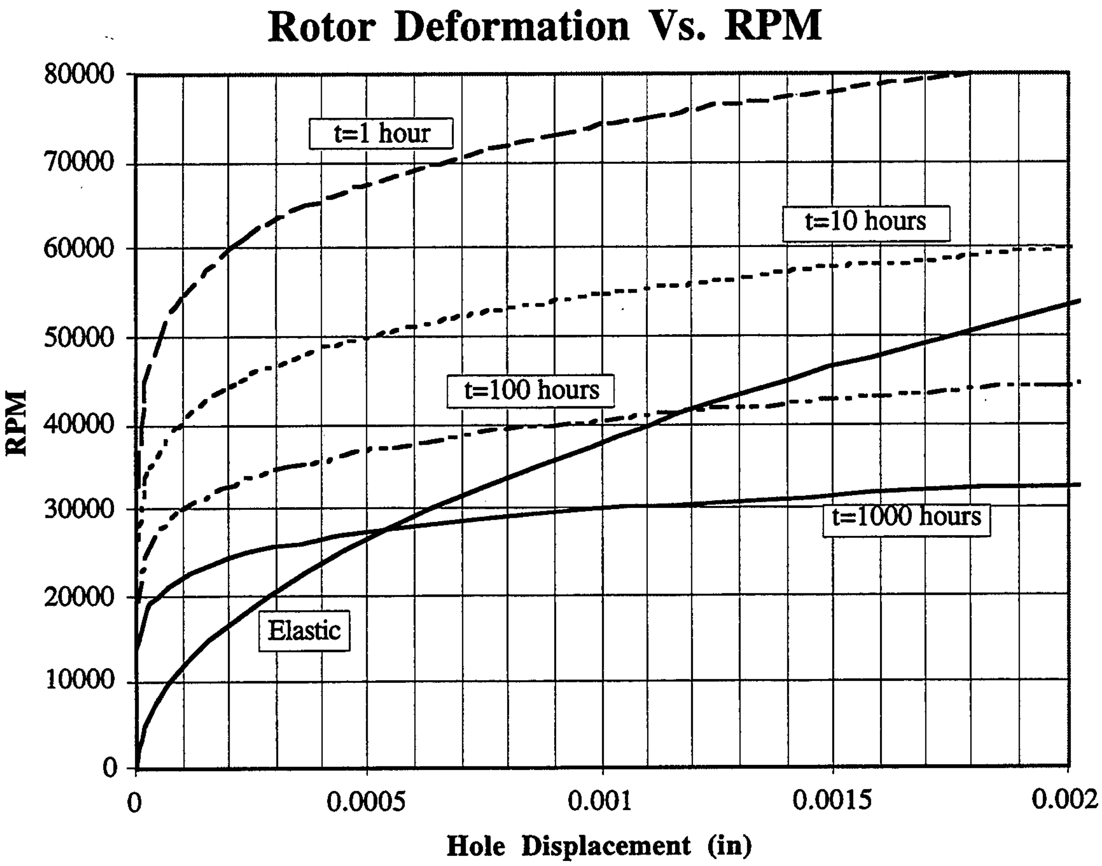

Figure 5.13 Calculated Inner Radius Deformations of Rotor Configuration #3, Tested at 1000°F, as a Function of the Rotor Speed.

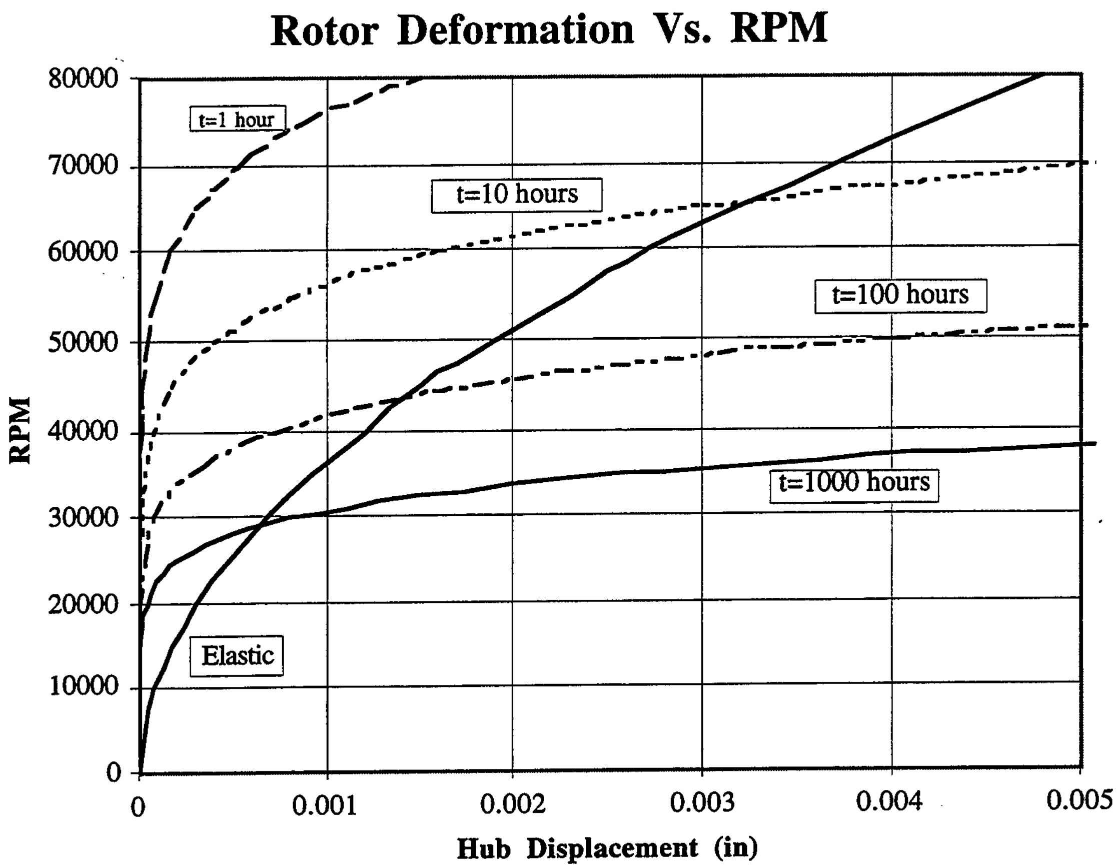

Figure 5.14 Calculated Hub Radius Deformations of Rotor Configuration #3, Tested at 1000°F, as a Function of the Rotor Speed.

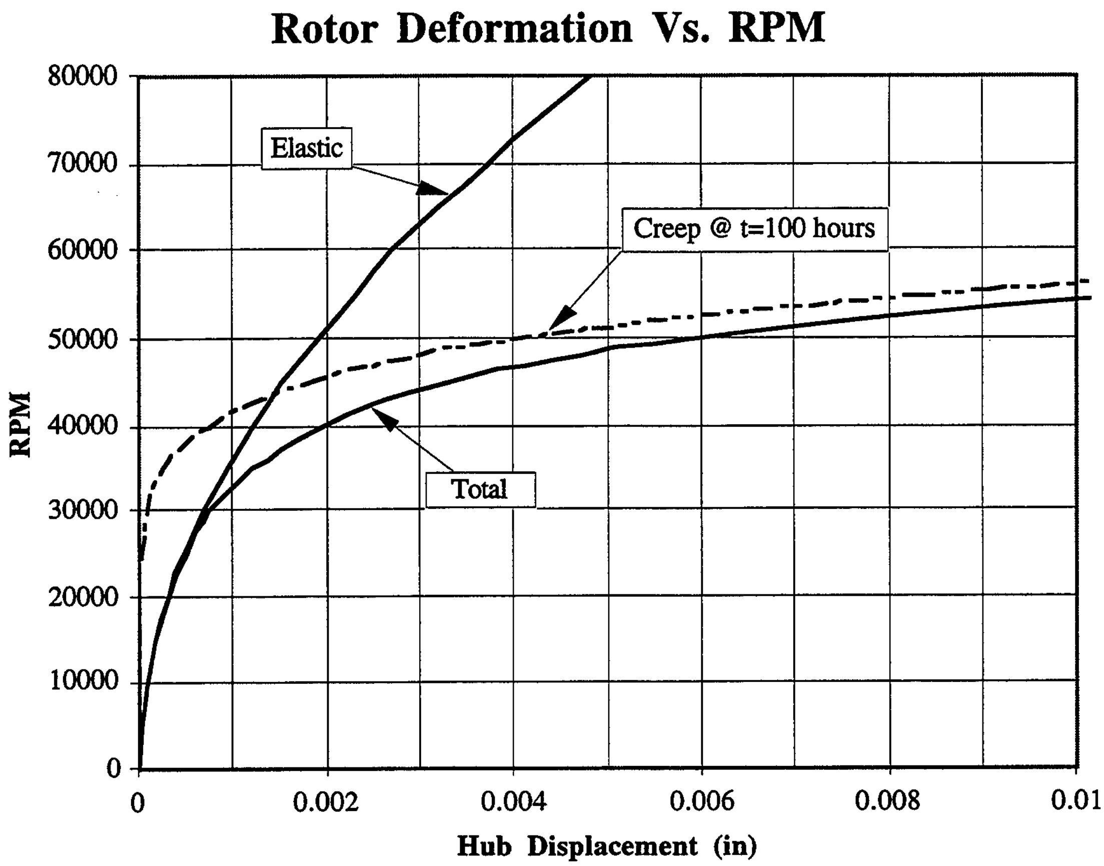

Figure 5.15 Calculated Elastic and Creep Deformations and Estimated Total Displacement of the Hub Radius of Rotor Configuration #3, Tested at 1000°F, as a Function of the Rotor Speed.

A typical air gap between the rotor and stator poles may be as small as 0.020 inches. This small spacing requires careful consideration of the hub and, subsequently, pole displacements. Figures 5.14 and 5.15 would be useful in predicting the allowable change in air gap as a function of operating time, temperature, and speed. A 0.020 inch air gap would be completely diminished in 214 hours according to the displacement curves of Figure 5.14. Obviously this displacement is governed by the creep component of the total deformation as the elastic response indicates a hub displacement of only 0.0023 inches.

6. Summary/Conclusions

6.1 Accomplishments

A great deal of new research and testing was conducted under this study, which contributed to the body of knowledge pertaining to the tensile and creep behavior of thin sheets of iron-cobalt alloys. Uniaxial tensile testing was accomplished as a function of orientation to the manufacturer's rolling direction as well as the annealing process. Additional tensile testing contributed information about the stress versus strain deformation as a function of test temperature and strain rate. A great deal of creep testing was conducted and provided deformation characteristics as a function of applied stress, test temperature, and proximity to the material yield strength. Finally, analyses were done, which incorporated experimentally determined material properties into analytical approaches to estimate the deformation of a rotor proposed for use in a potential Air Force application.

6.1.1. Tensile Testing

Of the three different annealing temperatures, the lowest temperature anneal consistently resulted in the highest strength. This relationship was anticipated and supports the Petch-Hall theory relating a larger grain size to a lower yield strength. Of the three orientations examined, the 45° orientation to the manufacturer's rolling direction was concluded to be the weakest orientation. This result was theoretically explained by pole mapping and determining the orientation and magnitude of the material texture.

Specimen geometry also played a significant role in the screening phase of this study. The second generation of specimens consistently resulted in higher yield strengths than those recorded for the original specimens. The higher yield strengths of the second specimen type indicated that the increase of the fillet radius reduced the stress concentrations, and that the recorded yield strengths were approaching the actual material property. The third generation specimen was designed with an even larger blend radius; however, its longer anneal time dominated the tensile behavior and a decrease in strength of about 9% resulted.

Nearly 50 uniaxial tensile tests were conducted on the third generation specimens, which were fabricated in the 45° orientation and annealed at 1328°F for one hour. The tests were done at temperatures ranging from -65°F to 1100°F. All of the recorded tests showed some magnitude of Lüders elongation with a yield point that was obvious at the test temperatures up to about 600°F. This behavior was eventually replaced by the Portevin-LeChatelier effect at the higher test temperatures. The elastic strain and total strain generally increased with test temperature. The ultimate strength reached a maximum value corresponding to a test temperature of about 700°F. The yield strength decreased linearly up to about 600°F, where it became virtually independent of test temperature for the higher temperatures.

Eight uniaxial tensile tests were conducted at creep regime temperatures and at constant strain rates. Rates on the order of 10^{-4} hr^{-1} up to 10^{-1} hr^{-1} were employed in order to determine the strain rate sensitivity of the material. Both upper and lower yield strengths were determined to be essentially insensitive to variations in strain rate for the 800°F and 900°F tests. This apparent independence allowed for the relatively quickly generated tensile data to be used in comparison with the relatively slowly generated creep data.

6.1.2. Creep Testing

Thirty uniaxial creep tests were conducted in this study. A potential Air Force application, requiring a rotor material capable of sustained integrity at 900°F and 85 ksi was the prime consideration for the development of the creep test matrix. Test temperatures ranged from 700°F to 1100°F which correspond to homologous temperatures of 0.36 and 0.49, respectively. The applied constant loads resulted in engineering stresses ranging from 30 to 130 ksi. Some of the creep strain versus time responses resembled the traditionally recognized creep curve while others could be characterized by an abrupt increase in the steady-state strain rate. It was concluded that the proximity of the applied stress level to the material yield strength resulted in the various response types. All of the creep testing was done at temperatures which were determined to correspond to the dynamic strain aging regime. Therefore, an upper and lower or a maximum and minimum serration stress could be determined at each test temperature. It was concluded that if the applied stress in a creep test was between the minimum and maximum serration stresses, then the abrupt increase in the steady-state strain rate would be recorded. Stress levels below the minimum serration stress resulted in a traditional creep curve while stress levels above the maximum serration stress level resulted in curves similar to the traditional response with little or no primary deformation region. With only one exception, the abrupt increase in steady-state strain rate occurred at approximately 0.65% creep strain.

Isochronous stress versus strain curves were generated from the creep test data. The curves depicted the elasto-plastic deformation, which could be estimated to occur at various constant values of time. Also, the time required for the specimen to reach a specific value creep strain was generated from the sets of creep test data. Linear relationships between stress and time were determined for constant temperatures. These curves are useful when a component failure has been determined to be a critical amount of deformation instead of an actual fracture.

As done with most creep life models, an emphasis was placed on the steady-state deformation. Since the three distinct creep strain versus time responses resulted in four separable steady-state regions, all four were modeled as well as a combination of two of the linear regions. Double linear regression analyses were applied to the applicable form of the Arrhenius rate equation to determine the necessary creep constants and corresponding statistical figures of merit. The appropriate creep constants were incorporated into the steady-state rate equation which was, in turn, plotted with the experimentally determined values. It was shown that as the strain rate increased, the stress exponent also increased, while the activation energy decreased. The applicability of the form of the Arrhenius rate equation to the higher strain rate responses was questioned, and an additional analysis, which accounts for the breakdown in the power law relationship, was done.

It was speculated within this study that the abrupt increases in the steady-state strain rate were a result of a strain, or strain-rate, induced disordering of the atomic structure. It was also speculated that the increase could be due to the onset of recrystallization along the grain boundaries. Either of these occurrences would explain the decrease in creep resistance. With these speculations in mind, an X-ray diffraction analysis was conducted on various specimens as an attempt to measure the relative amounts of atomic order. Also, microstructural investigations were done as an attempt to visually detect recrystallization. There were no indications of recrystallization, and the diffraction peaks and corresponding intensities were apparently affected by the oxidation which developed during the creep test. Unfortunately neither of these examinations provided conclusive support for either deformation theory.

One final speculation involving the abrupt increase in steady-state strain rate is based on the same phenomena associated with the occurrence of a yield point. Due to the fact that the increases occur at approximately equal creep strains, it is proposed that the number of mobile dislocations is increased proportionally with the steady-state strain rate. Considering the observed behaviors of yield point phenomena and the Portevin-LeChatelier effect, this speculation is the most likely reason for the sudden increase in steady-state strain rate. It is not certain, however, if the pinned dislocations are suddenly unpinned, or, if a dislocation source is created which quickly generates new mobile dislocations. Although not yet pursued in this study, transmission electron microscopy would illustrate whether or not a sudden increase of mobile dislocations occurred, as well as a significant increase in the total number of dislocations.

Deformation analyses were conducted on four different rotor geometries. Creep constants determined from the responses associated with applied stresses below the minimum serration stress levels were incorporated into an analytical approach for estimating the amount of time dependent deformation. Elasticity theory was used to predict stress and displacement profiles for plane strain and plane stress conditions as a function of radial position. Comparisons were made of the estimated elastic and creep displacements for the most appropriate combination of boundary conditions. Displacements at the hole edge as well as the hub edge were plotted as a function of rotor rpm for the elastic and plastic estimations.

6.2 Limitations and Applications

Curves resulting from a specific type of creep response, as discussed in section 4.3.1, can only be used reliably when the operational environment is within the limits of the test parameters used to generate the curves. Although the stress thresholds segregating the responses are fairly constant at the corresponding temperatures, there is some variation which needs to be considered. A stress threshold should never be crossed, as the strain rates are significantly affected.

It was assumed in the deformation analyses that the mass of the rotor poles was evenly distributed along the circumference of the rotor hub. This assumption allowed for axial symmetry simplifications; however, it may also have reduced the maximum pole contribution to stress at various locations. The Tresca yield criterion was assumed based on the reportings of Wahl. The neglect of the radial stress imposed by this criterion may impact the accuracy of this estimation of deformation, especially at the hole edge.

The most representative set of boundary conditions imposed is comprised of hole and hub radii that are free to deform. The radial stresses are equal to zero at the hole edge and equal to the peripheral loading at the hub edge. An actual motor or generator rotor will be comprised of many stacked laminates, most likely attached to a central shaft by an interference fit. Since the interference fit causes an inner radial stress not equal to zero, the configuration analyzed represents the real configuration only as the rotor begins to separate from the central shaft. The estimates for this configuration are still useful in that they provide the maximum deformations which may be expected.

6.3 Future Research Topics

As the Air Force requirement is new and the material is also new a great deal of mechanical information is yet to be determined. Only a cursory investigation was done on the effect of the annealing process on mechanical behavior. Although the anneal temperature range centered on the order/disorder transition temperature, it only spanned 50°F. A larger scope of annealing processes and the influence on mechanical behavior could be explored.

A detailed investigation of the abrupt increase in the steady-state strain rate may be worthwhile as the location in time of this occurrence would most likely relate to a failure of many components. Specimens used in creep tests terminated before the strain rate increase could be compared to specimens that were taken to a strain or time beyond the increase. A variation in the ordering parameter is a possible cause worth investigating. A comparison of the relative intensities of X-ray diffraction peaks may be possible if the oxidation can be removed from the specimens prior to scanning. Also neutron diffraction would certainly be capable of measuring the corresponding ordering parameters. Transmission electron microscopy to examine the type and amount of mobile dislocations would also provide supporting information when comparing the mechanical behaviors of pre- and post-knee deformations.

A probabilistic approach of life estimation, which incorporates damage due to fatigue as well as creep could be investigated. A methodology as described by Heller and Thangjitham [109] would certainly be applicable to the IPU rotor, which is cyclically loaded throughout normal operation. Placement of the rotor within the IPU or IS/G dictate the amount of cooling air available. Also, the heat generated by the windage loss and magnetic core losses will impact the operating environment of the rotor. The effects of temperature variations as a function of radial or tangential position could be investigated and incorporated into the elastic and creep deformation models.

6.4 Study Impact

As this material was introduced approximately three years ago many researchers became interested in its properties and many designers began to incorporate it into their designs. Throughout the time period of which this study was conducted, numerous inquiries and requests were made for information. Requests for mechanical data pertaining to the Hiperco® Alloy came from within the Air Force, the Army and the Navy. Also, jet engine manufacturers, magnetic bearing manufacturers, universities, and automobile industry representatives requested this data. Information relating to this Air Force study has been sent to London, Australia and all across the United States. This research has been presented to the Air Force Scientific Advisory Board and the Partners for the Next Generation Vehicle. Characterization of this material also occurred elsewhere, although it was not abundant and, due to industrial competition, the results were not often shared. Perhaps, as a result of the periodic release of data from this study, conceptual designs were changed and smaller companies had the opportunity to become more involved. Directly related to this study, contracts were awarded to universities and national laboratories to improve the creep resistance of soft magnetic iron-cobalt alloys.

It was the continual goal of this researcher to enhance the development of key technologies required for the successful demonstration of the More Electric Aircraft. It is hoped that by providing the data assimilated during this study to all of those involved, the Air Force will receive a better product in return.

7. REFERENCES

1. Quigley, R. E., "More Electric Aircraft," Conference Record, IEEE Applied Power Electronics Conference, March 7-11, 1993, p. 906-911.

2. Weimer, J., A., "Electrical Power Technology For The More Electric Aircraft," Conference Record, AIAA/AHS/ASEE Aerospace Design Conference, February 16-19, 1993, p. 445-450.

3. Cronin, M., "The All Electric Airplane Revisited," SAE Paper No. 881407, Aerospace Technology Conference and Exposition, Anaheim, CA, October 1988, p. 1-18.

4. Feiner, L., J., "Power-By-Wire Aircraft Secondary power Systems," Conference Record, AIAA/AHS/ASEE Aerospace Design Conference, February 16-19, 1993, p. 439-444.

5. Colegrove, P. G. "Integrated Power Unit for a More Electric Airplane," AIAA Paper No. 93-1188, Aerospace Design Conference, February 16-19, 1993.

6. Klaass, R. M. and B. L. McFadden, "More Electric Aircraft Integrated Power Unit Designed for Dual Use," SAE Paper No. 941159, 1994.

7. Richter, E., Lyons, J. P., Ferriera, C., Radun, A., V., and E. Ruckstadter, "Initial Testing of a 250 kW Starter/Generator for Aircraft Applications," SAE Paper No. 941160, 1994 SAE Aerospace Atlantic Conference, Dayton, OH, April 18-20, 1994.

8. Richter, E., Anstead, D. H., Bartos, J. W., and T. U. Watson, "Preliminary Design of an Internal Starter/Generator for Application in the F110-129 Engine," SAE Paper No. 951406, 1995 SAE Aerospace Atlantic Conference, Dayton, OH, 1995.

9. Richter, E. and C. A. Ferriera, "Performance Evaluation of a 250 kW Switched Reluctance Starter Generator," IEEE-IAS 95 Conference Proceedings, Orlando FL, 1995.

10. Nippes, P. I., "Magnetism and Stray Currents in Rotating Machinery," Technical Brief, Vol. 118, Journal of Engineering for Gas Turbines and Power, January 1996, p. 225-228.

11. Miller, T. J. E., "Faults and Unbalance Forces in the Switched Reluctance Machine," IAS 1993 Conference Record, Vol. 1, October 2-8, 1993, p. 87-96.

12. Quigley, R. E., "Technical and Programmatic Discussions," More Electric Aircraft Program Office, Wright Laboratory, Wright Patterson Air Force Base, Ohio, 1993-1995.

13. Cloyd, J. S., "Technical and Programmatic Discussions," More Electric Aircraft Program Office, Air Force Research Laboratory, Wright Patterson Air Force Base, Ohio, 1996-1998.

14. Loh, J. M., "Indorsement of the More Electric Aircraft," Letter From Air Combat Command, Commander to the Director of Defense, Research and Engineering, Office of the Secretary of Defense, 25 March, 1993.

15. Friedel, J., *Dislocations*, Pergamon Press, Reading, MA, 1964.

16 ASM, *Metals Handbook*, American Society for Metals, Vol. 8 Mechanical Testing, 1985.

17. Cottrell, A. H., *Dislocations and Plastic Flows in Crystals*, Oxford University Press, London, 1953.

18. Reed-Hill, R. E., *Physical Metallurgy Principles*, Litton Educational Publishing, Inc., Monterey, California, 1973.

19. Leslie, W. C., *The Physical Metallurgy of Steels*, McGraw-Hill Book Company, New York, New York, 1981.

20. Ghosh, B. and M. A. Crimp, "TEM In Situ Study of Dislocation Motion in B2 NiAl Single Crystals", Material Research Society Symposia Proceedings, Vol. 460, p. 467-472, 1996.

21. Johnston, W. G. and J. J. Gilman, "Dislocation Velocities, Dislocation Densities and Plastic Flow in Lithium Flouride Crystals," Journal of Applied Physics, Vol. 30, p. 129-144, 1959.

22. Ananthan V. S. and Hall E. O., "Macroscopic Aspects of Lüders Band Deformation In Mild Steel," Acta Metallurgica Materialia, Vol. 39, No. 12, p. 3153-3160, 1991.

23. Portevin, A. and F. LeChatelier, "Sur un phenomene observe lors de l'essai de traction d'alliages en cours de transformation," Comptes Rendus Des Seances De l'Academie Des Sciences, Vol. 176, p. 507-510, 1923.

24. Boyer, H. E., *Atlas of Stress-Strain Curves*, ASM International, Metals Park, Ohio, 1987.

25. Courtney, T. H. *Mechanical Behavior of Materials*, McGraw-Hill Publishing Company, New York, New York, 1990.

26. Hall, E. O., *Yield Point Phenomena in Metals and Alloys*, Plenum Press, NY, 1970.

27. Nabarro, F. R. N., *Theory of Crystal Dislocations*, Oxford Press, London, 1967.

28. Dinhut, J. F., Bonou, T. and P. Moine, "Phenomene Portevin-Le-Chatelier Dans Les Alliages Fe-Co Ordonnes Et Desordonnes", Acta Metallurgica, Vol. 24, p. 445-451, 1976.

29. Gonzalez-Doncel, G., Adeva, P., Cristina, M. C., and J. Ibanez, "Lüders Bands Formation In A Rapidly Solidified Ni3Al Alloy Ribbon," Acta Metallurgica, Vol. 43, No. 12, 1995, p. 4281-4287.

30. Korbel, A., Zasadzinski, J., and Z. Sieklucka, "A New Approach to the Portevin-LeChatelier Effect," Acta Metallurgica, Vol. 24, 1976, p. 919-923.

31. Marcinkowski, M. J., "Ti Effect of Atomic Order on the Mechanical Properties of Alloys with Emphasis on Fe-Co," Int Symp on Order-Disorder Transform in Alloys, Proc, Tuebingen, Ger, Sep 3-6 1973 pp. 364-403. Publ by Springer-Verlag (Reine und Angew Metallkund in Einzeldarst, Band 24), New York, 1974.

32. Gonzalez-Doncel, G., P. Adeva, M. C. Cristina and J. Ibanez, "Lüders Bands Formation in Rapidly Solidified Ni3Al Alloy Ribbon," Acta Metallurgica Materialia, Vol. 43, No. 12, pp. 4281-4287, 1995.

33. Neuhauser, H. and A. Hampel, "Observation of Lüders Bands in Single Crystals," Scripta Metallurgica et Materialia, Vol. 29, pp. 1151-1157, 1993.

34. Owen, W. S., M. Cohen, and B. L. Averbach, "Some Aspects of Preyield Phenomena in Mild Steel at Low Temperatures," Transactions of the American Society of Metals, Vol. 50, pp. 517-535, 1958.

35. Popille, F., L. P. Kubin, J. Douin, and S. Naka, "Portevin-LeChatelier Instabilities and Stoichiometric effects in B2 Titanium Aluminides," Scripta Metallurgica et Materialia, Vol. 34, No. 6, pp. 997-984, 1996.

36. Stoloff, N. S. and R. G. Davies, "The Plastic deformation of Ordered FeCo and Fe_3Al Alloys," Acta Metallurgica, Vol. 12, p. 473-485, 1964.

37. Stoloff, N. S. and R. G. Davies, "The Mechanical Properties of Ordered Alloys," Progress in Material Sciences, Vol. 13, p. 1-84, 1966.

38. Zhao, L., Baker, I. and E. P. George, "Room Temperature Fracture of FeCo", Material Research Society Symposia Proceedings, Vol. 288, p. 501-506, 1993.

39. Baker, I. and E. M. Schulson, "On Grain Boundary Disorder and the Tensile Ductility of Polycrystalline Ordered Alloys: A Hypothesis", Scripta Metallurgica, Vol. 23, p. 345-348, 1989.

40. Glezer, A. M. and I. V. Maleyeva, "Structural Features of Alloy Fe-Co Produced by Quenching from the Molten State", Physics of Metals and Metallography, Vol. 68, No. 5, p. 65-72, 1989.

41. Marcinkowski, M. J. and R. M. Fisher, "Atomic Order and Petch Relation in an FeCo Alloy", Transactions of the Metallurgical Society of AIME, Vol. 233, p. 293-298, 1965.

42. Jordan, K. R. and N. S. Stoloff, "Plastic Deformation and Fracture in FeCo-2pct V," Transactions of the Metallurgical Society of AIME, Vol. 245, p. 2027-2034, 1969.

43. Schulson, E. M., "The Effect of Grain Size on the Flow and Fracture of Long-Range Ordered Alloys", Material Research Society Symposia Proceedings, Vol. 39, p. 193-204, 1985.

44. Farkas, D. and Z. Y. Xie, "Possibilities of Slip Modification in B2 NiAl", Material Research Society Symposia Proceedings, Vol. 288, p. 435-440, 1993.

45. Boyer, H. E., *Atlas of Creep and Stress-Rupture Curves*, ASM International, Metals Park, Ohio, 1988.

46. Finnie, I., and W. R. Heller, *Creep of Engineering Materials*, McGraw-Hill Book Company, New York, New York, 1959.

47. Menon, M. N. "A Model for Primary, Secondary and Tertiary Creep Rates", Proceedings of the Fifth International Conference on Creep of Materials, pp. 163-169, 1992.

48. Andrade, E. N. DaC. "On the Viscous Flow of Metals, and Allied Phenomena," Proceedings of the Royal Society, Section A, 84, pp. 1-12, 1910.

49. Andrade, E. N. DaC. "The Flow in Metals Under Large Constant Stresses," Proceedings of the Royal Society, Section A, Vol. 90, p. 329-341, 1914.

50. Dowling, N. E., *Mechanical Behavior of Materials*, Prentice Hall, Englewood Cliffs, New Jersey, 1993.

51. Nabarro, F. R. N., "Report of a Conference on the Strength of Solids," Physical Society, London, p.75, 1948.

52. Herring, C., "Diffusional Viscosity of a Polycrystalline Solid," Journal of Applied Physics, Vol. 21, pp. 437-445, 1950.

53. Coble, R. L., "A Model for Boundary Diffusion Controlled Creep in Polycrystalline Materials," Journal of Applied Physics, Vol. 34, pp. 1679-1682, 1963.

54. Weertman, J., "Steady-State Creep Through Dislocation Climb," Journal of Applied Physics, Vol. 28, pp. 362-364, 1957.

55. Weertman, J., "Steady-State Creep 0f Crystals," Journal of Applied Physics, 28, pp. 1185-1189, 1957.

56. Shi, L. and D. O. Northwood, "Recent Progress in the Modeling of High Temperature Creep and Its Application to Alloy Development," Journal of Materials Engineering and Performance, Vol. 4(2), pp. 196-211, 1995.

57. Raj, R. and M. F. Ashby, "On Grain Boundary Sliding and Diffusional Creep," Metallurgical Transactions, Vol. 2, pp. 1113-1127, 1971.

58. Sherby, O. D., and J. E. Dorn, "Creep Correlations in Alpha Solid Solutions of Aluminum", Transactions of the AIME, Journal of Metals, p. 959-964, 1952.

59. Larson, F. R., and J. Miller, "A Time-Temperature Relationship for Rupture and Creep Stresses", American Society of Mechanical Engineers, Paper No. 51-A-36, p. 765-775, 1952.

60. Manson, S. S., and A. A. Haferd, "A Linear Time-Temperature Relation for Extrapolation of Creep and Stress Rupture Data", National Advisory Committee for Aeronautics, Technical Note 2890, 1953.

61. Conway, J. B. *Stress Rupture Parameters: Origin, Calculation and Use*, Gordon and Breach, New York, 1969.

62. Goldhoff, R. M., "A Comparison of Parameter Methods for Extrapolating High-Temperature Data", Journal of Basic Engineering, p. 629-643, 1959.

63. Frost, H. J., and M. F. Ashby, *Deformation-Mechanism Maps The Plasticity and Creep of Metals and Ceramics*, Pergamon Press, Elmsford, New York, 1982.

64. Arrhenius, S., "Über die Reaktionsgeschwindigkeit bei der Inversion von Rohrzucker durch Sauren," Zeitschrift Feur Physikalische Chemie, Vol. 4, p. 226-248, 1889.

65. Kampe, S. L., "Technical Discussions," Material Science and Engineering Department, Virginia Polytechnic Institute and State University, Blacksburg, Virginia, 1998.

66. Crossman, F. W. and M. F. Ashby, "The Nonuniform Flow of Polycrystals by Grain Boundary Sliding Accommodated by Power Law Creep," Acta Metallurgica, Vol. 23, No. 4, pp. 425-440, 1975.

67. Orowan, E., "The Creep of Metals," Journal of West Scotland Iron Steel Inst., Vol. 54, pp. 45-96, 1947.

68. Langdon, T. G., "Grain Boundary Sliding as a Deformation Mechanism During Creep," Philosophy Magazine, Vol. 22, No. 178, pp. 689-100, 1970.

69. Cullity, B. D., *Introduction to Magnetic Materials*, Addison-Wesley Publishing Company, Inc., Reading, MA, 1972.

70. Simon, G. K., Perrin, R. E., Ohmer, M. C., and Peterson, T. L., 1996, "Resistivity of $Fe_{.49}Co_{.49}V_{.02}$ High Strength Laminates From -73C to +650C," Wright Laboratory Report No. WL-TR-97-4006, Wright Laboratory, Wright-Patterson Air Force Base, Ohio.

71. Simon, G. K., Perrin, R. E., Ohmer, M. C., and Peterson, T. L., 1997, "Resistivity of $Fe_{.49}Co_{.49}Ta_{.01}$ High Strength Laminates From -73C to +650C," Wright Laboratory Report No. WL-TR-97-4047, Wright Laboratory, Wright-Patterson Air Force Base, Ohio.

72. Certificate of Conformity of HS 50 Strip, Serial Number 55912, Telcon Limited, 26 May, 1995.

73. Hiperco® Alloy 50HS Data Sheet, *Electronic Alloys*, Carpenter Technology Corporation, 1995.

74. Fingers, R. T., and Kozlowski, G., 1997, "Microstructure and Magnetic Properties of Fe-Co Alloys," Journal of Applied Physics, Vol. 81, No. 8, p. 4110 - 4111.

75. Masteller, M. S., "Technical Discussions," Carpenter Technology Corporation, Reading, PA, 1993-1995.

76. Kelly, A. and R. B. Nicholson, *Strengthening Methods in Crystals*, p 195, Halsted Press Division John Wiley & Sons, Inc., New York, 1971.

77. Stoloff, N. S., "Ordered Alloys for High Temperature Applications," Material Research Society Symposia Proceedings, Vol. 39, p. 3-27, 1985.

78. Kawahara, K., "Effect of Additive Elements on Cold Workability in FeCo Alloys," Journal of Material Science, Vol. 18, p. 1709-1718, 1983.

79 ASTM, "Standard Test Methods for Tension Testing of Metallic Materials," American Society for Testing and Materials, Standard E8-94c, 1994.

80 ASTM, "Standard Test Methods for Elevated Tension Tests of Metallic Materials," American Society for Testing and Materials, Standard E21-92, 1992.

81 ASTM, "Standard Practice for Conducting Creep, Creep Rupture, and Stress Rupture Tests of Metallic Materials," American Society for Testing and Materials, Standard E139-83, 1990.

82. Peterson, R. E., *Stress Concentration Factors*, John Wiley & Sons, New York, 1974.

83. Honeycombe, R. W. K., *The Plastic Deformation of Metals*, Edward Arnold PTY Ltd, Victoria, Australia, 1984.

84. Kueser, P. E., Pavlovic, D. M., Lane, D. H., Clark, J. J. and M. Spewok, "Properties of Magnetic Materials for Use in High-Temperature Space Power Systems," National Aeronautics and Space Administration, NASA SP-3043, 1966.

85. Fingers, R. T., Coate, J. E., and N. E. Dowling, "Mechanical Properties of Iron-Cobalt Alloys for Power Applications," Proceedings of the 32nd Intersociety Energy Conversion Engineering Conference, Vol. 4, Paper No. 97364, p. 563-568, 1997.

86. Shanley, F. R., *Weight-Strength Analysis of Aircraft Structures*, McGraw Hill Book Company, Inc., New York, 1952.

87. McClave, J. T. and F. H. Dietrich II, *Statistics*, Dellen Publishing Company, San Francisco, California, 1982.

88. Tang, W. H. and A. H. S. Ang, *Probability Concepts in Engineering, Planning and Design*, Wiley Publishing Company, New York, 1975.

89. Dowdy, S. and S. Wearden, *Statistics for Research*, John Wiley and Sons, New York, 1983.

90. Jonas, J. J., "A Comparison of Creep and Hot Working Strain-Rate Relationships," Transactions of the American Society for Metals, Vol. 62, No. 1, p. 300-303, 1969.

91. Jonas, J. J., Sellers, C. M., and W. J. McG. Tegart, "Strength and Structure Under Hot Working Conditions," Metals Review, Vol. 14, p. 1-24, 1969.

92. Garafalo, F., "An Empirical Relation Defining the Stress Dependence of Minimum Creep Rate in Metals," Transactions of the Metallurgical Society of AIME, Vol. 227, p. 351-356, 1963.

93. Hosford, W. F. and R. M. Caddell, *Metal Forming Mechanics and Metallurgy*, PTR Prentice Hall, Englewood Cliffs, New Jersey, 1993.

94. Cullity, B. D., *Elements of X-Ray Diffraction*, Addison-Wesley Publishing Company, Inc., Reading, MA, 1956.

95. Zhu, Q., Li, L., Masteller, M. S., and G. J. DelCorso, "An Increase of Structural Order Parameter in Fe-Co-V Soft Magnetic Alloy After Thermal Aging," Applied Physics Letters, Vol. 69, p. 3917-3919, 16 December, 1996.

96. Ashby, M. F. and A. Abel, "Materials Selection to Resist Creep," Philosophical Transactions of the Royal Society of London, Vol. 351, p. 451-468, 1995.

97. Sada, A. S., *Elasticity Theory and Application*, Krieger Publishing Company, Malabar, Florida, 1993.

98. Thangjitham, S., "Technical Discussions," Engineering Science and Mechanics Department, Virginia Polytechnic Institute and State University, Blacksburg, Virginia, 1998.

99. Budiansky, B., and O. L. Mangasarian, "Plastic Stress Concentration at a Circular Hole in an Infinite Sheet Subjected to Equal Biaxial Tension," Journal of Applied Mechanics, Paper No. 59-AMPW-16, p. 59-64, 1960.

100. Mangasarian, O. L., "Stresses in the Plastic Range Around a Normally Loaded Circular Hole in an Infinite Sheet," Journal of Applied Mechanics, Paper No. 59-A-130, p. 65-73, 1960.

101. Budiansky, B., "An Exact Solution to an Elastic-Plastic Stress-Concentration Problem," Prikladnaia Matematika I Mekhanika, Academy of Sciences, U.S.S.R, Vol. 35, No. 1, p. 40-48, 1971.

102. Wahl, A. M., Sankey, G. O., Manjoine, M. J., and E. Shoemaker, "Creep Tests of Rotating Disks at Elevated Temperature and Comparison with Theory," ASME Applied Mechanics Division, Paper No. 53-A-61, p. 225-235, 1953.

103. Wahl, A. M., "Analysis of Creep in Rotating Disks Based on the Tresca Criterion and Associated Flow Rule," ASME Applied Mechanics Division, Paper No. 55-A-46, p. 225-235, 1955.

104. Wahl, A. M., "Stress Distributions in Rotating Disks Subjected to Creep at Elevated Temperature," ASME Applied Mechanics Division, Paper No. 56-A-162, p. 299-305, 1956.

105. Wahl, A. M., "Further Studies of Stress Distribution in Rotating Disks and Cylinders Under Elevated-Temperature Creep Conditions," ASME Applied Mechanics Division, Paper No. 57-A-91, p. 243-250, 1957.

106. Wahl, A. M., "Effects of the Transient Period in Evaluating Rotating Disk Tests Under Creep Conditions," ASME Applied Mechanics Division, Paper No. 62-Met-10, p. 66-70, 1963.

107. Mendelson, A., *Plasticity: Theory and Application*, The Macmillan Company, New York, 1968.

108. Timoshenko, S., *Strength of Materials*, Robert E. Krieger Publishing Company, Malabar, Florida, 1983.

109. Heller, R. A. and S. Thangjitham, "Probabilistic Service Life Prediction for Creep-Fatigue Interaction," AIAA, Paper No. AIAA-96-1560-CP, p. 2144-2147, 1996.

8. APPENDIX A - HEAT TREATING SPECIFICATIONS

SPECIFICATION FOR ANNEALING OF HIPERCO® ALLOY 50 HS MAGNETIC LAMINATES

Prepared by:
AFRL/ML/PR

1. Scope: This specification covers dry hydrogen annealing of Hiperco® Alloy 50 HS which is an Fe-Co alloy (48.75% Co, balance Fe, 1.90% V, 0.30% Nb, 0.05% Mn, 0.05% Si, 0.01% C).

2. Applicable Documents: MIL-H-6875, Military Specification, Heat Treatment of Steel, Process for.

3. Furnaces and Temperature Controllers: The furnaces and temperature controllers shall conform to MIL-H-6875. The recorder shall provide a continuous time-temperature curve for the entire annealing cycle.

Caution: Any over temperature will result in 100% scrap since there is no annealing treatment to revert the over temperature exposed parts back to the required condition.

4. Material: The material to be annealed is Hiperco® Alloy 50 HS, which is an Fe-Co alloy, in the form of machined specimens of laminates. The specimens will include approximately 300 rectangles of 6 inches by one inch.

5. Processing:

Loading: Load uniformly in furnace to assure uniform heat distribution during annealing.

Annealing: The annealing should be carried out in an atmosphere of pure dry hydrogen, having an entry dew point of better than -60°F (-51°C) and an exit dew point dryer than -40°F (-40°C) when the inside retort temperature is above 900°F (482°C). There shall be one anneal to be done at a load temperature of **1328°F** (720°C).

Heat the parts to 600°F (316°C) and hold at temperature until the exit dew point is better than -40°F (-40°C). When satisfactory, increase the temperature to 900°F (482°C) and hold until a dew point of -40°F (-40°C) is achieved. Then, raise the temperature of the furnace until the specified load temperature is achieved. Hold at this temperature, ±5°F (2.8°C) is desirable, for **1 hour**, then cool at a rate between 150°F (66°C) and 350°F (177°C) per hour down to 600°F (316°C), after which any cooling rate can be employed.

Appearance: All annealed parts shall show a clean surface free of scale with some discoloration permissible.

6. Quality Assurance:

1. All indicating and recording instruments and controllers must have proper calibration records which show that the time between calibrations has not exceeded one month. The temperature uniformity within the furnace must have been confirmed from the results of the nine thermocouple temperature uniformity survey conducted with a survey frequency not to exceed one year.

2. All processing shall be performed by personnel who are adequately trained in the use and operation of the equipment.

3. The supplier shall submit an appropriate certificate of compliance, attesting that the parts have been processed in accordance with the above instructions. The deliverables include the temperature-time chart for the entire annealing cycle, and any records that are normally provided for the details pertaining to the maintaining of the dew point during annealing and the purity of the dry hydrogen atmosphere.

7. Contact: The AFRL point of contact will be Mr. Rick Fingers (937) 255-6549.

SPECIFICATION FOR OXIDATION OF HIPERCO® ALLOY 50 HS MAGNETIC LAMINATES

Prepared by:
AFRL/ML/PR

1. Scope: This specification covers oxidation of Hiperco® Alloy 50 HS which is an Fe-Co alloy (48.75% Co, balance Fe, 1.90% V, 0.30% Nb, 0.05% Mn, 0.05% Si, 0.01% C).

2. Applicable Documents: MIL-H-6875, Military Specification, Heat Treatment of Steel, Process for.

3. Furnaces and Temperature Controllers: The furnaces and temperature controllers shall conform to MIL-H-6875. The recorder shall provide a continuous time-temperature curve for the entire oxidizing cycle.

4. Material: The material to be oxidized is Hiperco® Alloy 50 HS, which is an Fe-Co alloy, in the form of machined specimens of laminates. The specimens will include approximately 300 rectangles of 6 inches by one inch.

5. Processing:

Loading: Load uniformly in furnace to assure uniform heat distribution during oxidation.

Oxidizing: The oxidizing should be carried out in an air atmosphere. The specimens shall be degreased and handled appropriately to avoid oily deposits (finger prints). Heat the parts to 750°F (399°C) and hold at temperature for approximately 45 minutes, then remove parts from the furnace and cool in air to room temperature.

Appearance: All oxidized parts shall show a very thin bluing oxidation.

6. Quality Assurance:

1. All indicating and recording instruments and controllers must have proper calibration records which show that the time between calibrations has not exceeded one month. The temperature uniformity within the furnace must have been

confirmed from the results of the nine thermocouple temperature uniformity survey conducted with a survey frequency not to exceed one year.

2. All processing shall be performed by personnel who are adequately trained in the use and operation of the equipment.

3. The supplier shall submit an appropriate certificate of compliance, attesting that the parts have been processed in accordance with the above instructions. The deliverables include the temperature-time chart for the entire oxidizing cycle.

7. Contact: The AFRL point of contact will be Mr. Rick Fingers (937) 255-6549.